U.S.NRC
United States Nuclear Regulatory Commission
Protecting People and the Environment

RIL 2024-13

Next Generation Liquefaction Models for Susceptibility, Triggering, and Manifestation, Rev. 0

March 2024

K. J. Ulmer[1]
K. S. Hudson[2,3]
S. J. Brandenberg[2]
P. Zimmaro[4,2]
R. Pretell[5]
B. Carlton[6]
S. L. Kramer[7]
J. P. Stewart[2]

[1]Southwest Research Institute
San Antonio, Texas

[2]University of California, Los Angeles
Los Angeles, California

[3]Hudson Geotechnics, Inc.
El Segundo, California

[4]University of Calabria
Arcavacata di Rende, Italy

[4]University of Nevada
Reno, Nevada

[6]Norwegian Geotechnical Institute
Oslo, Norway

[7]University of Washington
Seattle, Washington

Thomas Weaver, NRC Project Manager

Research Information Letter
Office of Nuclear Regulatory Research

Disclaimer

Legally binding regulatory requirements are stated only in laws, NRC regulations, licenses, including technical specifications, or orders; not in Research Information Letters (RILs). A RIL is not regulatory guidance, although NRC's regulatory offices may consider the information in a RIL to determine whether any regulatory actions are warranted.

EXECUTIVE SUMMARY

Seismic induced soil liquefaction is a phenomenon that can lead to soil instability and large ground deformations due to a reduction in soil stiffness and shear strength. Safety related structures, systems, or components are at greater risk of losing function if supported on soils that experience liquefaction. Regulatory Guide 1.198 provides guidance to applicants on acceptable methods for evaluating the potential for liquefaction initiation (triggering). Regulatory Guide 1.198 was last published in 2003 and is based on technical information developed prior to 2000. In 2016, the National Academies of Sciences, Engineering, and Medicine published a report providing recommendations for research that can improve scientific understanding of the liquefaction phenomenon and engineering practice in evaluating liquefaction triggering and consequences associated with liquefaction. This report documents research that implemented recommendations from the National Academies in developing new empirical liquefaction models. One goal of this research is to provide the technical basis for updating guidance on acceptable methods in evaluating risks to nuclear facilities from liquefaction triggering.

Three models were developed as part of the research documented in this report: a liquefaction susceptibility model, a liquefaction triggering model, and a liquefaction surface manifestation model. The liquefaction susceptibility model is used to evaluate the probability that soil can experience liquefaction under seismic shaking. The liquefaction triggering model is used to determine the probability that a susceptible soil will liquefy for a given intensity of ground shaking, and the manifestation model is used to estimate the probability that there will be surface manifestation of liquefaction. Examples of surface manifestation are ground cracking, ground settlement, and liquefied soil ejecta on the ground surface. The triggering and manifestation models were developed using data from the Next Generation Liquefaction database. Liquefaction triggering models have historically been used to determine if significant soil strength loss due to liquefaction is expected at a new nuclear power plant site, and the triggering model developed in this research is expected to be useful for future nuclear power plant siting evaluations. The surface manifestation model may be useful in assessing the risk that liquefaction poses to light weight surface founded micro-reactors.

The research presented in this report was reviewed by an external panel. Some external review comments were not addressed in this version of the report due to the timing of the authors receiving the review comments. This report will be revised under a new contract between the United States Nuclear Regulatory Commission and Southwest Research Institute to address all external peer review comments. The forthcoming revision is not expected to result in substantive changes to the models described in this report.

ABSTRACT

The objective of this letter report is to fulfill Task 7 of a contract that was jointly supported by the U.S. Nuclear Regulatory Commission (NRC) and the U.S. Bureau of Reclamation (USBR). Under Task 7, a probabilistic triggering model was developed that is capable of being used in combination with a seismic hazard analysis to obtain the annual frequency of liquefaction triggering. The purpose of this report is to document the development of this model. To that end, this report discusses the Supported Modeling Team's (SMT) approaches to (i) use the extensive NGL case history and laboratory test results database to perform analyses that previously would have been logistically impractical, and (ii) develop relationships required to compute the probabilities of liquefaction susceptibility, triggering, and ground surface manifestation.

The analysis framework developed by the SMT has several elements. First, we assess susceptibility solely in consideration of soil type and behavior considerations and express results in a probabilistic manner instead of binary "yes" or "no" determinations. Second, we evaluate the triggering of liquefaction in a manner that recognizes the distinction between what is generally available from case histories (surface manifestation or lack thereof) and what should be the outcome of a triggering analysis (probability of triggering of a given layer within a soil profile). Several approaches for evaluating triggering that account for this dichotomy are presented. Third, we introduce a probabilistic approach for evaluating probability of surface manifestation (or lack thereof) based on whether a layer within the profile has triggered, attributes of soil composition in that layer, and stratigraphic information such as layer thickness and depth.

In Chapter 2, we define technical terms that comprise the framework for liquefaction analysis presented in this report (susceptibility, triggering, manifestation), present the motivation for the work described in this report, and describe our research approach. In Chapter 3, we summarize some of the major previous liquefaction triggering models that utilize a critical layer framework for representing the conditions at a site and some of the challenges inherent to that approach. In Chapter 4, we outline the regression framework that has been used for developing the models. This approach relies on Bayes theorem and separately considers the mechanisms of liquefaction triggering and manifestation. In Chapter 5, we describe the steps required to process liquefaction case histories and assign layers and their properties for use in model development. These steps include several new elements including a Kriging interpolation method to consistently estimate peak ground acceleration (*PGA*) from nearby recording stations, a model to relate soil behavior type index (I_c) to fines content (*FC*), and an automated layer detection algorithm. In Chapter 6, we provide the components of the model, which include an equation to compute the probability of triggering based on data from cyclic tests performed in the laboratory and equations to compute the probability of surface manifestation based on soil layers derived from cone penetrometer test (CPT) data and triggering probabilities within the layers. We also explore sensitivities of the manifestation model. In Chapter 7 we outline the limitations of the models presented in this report and identify future work that has the potential to improve model performance. Finally, in Chapter 8, we summarize the conclusions of our work.

Although not designated as a formal Senior Seismic Hazard Analysis Committee (SSHAC) study, the approach and processes we relied on as the SMT to develop our models followed several of the basic SSHAC principles. These included evaluation and integration of available data, clearly defined roles and responsibilities of all project members, and transparent documentation of the SMT decisions needed to develop our findings. In addition, the model presented in a previous version of this report (August 2023) has been peer reviewed by the Modeling Review Team (MRT), with all comments received prior to March 22, 2024 documented

in a separate report along with SMT responses (Task 8, Ulmer et al., 2024). The purpose of the MRT review was to provide feedback on the SMT's methods but does not necessarily constitute an endorsement of the SMT's methods, results, or recommendations.

Our findings provided in this report are nearing their final form, although future refinements and improvements are possible. The content presented here is subject to change as we refine the methodologies, input parameters, and framework, and based on review comments from the MRT received after March 22, 2024. Where possible, comments from the MRT have been directly addressed in this report. Comments from the MRT that were not received with sufficient time remaining in the project schedule may be addressed in derivative products (e.g., journal papers) where feasible. While the general concepts behind our approach have been shared in meetings with the NGL Advisory Board and other NGL modeling teams, this document presents these concepts in greater detail and is more up-to-date than any prior presentation. Accordingly, we look forward to receiving feedback from regulatory agencies, topical experts, practicing engineers, and others about the modeling approach and the reasonableness and practicality for application of the models that have been presented.

Reference

Ulmer, K.J., K.S. Hudson, S.J. Brandenberg, P. Zimmaro, S.L. Kramer, and J.P. Stewart. "Task 8: Model Review Team Comments." Washington, DC: U.S. Nuclear Regulatory Commission. March 2024.

TABLE OF CONTENTS

LIST OF FIGURES

LIST OF TABLES

LIST OF SYMBOLS

Key Definitions

Clay-like – *Clay-like* is a description of soil behavior that applies to materials that exhibit characteristic features of clayey soils, including normalization of undrained shear strength with effective consolidation stress and relatively fat cyclic stress strain loops following the onset of cyclic strength loss.

initial liquefaction – *Initial liquefaction* occurs in saturated granular soil subjected to cyclic shear loading (e.g., earthquake ground motions) under undrained conditions when excess pore water pressure equals initial vertical effective stress.

liquefaction susceptibility – As used in this report, *liquefaction susceptibility* is related to fundamental material characteristics of the soil that control the level of pore pressure generation and strength loss that is possible if the soil were to be cyclically sheared. Susceptibility is unrelated to the density and current saturation level of the soil; while both of these factors affect the potential for triggering, they do not control the fundamental behavior of a soil. Susceptible soils include both predominantly coarse-grained and fine-grained soils which exhibit "sand-like" behavior. Soils which exhibit "clay-like" behavior are not considered susceptible to liquefaction but could be subject to strength loss from cyclic softening.

liquefaction triggering – *Liquefaction triggering* occurs in liquefaction-susceptible soils when the liquefaction demand exceeds the soil's capacity to resist liquefaction. The demand and capacity terms can be expressed as metrics in a stress-, strain-, or energy-based framework. The stress-based framework is most commonly used in practice and is used in this report. In the stress-based framework, the demand term is the cyclic stress ratio (*CSR*) and the capacity term is the cyclic resistance ratio (*CRR*). Thus, liquefaction triggering occurs when *CSR* exceeds *CRR*.

liquefaction manifestation – *Liquefaction manifestation* is the observable consequence of liquefaction triggering in liquefaction-susceptible soils. The type and magnitude of the consequence can vary. Forms of manifestation include settlement and lateral displacement, sediment ejecta (e.g., sand boils), slumping and failure of embankments, loss of foundation support, increased lateral loads on and reduced lateral resistance of earth retaining structures and their foundations, buoyancy uplift of buried structures, and modification of free-field ground motions. Some of these are readily visible at the ground surface (i.e., *surficial manifestation*), while others such as decreased strength at depth may not be easily observed. The excess pore pressures and levels of strain that develop in a profile influence whether the effects of

liquefaction are visually apparent, or manifest, at the ground surface.

Sand-like – *Sand-like* is a description of soil behavior that applies to materials that exhibit characteristic features of granular soils, including non-parallel consolidation and critical state lines (indicating lack of strength normalization) and potential for substantial strength loss under cyclic loading when the material is saturated, sufficiently loose, and subjected to undrained cyclic loading.

state – The *state* of a soil refers to its position in void ratio – effective stress space relative to a critical state line (CSL). Contractive soils have void ratios above the CSL and would need to generate positive pore pressures under undrained conditions to reach the CSL at large strains. Dilative soils have void ratios below the CSL and would need to dilate to reach the CSL. A soil with a dilative state can be temporarily contractive when cyclically sheared at small strains, causing positive water pressures to develop.

Symbols

α ratio of τ_s to σ'_{v0}

CAV *cumulative absolute velocity*
CAV_5 *cumulative absolute velocity with a minimum acceleration cutoff of 5 cm/s²*
C_N overburden stress correction factor for in situ tests (e.g., SPT, CPT)
CSR cyclic stress ratio = τ_{cyc}/σ'_{v0}
$CSR_{\mathbf{M}7.5}$ *CSR* corrected for **M**7.5
$CSR_{\mathbf{M}7.5,1atm}$ *CSR* corrected for **M**7.5 and 1 atm of overburden stress
CRR cyclic resistance ratio
CRR_{lab} *CRR* as estimated from cyclic tests performed in the lab
CRR_{field} CRR_{lab} adjusted to more closely reflect field conditions
C_R crust layer resistance parameter (Hutabarat and Bray, 2022)

γ_w unit weight of water (9.81 kN/m^3)
γ_{DA} double-amplitude shear strain
γ_{SA} single-amplitude shear strain

D_r relative density

ε_v volumetric strain
ε_{DA} double-amplitude axial strain
ε_{SA} single-amplitude axial strain

FC percent fines content by weight, fines are defined as particles smaller than 0.075 mm
FS_L factor of safety against liquefaction = *CRR/CSR* (e.g., $CRR/CSR_{\mathbf{M}7.5,1atm}$)

g acceleration of gravity

ϕ_{cs} critical state friction angle
Φ Gaussian cumulative distribution function

H_1 thickness of a non-liquefiable (i.e., non-susceptible and/or non-saturated) surficial soil layer
H_2 thickness of an underlying liquefiable (i.e., susceptible and saturated) soil layer
h_A initial hydraulic head (Hutabarat and Bray, 2022)
h_{exc} excess hydraulic head

I_c soil behavior type index
$\hat{I}_c$ standardized variable of I_c
I_B modified soil behavior type index

K_0 coefficient of lateral pressure at-rest
$(K_0)_{field}$ coefficient of lateral pressure at-rest estimated for field conditions
$(K_0)_{lab}$ coefficient of lateral pressure at-rest imposed in laboratory tests
K_α initial static shear stress adjustment factor
K_d drainage adjustment factor
K_{sat} saturation correction factor
K_σ initial overburden stress adjustment factor
k_{cs} clean sand corrected vertical hydraulic conductivity
k_v vertical hydraulic conductivity

L_D liquefaction ejecta demand parameter (Hutabarat and Bray, 2022)
LL liquid limit from Atterberg limits tests
LPI liquefaction potential index (Iswasaki et al., 1978)
LPI_{ISH} Ishihara-inspired liquefaction potential index (Maurer et al., 2015a)
LSN liquefaction severity number (van Ballegooy et al., 2014)

M earthquake magnitude, typically moment magnitude
MSF magnitude scaling factor

N SPT blow count
N number of cycles to liquefaction in cyclic lab tests
$N_{1,60cs}$ $N_{1,60}$ adjusted for clean sand conditions
N_L number of layers
N_{ref} reference number of cycles to liquefaction associated with **M**7.5 (e.g., 10-15)
N_P number of profiles

p_a atmospheric pressure (1 atm = 101.3 kPa)
PF probability factor
PGA peak ground acceleration, generally taken as median component
PI plasticity index, or LL – PL
PL plastic limit from Atterberg limits tests
P_L probability of triggering of liquefaction (i.e., a function of *CSR* and penetration resistance as computed from probabilistic legacy models)

q_c cone tip resistance from CPT

q_{c1N} q_c adjusted for 1 atm overburden (through C_N)
q_{c1Ncs} q_{c1N} adjusted for clean sand conditions
$\hat{q}_{c1Ncs}$ standardized variable of q_{c1Ncs}
q_t cone tip resistance from CPT (q_c) corrected for pore pressure

r_d shear stress reduction factor
r_u pore pressure ratio

s_u undrained shear strength

σ_v total vertical stress
σ'_{v0} initial vertical effective stress

t layer thickness
t_c characteristic layer thickness
$T_{P[Mp]}$ threshold P[M_P] value associated with OOP

τ_{cyc} cyclic shear stress
$\tau_{cyc,max}$ maximum cyclic shear stress
τ_s initial static shear stress

u_{exc} excess pore water pressure

V_s small-strain shear wave velocity
V_{s30} time-averaged shear wave velocity within the upper 30 meters

w_c water content

z depth measured from ground surface
z_A the depth below the groundwater table depth or the bottom depth of a crust layer that is at least 250 mm thick with $I_c \geq 2.6$ if below the groundwater table, per Hutabarat and Bray (2022)
z_B the top depth of a soil layer that is at least 250 mm thick after the first continuous sand-like layer with $I_c \geq 2.6$ between depths of z_A and 10 m (z_B will be 10 m if there is no such soil layer), per Hutabarat and Bray (2022)
z_{top} depth to the top of a soil layer

P[T] probability of triggering
P[NT] probability of no triggering
P[M] probability of manifestation
P[NM] probability of no manifestation
P[$T|M$] probability that liquefaction did occur in a critical layer for case histories where manifestation was observed
P[$T|NM$] probability that liquefaction did occur in a critical layer for case histories where manifestation was *not* observed
P[$NT|NM$] probability that liquefaction did *not* occur in a critical layer for case histories where manifestation was *not* observed
P[$NT|M$] probability that the soil in the critical layer did *not* trigger for case histories where manifestation was observed
P[$M|T$] probability of manifestation given triggering

$P[M\|NT]$	probability of manifestation given no triggering
$P[NM\|T]$	probability of no manifestation given triggering
$P[NM\|NT]$	probability of no manifestation given no triggering
$P[T_L]$	probability of triggering in a layer
$P[NT_L]$	probability of no triggering in a layer
$P[M_L\|T_L]$	probability of manifestation at the surface conditional upon triggering in a particular layer
$P[M_L\|NT_L]$	probability of manifestation at the surface conditional upon no triggering in a particular layer
$P[M_L]$	probability of manifestation of a layer
$P[NM_L]$	probability of no manifestation of a layer
$P[M_P]$	probability of manifestation of the profile
$P[S]$	probability of susceptibility
$P[T\|S]$	probability of triggering conditioned on the soil being susceptible
$P[T_L\|S]$	probability of triggering in a layer conditioned on the layer being susceptible

ACRONYMS/ABBREVIATIONS

AUC	area under the curve in a ROC analysis
BI06	Boulanger and Idriss (2006) susceptibility criterion
BI12	Boulanger and Idriss (2012)
BI14	Boulanger and Idriss (2014)
BI16	Boulanger and Idriss (2016)
BS06	Bray and Sancio (2006) susceptibility criterion
CDSS	cyclic direct simple shear
CPT	cone penetrometer test
CSL	critical state line
CSV	comma separated value
CTRX	cyclic triaxial
CTS	cyclic torsional shear
CV-CDSS	constant-volume CDSS
DWG	Database Working Group
FN	false negative prediction
FLDM	field manifestation (e.g., FLDM ID in the NGL database)
FP	false positive prediction
FPR	false positive rate
FRS	Fraser River Sand
GED	Geosciences and Engineering Department
GMIM	ground motion intensity measure
GMM	ground motion model
GUI	graphical user interface
HB22	Hutabarat and Bray (2022)
IM	intensity measure
ICL	isotropic consolidation line
MAP	maximum a posteriori probability
MRT	Model Review Team
NASEM	National Academies of Science, Engineering, and Medicine
NGA	Next Generation Attenuation
NGL	Next Generation Liquefaction
NRC	U.S. Nuclear Regulatory Commission
OOP	optimum operating point from ROC curve

PEER	Pacific Earthquake Engineering Research
PLHA	probabilistic liquefaction hazard analysis
PMT	Project Management Team
RG	Regulatory Guide
ROC	receiver operating characteristic
SFEV	surface evidence tag (0 = no surface manifestation, 1 = yes surface manifestation)
SMT	Supported Modeling Team
SPT	standard penetration test
SQL	structured query language
SwRI®	Southwest Research Institute®
TN	true negative prediction
TP	true positive prediction
TPR	true positive rate
UCLA	University of California, Los Angeles
U.S.	United States
USGS	United States Geological Survey
USBR	United States Bureau of Reclamation

ACKNOWLEDGMENTS

This report was prepared to document work performed by the Geoscience and Engineering Department (GED) at Southwest Research Institute® and its contractors for the U.S. Nuclear Regulatory Commission (NRC) under Contract No. 31310018D0002 and through an interagency agreement with the U.S. Bureau of Reclamation (Agreement Number R20PG00126). The activities reported here were performed on behalf of the NRC Office of Nuclear Regulatory Research. The report is an independent product of GED and does not necessarily reflect the views or regulatory position of the NRC.

The authors wish to acknowledge members of the Next Generation Liquefaction (NGL) community for their contributions to the aims of NGL that have supported this work, including:

- NGL Database Working Group (DWG) members for their work on the NGL database;
- NGL Executive Advisor Prof. I.M. Idriss and NGL Advisory Board members (Profs. Misko Cubrinovski, Jonathan Bray, and Ross Boulanger) for their suggestions and insight;
- Dr. Brian Carlton and Prof. Armin Stuedlein for their work on NGL supporting studies; and
- members of other NGL modeling teams for fruitful discussions.

We also gratefully acknowledge Miriam Juckett and Lane Howard for project management, John Stamatakos for technical review of this report, and Arturo Ramos for administrative support.

QUALITY OF DATA, ANALYSES, AND CODE DEVELOPMENT

DATA: The primary data source for the work described herein is the NGL database (http://nextgenerationliquefaction.org, doi: 10.21222/C23P70, Ulmer et al., 2023; Brandenberg et al., 2020). The NGL database contains data related to case histories of earthquake-induced liquefaction. These data are from the geotechnical community, including academic researchers and practicing engineers. Because the intent of the database is to accumulate as much useful and publicly available data as possible from the technical community, some of this data is from existing scientific and technical publications and peer reviewed journals, but some could also be sourced from the working records of researchers and engineers. The data are uploaded to the database via a graphical user interface (GUI). Reviewers evaluate the quality of data after it is uploaded to provide quality control. For other data references in the database, such as the earthquake records from the Next Generation Attenuation project, users should consult the original sources to determine the level of quality of those data.

Other data sources are cited throughout the report and stored in project folders PRJ-3368 and PRJ-2923 on DesignSafe-CI (designsafe-ci.org)

ANALYSES AND CODES: The NGL database is a relational database that was developed using the My Structured Query Language (MySQL) relational database management system. The NGL database schema (i.e., its organizational structure) and a meta-dictionary that

contains information about each database entry are available at http://nextgenerationliquefaction.org (Brandenberg et al., 2020).

REFERENCES

Brandenberg, S.J., P. Zimmaro, J.P. Stewart, D.Y. Kwak, K.W. Franke, R.E.S. Moss, K.O. Cetin, G. Can, M. Ilgac, J. Stamatakos, T. Weaver, and S.L. Kramer. “Next-Generation Liquefaction Database.” *Earthquake Spectra*. Vol. 36, No. 2. pp. 939–959. 2020.

Ulmer K.J., P. Zimmaro, S.J. Brandenberg, J.P. Stewart, K.S. Hudson, A.W. Stuedlein, A. Jana, A. Dadashiserej, S.L. Kramer, K.O. Cetin, G. Can, M. Ilgac, K.W. Franke, R.E.S. Moss, S.F. Bartlett, M. Hosseinali, H. Dacayanan, DY. Kwak, J. Stamatakos,J. Mukherjee, U. Salman, S. Ybarra, and T. Weaver. Next-Generation Liquefaction Database, Version 2. Next-Generation Liquefaction Consortium. doi: 10.21222/C23P70. 2023.

1 INTRODUCTION

1.1 Project Background

The U.S. Nuclear Regulatory Commission (NRC) has identified the need to update existing regulatory guidance on the methods used to evaluate seismic soil liquefaction in Regulatory Guide (RG) 1.198, "Procedures and Criteria for Assessing Seismic Soil Liquefaction at Nuclear Power Plant Sites" (NRC, 2003). RG 1.198 provides guidance to NRC licensees on acceptable methods for evaluating seismic induced liquefaction that demonstrates compliance with Title 10 of the *Code of Federal Regulations* (10 CFR) 100.23, "Geologic and Seismic Siting Criteria." The U.S. Bureau of Reclamation (USBR) is also interested in updated methods to assess liquefaction in support of its Dam Safety Program.

Within the largely deterministic and semi-empirical NRC guidance in RG 1.198, sites that do not pass screening or susceptibility criteria are required to undergo more detailed analysis methods. RG 1.198 recommends application of relationships from Youd et al. (2001) when using semi-empirical procedures to assess the potential for liquefaction triggering. This method, which was the consensus industry standard in the late 1990s and early 2000s, is a semi-empirical relationship based on a database of case histories that was initially developed by Seed et al. (1985). More recent liquefaction case history databases have been developed by research groups at several universities. Alternate approaches to model development and different interpretations of available data by various modeling teams have resulted in different semi-empirical relationships that often produce divergent estimates of liquefaction triggering potential. This issue was at the core of a National Academies of Sciences, Engineering and Medicine (NASEM) Report on the State of Practice in evaluating the potential for earthquake-induced liquefaction triggering and consequences (NASEM, 2016, 2021). The recommendations in that report informed the scope and purpose of this project, as discussed in this report.

The alternative of a probabilistic approach for liquefaction triggering analysis is mentioned in RG 1.198 but details on what would comprise an acceptable probabilistic approach are not described. The recommendations from the NASEM (2016, 2021) report also point to the need for probabilistic liquefaction analysis methods. Specifically, the NASEM report recommends that more fully probabilistic analyses should "incorporate the complete range of possible damaging earthquake ground motions (in terms of both ground motion intensity and earthquake magnitude), their probable frequency of occurrence, and the variability in the parameters and adjustment factors used to estimate the *CRR*." In addition, the NASEM report recommends that "these probabilistic analyses can incorporate the epistemic uncertainty among the available empirical models by using a logic tree approach that can also be used to consider uncertainty in the site characterization. The uncertainties involved in the assessment of earthquake ground motions, system response, physical damage, and losses make probabilistic methods for liquefaction consequence assessment central to performance- based evaluation and design."

Under the current task order (31310019F0030), supported jointly by the NRC and the USBR, staff in the Geosciences and Engineering Department (GED) at Southwest Research Institute® (SwRI®) and subcontractors at the University of California, Los Angeles (UCLA) are tasked with developing a liquefaction triggering model based on an expanded database of liquefaction case histories. Because liquefaction models are subject to interpretation of available data, it is important that new probabilistic models capture epistemic uncertainty and aleatory variability of inputs. Accordingly, the goal of this modeling task aims to capture the center, body, and range of technically defensible interpretations. Past reports provided to the NRC and USBR (e.g., Task 2 report, Ulmer et al., 2021; Task 4 report Ulmer et al., 2022c; Task 5b report,

Ulmer et al., 2022a; and Task 7a report Ulmer et al., 2023c) discuss the expanded database, other relevant supporting studies, and earlier phases of model development in more detail.

Prior to the USBR and the NRC's efforts, the Pacific Earthquake Engineering Research (PEER) Center initiated the Next Generation Liquefaction (NGL) project in 2013. The objective of the NGL initiative is to organize research in soil liquefaction and related topics into a framework conducive to broad data dissemination and development of improved procedures for modeling of liquefaction susceptibility, triggering, and various effects. To meet these objectives, the NGL project is organized into several activities, including database development (Brandenberg et al., 2020; NGL, 2021), supporting studies, and model development. Through the current contract between NRC/USBR-SwRI, we are collaborating with the NGL project to work toward common goals. The work described herein was performed by the Supported Modeling Team (SMT) and is part of NGL's model development efforts. Other NGL modeling teams are developing alternative models to evaluate liquefaction triggering and its effects, but their efforts are not supported by the NRC/USBR-SwRI contract and are not detailed herein.

The NGL project is organized into several teams as shown in Table 1-1. Some of these teams operate outside of the current NRC/USBR-SwRI contract while others were fully or partially supported by the contract as noted in the table. Each team had an assigned role associated with one or more of the three main NGL activities (i.e., database development, supporting studies, model development).

Table 1-1 NGL project participants

Team		Role	Individuals
SMT	Supported Modeling Team*	Develop preliminary and final liquefaction triggering model	Steven L. Kramer (SMT-Lead) Scott J. Brandenberg Kenneth S. Hudson Kristin J. Ulmer Paolo Zimmaro
MRT	Modeling Review Team*	Participatory peer review of preliminary and final model	Izzat. M. Idriss Lelio Mejia Thomas J. Weaver Derek Wittwer
PMT	Project Management Team*	Manage budget, schedule, meetings, and supporting activities	John Stamatakos Jonathan P. Stewart Steven L. Kramer
NGL Advisory Board (active through July 2023[1])		Technical advice for all NGL activities	Ross W. Boulanger Jonathan D. Bray Misko Cubrinovski Izzat. M. Idriss (Executive Advisor)

[1]Prof. Ross Boulanger was a named member of the NGL Advisory Board and his initial reviews and comments were appreciated. Over the course of the work (since 2021), Prof. Boulanger was absent from NGL engagements with the SMT and PMT despite attempts to reengage.

Table 1-1 NGL project participants (cont'd)			
Team	**Role**	**Individuals**	**Team**
DWG	Database Working Group**	Technical and programmatic management of the NGL Database	Scott J. Brandenberg Paolo Zimmaro Kristin J. Ulmer Kenneth S. Hudson Robb E.S. Moss K. Önder Cetin Kevin W. Franke
NGL Modeling Teams		Develop models for liquefaction susceptibility, triggering, and/or consequences using the NGL database	Kramer et al. (SMT) Moss/Çetin/Kayen et al., Franke/Lingwall/Stuedlein/Olson Green/Rodriguez-Marek et al., Baise/Maurer/Thompson Dashti/Kamai/Liel et al., Okamura/Kiyota Carlton/Geyin et al.,
NGL Supporting Studies**		Perform supporting research to fill knowledge gaps not represented by the case history database	Stuedlein et al. (susceptibility) Carlton et al. (overburden and shear stress effects)
*Supported by SwRI/NRC-USBR contract **Partial support from SwRI/NRC-USBR contract			

1.2 Tasks Under the Current NRC/USBR-SwRI Contract

Table 1-2 summarizes the tasks under the current NRC/USBR-SwRI contract. This current contract has a period of performance from September 2019 through the end of March 2024. This report provides CPT-based models to fulfill Task 7, and an addendum to this report that provides SPT-based models fulfills Task 9.

Table 1-2 Summary of tasks under the current NRC/USBR-SwRI contract	
1	Kickoff Meeting
2	Liquefaction Case History Database 2a: Add Case Histories to the NGL Database 2b: Address Feedback from Modeling Teams 2c: Database Maintenance
3	Establish Modeling Team
4	Develop Preliminary CPT-based Model Using NGL Database

Table 1-2	Summary of tasks under the current NRC/USBR-SwRI contract (cont'd)
5	Evaluate the Effects of Confining Stress and Initial Static Shear Stress on Liquefaction Triggering 5a: Test/analysis plan 5b: Draft technical letter report 5c: Final draft technical letter report
6	Preliminary Model Peer Review
7	Develop Updated Triggering Model 7a: Technical letter report documenting progress 7b: Draft technical letter report on updated models 7c: Final technical letter report on updated models
8	Peer Review of Updated CPT-based Models
9	Develop SPT-based Model(s) 9a: Draft technical letter report on model(s) 9b: Final technical letter report on model(s)

The authors of this report are responsible for Tasks 4 and 7. The main goal of Tasks 4 and 7 is to develop a model for predicting the occurrence or non-occurrence of liquefaction using an expanded dataset of liquefaction case histories and results of supporting studies. Under a previous contract with the NRC, the graphical user interface (GUI) for this expanded database was developed by SwRI staff and the Database Working Group (DWG). The DWG continues to provide oversight for and expand the database under Task 2 of the current NRC/USBR-SwRI contract. We met frequently with the DWG to identify data needs, reconcile discrepancies in documentation of the case histories, and clarify interpretations of the data in the NGL database.

The Model Review Team (MRT) is responsible for reviewing the main products of the SMT and assessing whether the SMT used appropriate methods and considered a broad range of data and models, as outlined in Tasks 6 and 8. This review does not necessarily constitute an endorsement by the MRT of the SMT's methods, results, or recommendations. The MRT is composed of two external consultants, a representative from NRC, and a former representative from USBR. An earlier version of this report was provided to the MRT for their review (August 2023). The earlier version of this report has been peer reviewed by the MRT, with all comments received prior to March 22, 2024 documented in a separate report along with SMT responses (Task 8, Ulmer et al. 2024)..

1.3 Objectives of Study and Scope of Report

The original scope of Tasks 4 and 7 of the current NRC/USBR-SwRI contract was to develop a probabilistic triggering model that is capable of being used in combination with a seismic hazard analysis to obtain the annual frequency of liquefaction triggering. In the course of the project and in consultation with members of the NGL Advisory Board and other NGL modeling teams, we concluded that models developed using case history data need to consider triggering in combination with manifestation. Accordingly, as part of the deliverables for Tasks 4 and 7, we provide liquefaction models which include susceptibility, triggering, and manifestation. By

making this change, we clarify the meaning of key terms in liquefaction analysis, provide a framework by which the different effects can be evaluated in a consistent and rational manner, and highlight a major innovation of this study relative to prior work.

The purpose of this report is to document the development of these susceptibility, triggering, and manifestation models. To that end, this report discusses the SMT's approaches to (i) use the extensive NGL case history database to perform analyses that previously would have been logistically impractical and (ii) develop relationships required to compute probabilities of liquefaction susceptibility, triggering, and surface manifestation. A preliminary version of these models was presented in the Task 4 report (Ulmer et al., 2022c) and an update to those models was provided in the Task 7A report (Ulmer et al., 2023c).

Several independent groups provided feedback on the Task 4 report in its entirety or on individual concepts or approaches documented therein. Some of these groups are contractually obligated to support the current NRC/USBR-SwRI project, and others are part of the worldwide NGL project. A summary of the sources of feedback to date on the Task 4 report include:

- The MRT. The MRT was composed of liquefaction experts, including external consultants and members of the USBR and NRC project management teams that oversaw the NRC/USBR-SwRI project. The MRT was tasked with providing review comments as part of Task 6 and Task 8 in Table 1-1. Their feedback on the Task 4 report was formally documented in the Task 6 report and more informally through several virtual discussions with the SMT.

- NGL Advisory Board. The NGL Advisory Board was composed of liquefaction experts who were not formally supported on the NRC/USBR-SwRI project. They provided advice and recommendations related to all NGL activities over most of the project duration (through July 2023). Members of the SMT met with the Advisory Board monthly or bi-monthly. Some members of the NGL Advisory Board provided written comments to the Task 4 report and the SMT informally discussed these comments in regular NGL Advisory Board meetings.

- Others, including members of the NGL modeling teams. NGL modeling teams are those teams who intend to use the NGL database to develop liquefaction models and meet bi-monthly to share results and discuss relevant topics of interest. The SMT is one of the NGL modeling teams. Although the Task 4 report in its entirety was not shared with the NGL modeling teams, the SMT presented several of the concepts in the Task 4 report as they were being developed in order to solicit informal feedback from other NGL modeling teams.

The following chapters describe updated liquefaction models. As such these models replace those presented in the Task 4 report. In Chapter 2, we define technical terms that comprise the framework for liquefaction analysis presented in this report (susceptibility, triggering, manifestation), present the motivation for the work described in this report, and describe our research approach. In Chapter 3, we summarize some of the major previous liquefaction triggering models that utilize a critical layer framework for representing the conditions at a site and some of the challenges inherent to that approach. In Chapter 4, we outline the regression framework that has been used for developing the updated triggering models. This approach separately considers the mechanisms of liquefaction triggering and manifestation. In Chapter 5, we describe the steps required to process liquefaction case histories and assign layers and their properties for use in model development. These steps include several elements including a

model to relate soil behavior type index (I_c) to fines content (FC), an automated layer detection algorithm, and a modeling approach for predicting the probability of surface manifestation. In Chapter 6, we provide the components of the updated model, which include equations to compute the probability of triggering based on data from cyclic tests performed in the laboratory and equations to compute the probability of surface manifestation based on soil layers derived from cone penetrometer test (CPT) data and triggering probabilities within the layers. In Chapter 7 we outline the limitations of the models presented in this report and identify future work that has the potential to improve model performance. Finally, in Chapter 8, we summarize the conclusions of our work.

2 BACKGROUND

To provide a better understanding of the components of the proposed preliminary model and the necessity of the advances presented in this report, we provide the following brief summary of the mechanics of liquefaction and the current state-of-the-art in liquefaction evaluation. For a more detailed description, we recommend reviewing summary documents such as the 2016 state-of-the-art and state-of-the-practice report by the NASEM (2016; 2021).

2.1 Liquefaction Mechanics

Soil liquefaction (referred to simply as "liquefaction" for the rest of this document) is a substantial loss of soil stiffness and shear strength that results from increased pore water pressures. Increased pore water pressures occur in contractive or temporarily contractive saturated granular soil subjected to cyclic shear loading (e.g., earthquake ground motions) under undrained loading that if continued for a sufficient duration can cause the pore water pressures to approach the level of the initial vertical effective stress (σ'_{v0}). If the pore pressures reach σ'_{v0}, a state of *initial liquefaction* (Seed and Lee, 1966) is reached. Alternative definitions of liquefaction have been based on granular soil reaching certain levels of cyclic shear strains, which may occur at different times than initial liquefaction. The levels of strain that develop in a profile, and their proximity to the ground surface, influence whether the effects of liquefaction are visually apparent, or *manifest*, at the ground surface.

Some soil types cannot experience liquefaction–for example, clays generally do not develop cyclic pore pressures as large as those for sands, and while they can experience strength loss, it is generally less severe than that for sands (with the exception of quick clays). For this reason, it is necessary to distinguish soils *susceptible* to liquefaction from those that are not. The use of different terms in relation to liquefaction problems (susceptibility, triggering, manifestation) has the potential to cause confusion. Our aims here are to clearly define those terms and to describe the past modeling approaches relied on by the liquefaction research and engineering community.

2.1.1 Liquefaction Susceptibility

Within the geotechnical engineering community, different engineers have different understandings of the word "susceptibility" as applied to liquefaction problems (Chapter 3 of Stuedlein et al., 2023b). However, as used here, *liquefaction susceptibility* is related to fundamental material characteristics of the soil that control the level of pore pressure generation and strength loss that is possible if the soil were to be cyclically sheared. Susceptibility is unrelated to the density and current saturation level of the soil; while both of these factors affect the potential for triggering, they do not control the fundamental behavior of a soil.

Two end members of soil response to cyclic loading can be simply summarized as "sand-like" behavior (i.e., liquefiable) and "clay-like" behavior (i.e., not liquefiable). Fine-grained soils can either exhibit clay-like or sand-like behavior. Clays will tend to exhibit clay-like behavior. The mechanical properties of clays are controlled by inter-particle interactions that are influenced by various types of chemical bonding; such materials experience strength loss from pore pressure increase, but strength from chemical bonding remains and strength loss is somewhat moderated. Silts can have different levels of plasticity and may exhibit sand-like or clay-like behavior. Some silt particles are sand-like in that they exhibit the same mechanical properties as sands (strength is related to gravitational forces and becomes very small when pore pressure approaches the initial effective stress). Other silts can be influenced by chemical bonding, as for

clays. Soil plasticity, as described by the plasticity index (*PI*), is loosely connected to these soil behavior types; granular soils including some silts (e.g., rock flour) are non-plastic whereas clays are by definition plastic. An analysis of susceptibility seeks to distinguish these soil behavior types.

Based on these considerations, Boulanger and Idriss (2006) (BI06) recommended procedures to distinguish fine-grained soils for modeling purposes as either “sand-like” materials that can liquefy or “clay-like” materials that can experience cyclic softening. Figure 2-1 shows the positions of different soil materials in *PI*-*LL* space (as used for a plasticity chart, where *LL* is the liquid limit), and suggests that soils with $PI > 7$ are clay-like and soils with $PI < 4$ are sand-like. Boulanger (2023) argued that BI06 should not be considered to be a susceptibility model due to its intended purpose to guide the selection of tools for ground failure modeling. However, given the definition of susceptibility adopted here, for practical purposes we consider BI06 to be a laboratory-based susceptibility model.

Another susceptibility model is that of Bray and Sancio (2006) (BS06), who assembled cyclic test data from soil samples from Adapazari, Turkey, which experienced ground failure in the 1999 Kocaeli earthquake. The cyclic test results were used to distinguish materials with different engineering responses. Materials were considered to be liquefiable if they experience excess pore water pressure ratios, $r_u > 90\%$ and similar ‘banana-shaped’ cyclic shear stress vs. cyclic shear strain loops and to be not liquefiable if they lack those characteristics. As shown in Figure 2-2, they found that silts and clays with $PI \leq 12$ and water content (w_c) greater than 85% of *LL* were liquefiable according to this definition, while soils with $PI > 18$ and $w_c < 0.8$LL were not.

Boulanger (2023) argued that the BI06 and BS06 criteria serve different purposes and should not be compared. This issue was discussed extensively at a 2022 PEER workshop (Stuedlein et al., 2023b), because most practitioners use these as alternative susceptibility models. We consider the two models to, in effect, represent alternative methods for evaluating whether a soil should be considered susceptible to liquefaction for modeling purposes. As noted by Stuedlein et al. (2023b) – “The models are supported by experimental data and the expert interpretation of that data by their developers. Differences in the models can largely be attributed to differences in the data they are based upon, and differences in the developers’ interpretation of that data.” Accordingly, the differences between the models represents epistemic uncertainty, which can be significant for many applications. Potential causes for these differences include the different soils that were tested; different methods of test data interpretation to judge different types of soil behavior; and the cyclic testing for the two studies having been performed at different stress levels (i.e., the ratio of applied shear stress to undrained strength was generally < 0.3 for BS06 and was generally > 0.5 for BI06). It should also be noted that the BS06 criterion includes, through its use of the water content, information about the density (or “state”) of the soil, which is inconsistent with the previously described definition of susceptibility.

Despite the use of soil index properties in current criteria (*PI* and *LL*), the soil behavior that indicates whether a soil is sand-like or clay-like is better assessed from: (i) the similarity of slope between the critical state line (CSL) and isotropic consolidation line (ICL), (ii) the shape of cyclic stress-strain loops, and (iii) the maximum pore pressure ratios that develop during cyclic shearing. We currently lack specific metrics, and identified limits on those metrics, that can be used to translate these more advanced indicators of soil behavior into assessments of

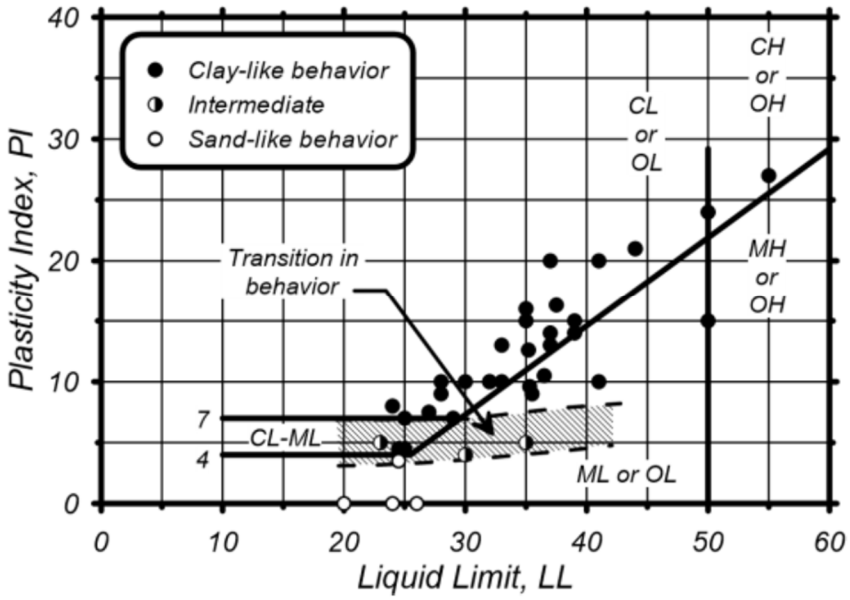

Figure 2-1 Criterion to distinguish sand-like from clay-like soil behavior for modeling purposes by Boulanger and Idriss (2006)

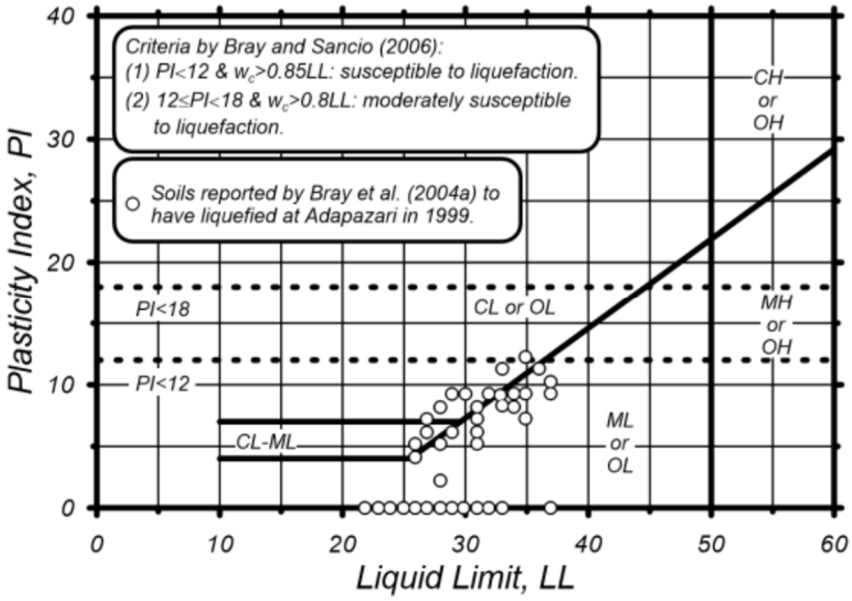

Figure 2-2 Susceptibility criteria by Bray and Sancio (2006); figure from R.W. Boulanger in Stuedlein et al. (2023b)

susceptibility potential, although some work has been done to move toward quantitative metrics to distinguish sand-like vs clay-like behavior (Stuedlein et al., 2023a). Both the BI06 criterion in Figure 2-1 and the BS06 criterion in Figure 2-2 show intermediate zones between sand-like (or susceptible) and clay-like (non-susceptible) where the soil's behavior is ambiguous. This class of "intermediate" soils includes low-plasticity fine-grained soils and sands with a significant content of plastic fines. Any future susceptibility criteria are likely to not have a clean cutoff between the two end members and thus to remain ambiguous with respect to these materials.

The rationale for the SMT's choice of susceptibility criteria as part of case history processing is described in Chapter 4.

2.1.2 Liquefaction Triggering

In liquefiable soils (i.e., materials judged as susceptible to liquefaction), cyclic undrained shear can produce progressive pore pressure increase and effective vertical stress decrease as the number of cycles of loading increases (e.g., Figure 2-3). This increase is often expressed as a ratio of the excess pore water pressure (u_{exc}) to σ'_{v0}, which is the excess pore pressure ratio (r_u),

$$r_u = u_{exc}/\sigma'_{v0} \quad \text{2-1}$$

Prior to cyclic loading, $r_u = 0$. A between-cycle increase in r_u indicates the soil may be advancing towards liquefaction. Initial liquefaction is defined as having occurred at the first cycle number where $r_u = 1.0$ is achieved. In Figure 2-3, initial liquefaction occurs at 21 cycles. An alternative definition of liquefaction is when a certain level of cyclic shear strain (e.g., +/- 3%) is first exceeded. Based on that definition, liquefaction occurs at 22 cycles in Figure 2-3.

Tests such as that shown in Figure 2-3 can be used to evaluate the resistance of a given soil to liquefaction. The resistance is typically expressed as the cyclic resistance ratio, *CRR*, which is the cyclic stress ratio, *CSR* required to liquefy granular soils in a standard number of cycles, typically 15 to 20, corresponding approximately to the duration of shaking from a reference moment magnitude (**M**) **M**7.5 earthquake. The demand on a given soil element from a given earthquake is the ratio of a representative cyclic shear stress amplitude (typically 65% of the peak) to the initial vertical effective stress and is denoted cyclic stress ratio, *CSR*. Thus, *liquefaction triggering* occurs when the demand exceeds the capacity, or when *CSR* > *CRR*. This stress-based analysis is one of three general options, the others being strain-based (e.g., Dobry et al., 1982) or energy-based (e.g., Ulmer et al., 2023b). The stress-based approach is the most commonly used framework (NASEM, 2016, 2021). The SMT chose to use the stress-based framework because (i) of its common utilization in practice, which provides a strong precedent for the eventual NGL models and (ii) it provides a direct and simple way to estimate seismic demands at the NGL case history sites and in forward applications. For more information on the strain- and energy-based methods, we recommend relevant sections in the NASEM report (2016, 2021).

The use of liquefaction case histories was initiated in the late 1960s (Seed and Idriss, 1971; Whitman, 1971). Seed and Idriss (1970) and Whitman (1971) estimated peak shear stress at depth *z* as the product of peak ground acceleration (*PGA*) and total stress (σ_v) at depth *z*. This product represents the stress if the soil profile were behaving as a rigid body. Seed and Idriss (1971) included a depth-dependent shear stress reduction coefficient, r_d, to account for the flexibility of the soil as:

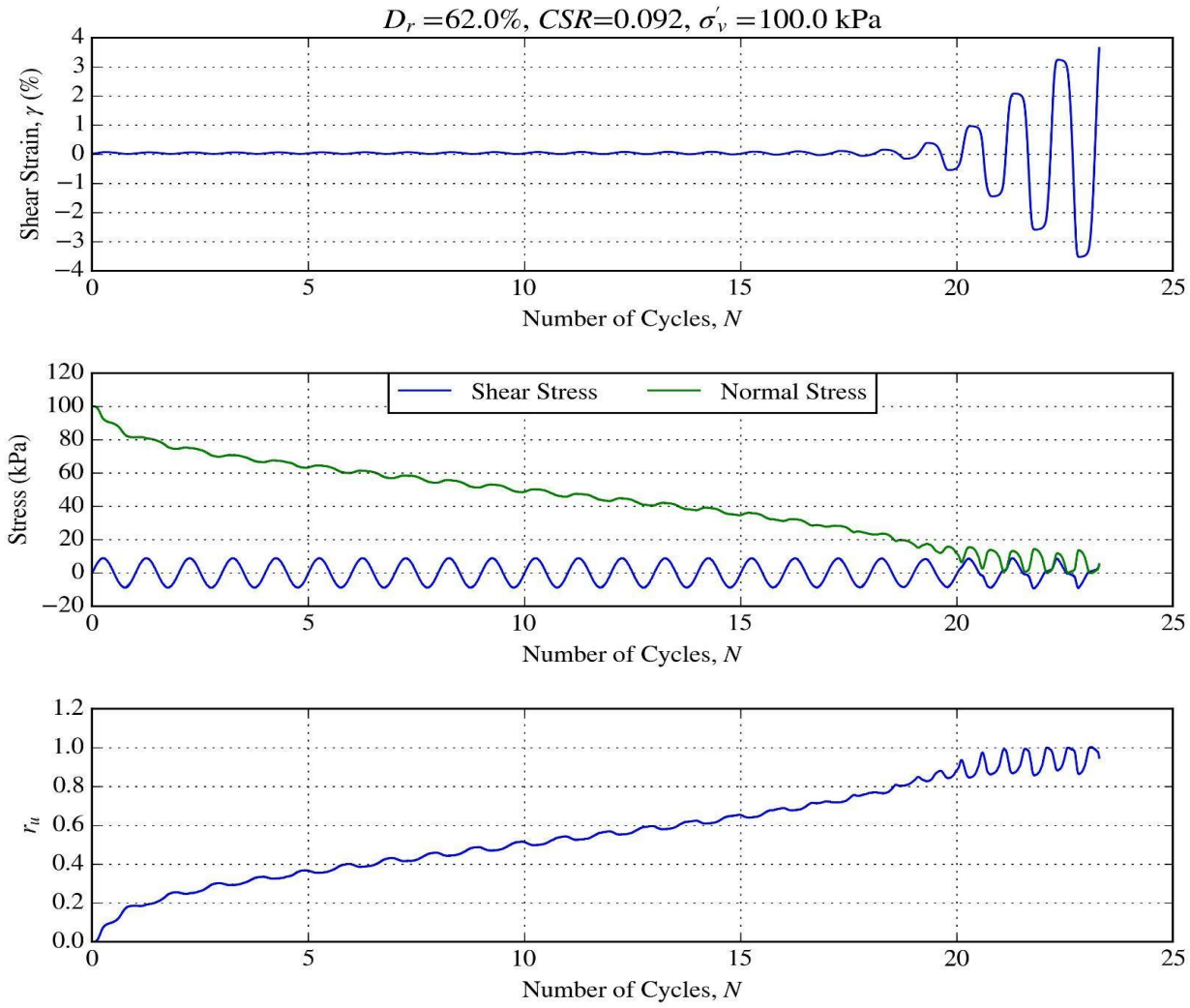

Figure 2-3 Shear strain, shear stress, normal effective stress, and r_u vs number of cycles of loading during a cyclic test performed on a specimen of Monterey 0/30 sand (data from tests performed by Ulmer, 2019)

$$CSR_{\boldsymbol{M}=m}(z) = \frac{0.65 \cdot \tau_{cyc,max}(z)}{\sigma'_{v,0}(z)} = \frac{0.65 \cdot {PGA}/{g} \cdot \sigma_v(z) \cdot r_d(z)}{\sigma'_{v,0}(z)} \qquad 2\text{-}2$$

where $\tau_{cyc,max}$ is the maximum cyclic shear stress at depth z, *PGA* is the horizontal peak ground acceleration at the ground surface, *g* is the acceleration of gravity, σ_v is the total vertical stress, and r_d is a depth-dependent shear stress reduction coefficient that accounts for the nonrigid response of the soil deposit. The 0.65 coefficient reduces the *CSR* from the peak value of the shear stress to a more representative value.

Liquefaction triggering is not only dependent on the *CSR* but also on the number of loading cycles or duration of shaking. To account for the number of cycles, *CSR* is typically adjusted using a magnitude scaling factor (*MSF*) to compute an equivalent *CSR* for a reference **M**7.5:

$$CSR_{\boldsymbol{M}7.5}(z) = CSR_{\boldsymbol{M}}(z) \cdot \frac{1}{MSF} \quad \text{2-3}$$

Commonly used relationships for *MSF* are provided by Youd et al. (2001), Cetin et al. (2004), Cetin and Bilge (2012), and Boulanger and Idriss (2014). Some investigators have recently suggested that the slope of *MSF* with magnitude is dependent on relative density (Boulanger and Idriss, 2014; Kishida and Tsai, 2014), whereas others have found that this density-dependence of slope is not supported by all available data (Ulmer et al., 2018; Ulmer et al., 2022b). This topic is addressed in Section 6.2.8 of this report.

Liquefaction resistance, *CRR*, has often been evaluated from case histories of observations of ground failure in the field during past earthquake events. As described further in Chapter 3, these traditional methods require critical assumptions regarding identification of the layer causing the ground failure when it has occurred, or the layer mostly likely to have caused ground failure when it did not occur. The fundamental problem is that the field data of yes/no manifestation is non-uniquely related to layer performance. For these reasons, we apply an alternative approach using cyclic testing performed in the laboratory to develop an initial estimate (or "prior") for *CRR*. Details about these specific approaches are discussed throughout the report, but particularly in Chapter 3 and Section 6.2. Definition of the resulting *CRR* as a function of some in situ penetration resistance or relative density (D_r) is the objective of most past liquefaction triggering modeling efforts, as discussed in Chapter 3.

Once the *CRR* and *CSR* are established, the factor of safety against liquefaction (FS_L) is computed as the ratio of *CRR* to *CSR*. Alternatively, in probabilistic models, the probability of liquefaction (P_L) can be computed as a function of *CSR* and penetration resistance. Using a probabilistic approach provides advantages over a binary "yes" or "no" evaluation typically used in the deterministic simplified triggering procedures because it conveys more information on the likelihood that liquefaction will occur, which is needed for performance-based earthquake engineering applications.

2.1.3 Liquefaction Manifestation

Once liquefaction triggers in a soil layer, the type and magnitude of consequences can vary significantly. Potential consequences include settlement and lateral displacement, sediment ejecta (e.g., sand boils), slumping and failure of embankments, loss of foundation support, increased lateral loads on and reduced lateral resistance of earth retaining structures and their foundations, buoyancy uplift of buried structures, and modification of free-field ground motions. Some of these effects (e.g., slope, foundation, retaining structure movements) are stability problems and as such their potential for occurring is derived using equilibrium calculations with reduced strengths in liquefied strata. Others can occur in flat or nearly flat ground (sand boils, ground oscillation) and the likelihood of occurrence is determined using a liquefaction manifestation analysis that considers the thickness and depth of liquefied strata and the properties of other (non-liquefied) strata in a profile. Here we describe three methods for manifestation analysis from the literature: relative layer thickness criteria, severity index criteria, and hydraulic profile analysis criteria.

2.1.3.1 Relative Layer Thickness Criteria

Ishihara (1985) proposed bounding curves of thickness of a non-liquefiable surficial soil layer (H_1) vs thickness of an underlying liquefiable sand layer (H_2) to predict the occurrence of

surficial manifestation of liquefaction-induced ground damage. This is illustrated in Figure 2-4. This method is widely used to essentially indicate whether a non-liquefiable crust can suppress surficial manifestation of liquefaction that triggers at depth. Rateria and Maurer (2022) revisited this relationship and provided updated H_1-H_2 models. However, they noted that H_1 and H_2 are not necessarily entirely efficient nor sufficient to predict manifestation, and they recommended that new manifestation models are needed to explicitly account for other influential factors (e.g., effects of strata permeability, sequencing of layers, depth, and thickness on pore pressure gradients and transmission).

2.1.3.2 Severity Index Criteria

Liquefaction severity indices estimate the severity of surface manifestations based on the cumulative liquefaction response of a profile. These models are useful because they provide indices of cumulative soil profile response, which can then be related to surface manifestations empirically. These methods do not require the identification of a critical layer as triggering models do.

Examples of common liquefaction severity indices include: the Liquefaction Potential Index (*LPI*;-Iwasaki et al., 1978); the Ishihara-inspired Liquefaction Potential Index (LPI_{ISH}; Maurer et al., 2015a); and the liquefaction severity number (*LSN*; van Ballegooy et al., 2014).

The *LPI* provides a depth-weighted index of the potential for triggering of liquefaction at a site using the following equation:

$$LPI = \int_0^{20m} F \cdot W(z)dz \qquad 2\text{-}4$$

where $F = 1 - FS_L$ for $FS_L \leq 1$ and $F = 0$ for $FS_L > 1$, $W(z)$ is the linear depth weighting function, $W(z) = 10\text{-}0.5z$ for $z \leq 20$ m and $W(z) = 0$ for $z > 20$, and z is depth in meters.

LPI depends on FS_L within the upper 20 m of the soil profile and can apply to profiles with multiple liquefiable layers rather than selecting one critical layer. *LPI* ranges from 0 to 100 and Iwasaki et al. (1978) found that among 45 sites that liquefied in the 1964 Niigata earthquake, the *LPI* corresponds to the severity categories presented in Table 2-1. Conditions for which “low” severity is predicted effectively amount to no manifestation in these criteria.

Maurer et al. (2015a) modified the *LPI* framework to include a power law depth weighting function instead of a linear function and to account for limiting thickness of non-liquefiable capping layer according to the H_1-H_2 chart developed by Ishihara (1985) (Section 2.1.3.1). This modified *LPI* is called LPI_{ISH}, which Maurer et al. (2015a) found to improve predictive capacity for 60 case histories from several earthquakes in different regions outside Japan.

LSN uses a power law depth weighting factor to determine cumulative liquefaction response of a profile and includes contributions from layers that have $FS_L < 2$ with the following equation:

$$LSN = 1000 \int \frac{\varepsilon_v}{z} dz \qquad 2\text{-}5$$

where ε_v is the post-earthquake volumetric strain at depth z in decimal form and z is the depth in meters. A method developed by Ishihara and Yoshimine (1992) and implemented by Zhang et

al. (2004) with CPT data can be used to compute ε_v. This method computes post-liquefaction volumetric strain as a function of FS_L. The *LSN* index value corresponds to severity categories shown in Table 2-1.

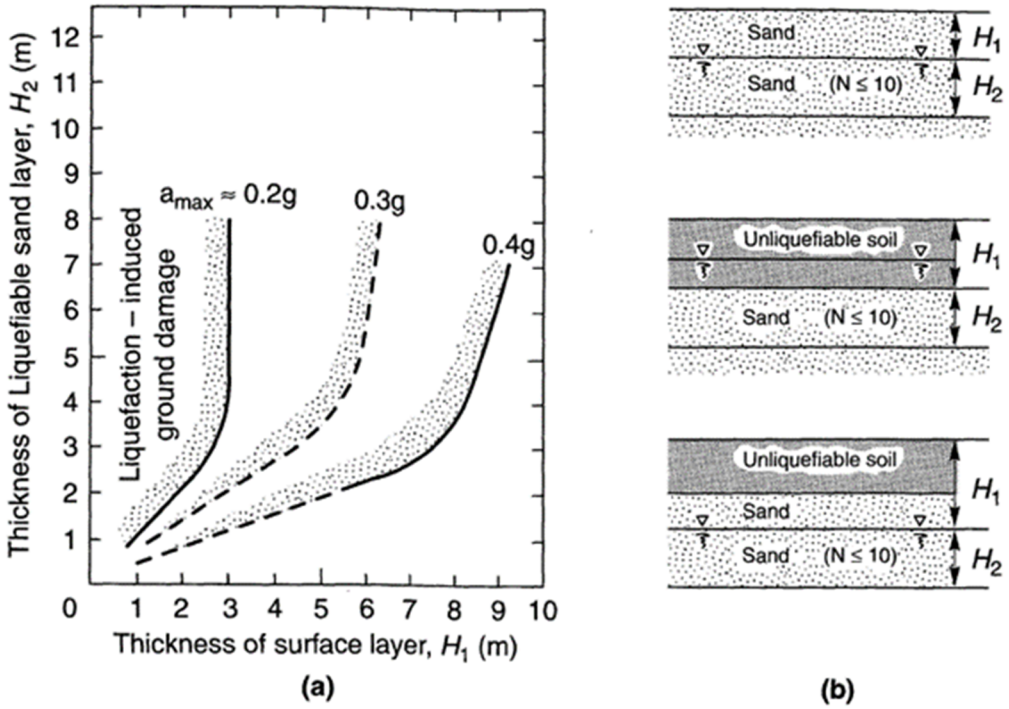

Figure 2-4 **(a) Relationship between thickness of liquefiable layer and thickness of overlying layer at sites for which surface manifestation of level ground liquefaction has been observed and (b) guides to evaluation of respective layer thicknesses (after Ishihara, 1985)**

Table 2-1 ***LPI* and *LSN* severity categories and index values**

Severity	*LPI* Value	*LSN* Value
Low	NA	≤ 20
Moderate	≤ 5	20 to 40
High	5 to 15	> 40
Very High	> 15	NA

2.1.3.3 Hydraulic Profile Analysis Criteria

A method for estimating severity of sediment ejecta onto the ground surface has recently been presented by Hutabarat and Bray (2021) using effective stress analyses. They have also presented a simplified method to estimate sediment ejecta using CPT data (Hutabarat and Bray, 2022). They define a liquefaction ejecta demand parameter (L_D) that estimates the upward seepage pressure that could produce artesian flow due to elevated excess hydraulic head and a crust layer resistance parameter (C_R) that captures the strength and thickness of the non-liquefiable crust layer. The method is illustrated in Figure 2-5.

The required parameters are calculated as follows:

$$C_R\left(\frac{kN}{m}\right) = \int_{0m}^{H_1} s_u dz \begin{cases} s_u = K_0 \sigma'_{v0} \tan\phi_{cs} & if\ I_B > 22 \\ s_u = \frac{q_t - \sigma_{v0}}{N_{kt}} & if\ I_B \le 22 \end{cases} \quad \text{2-6}$$

where H_1 is the thickness of the non-liquefiable layer in meters as defined in Ishihara (1985), s_u is the undrained shear strength of the crust layers in kN/m^2, K_o is the coefficient of lateral pressure at-rest (usually assumed to be 0.5), ϕ_{cs} is the critical state friction angle assumed to be 33 degrees (for quartz sand), q_t is the tip resistance from CPT corrected for pore pressure, and N_{kt} is between 14 and 20 based on I_c, and I_B is the modified soil behavior type index (Robertson, 2016). To compute L_D, first r_u is estimated as a function of FS_L (as computed using Boulanger and Idriss, 2016) using a relationship proposed by Tokimatsu and Yoshimi (1983):

$$r_u = \begin{cases} 0.5 + \sin^{-1}\left[\dfrac{2FS_L^{\left(\frac{1}{\alpha\beta}\right)} - 1}{\pi}\right] & if\ 1 \le FS_L \le 3 \\ 1\ if\ FS_L < 1 \end{cases} \quad \text{2-7}$$

where α is 1.0 and β is -0.2. Next, the excess head (h_{exc}) is computed:

$$h_{exc} = \frac{r_u \sigma'_{v0}}{\gamma_w} \quad \text{2-8}$$

where γ_w is the unit weight of water (9.81 kN/m^3). The excess head can be used to estimate liquefaction ejecta demand. Another factor in ejecta demand is the vertical hydraulic conductivity (k_v) of the profile which can be estimated from CPT data using the Robertson and Cabal (2015) method:

$$k_v(m/s) = 10^{(0.952 - 3.04 I_c)} \quad \text{2-9}$$

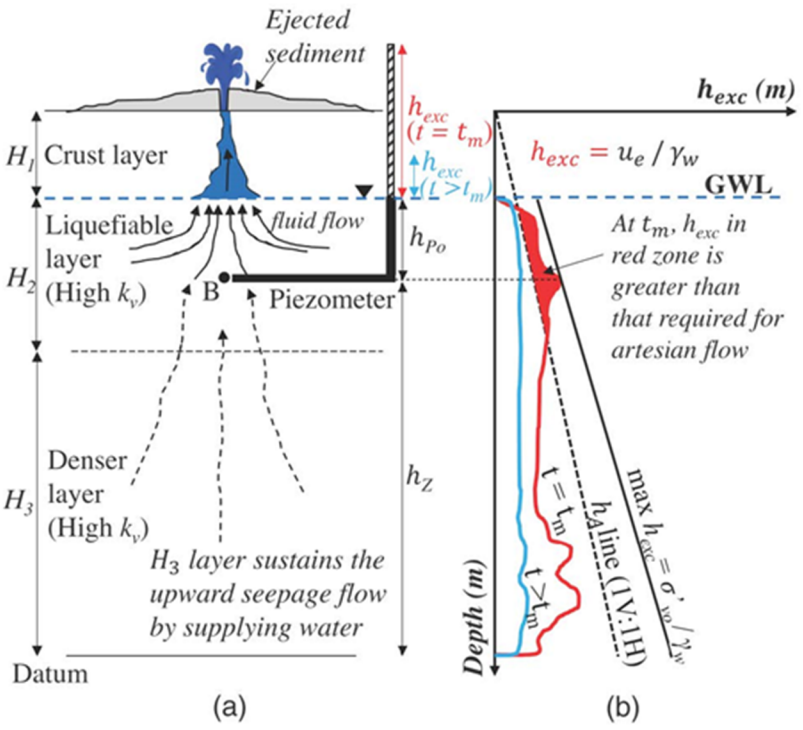

Figure 2-5 (a) Sediment ejecta mechanisms in a typical thick sand site and (b) artesian flow potential concept (Hutabarat and Bray, 2022)

This correlation is only applicable when I_c is between 1 and 3.27. The k_v for a clean sand with I_c = 1.8 yields k_{cs} = 3.0E-5 m/s which is used to normalize the k_v in this method. Finally, L_D can be calculated as an integral of the normalized k_v and head with depth:

$$L_D(kN/m) = \begin{cases} \gamma_w \int_{z_A}^{z_B} \frac{k_v}{k_{cs}} (h_{exc} - h_A) dz \; if \; h_{exc} \geq h_A \\ 0 \; if \; h_{exc} < h_A \end{cases} \quad \text{2-10}$$

where z_A is the depth below the groundwater table depth or the bottom depth of a crust layer that is at least 250 mm thick with $I_c \geq 2.6$ if below the groundwater table, z_B is the top depth of a soil layer that is at least 250 mm thick after the first continuous sand-like layer with $I_c \geq 2.6$ between depths of z_A and 10 m (z_B will be 10 m if there is no such soil layer), and h_A is the initial hydraulic head (i.e., the depth in m).

Hutabarat and Bray (2022) computed the L_D and C_R at 176 field case histories and used observations of ejecta severity at those sites. Using this data, they created a chart with categories based on the L_D-C_R position as shown in Figure 2-6. This provides a useful approach for estimating liquefaction severity in terms of ejecta at a site based on CPT data.

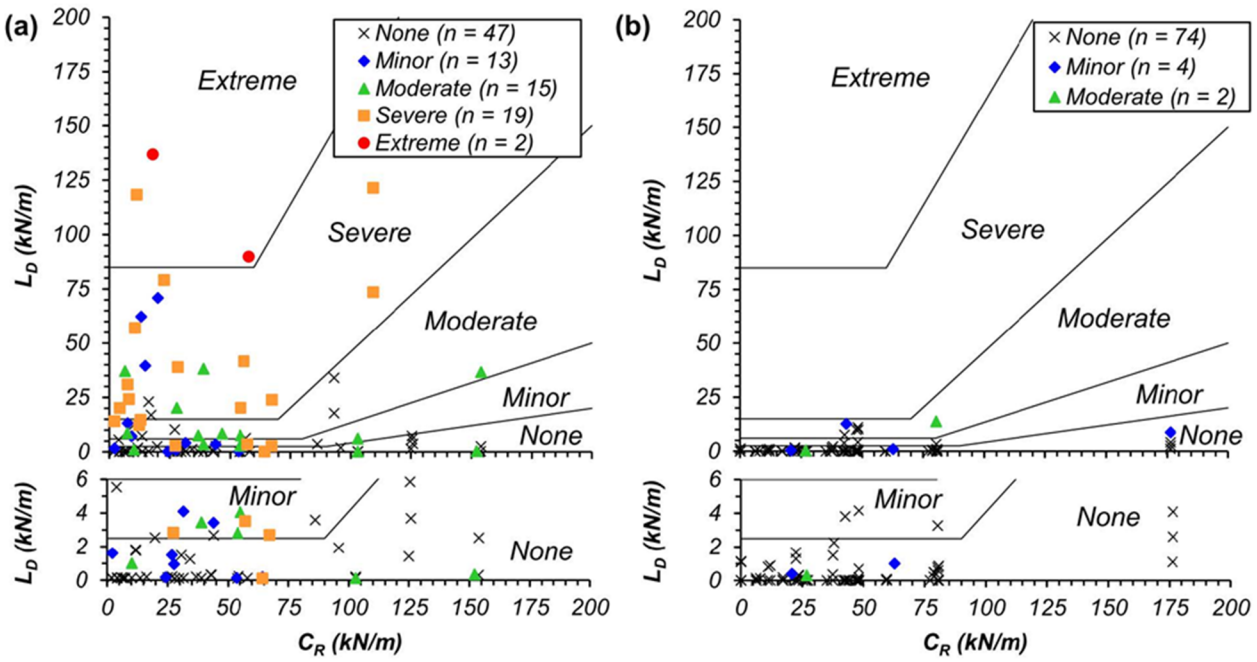

Figure 2-6 Ejecta severity using L_D and C_R parameters at: (a) thick sand sites and (b) stratified soil sites. The inserts below each plot clearly show data for L_D < 6 kN/m (Hutabarat and Bray, 2022).

2.2 NGL Approach

In this section we describe two aspects of the NGL approach. The first concerns the philosophy and organization of the project as a whole while the second concerns model development.

2.2.1 NGL Objectives and Organization

The NGL project has different objectives and is organized in a fundamentally different manner than typical research projects. As described in Section 1.1, NGL aims to advance the state-of-the-art in liquefaction research and to provide end users with consensus approaches to assess liquefaction potential within a probabilistic and risk-informed framework. To accomplish this, we have collected and organized liquefaction information in a common and comprehensive database to provide all researchers with a substantially larger, more detailed, more consistent, and more reliable source of liquefaction data than existed previously. Based in part on this database, as well as results of supporting studies, it is possible to create probabilistic models that provide hazard- and risk-consistent bases for assessing liquefaction susceptibility, the potential for liquefaction to be triggered in susceptible soils, and the likelihood of surface manifestation. By making all information publicly available and disseminating tools and interim research products, the process is transparent and inclusive at the levels of database development, design, and execution of supporting studies, and model development, as recommended by NASEM (2016; 2021).

The three major phases of the NGL project scope are database development and maintenance, supporting studies, and model development.

The database has been developed by a *Database Working Group* (DWG; Chair – Brandenberg) with regular community interaction and feedback. At the present time and throughout its

development, reviewed portions of the database have been publicly accessible. The database is described further in Section 2.3 and in a journal paper (Brandenberg et al., 2020), and is available at: http://www.nextgenerationliquefaction.org (Ulmer et al., 2023d).

NGL supporting studies aim to constrain components of liquefaction models using information derived from sources other than case histories. These external constraints are needed when the effect in question can be reasonably predicted using principles of soil mechanics or related fields but cannot be reliably established from case histories alone. The two topics addressed to date using supporting studies are stress effects on liquefaction resistance and liquefaction susceptibility (as defined in Section 2.1.1). The work on stress effects is presented in a separate report (Ulmer et al., 2022a) and summarized in Section 6.2. The work on susceptibility is largely supported from separate contracts and the results of a major workshop on the topic are provided separately (Stuedlein et al., 2023b). Our current thoughts on the modeling of susceptibility are presented in Section 6.1.

The third major project component is modeling, which is the subject of the next subsection.

2.2.2 Model Development

NGL modeling can be viewed as having two general aspects. The first is the modeling activity supported by and initiated under this present contract. The researchers undertaking this work are the SMT (Chair – Kramer). The second is a broader, community-based modeling activity with multiple teams that are coordinated by NGL project personnel; these teams are not financially supported by the current NRC/USBR-SwRI contract. The modeling-related activities of the SMT are the subject of this report (Chapters 4-6). The community-based modeling activity includes seven teams in addition to the SMT. These teams are all using (or planning to use) the NGL database and have agreed to share interim findings in regular meetings. The work of these teams is generally at early stages; their research approaches and preliminary findings will be presented in due course and are not the subject of this report. NGL facilitates the use of NGL resources by other modeling teams and organizes bi-monthly coordination meetings among modelers.

The SMT approach for model development aims to utilize soil mechanics principles to the maximum extent possible for prediction of soil responses (susceptibility, triggering) and to utilize field case histories to guide the development of models for profile responses (manifestation). An important aspect of our approach is that we seek to interpret the data in an objective, systematic and repeatable manner. We do not consider “systematic” or “repeatable” to be incompatible with the use of engineering judgment; rather, we apply our judgment, informed from case history interpretation, to develop the proposed systematic procedures. This has the advantage of producing procedures that can be used in forward applications (i.e., by practitioners) in a manner that is consistent with how the models were developed. As will be discussed in Chapter 3, this is not always the case with current models.

The flow chart in Figure 2-7 illustrates the components of the SMT’s model building process. This flow chart highlights the main components of this process:

1) Objective data used as inputs to the models and prior relationships. This includes data obtained from the NGL database (Section 2.3) and published studies, such as laboratory tests used to estimate the cyclic resistance of soils against liquefaction.

2) Objective algorithms used to quickly and consistently process the case history data from the NGL database. These are described in Chapter 5, and include a layer detection algorithm for CPT data.

3) Human review of the individual case histories and the iterative review of regression results. The SMT manually reviewed case histories (e.g., Section 5.1) and discussed the results of the regression products (e.g., Section 6.2.7, Section 6.3) at several stages throughout the model development process to verify that the data-driven results are reasonably aligned with our current understanding of liquefaction mechanics.

4) The regression process (Section 4.4, Section 6.3) and its resulting products (Section 6.3.5, Section 6.3.7).

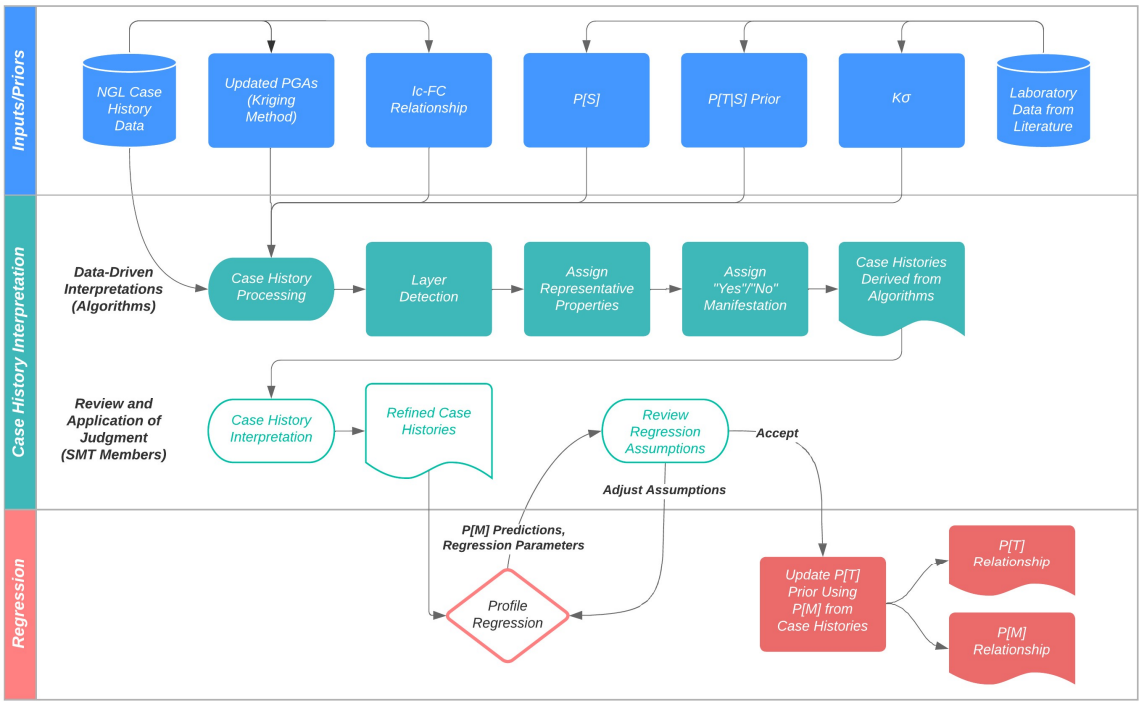

Figure 2-7 Flow chart illustrating the components of the SMT's model building process

2.3 NGL Database Summary

The NGL database is publicly available and contains geotechnical site investigation data, post-earthquake observations of liquefaction manifestations (or lack thereof), and earthquake ground motion data. The organizational structure of the database was developed over the span of several years with input from the technical community, and the development was overseen by the database working group. Details are discussed by Brandenberg et al. (2020). The database is accessible via a web-based GUI) at nextgenerationliquefaction.org (Ulmer et al., 2023d) where users can upload new data, view and download existing data, and where the database working group can review uploaded data after it is submitted for review. Figure 2-8 is a screenshot of the NGL database GUI showing focal mechanisms for earthquake events, and locations of liquefaction case history sites. Figure 2-9 is a screenshot zoomed in on the

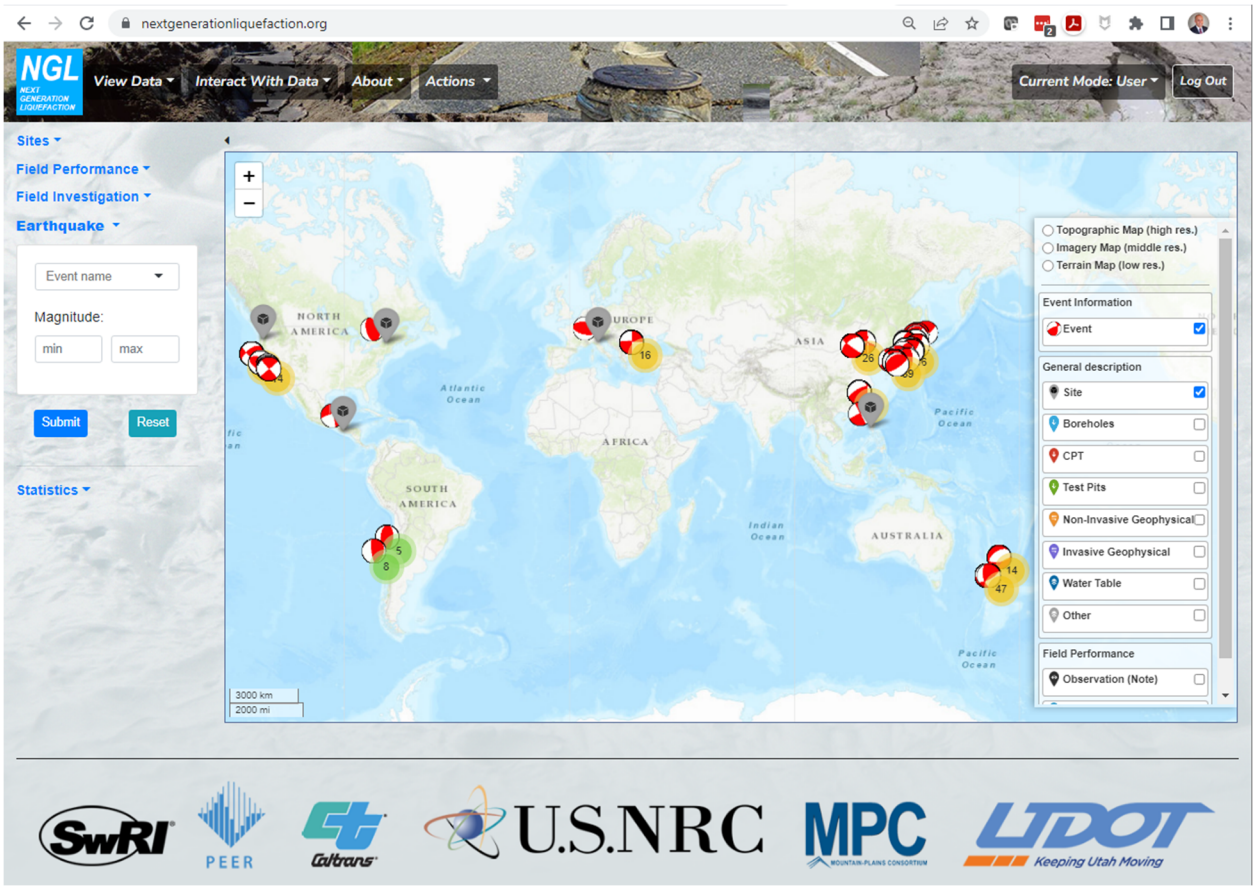

Figure 2-8 Screenshot of NGL web-based GUI showing event focal mechanisms and site locations

Christchurch region (New Zealand), where metadata for a cone penetration test has been activated by clicking on a CPT icon. Figure 2-10 is a screenshot showing measured cone penetration test data. Data for any site may also be downloaded in a CSV format, which is generated from the database on command.

Table 2-2 summarizes the number of different site investigations and liquefaction/non-liquefaction observations contained in the NGL database. The numbers of observations and site investigations available in the NGL database are several times more than the number of case histories contained in legacy datasets (presented subsequently in Table 3-1) and constitute a significant increase in publicly available data for producing liquefaction models compared to what was available before the NGL database. Note, each investigation-observation pair cannot necessarily be treated as an independent case history because in many cases there are multiple investigations and observations in close proximity at the same site, as is discussed in more detail in Section 5.1. Thus, the number of case histories that can be potentially extracted from the NGL database is less than the number of reviewed observations.

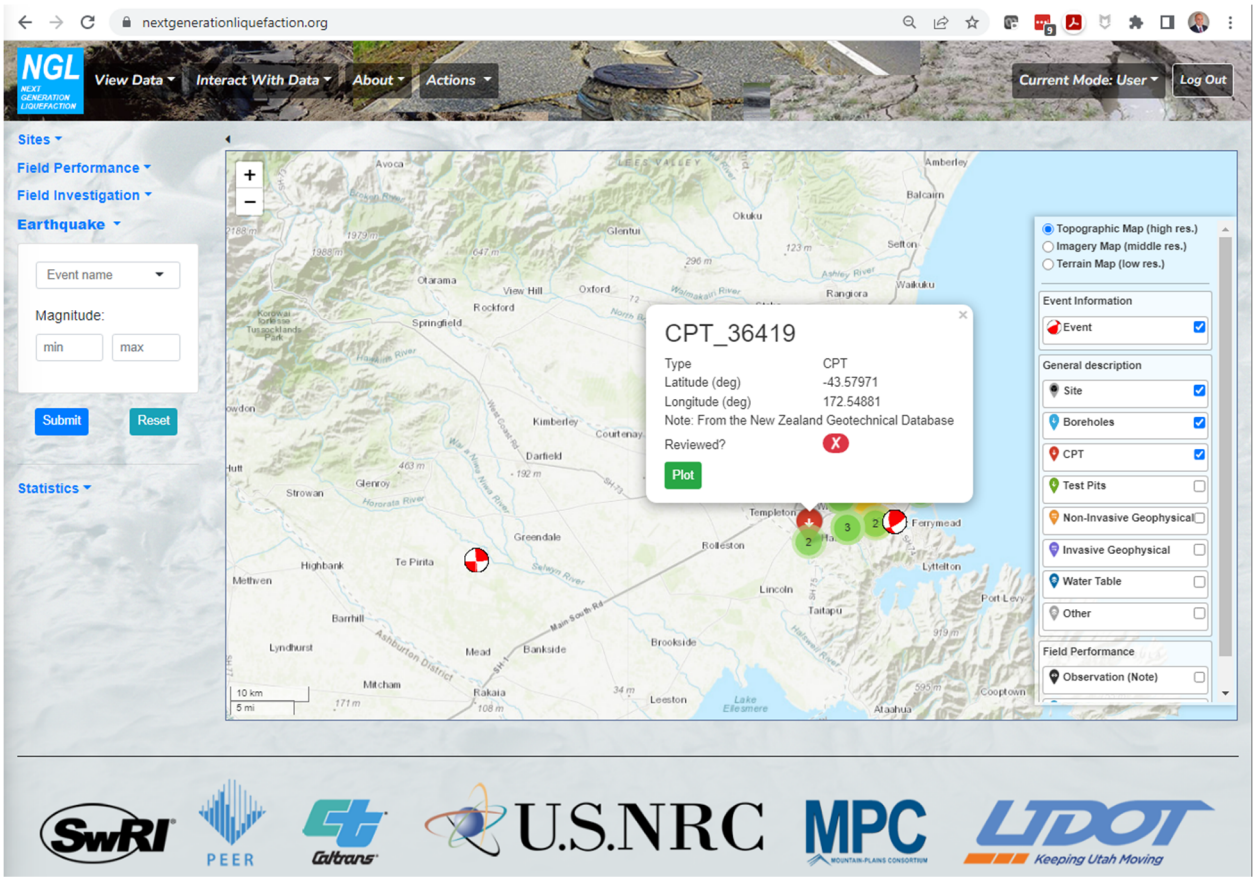

Figure 2-9 **Screenshot of data available in Christchurch Region, including metadata for one of the cone penetration tests activated by clicking a red CPT icon**

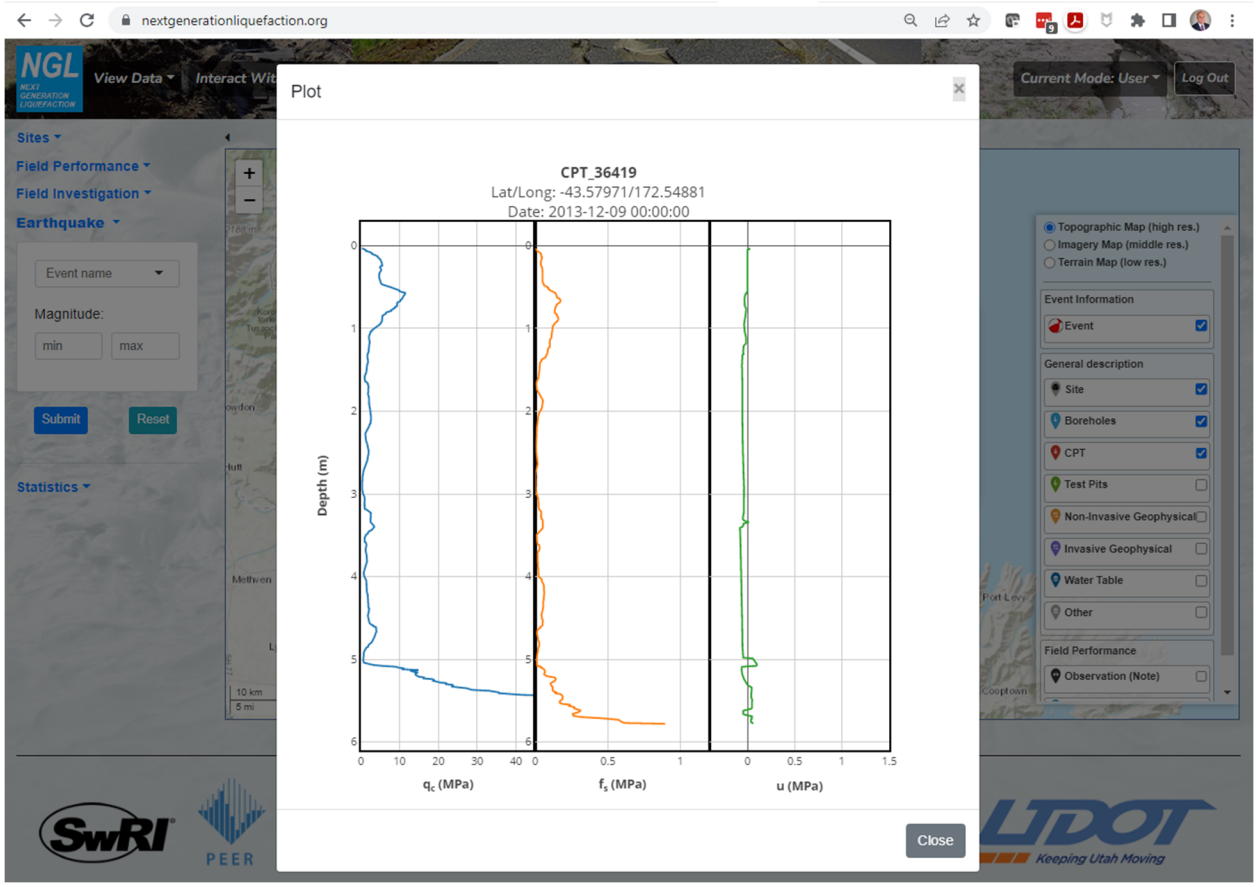

Figure 2-10 Screenshot of CPT data obtained by pushing the green plot button from Figure 2-8

Table 2-2 Status of data quantities contained in NGL database

Type	Total Number	In Preparation	Under Review		Reviewed (Two Reviews)
			(No Reviews)	(One Review)	
CPT Soundings	975	219	89	20	647
Boreholes	994	109	190	33	662
Surface Wave Measurements	48	2	20	4	22
Invasive *Vs* Profiles	154	0	14	0	140
Liquefaction Observations	752	84	54	9	605
Non-Liquefaction Observations	490	50	25	7	408

The GUI does not facilitate development of end-to-end workflows in which users can query data, analyze it, and draw conclusions. To facilitate such workflows, the database is replicated daily to DesignSafe (Rathje et al., 2017) where users can query the data via Python scripts in Jupyter Notebooks. Example-use case notebooks have been developed by the project team to provide building blocks upon which other users can build custom workflows. The use cases are documented at https://www.designsafe-ci.org/rw/use-cases/. Figure 2-11 is a screenshot of the documentation page for the use case, which is accessible from the DesignSafe main page through the Workspace dropdown menu. The documentation briefly describes the contents of various Jupyter Notebooks and contains links where users can open the notebooks and run the example queries. Figure 2-12 shows one of the cells in the ExampleNotebooks.ipynb Jupyter notebook that makes use of SQL join statements to synthesize CPT and site data for the Wildlife Array site. Other notebooks available in the use case documentation include a cone penetration test viewer, shear wave velocity test viewer, and a notebook developed during a webinar in October 2021 (https://youtu.be/TNOPOU4Ix5w).

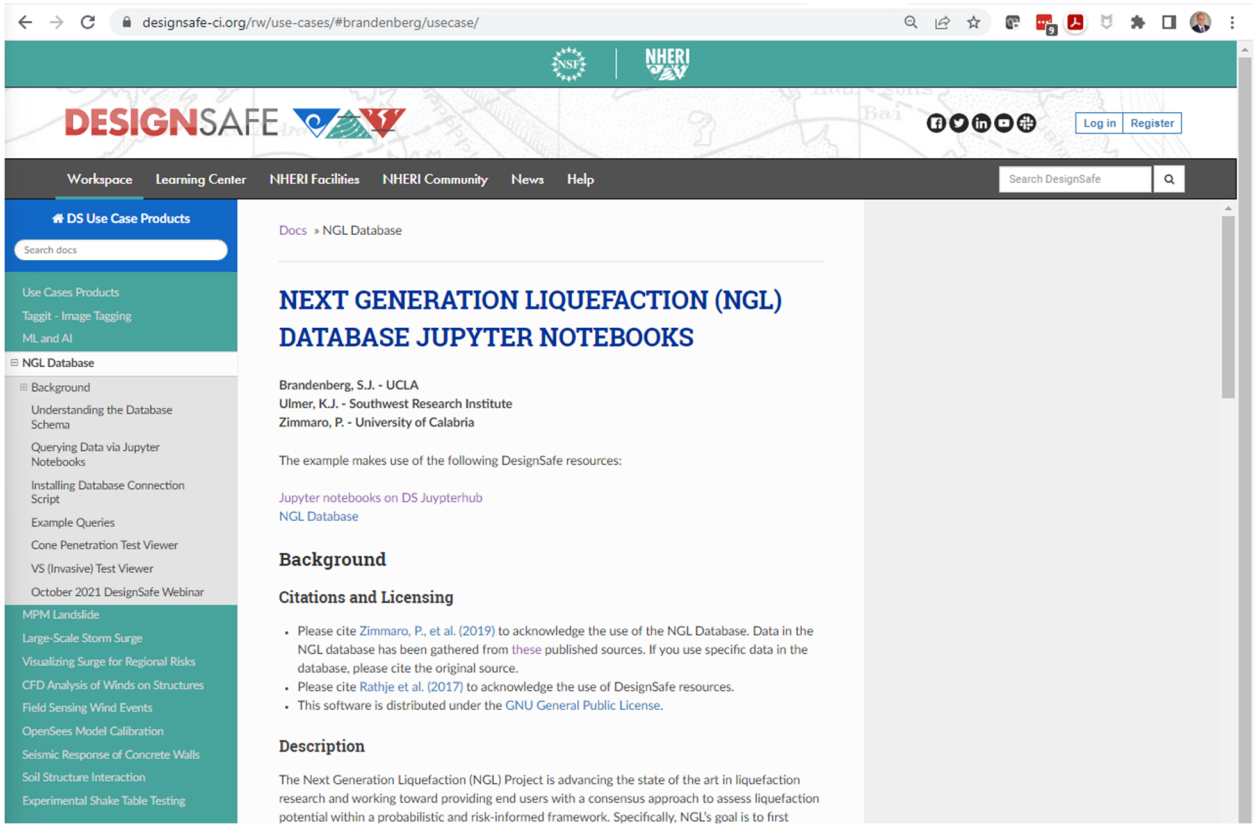

Figure 2-11 Use case documentation describing interactions between NGL database and Jupyter Notebooks in DesignSafe

3. Query cone penetration test data at Wildlife liquefaction array

This query retrieves all cone penetration test data from the Wildlife liquefaction array. INNER JOIN statements are needed to link SCPT to SCPG (using SCPG_ID), SCPG to TEST (using TEST_ID), and TEST to SITE (using SITE_ID). This query demonstrates propagation of primary and foreign keys through the schema heirarchy.

[4]:
```
import designsafe_db.ngl_db as ngl
import pandas as pd

command = 'SELECT TEST.TEST_ID, TEST.TEST_NAME, SCPT. SCPT_DPTH, SCPT.SCPT_RES, SCPT.SCPT_FRES FROM SCP
command += 'INNER JOIN SCPG ON SCPT.SCPG_ID = SCPG.SCPG_ID '
command += 'INNER JOIN TEST ON TEST.TEST_ID = SCPG.TEST_ID '
command += 'INNER JOIN SITE ON SITE.SITE_ID = TEST.SITE_ID '
command += 'WHERE SITE.SITE_NAME = "Wildlife Array"'
df = ngl.read_sql(command)
pd.set_option('display.max_rows', 10)
df
```

[4]:

	TEST_ID	TEST_NAME	SCPT_DPTH	SCPT_RES	SCPT_FRES
0	977	3Cg_pre	0.0	0.0000	0.000000
1	977	3Cg_pre	0.1	0.0000	0.000000
2	977	3Cg_pre	0.2	0.0000	0.000000
3	977	3Cg_pre	0.3	0.0000	0.000000
4	977	3Cg_pre	0.4	0.5886	0.021950
...	...	...	...	...	...
2384	1974	7Cp	11.2	0.9810	0.194238
2385	1974	7Cp	11.3	0.9810	0.144207
2386	1974	7Cp	11.4	1.4715	0.112864

Figure 2-12 Screenshot of "ExampleQueries.ipynb" Jupyter notebook illustrating a SQL query to retrieve cone penetration test data for the Wildlife Array site

3 LEGACY MODELS AND CRITICAL LAYER SELECTION

3.1 Past Approaches to Developing Triggering Models

Since its devastating effects became widely recognized following the 1964 Niigata and Good Friday earthquakes in Japan and Alaska, respectively, soil liquefaction has become an important topic of both research and engineering practice. Early efforts at understanding the basic mechanics of liquefaction utilized laboratory tests, principally cyclic triaxial tests, to identify the material, environmental, and loading parameters that most strongly affected the potential for triggering of liquefaction. Because the loose, clean, saturated sands in which liquefaction had typically been observed were extremely difficult to sample, laboratory tests were typically performed on reconstituted test specimens. These testing programs revealed the influence of important factors such as loading amplitude and duration, soil density, and initial effective stress on liquefaction potential.

Cyclic laboratory tests involved the application of uniform cycles of harmonic loading and their results were most commonly expressed in terms of the amplitude and number of cycles required to trigger liquefaction, either by developing a pore pressure ratio of 100% (initial liquefaction) or by exceeding some limiting shear strain amplitude. Plots of cyclic stress amplitude (normalized by initial effective stress to form a cyclic stress ratio, CSR) versus number of loading cycles to trigger liquefaction, often referred to as cyclic strength curves, were used to characterize liquefaction resistance. Over time, cyclic triaxial testing has been supplemented by cyclic simple shear testing – each has advantages and limitations. Both have provided tremendous insight into trends in the fundamental behavior of liquefiable soils under carefully controlled and measured conditions and have allowed testing over wide ranges of conditions (e.g., initial effective stress levels) that are important in geotechnical engineering practice.

Further testing, however, showed that the positions of cyclic strength curves were strongly influenced by the manner in which test specimens had been reconstituted (i.e., by the initial fabric of the soil). Because the in situ fabric of any particular soil, which is recognized as a complex function of its grain size characteristics, original depositional environment, and subsequent stress/strain history, cannot be accurately reproduced by laboratory reconstitution, laboratory-based characterization of liquefaction potential fell out of favor in some regions (like the U.S.) but remained in use for intact specimens in other regions (Japan). The profession in the U.S. then turned to case history-based methods for evaluating the potential for the triggering of liquefaction; these methods have become the de facto standard in geotechnical engineering practice.

The most common method used to obtain what is commonly considered a “triggering” model is to analyze case histories of observations of liquefaction manifestation or lack thereof in the field during past earthquake events. In principle, other information, including in situ pore pressure measurements, subsurface deformations, or ground motion recordings, could indicate the triggering of liquefaction within a subsurface layer at a site. However, such information has not been available nor used to any significant degree in the development of previous models. Thus, existing models tend to rely on evidence of manifestation or no manifestation to indicate that triggering occurred at some depth within the profile or did not occur within any layer in the profile, respectively.

Efforts to document and process liquefaction case histories have been ongoing for decades (e.g., Seed and Idriss, 1971; Seed et al., 1984; Cetin et al., 2000; Andrus et al., 2003; Moss, 2003; Cetin et al., 2004; Kayen et al., 2013; Boulanger and Idriss, 2014; Cetin et al.,

2018), and have supported the development of multiple previous liquefaction models. These datasets provide information for each case history used in model development, such as:

- earthquake magnitude (**M**) and ground motion at the site (e.g., *PGA*),
- brief descriptions of observations at the ground surface (e.g., presence or absence of ground failure),
- depth to groundwater table,
- attributes of the soil layer considered by the respective authors to indicate the single layer most likely to have liquefied (e.g., σ_v, σ'_{v0}, in situ test measurements, *FC),*
- *CSR* as computed by the respective authors.

The triggering models developed from these case history datasets consist of a relationship between *CRR* and some indirect measure of soil relative density such as SPT blow counts (*N*), CPT tip resistance (q_c), or small-strain shear wave velocity (*Vs*). These relationships were derived by plotting *CSR* vs the soil density parameter for "liquefaction" and "non-liquefaction" data points and drawing a boundary curve separating the two domains (e.g., Figure 3-1 from Seed et al., 1985). That curve, historically drawn to be conservative but more recently determined through regression, is assumed to represent *CRR*. The relationships predict *CRR* for reference conditions of σ'_{v0} = 1 atmosphere, **M** = 7.5, clean sand (fines content less than 5%) and no initial static shear stress (i.e., a relatively flat site and no finite loads, also known as free-field sites).

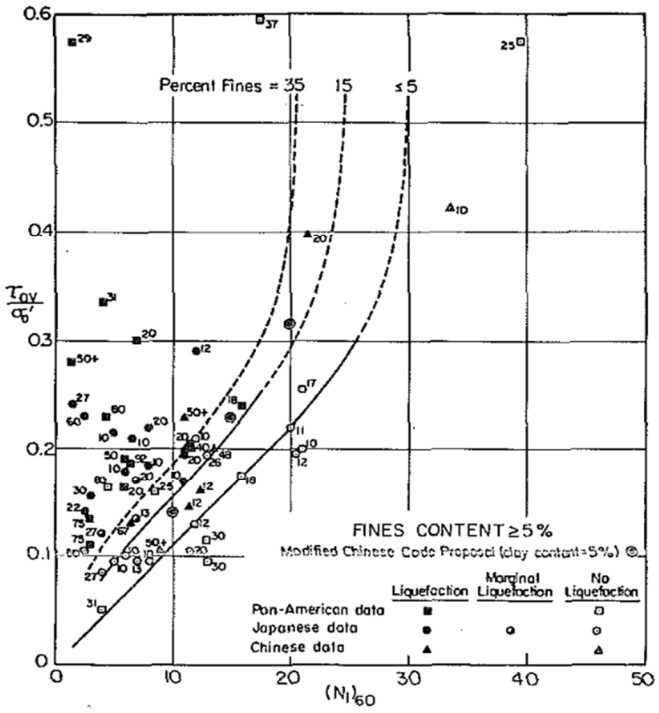

Figure 3-1 An example of a suite of *CRR* curves for different levels of fines content (from Seed et al., 1985)

Liquefaction “triggering” models also include adjustment factors to relate actual conditions to the assumed reference conditions. One group of factors are applied to the measured in situ parameter (i.e., N, q_c, or V_s) whereas the other group of factors are applied to the computed *CRR* or *CSR* (i.e., to compute the normalized value, $CSR_{\mathbf{M}7.5,1atm}$). The in situ parameters are adjusted for the effects of overburden stress (through the C_N term) so that they apply for a common reference stress of 1 atm. The in situ penetration resistance parameters are also corrected for fines contents that deviate from zero, to account for both the reduced penetration resistance of fine-grained soils at a common relative density, which is mainly a consequence of reduced moduli (Cubrinovski and Ishihara 2002, Carraro et al., 2003; Ecemis and Karaman, 2014; Jefferies and Been, 2016), and changes in the cyclic strength of soils with fines (Polito and Martin, 2001; Park and Kim, 2013). The resulting overburden and clean sand values are clean sand corrected SPT blow count ($N_{1,60cs}$) and CPT tip resistance (q_{c1Ncs}). The *CRR* adjustments are applied to correct for **M** different from 7.5, overburden stresses different from 1.0 atm, and static shear stresses different from zero. The magnitude correction (*MSF*) is used to account for reductions of resistance with increasing number of cycles, which is correlated with magnitude. The overburden correction (via the K_σ term) accounts for the suppression of dilatancy with increasing effective stress. The shear stress adjustment factor (K_α) modifies the *CRR* to adjust for effects of initial static shear stress on the horizontal plane. More details about the K_σ and K_α correction factors are discussed in the Task 5 report (Ulmer et al., 2022a) and Section 6.2.4.

Historically, the case history datasets have not represented a broad enough parameter range to constrain many of these correction factors for in situ conditions considered in liquefaction triggering evaluations. Compilations of case history data have shown that the overwhelming majority of case histories in legacy triggering models have involved liquefaction interpreted as occurring at depths of less than 8 m, but engineers dealing with large structures such as earth dams can be required to assess liquefaction potential at depths of hundreds of meters. Similarly, few well documented case histories exist for significantly sloping ground. As a result, the K_σ and K_α correction factors have typically been obtained by applying soil mechanics principles to the interpretation of experimental laboratory data (e.g., Boulanger, 2003a; 2003b; Cetin and Bilge 2014; Boulanger and Idriss, 2014), although other researchers have sought to obtain K_σ through direct regression of the field case history data (Cetin et al., 2004; Moss et al., 2006). The former approach is generally favored for its incorporation of the fundamental mechanics of soil liquefaction, and its use in extrapolating beyond the range of available case history data is considered more reliable. Thus, this preferred approach uses both laboratory and case history data in model development but does so in a disconnected manner – the laboratory-based correction is established and essentially used as a fixed, deterministic relationship (i.e., implicitly assumed to be correct and not subsequently modified by case history data) in the model development process.

Other adjustments can be made to the in situ measurements or *CRR* but are not accounted for in any commonly used relationships. These include drainage effects due to impeded drainage boundaries on the borders of susceptible layers (accounted for in the K_d correction factor; Abdoun et al., 2020, Ni et al., 2020), and partial saturation effects of soils beneath the water table that may not be fully saturated (Hossain et al., 2013, Tsukamoto et al., 2014; Zhang et al., 2016). Additional complexities that may not be amenable to correction with simple adjustment factors are system effects caused by interlayering of more and less resistant soils that affect the ability of liquefaction at a particular depth to manifest, reductions of demand in relatively deep strata, and strength loss in shallow layers induced by large flow gradients from liquefaction of deeper strata (Cubrinovski et al., 2019).

There also exist alternative methods for assessing liquefaction triggering such as regional map-based assessments, cyclic strain-based approaches, energy-based approaches, laboratory and physical model tests, field measurement of pore pressure generation under dynamic loading, and computational mechanics approaches. For brevity, these methods are not discussed in this report. A summary of these and other methods is provided in the NASEM (2016, 2021) report.

For the reasons previously discussed, the use of both case history and laboratory data in the development of liquefaction triggering models is considered to be advantageous. Laboratory tests allow control of stress, density, and loading conditions in a manner that does not exist in field case history data. They allow measurement of stresses, strains, and porewater pressures so that the conditions at the actual point of triggering are accurately and objectively known rather than inferred as they must be from interpretation of case histories. Laboratory data reveals trends in liquefiable soil behavior for conditions that cannot be extracted from available case history data, thereby allowing more confident extrapolation of empirical triggering models to conditions that can be important in geotechnical practice. The question then becomes one of how laboratory data should best be implemented in the model development process.

The procedure adopted by the SMT makes use of Bayesian updating, a common procedure in the development of probabilistic models. In our implementation, laboratory data is used as a starting point (i.e., to establish a prior distribution in Bayesian terminology). That starting point is then updated by the consideration of case history data to form a final triggering model (a posterior distribution, again in Bayesian terminology). The updating process allows the model to be controlled by the case history data for conditions that are well constrained by the case history database with control shifting to the prior distribution for conditions not well represented in the case history database. It also allows uncertainty in the laboratory data to be properly accounted for in the model development process. From the standpoint of the distinction between triggering and manifestation, which is a major part of the SMT model, comparison of the posterior and prior triggering distributions provides valuable insight into the applicability of laboratory data to the assessment of liquefaction potential. These issues, and the benefits of the SMT approach, are discussed in more detail in Chapter 6.

3.2 Legacy Models

In this report, we refer to models developed prior to the 2016 NASEM report as “legacy” models. Of these legacy models, common relationships for predicting *CRR* from SPT *N* are Youd et al. (2001), Cetin et al. (2004, 2018), Idriss and Boulanger (2008), and Boulanger and Idriss (2012). Common relationships for *CRR* from CPT q_c are Robertson and Wride (1998), Moss et al. (2006), Idriss and Boulanger (2008), and Boulanger and Idriss (2016). Relationships for predicting *CRR* from V_s are Andrus and Stokoe (2000) and Kayen et al. (2013). Some models have been developed based on laboratory testing of soil specimens that were sampled from case history sites (e.g., Tokimatsu and Yoshimi, 1983; Matsuo, 2004; PWRI, 2016). Some relationships were developed within a probabilistic framework (Liao et al., 1988; Youd and Noble, 1997; Cetin et al., 2004; 2018; Moss et al., 2006; Kayen et al., 2013; Boulanger and Idriss, 2012; 2016), meaning they produce a probability of liquefaction (P_L) as opposed to a deterministic *CRR* to be used in a FS_L computation.

For brevity, not all *CRR* models are discussed here. For the purposes of this report, we provide additional details about the components of the widely used Boulanger and Idriss (2016) CPT-based model only. This does not indicate endorsement of this model over any other model, but it is simply for the purpose of comparison in several points throughout the report. The parameter range and number of case histories represented in several legacy models are

summarized in Table 3-1. Note that the range of σ'_{v0} is limited to less than 200 kPa (and less than 150 kPa in some cases) and the critical depth is within about 12 m (and most often less than 8 m). These relatively shallow critical depths are due in part because manifestation at the surface is less likely the deeper the liquefied layer. Thus, there are possibly some cases where no liquefaction manifestation was observed at the surface, yet liquefaction could have occurred at depth.

As is typical of geotechnical engineering research, the projects that produced the legacy models were conducted by individual investigators or small teams of investigators. The investigators collected data, analyzed the data, and developed the models. Datasets used in model development were often never published in full, or if they were, it was after the model development process had been completed. Furthermore, published data products generally consisted of properties of the critical layer selected by the research group, and properties of other layers were not included. Research results were generally not widely shared with the community during model development.

This traditional research approach has drawbacks, such as lack of transparency (case history data not fully presented) and repeatability (case history interpretations made during model development that are not documented) that we have sought to overcome in the manner the NGL project has been organized (Section 2.2). These drawbacks can create divergence between how models are applied in forward applications vs how they were developed, which can limit model effectiveness. One of the most important elements of this disconnect is related to critical layer selection, which is examined further in the next section.

Table 3-1 Summary of recent liquefaction triggering case history databases for level-ground conditions showing ranges in values of the parameters (from NASEM, 2021)

Parameter	SPT		CPT		V_s
	Cetin et al. (2004)	**Boulanger and Idriss (2016)**	**Moss et al. (2006)**	**Boulanger and Idriss (2016)**	**Kayen et al. (2013)**
"yes" cases	109	133	139	180	287
"no" cases	88	118	44	71	124
"yes/no" cases	3	3	0	2	4
Critical depth (m)	1.1-20.5	1.8-14.3	1.4-14.0	1.4-11.8	1.1-18.5
σ'_{v0} (kPa)	8.1-198.7	20.3-170.9	14.1-145.0	19.0-147.0	11.0-176.1
FC (%)	0-92	0-92	--	0-85	--
$N_{1,60cs}$ (blows/30cm), q_{c1Ncs} (atm), or V_{s1} (m/s)	2.2-66.1[a]	4.6-63.7	11.2-252.0	16.1-311.9	81.7-362.9
$CSR_{M7.5}$	0.05-0.66	0.04-0.69	0.08-0.55[b]	0.06-0.65	0.02-0.73
M	5.9-8.0	5.9-8.3	5.9-8.0	5.9-9.0	5.9-9.0

[a] $N_{1,60}$ values listed for Cetin et al. (2004) as opposed to $N_{1,60cs}$
[b] CSR values listed for Moss et al. (2006) and Kayen et al. (2013), as opposed to $CSR_{M7.5}$

3.3 Critical Layer Selection

The concept, meaning, and identification of critical layers as representing the characteristics of an entire liquefiable soil profile are complex. They are, however, central to both the development and use of legacy triggering models. Their importance warrants recognition and discussion as background to the development of new triggering models.

3.3.1 Non-uniqueness

The legacy models described in Section 3.2 utilized a critical layer framework in which the layer most likely to produce manifestation was selected as being representative of the profile or site. For “yes” cases, the critical layer is selected as the layer that is considered to have been most likely to have liquefied. In some cases, this layer can be established with a high degree of confidence. For example, the Wildlife Liquefaction Array in California (NGL site ID 187; Holzer and Youd, 2007) and the Nakashimo levee site in Japan (NGL site ID 423; Zimmaro et al., 2020) include piezometers in layers that developed significant excess pore pressures, which confirms that liquefaction triggered in those layers. Another such example is the Sandholdt Road site from Moss Landing, California, where an inclinometer indicated lateral deformation within a layer during the Loma Prieta earthquake (NGL site ID 696; Boulanger et al., 1995, 1997), which indicates liquefaction-induced strength loss likely occurred in that layer. However, in most cases, the only evidence of liquefaction is surface manifestation such as sand boils or ground cracking or other deformations. In such cases, the case history interpretation is often inconclusive with respect to which layer produced manifestation.

One approach is to assign the critical layer as the weakest link in the chain, which is accomplished, in the case of CPT data, by finding the layer with smallest continuous interval of tip resistance with low friction ratio, or the susceptible layer with the smallest *CRR* (Moss et al., 2006; Kayen et al., 2013; Cetin et al., 2018). Although the documentation of these studies does not clearly distinguish manifestation from triggering in the reasoning behind critical layer selection, we interpret the weakest link approach as favoring triggering. A complication with the weakest link framework is that a pre-existing model is used to compute *CRR*, which is then used to select the critical layer whose properties are used to develop a new model. The use of pre-existing models in critical layer selection and model development can lead to confirmation bias, as discussed in Section 3.3.3.

Consider for example the Landing Road Bridge site (NGL site ID 161), for which surface manifestation was observed following the 1987 Edgecumbe, New Zealand earthquake in the form of lateral spreading, surface cracks, sand boils, and damage to the foundations of a nearby bridge. Figure 3-2 shows a CPT profile for this site, interpreted using procedures described in Sections 5.3-5.4. Layer numbers are indicated to the right of the profile of q_{c1Ncs}. While many of the layers at the site are likely not susceptible, layers 2 and 6 near depths of 1.5m and 5m, respectively, are granular soils (low I_c) with somewhat higher relative density (q_{c1Ncs}) in the deeper layer than the shallower one (115 vs. 90). It could be reasonably argued that either is critical. In the case of layer 2, it is closer to the ground surface and has the lower q_{c1Ncs} and therefore is most likely to manifest. However, since it is immediately beneath the groundwater table, partial saturation is possible, which would increase liquefaction resistance. Accordingly, it could be argued that the deeper but thicker layer 6 is more critical. As this example illustrates, the selection of the critical layer often involves considerable judgment, and this judgment naturally varies between different analysts, as described further in Section 3.4.

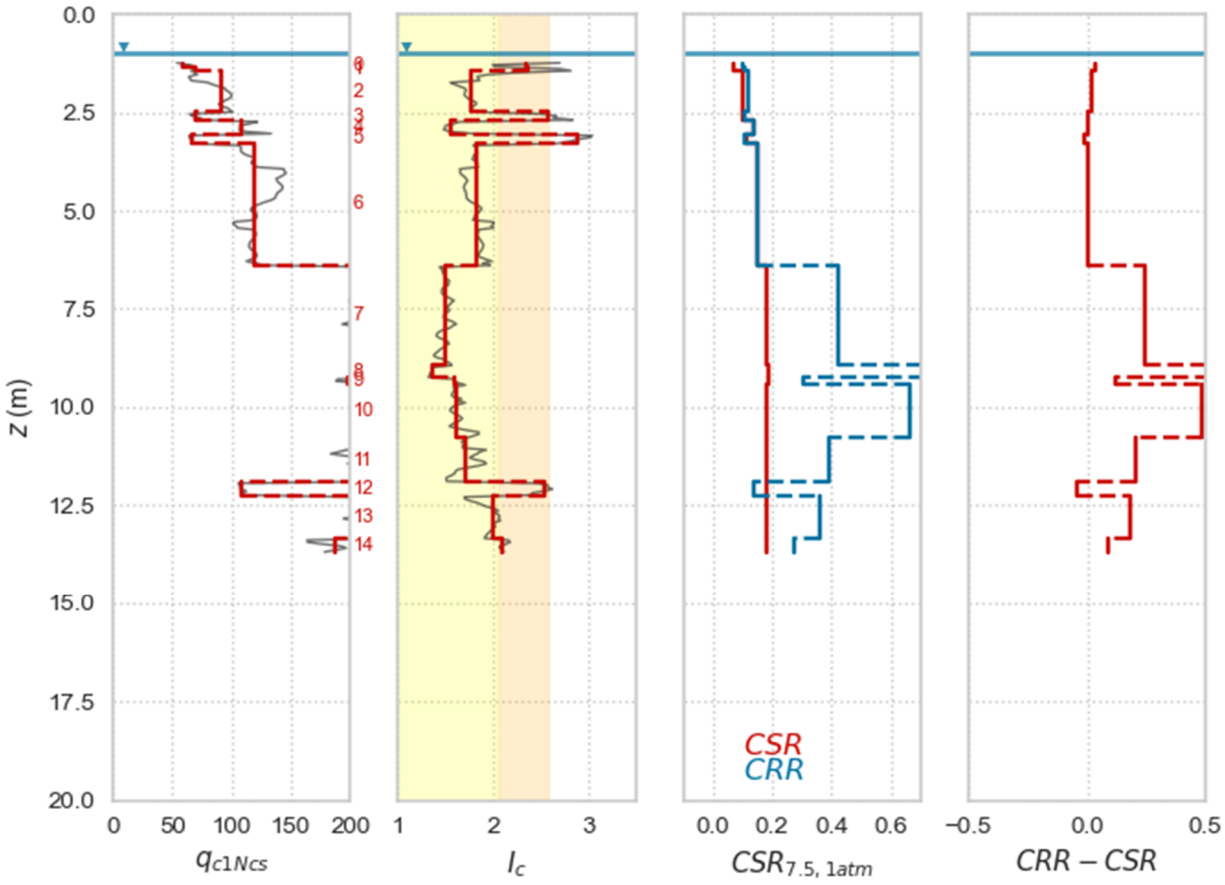

Figure 3-2 Example CPT profiles for the Landing Road Bridge site (CPT LRB007) from the 1987 Edgecumbe, New Zealand earthquake derived using procedures presented in Sections 5.3-5.4. This is an example of a site for which multiple critical layers could be selected for use in model development.

One way to resolve ambiguities like that illustrated in Figure 3-2, in cases where sand boils form, is to identify the critical layer by matching gradation and coloration characteristics of ejecta to soils at depth (Liao and Whitman, 1986; Cetin et al., 2000; Green et al., 2011). However, upward flowing sand can entrain soil from overlying layers with it and/or deeper soils might have also liquefied but not formed ejecta. As a result, uncertainties in critical layer identification remain.

These uncertainties are also present for “no” manifestation cases. In such cases, the critical layer is intended to represent the layer that most likely would have liquefied and manifested had the intensity of shaking been larger or the duration longer (Whitman 1971, Seed and Idriss, 1971). Consider for example the Radio Tower site (NGL site ID 318), for which no surface manifestation was observed following the 1979 Imperial Valley earthquake. Figure 3-3 shows a CPT profile for this site, interpreted using procedures described in Sections 5.3-5.4. While many of the layers at the site are likely not susceptible, layers 3-4 near 2.5 m depth and layer 7 near5 m depth are granular soils (low I_c) with apparently similar relative densities (q_{c1Ncs}). It could be reasonably argued that either is critical. In the case of layers 3-4, it is close to the ground surface and therefore is most likely to manifest. However, because it is immediately

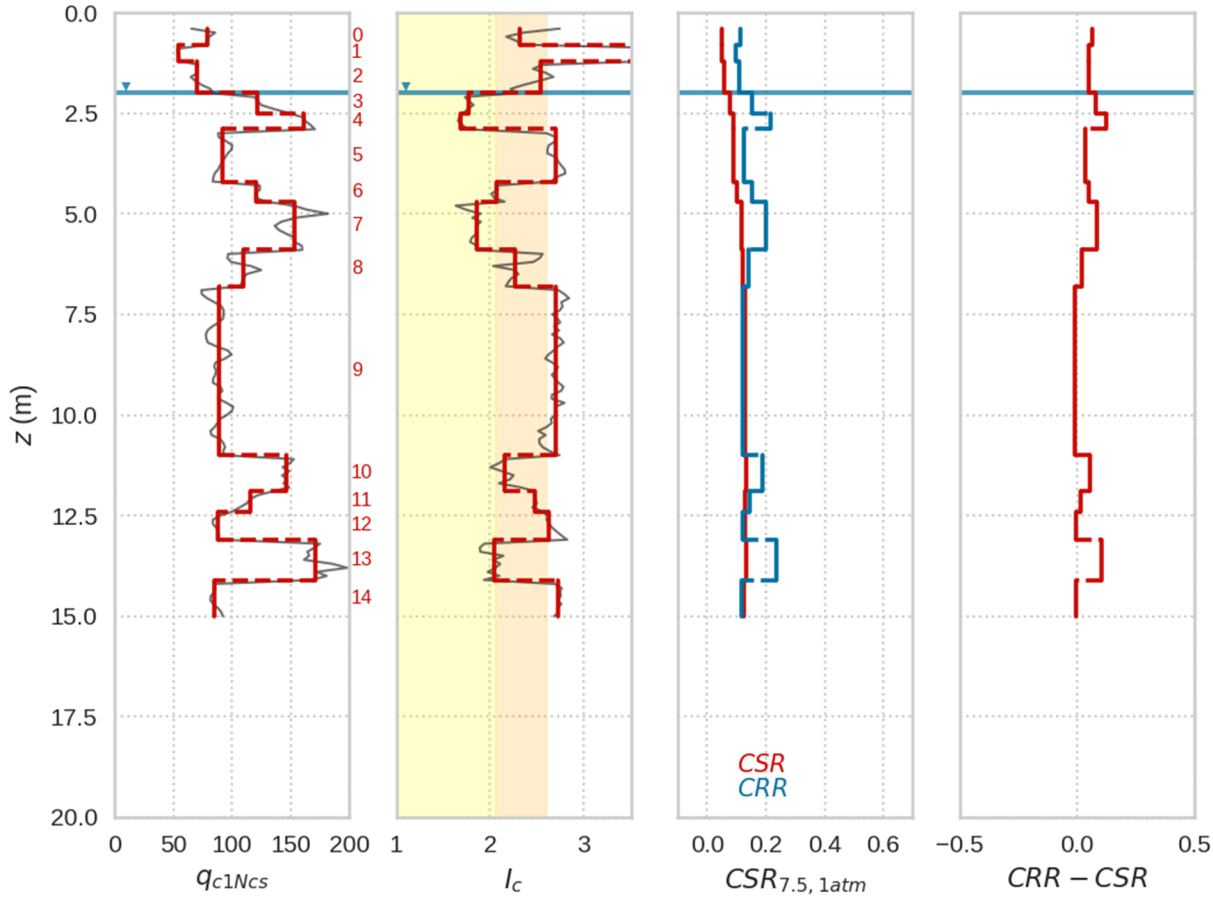

Figure 3-3 Example CPT profiles for site Radio Tower (CPT R4) from the 1979 Imperial Valley earthquake derived using procedures presented in Sections 5.3-5.4. This is an example of no manifestation for which multiple critical layers could be selected for use in model development.

beneath the groundwater table, partial saturation is possible, which would increase liquefaction resistance. Accordingly, it could be argued that layer 7 is more critical. On the other hand, layer 5 or layer 9 could also be considered critical, despite being less likely to be susceptible (high I_c), given that they have lower q_{c1Ncs} values and are as thick or thicker than layers 3, 4, and 7.

As these examples illustrate, in the absence of a model for predicting triggering/manifestation, it can be difficult to identify which layer within a profile is most critical for surface manifestation. While some semi-empirical models were developed through use of the “weakest link” approach, the extent to which that process of identifying critical layers considers manifestation is not clear. When manifestation is considered, a great deal of judgment is required. Critical layer selection should consider layer thickness, depth, stratigraphy, surface geology, spatial variability and lateral continuity of potentially liquefiable layers, and presence of sloping ground or a free face (Boulanger and Idriss, 2014; Green and Olson, 2015), each of which affect how a complex system of soil layers responds to an earthquake (Cubrinovski et al., 2019). In the development of legacy models, these judgments are operator-dependent, generally not well documented, and therefore not repeatable. We recognize that critical layer selections in some cases are made in

consideration of information beyond that represented by a CPT log. This can include multiple CPTs at a given site or boring logs with samples that may include laboratory data. Different modelers looking at these different data sources may consider different data sources in their selections, which can influence variability. Our focus in this section has been on CPT data because arguably a CPT-based model should be able to operate solely based on CPT data, because this represents a common situation for forward applications.

3.3.2 Implications for Forward Application of Models

Important differences between development of a triggering/manifestation model and the manner in which such models are applied in practice further complicate their use. Model development generally involves utilizing all available evidence to make an informed decision about the critical layer. Engineers tasked with a forward application of a model to assess liquefaction at a particular site do not have access to the same information, and therefore cannot replicate judgments made in critical layer selection during model development. For example, matching the ejecta to a specific layer cannot be performed in a forward assessment of a site that has not yet been shaken strongly enough to liquefy. Moreover, in forward applications engineers seldom apply a critical layer approach, instead opting to compute FS_L for every susceptible layer within the profile, and subsequently making judgments about the potential consequences (manifestation severity and ground deformations) of liquefaction. For example, Figure 3-4 is a screenshot of the CLiq (GeoLogismiki, 2018) software that evaluates liquefaction based on CPT data. This is a markedly different approach to first selecting a critical layer and evaluating only that layer.

Another distinction between model development and application in some cases is the level of care applied during site characterization. In research studies to develop case histories like many of those in the NGL database, CPT data is supplemented by borings with sampling that can be used to measure index properties like fines content and plasticity. Frequently, due to budget constraints, in forward applications engineers may utilize cone penetration testing alone in the absence of sampling. Fines content and susceptibility must therefore be inferred from the CPT data.

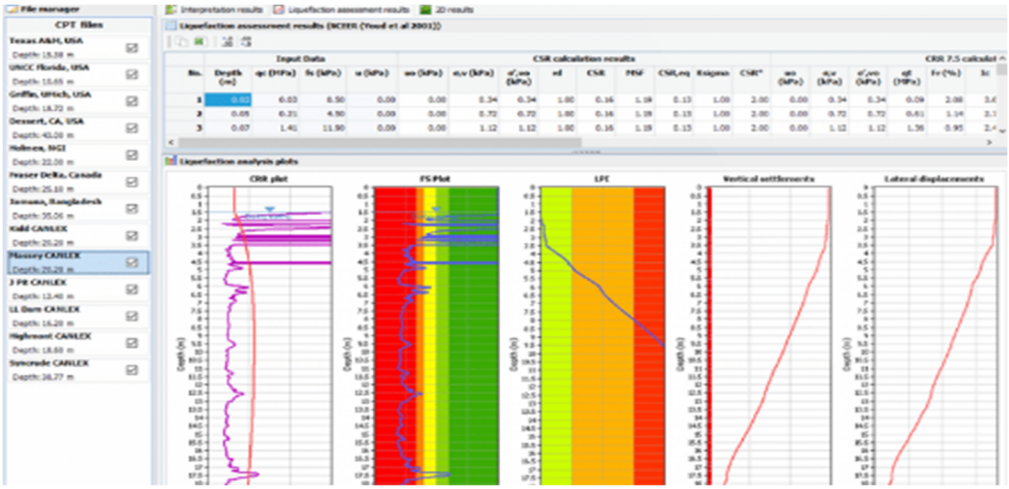

Figure 3-4 Screenshot of CLiq software showing evaluation of CPT data at all depths (GeoLogismiki, 2018)

3.3.3 Potential for Confirmation Bias

The need to apply judgment in the selection of critical layers during a process of model development sets up the potential for *confirmation bias*, which is defined as “the tendency to interpret new evidence as confirmation of one's existing beliefs or theories” (Oxford Languages dictionary). Confirmation bias is often unintentional and can arise from a person’s beliefs about a particular outcome. Consider for example a case history in which two alternative critical layer selections are essentially equally viable, in which one choice produces a *CSR*-q_{c1ncs} data point that is in agreement with a model (i.e. a “yes” case above the curve or a “no” case below the curve) whereas the other choice places the data point in conflict with the model. The temptation would be strong to select the choice that agrees with the model, especially if the alternative is a data point that would comprise a strong outlier (i.e., a “no” case well above the curve or a “yes” case well below the curve). Such cognitive biases are widely recognized in scientific research in other fields (e.g., Nickerson, 1998; Hirschhorn and Schonberg, 2024).

An example of such a case is NGL site “Imazu Elementary School” (NGL site id = 539, test ID = 2584), shown in Figure 3-5, which experienced surface manifestation of liquefaction from the 1995 Kobe earthquake (NGL field manifestation ID, FLDM ID = 1432). As in Figures 3-2 and 3-3, multiple critical layers could reasonably be identified. Layer 2 might be preferred on account of being near the ground surface (thus liquefaction would be more likely to manifest), although the q_{c1Ncs} is relatively high and its shallow depth below the ground water table could lead to partial saturation. On the other hand, layer 4 could be preferred because it is thicker, has lower q_{c1Ncs}, and its depth below the ground water table makes partial saturation unlikely. As shown in Figure 3-6, the first choice (shallower critical layer) would place the case history below both the triggering curve developed in this study and the BI16 curve, whereas the second choice (deeper critical layer) places the case history above the two curves. The BI16-selected layer was the deeper layer in agreement with models whereas five out of six of the SMT members selected the shallower layer in the exercise described in Section 3.4.

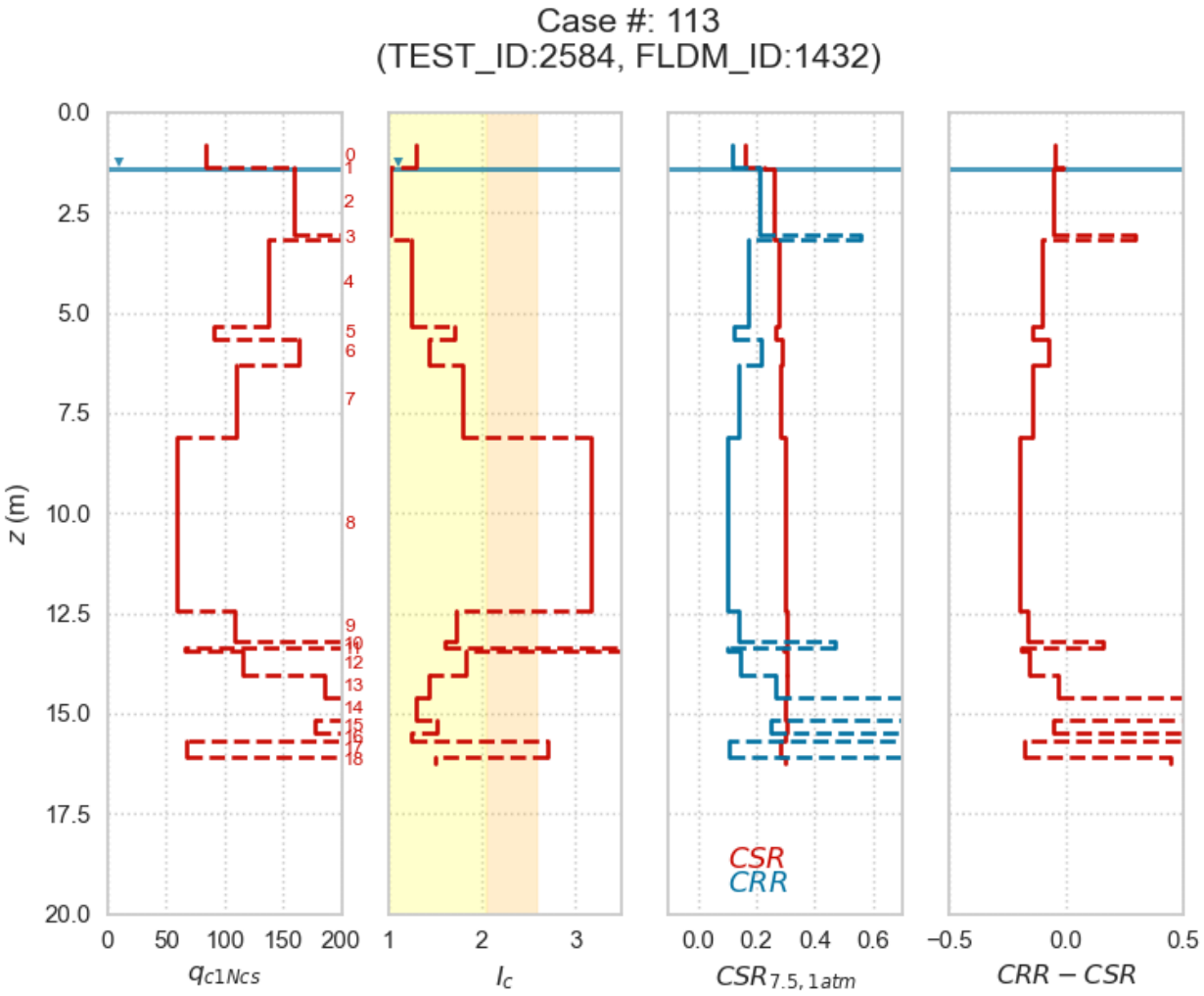

Figure 3-5 **Example CPT profiles for Imazu Elementary School site from the 1995 Kobe earthquake derived using procedures presented in Sections 5.3-5.4. Surface manifestation occurred at the site**

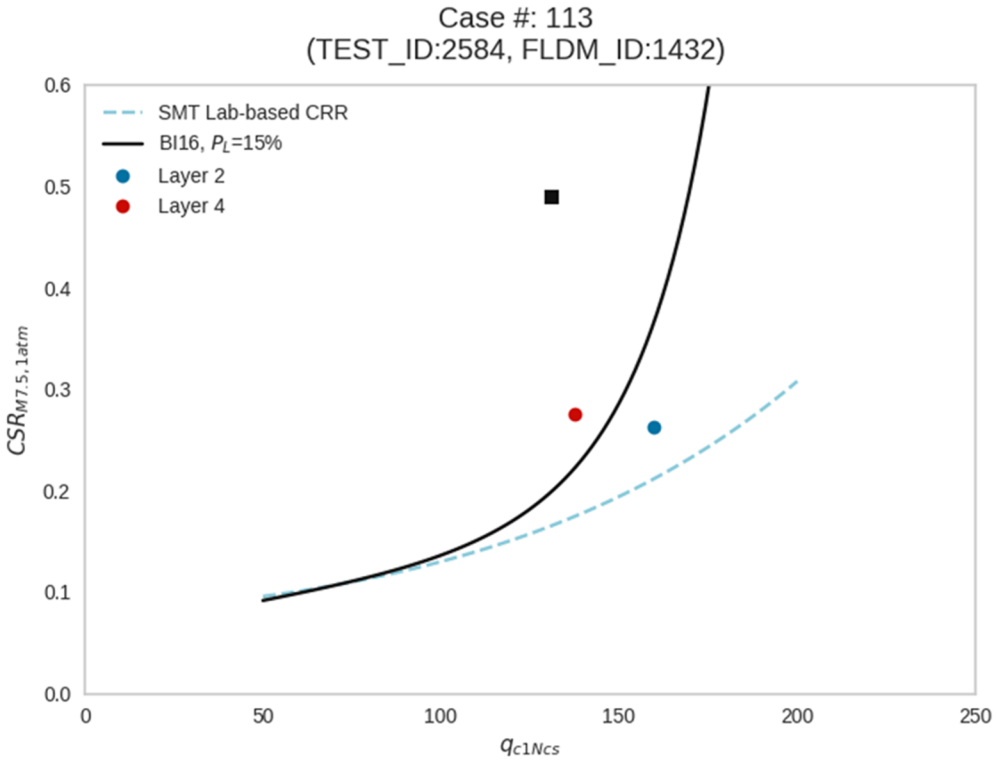

Figure 3-6 **Position of Imazu Elementary school case history in $CSR_{M7.5,1atm}$ - q_{c1Ncs} space using alternate critical layer selections. Black square represents this case history as reported in Boulanger and Idriss (2016) (e.g., their interpretation of PGA), computation of $CSR_{M7.5,1atm}$ and q_{c1Ncs}**

A second example case of interest is NGL site “Port of Oakland, 7th Street Terminal (POO7)” (NGL site ID = 562), CPT “POO7-3” (NGL test ID = 2651) during the 1989 Loma Prieta earthquake (NGL FLDM ID = 1467), the interpreted CPT logs for which are shown in Figure 3-7. As in Figures 3-2 and 3-3, multiple critical layers could reasonably be identified. Layers 4-5 might be preferred on account of being near the ground surface (thus liquefaction would be more likely to manifest), although the q_{c1Ncs} is relatively high and its shallow depth below the ground water table could lead to partial saturation. On the other hand, layer 13 could be preferred because it is relatively thick, has lower q_{c1Ncs}, and is likely saturated, however the greater depth could suppress manifestation potential. As shown in Figure 3-8, the first choice (shallower critical layer, e.g., layers 4-5) would place the case history well below both the laboratory-based triggering curve developed in this study and the BI16 curve, whereas the second choice (deeper critical layer, e.g., layer 13) places the case history near to these two curves. Adopting the BI16-selected layer using their computed q_{c1Ncs} and *CSR* places the case history well above both curves. An interesting aspect of this case study is the varying interpretations of whether liquefaction occurred or not. POO7-3 was initially identified as an area that had “no surface manifestations of liquefaction” (Kayen et al., 1998), but subsequent interpretations indicated that this site could be considered as having experienced liquefaction (Cetin et al., 2004, 2018) or "marginal" liquefaction (Idriss and Boulanger, 2012; Boulanger and Idriss, 2014). No sand boils were observed within 15-20 meters of POO7-3, but the CPT is located approximately 20-30m away from a zone of ample fissures and sand boils, deformations toward the free face, and a small lateral spread into the bay. We do not take a position on the field observations, but rather point out that the intense scrutiny of this case was likely a consequence of its being an outlier, particularly if the original field observation of no manifestation is adopted. A relatively high degree of scrutiny for strong outliers is another characteristic of cognitive bias.

We cannot know to what extent confirmation bias may or may not have affected the development of any particular semi-empirical triggering model. However, the circumstances for it to have influenced decision making were clearly present, especially given the traditional research approaches that led to the models (i.e., small teams of investigators who assemble their own database and develop a model with relatively limited outside interaction). Independent assessments of model performance have indicated large numbers of mis-predictions (Maurer et al., 2015b; Geyin et al., 2020a), especially false positives, which could be interpreted to suggest that absent cognitive bias in the critical layer selections, less favorable performance may be achieved. In a similar manner, the following section shows an appreciable rate of different critical layer selections, again suggesting (though not proving) the potential for cognitive bias to have played a role. Ultimately, the problem when cognitive bias influences a fundamental aspect of the model development process, is that it further separates the data analysis undertaken in model development from what can be done in application. This can produce outcomes with too-small levels of model uncertainty and potentially other problems.

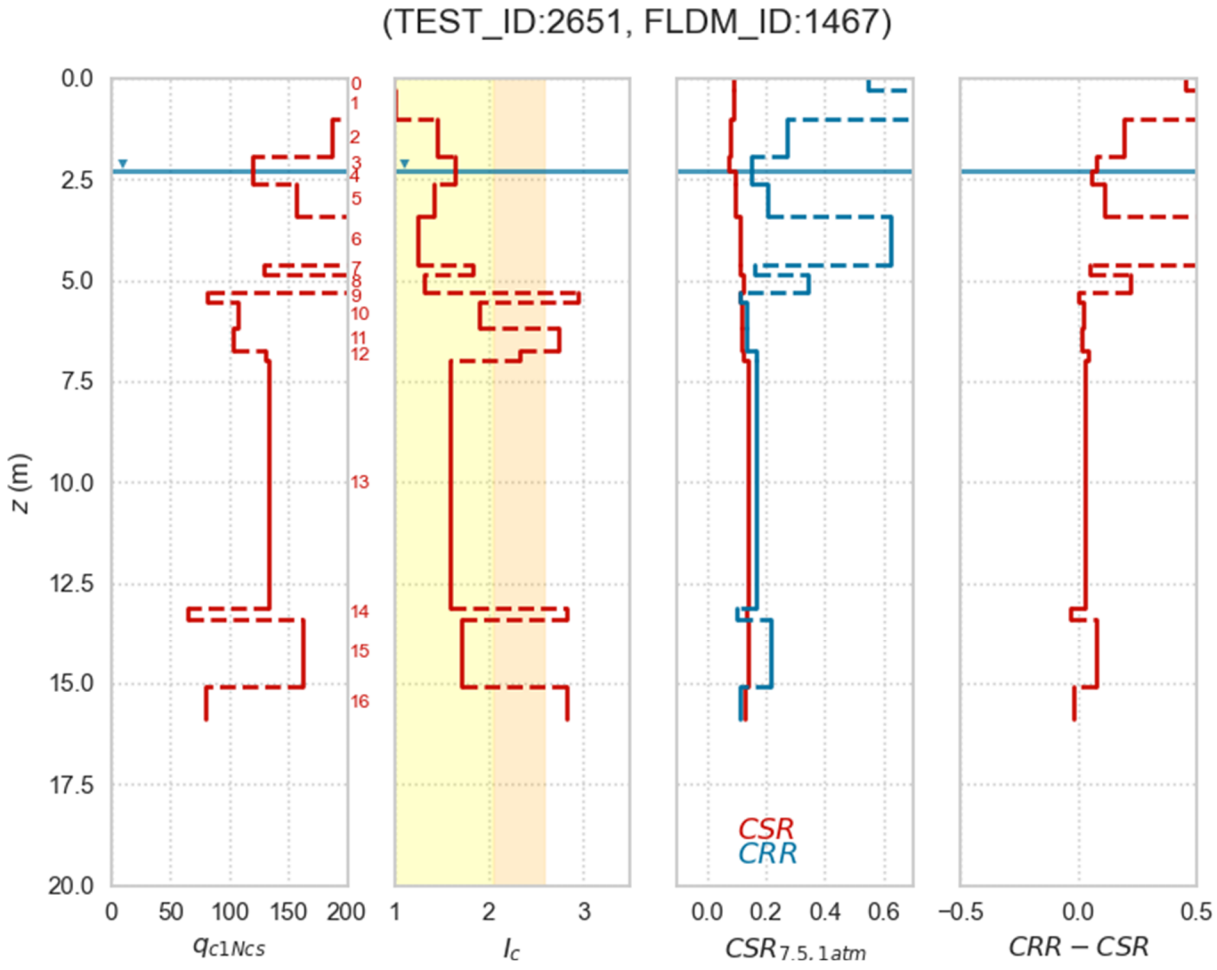

Figure 3-7 **Example CPT profiles for Port of Oakland, 7th Street Terminal (POO7) site (CPT POO7-3) from the 1989 Loma Prieta earthquake derived using procedures presented in Sections 5.3-5.4. This is an example where the manifestation or lack of manifestation of liquefaction is unclear.**

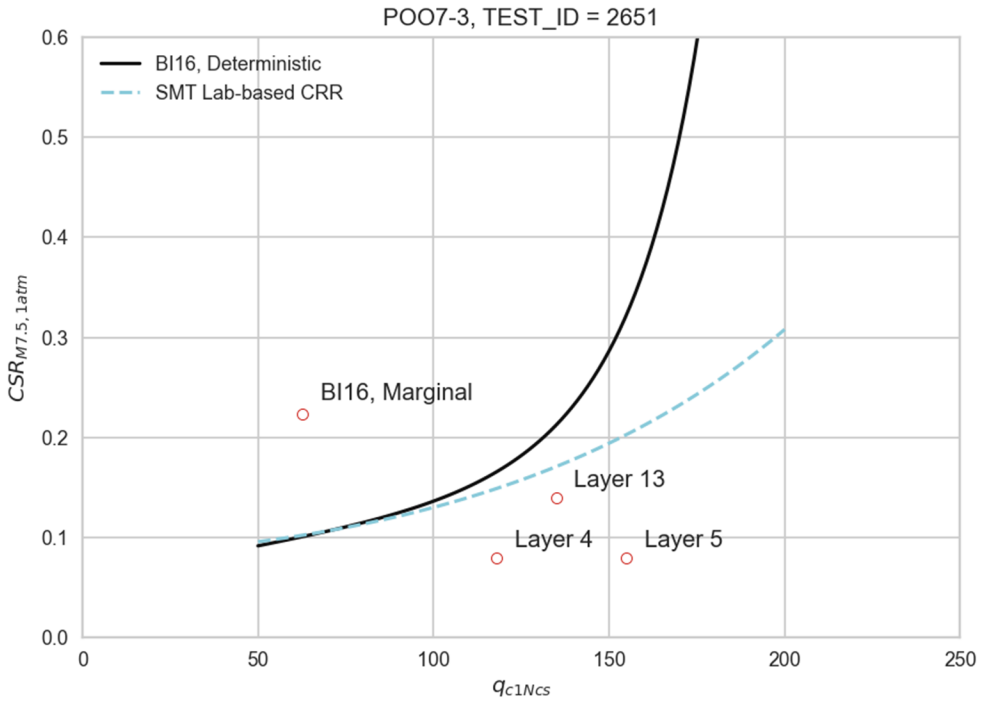

Figure 3-8 Position of Port of Oakland, 7th Street Terminal (POO7-3) case history in $CSR_{M7.5,1atm}$ - q_{c1Ncs} space using alternate critical layer selections and alternate selections of whether manifestation occurred or not

3.4 Critical Layer Selection Study

A study was conducted to explore the analyst-to-analyst variabilities in critical layer selection. We randomly selected 40 CPTs from sites utilized in legacy models, and each member of the SMT made critical layer selections. We deliberately restricted the information available to each analyst to be the same as what is available to an engineer in a forward assessment of liquefaction. Specifically, we included profiles of q_{c1Ncs}, I_c, $CSR_{7.5,1atm}$, and the difference between *CRR* and *CSR* where *CRR* here is estimated using the laboratory-derived prior relationship as a function of q_{c1Ncs} (Section 6.1). Prior to selecting critical layers, the SMT agreed that each member would independently identify the layer most likely to cause surface manifestation. In some cases, the layer most likely to trigger may not be the layer most likely to manifest because the triggered layer is deep, the layer is thin, a strong non-liquefiable layer lies atop the layer, etc.

A screenshot of the tool utilized by the SMT to make critical layer selections is shown in Figure 3-9. No indication of the site name, earthquake, or whether manifestation was or was not observed at the site is included in the tool because such information might contribute unwittingly to confirmation bias and would not be available to engineers applying the model in a forward sense. SMT members would select one of the layers identified by the agglomerative clustering algorithm (Hudson et al., 2023a) as the critical layer. Furthermore, SMT members could indicate whether interbedding was present within the critical layer and/or profile, whether the critical layer is particularly deep, whether a strong crust exists at the site, and/or if partial drainage could exist in cases with shallow liquefiable layers in the absence of a low-permeability capping layer.

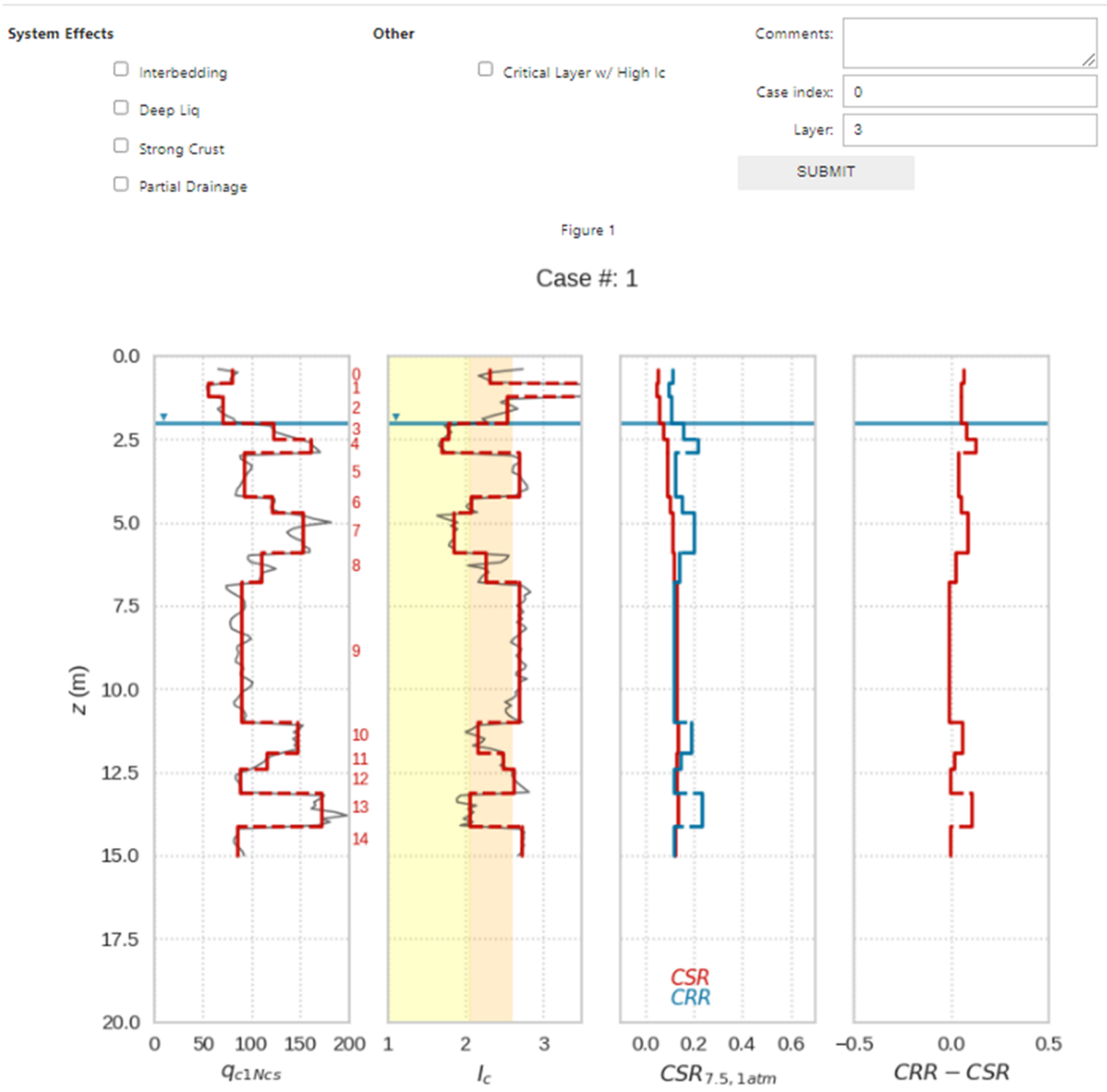

Figure 3-9 Screenshot of the tool used by SMT members to select critical layers

They could also indicate whether the critical layer has a high I_c, and therefore might contain plastic fines. Open-ended comments could also be entered.

The depths to the top of the critical layer selected by the SMT members are compared with those selected by Boulanger and Idriss (2016, "BI16") in Figure 3-10, along with R^2 values indicated in the upper-left corner of each figure. Open symbols indicate sites that did not manifest liquefaction, while closed circles did manifest. Significant differences are apparent in the selections made by the SMT members compared with those by Boulanger and Idriss (2016), with R^2 values ranging from 0.22 to 0.37. Notably, differences *between* the SMT members are also significant, as illustrated subsequently. BI16 did not select from the layers identified by the

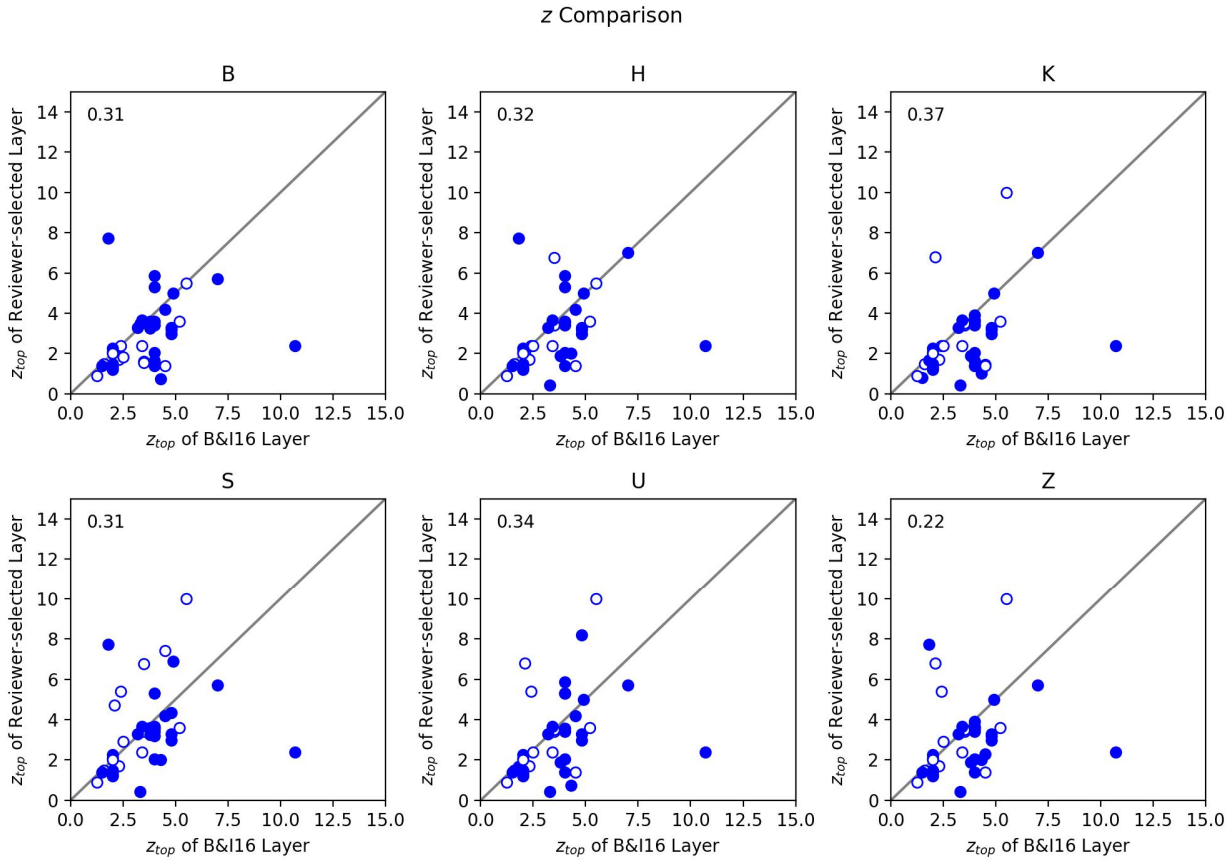

Figure 3-10 ***z_{top}* of critical layers selected by SMT members compared with Boulanger and Idriss (2016). R^2 values shown in upper-left corners. Open circles represent "no manifestation" observations. Closed circles represent "manifestation" observations.**

clustering algorithm, and therefore their z_{top} value for a particular profile might not be available as an option for the SMT members. However, differences in the selections are much more significant than can be explained by that detail. In general, members of the SMT tended to select shallower layers than BI16, which may be caused by the SMT team's focus on manifestation over triggering, combined with the expectation that shallower layers are more likely to manifest. Similar figures are provided for I_c, q_{c1Ncs}, and *CSR* in Figures 3-11 through 3-13. The R^2 values tend to be higher, on average, than for z_{top}, but nevertheless exhibit significant differences from BI16.

As shown in Figure 3-13, a notable feature of the BI16-to-SMT comparison plots are lower SMT *CSR* values for relatively strong shaking conditions (*CSR* > ~ 0.2). Many of the sites for which these estimates differ have *CSR* values from legacy data sets taken from nearby recordings on relatively stiff soil sites compared to the neighboring soft soil sites that comprise the case histories. This method of estimation is described further in Section 5.2 (labeled as Approach 5 in that section). The *CSR* values estimated by the SMT are lower due to consideration of nonlinearities associated with the strong shaking and soft soils site conditions at the liquefaction sites.

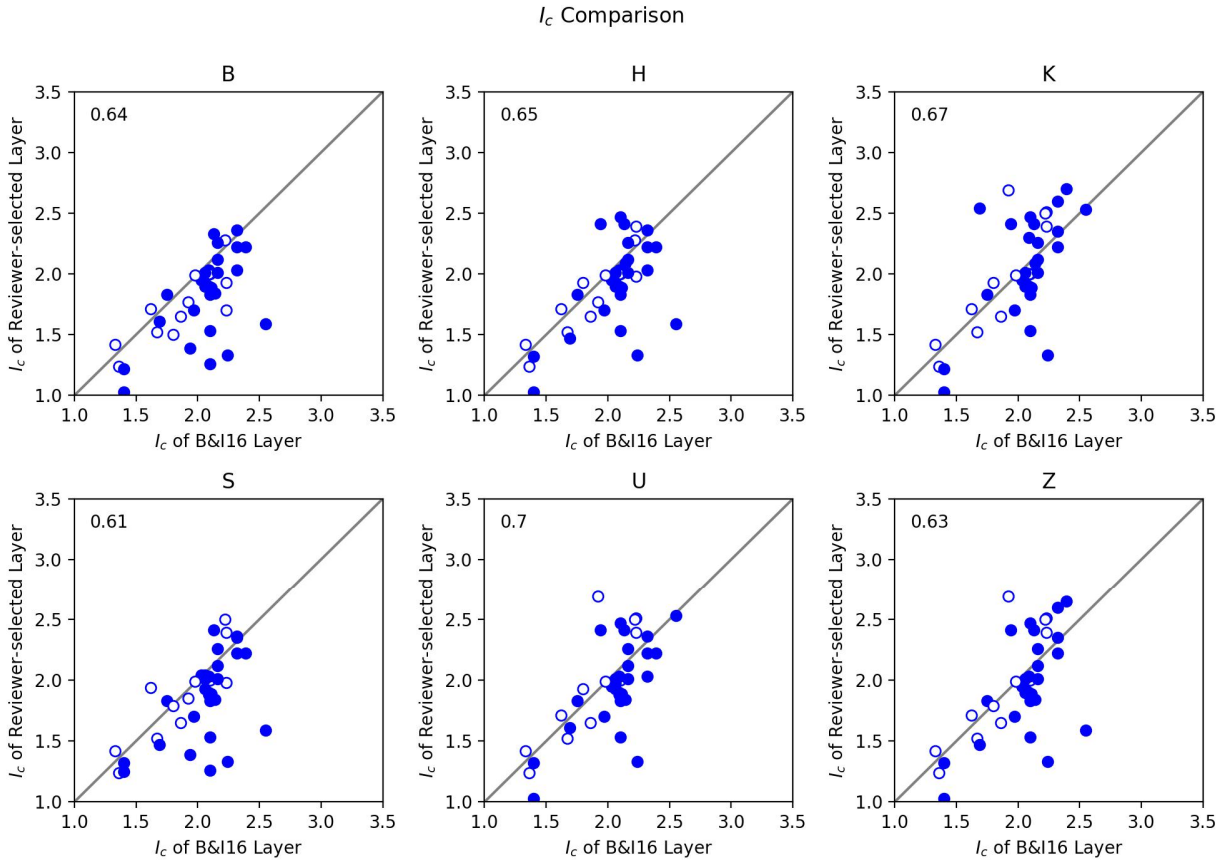

Figure 3-11 ***I_c*, of critical layers selected by SMT members compared with Boulanger and Idriss (2016). R^2 values shown in upper-left corners. Open circles represent "no manifestation" observations. Closed circles represent "manifestation" observations.**

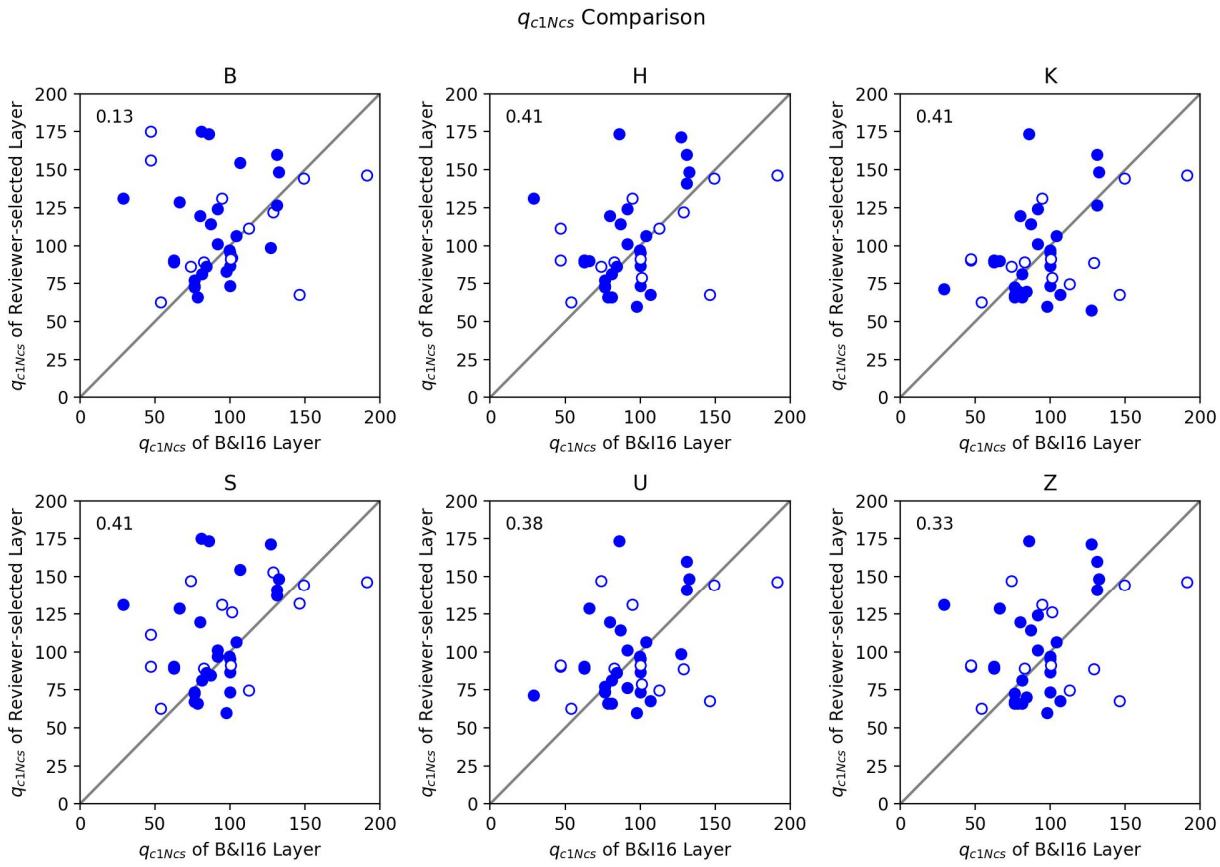

Figure 3-12 ***q_{c1Ncs}*, of critical layers selected by SMT members compared with Boulanger and Idriss (2016). R^2 values shown in upper-left corners. Open circles represent "no manifestation" observations. Closed circles represent "manifestation" observations.**

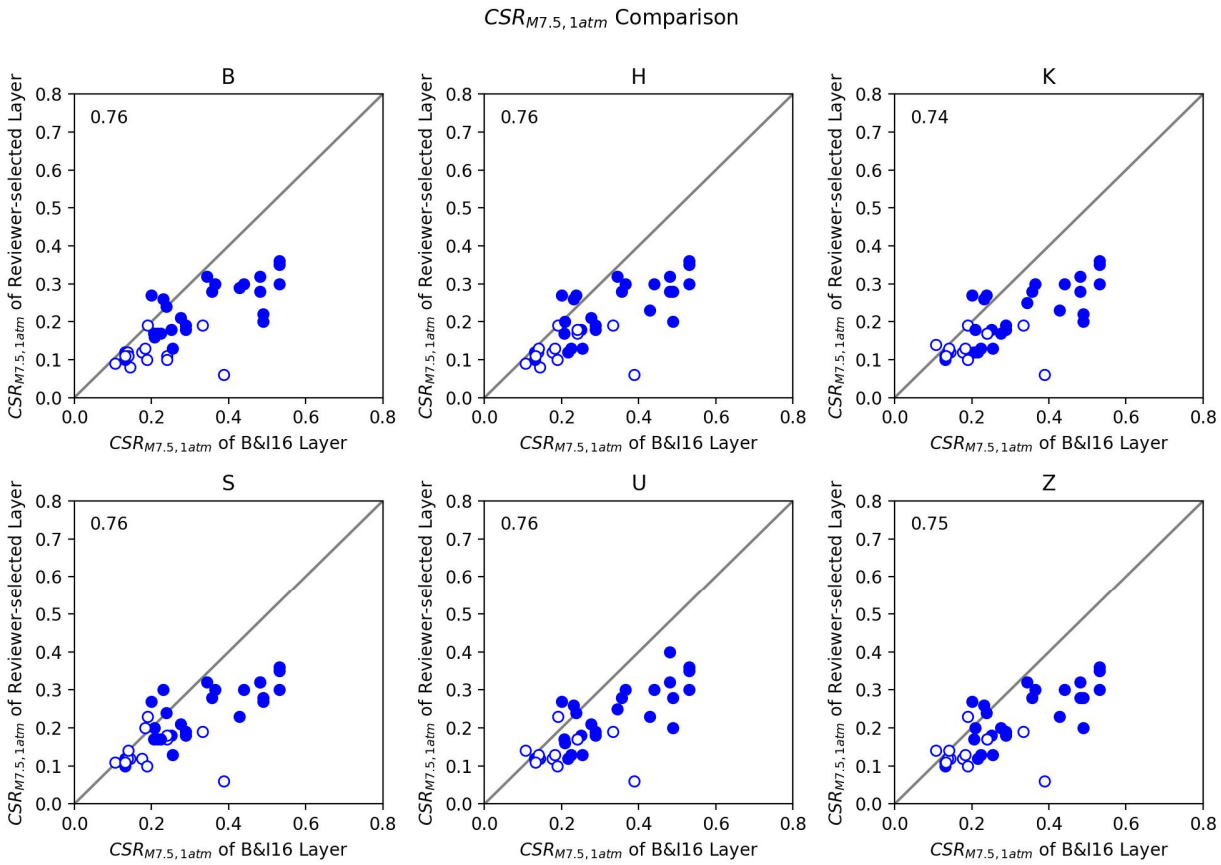

Figure 3-13 $CSR_{M7.5,1atm}$ of critical layers selected by SMT members compared with Boulanger and Idriss (2016). R^2 values shown in upper-left corners. Open circles represent "no manifestation" observations. Closed circles represent "manifestation" observations.

Figure 3-14 compares critical layer selections by the SMT with those of BI16 in q_{c1Ncs}-CSR space. Open circles are profiles that did not manifest, while closed circles are profiles that manifested. Significant differences are observed in the positions of the points on these graphs for each SMT member compared with BI16; differences between SMT members also exist. In all cases, the BI16 model represents a broader range of q_{c1Ncs} values. Another important difference is that, among these 40 cases, the BI16 selections do not include any false negatives (FN, false predictions of no manifestation (i.e., closed circles below the curve), whereas the SMT members had 2 to 5 false negatives). Note that BI16 do have some false negatives among the dataset utilized to form their model; however, those cases were not among the 40 selected for this exercise. The SMT members tended to have fewer false positives (FP, false predictions of manifestation) than BI16, rendering overall accuracy values that are similar. Defining accuracy as the number of true predictions (TP, accurate predictions of manifestation) divided by the total number of cases, the resulting accuracy values are 82.5% for BI16, 82.5% for Brandenberg (SMT member "B"), 77.5% for Hudson, 75% for Kramer, 80% for Stewart, 80% for Ulmer, and 77.5% for Zimmaro. Despite the different selections, the accuracy of the SMT analysts' selections are all reasonably close to each other, and reasonably close to BI16. This indicates that the various individual biases each analyst brings to their selections may have offsetting effects from profile-to-profile with respect to accuracy.

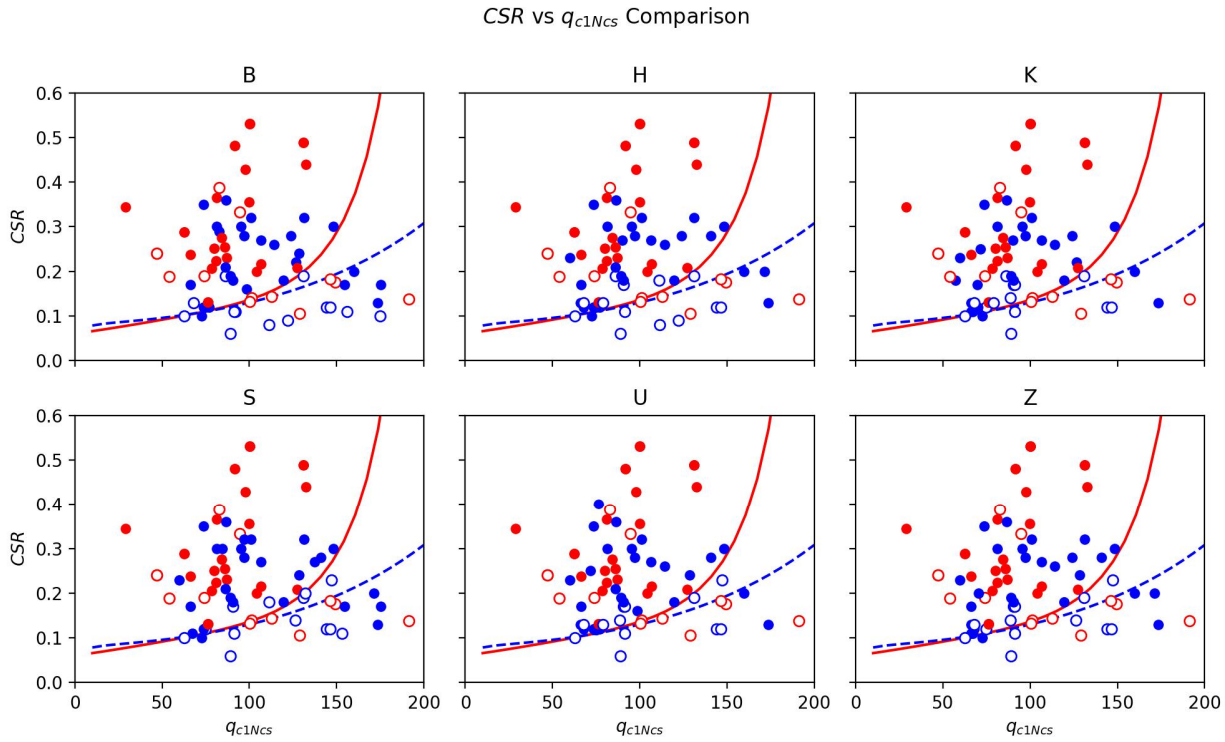

Figure 3-14 Critical layer properties selected by SMT compared with Boulanger and Idriss (2016). Red points represent locations of $CSR_{M7.5,1atm}$ vs q_{c1Ncs} points as defined by BI16-selected critical layers, whereas blue points represent locations as defined by reviewer-selected critical layers. Red line represents the BI16 deterministic *CRR* curve, blue dashed line represents the SMT's CRR curve (Section 6.2). Open circles represent "no manifestation" observations. Closed circles represent "manifestation" observations.

Figures 3-15 through 3-18 compare properties of critical layers selected by the SMT members. In general, R^2 values are higher among the critical layers selected by the SMT members than for each member compared with BI16. This outcome likely reflects differences in information available to analysts at the time the critical layer selections were made. Although the SMT members selections are more similar with each other than with BI16, significant differences nevertheless are observed in the critical layers selected by the SMT members. This is an indication that the judgment of individual analysts is different, even when those analysts have worked closely together for years. This points to a need for objectivity in critical layer selections so that liquefaction manifestation models are repeatable and independent of any one analysist's view.

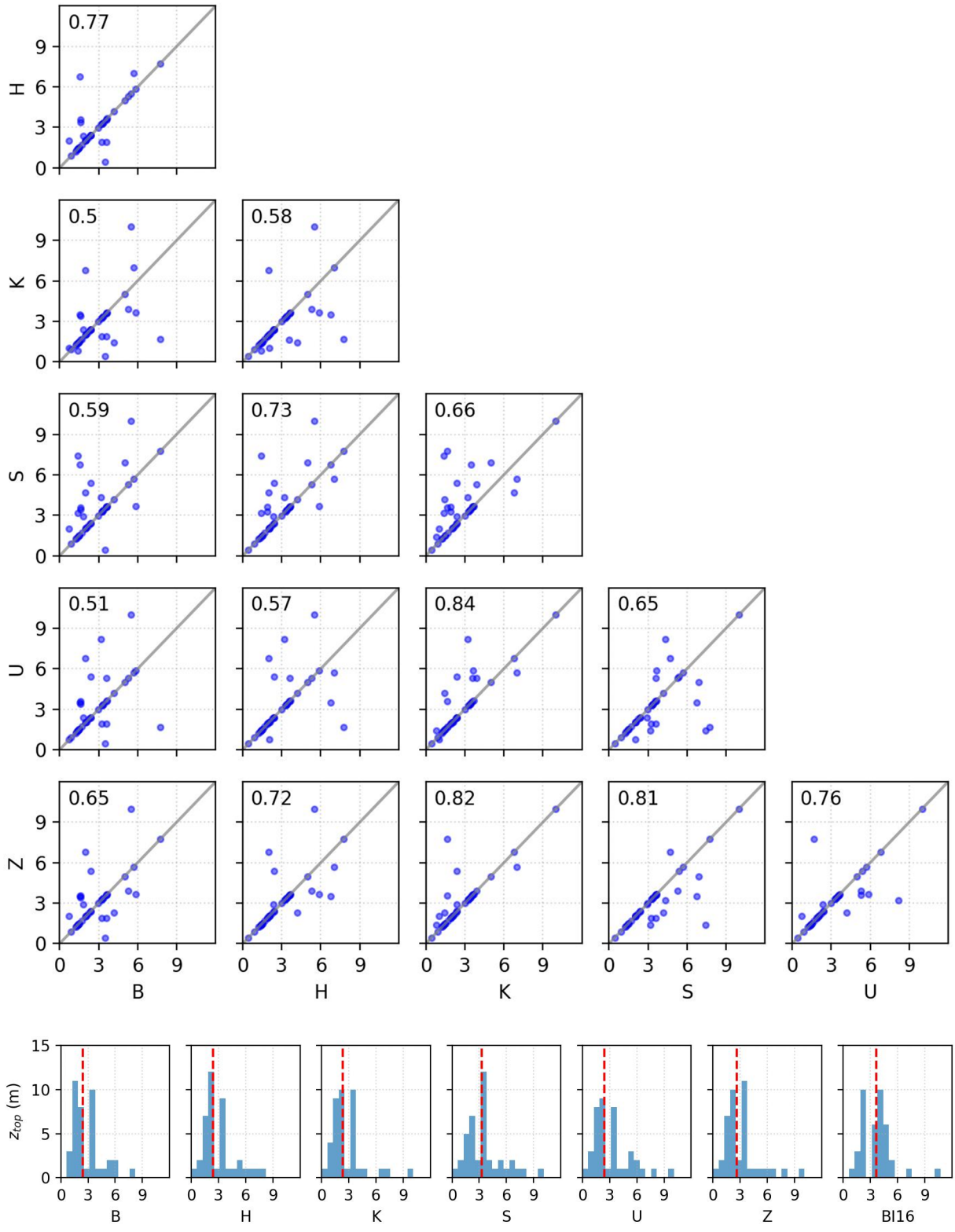

Figure 3-15 Correlation of z_{top} values among critical layers selected by SMT members

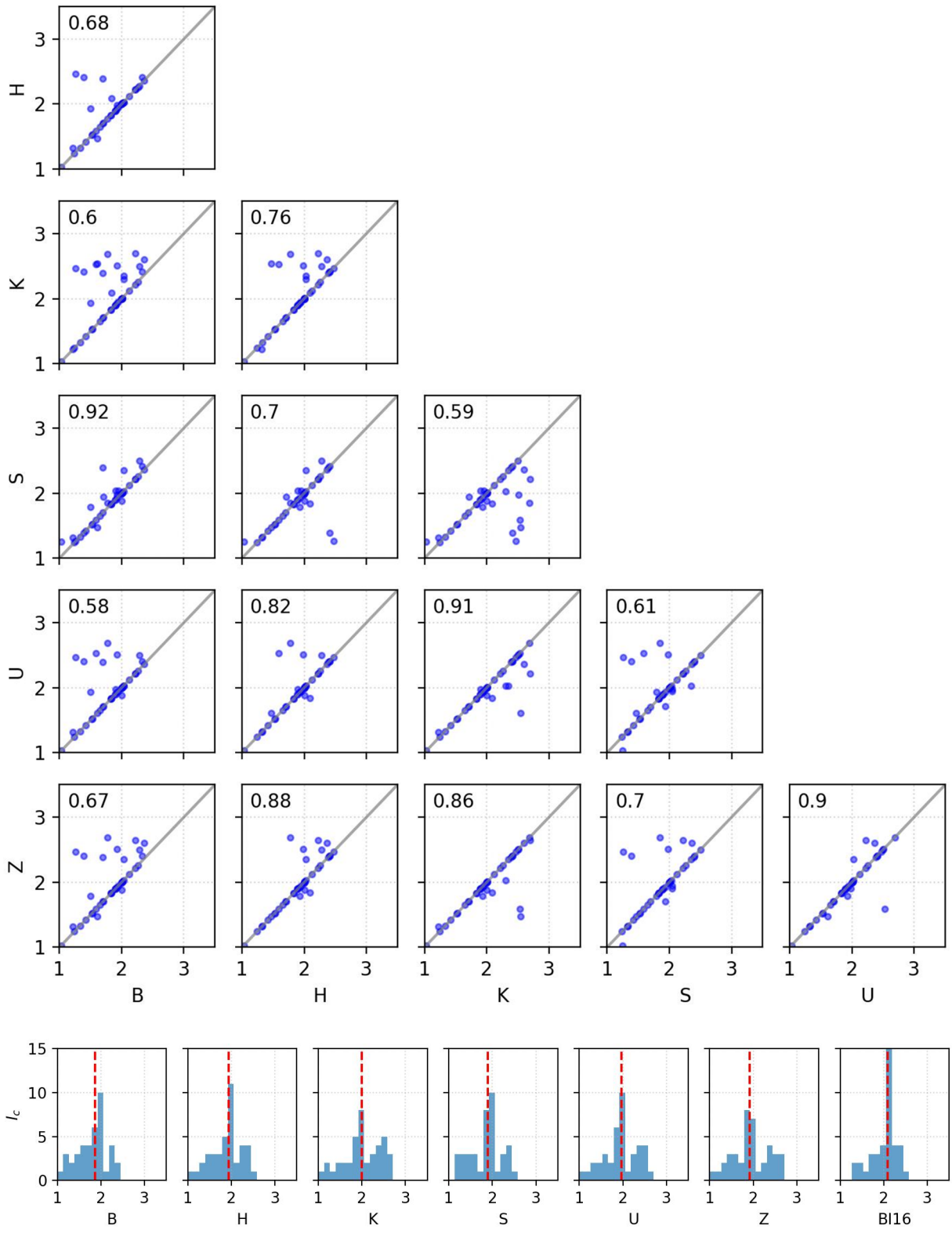

Figure 3-16 Correlation of I_c values among critical layers selected by SMT members

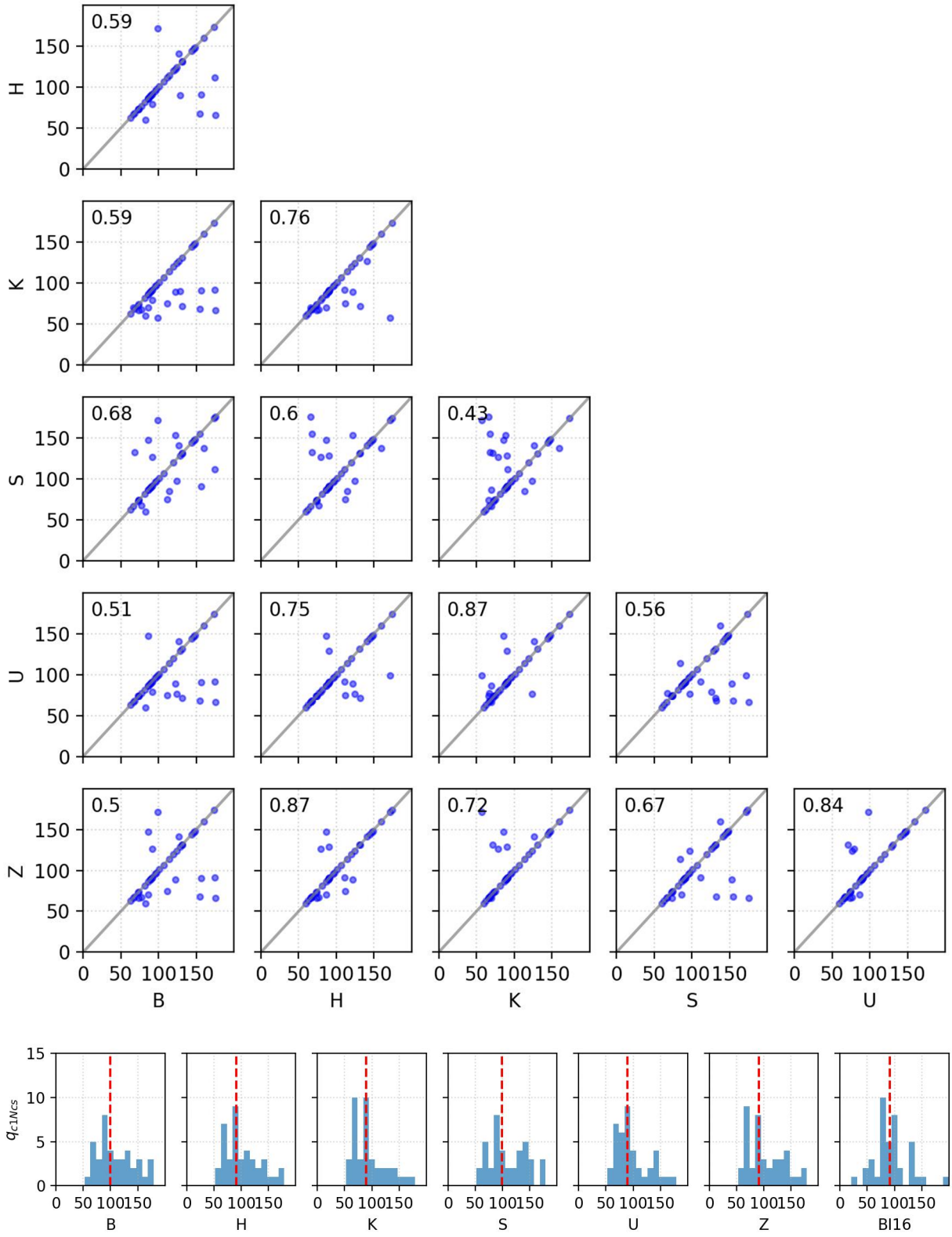

Figure 3-17 Correlation of q_{c1Ncs} values among critical layers selected by SMT members

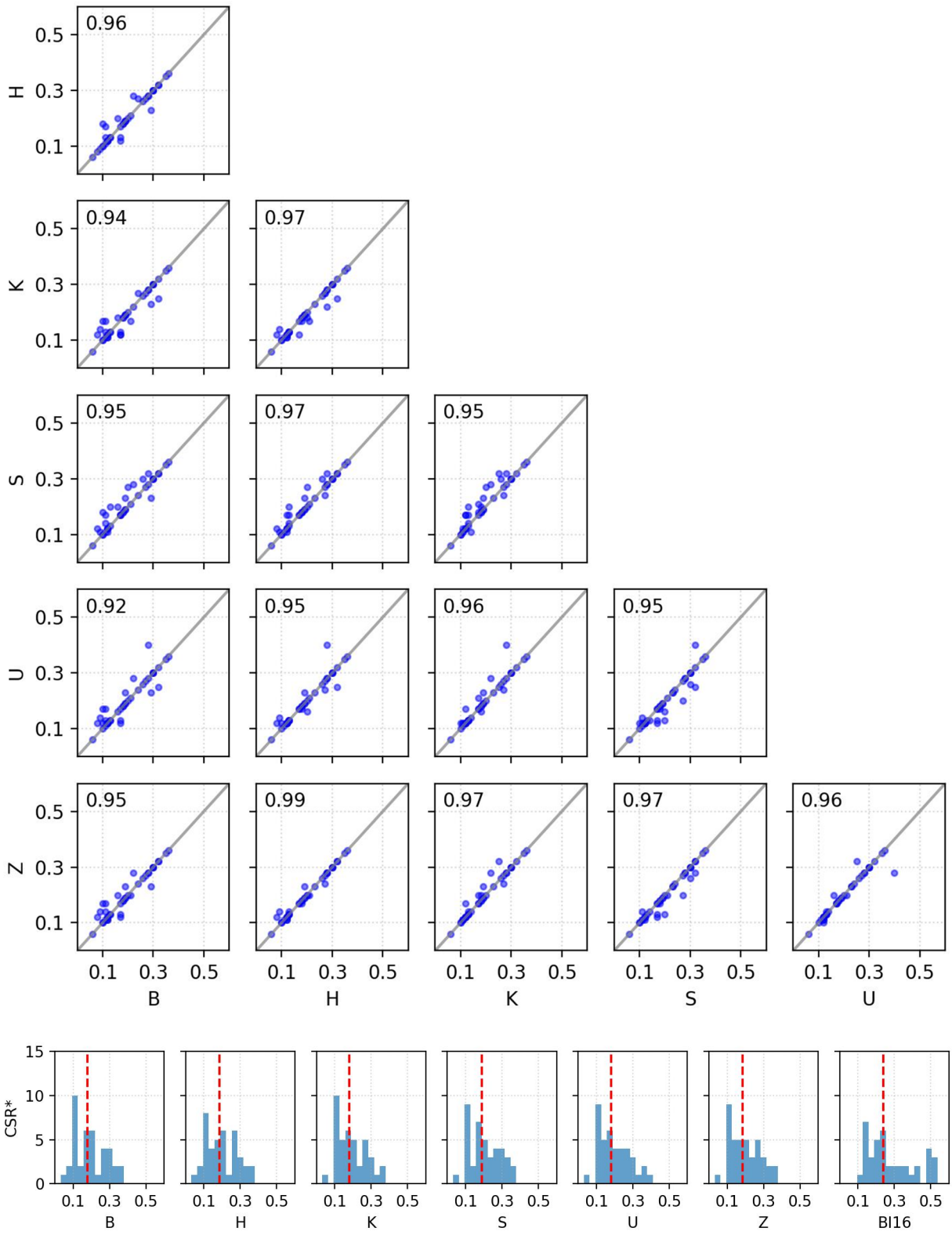

Figure 3-18 Correlation of *CSR values among critical layers selected by SMT members**

4 TRIGGERING AND MANIFESTATION

As discussed in Chapter 2, the occurrence of liquefaction is often identified by the observation of surficial manifestation of its effects. Historically, it has been common to interpret manifestation at case history sites as positive evidence of triggering (i.e., that manifestation = triggering) and the absence of manifestation as positive evidence that triggering did not occur (no manifestation = no triggering). However, it is possible for liquefaction to be triggered in thin, deep susceptible layers without producing surface manifestation. It is also possible for manifestation evidence such as ground failure due to cyclic softening or sand boils to develop at sites where pore pressures in thick, shallow, susceptible layers increase significantly but not to the level of liquefaction triggering (Tokimatsu et al., 2012; Kramer et al., 2016).

Manifestation, or its absence, must therefore be recognized as a consequence of pore pressure generation mediated by the characteristics of the soil profile. Detailed investigations and modeling of sites in Christchurch, New Zealand have illustrated the extent to which interlayering of liquefiable and non-liquefiable soil layers can influence surface manifestation (Cubrinovski et al., 2019; Hutabarat and Bray, 2021, 2022).

4.1 Bayesian Framework

In our view, the historical reliance on manifestation as an indicator of liquefaction triggering and lack of manifestation as an indicator of a lack of triggering has led to conventional liquefaction triggering procedures producing factors of safety against manifestation rather than of liquefaction triggering. The most recent versions of these procedures produce a probability of manifestation, P[*M*] (and consequently a probability of no manifestation, P[*NM*] = 1 – P[*M*]). Implicit in the interpretation of the results of these procedures is the assumption that the probability of triggering is equal to the probability of manifestation, P[*T*] = P[*M*] (and the probability of no triggering, P[*NT*] = 1-P[*T*]).

Surface manifestation can be important in many situations and can cause damage to light surface structures (e.g., pavements), contribute to settlement of lightweight structures (e.g., private houses), and require significant clean-up efforts (e.g., Christchurch in 2011). However, the actual triggering of liquefaction at both shallow and large depths is more fundamentally important for many critical structures. For the purposes of damage and loss estimation, a more fundamental and useful analysis would be to estimate the actual probability of triggering, P[*T*], and with it, P[*NT*] = 1 – P[*T*], and separately evaluate the probability of manifestation conditional on triggering, P[*M*|*T*] or not triggering, P[*M*|*NT*]. In terms of case history interpretation of triggering, we need to evaluate the probability that the soil in the critical layer triggered for case histories where manifestation was observed, i.e., P[*T*|*M*]. At the same time, we need to evaluate the probability that liquefaction did *not* occur in a critical layer for case histories where manifestation was *not* observed, i.e., P[*NT*|*NM*]. To develop this more complete analysis, we need to distinguish between triggering and manifestation and recognize that triggering can occur without manifestation and vice versa. These distinctions can be made using a Bayesian approach.

4.1.1 Bayes' Theorem

Bayes' theorem derives directly from the total probability theorem. With respect to the Venn diagram in Figure 4-1, the intersection of Events *A* and *B* can be expressed as

$$P[A \cap B] = P[A|B]P[B] \; = \; P[B|A]P[A] \tag{4-1}$$

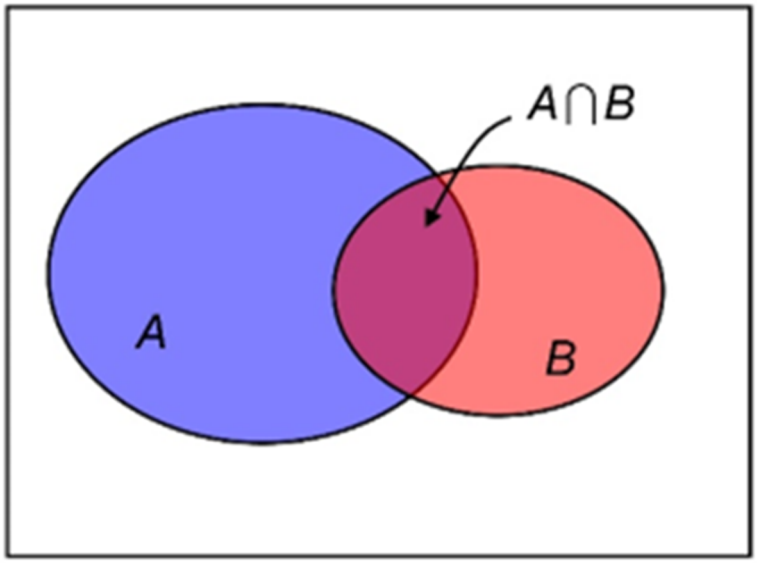

Figure 4-1 Venn diagram illustrating intersection of two events, *A* and *B*

Solving for the probability of *A* given *B* yields Bayes' theorem,

$$P[A|B] = \frac{P[B|A]P[A]}{P[B]} \tag{4-2}$$

In many cases, Event *A* is described as a hypothesis being true and Event *B* as the evidence that the hypothesis is true. In that case, it can be expressed as

$$P[hypothesis|evidence] = \frac{P[evidence|hypothesis]P[hypothesis]}{P[evidence]} \tag{4-3}$$

The denominator can be expanded by considering the evidence for both cases of the hypotheses, i.e., that the evidence is consistent with the hypothesis and that the evidence contradicts the hypothesis.

$$P[hypothesis|evidence] = \frac{P[evidence|hypothesis]P[hypothesis]}{P[evidence\ when\ hypothesis\ is\ true] + P[evidence\ when\ hypothesis\ is\ false]} \tag{4-4}$$

In the liquefaction triggering problem, the common interpretation hypothesizes that liquefaction has been triggered based on the evidence, or absence of evidence, of surface manifestation. However, because manifestation also depends on hydraulic and system-related factors, in addition to the actual triggering of liquefaction in some layer of soil, a direct correlation between

surface manifestation and triggering is not possible. Using the previously defined symbols for triggering and manifestation, Bayes' theorem can be expressed in the following manner for a soil that is susceptible to liquefaction (i.e., with P[*S*] = 1.0)

$$P[T|M] = \frac{P[M|T]P[T]}{P[M]} = \frac{P[M|T]P[T]}{P[M|T]P[T] + P[M|NT]P[NT]} \quad 4\text{-}5$$

The Bayesian framework can also be applied to case histories where no evidence of surficial manifestation was observed. Such cases have historically been interpreted as indicating the absence of triggering. For this case, Bayes' Theorem can be applied as

$$P[NT|NM] = \frac{P[NM|NT]P[NT]}{P[NM]} = \frac{P[NM|NT]P[NT]}{P[NM|NT]P[NT] + P[NM|T]P[T]} \quad 4\text{-}6$$

The Bayesian framework may also be extended to include manifestations from non-susceptible layers. Cyclic softening of clay-like soils may produce manifestations such as surface cracks, lateral ground deformations, and settlement. When manifestations occur in the absence of sand boils, it is often difficult to ascertain whether the cause was liquefaction or cyclic softening. However, cyclic softening is not included in the equations presented here for simplicity.

4.1.2 Probabilities of Interest

The probabilities in the Bayesian approach relate to both triggering (or not triggering) and manifestation (or lack thereof). Brief descriptions of each, using the notation in Figure 2-4 in which H_1 is the thickness of the non-liquefied crust and H_2 is the thickness of an underlying liquefaction-susceptible soil (after Ishihara 1985, see also Section 2.1.3.1), are presented in Table 4-1 below. Of the six probabilities listed here three are directly computed from their complements, so models for only three independent probabilities, P[*T*], P[*M*|*T*], and P[*M*|*NT*], are needed to explore their impacts on the relationship between triggering and manifestation.

Table 4-1 Descriptions of probabilities in the Bayesian approach

P[*T*]	Probability that the susceptible soil layer (H_2 layer) triggers. For now, assume we know this (more later).
P[*NT*]	Probability that H_2 layer does not trigger = 1 – P[*T*].
P[*M*|*T*]	Probability of manifestation given that H_2 layer triggers. Depends on H_1-H_2 relationship and other hydraulic factors.
P[*NM*|*T*]	Probability that no manifestation occurs even when H_2 layer triggers. Equal to 1 – P[*M*|*T*].
P[*M*|*NT*]	Probability that high pore pressures (but not high enough to trigger liquefaction) cause sand boils or other observations we usually interpret as manifestation of liquefaction. Can potentially occur with thick liquefiable layer (high H_2) under thin crust (low H_1).
P[*NM*|*NT*]	Probability that no manifestation is observed when liquefaction is not triggered – equal to 1 - P[*M*|*NT*].

4.1.3 Illustration of Bayes Calculations

Figure 4-2 illustrates the main components of Bayesian calculations. The left side (to the left of the thin vertical line) represents Event *T*, the triggering of liquefaction; the right side represents the event of non-triggering, *NT*. Within each of these columns, conditional probabilities are represented. The red zone is the probability of manifestation due to triggering of the liquefiable layer (its probability conditional upon triggering multiplied by the probability of triggering). The blue zone is the probability of manifestation in the absence of triggering, e.g., ground cracking caused by cyclic softening of non-liquefiable soils or sand boils caused by high (but not high enough to trigger liquefaction) pore pressures in a thick liquefiable layer below a thin crust. As shown in this example, there is a relatively high probability of triggering (loose soil), a high probability of manifestation given triggering, and a low probability of manifestation given no triggering – therefore, the probability that liquefaction actually triggered should be high if manifestation was observed. The probability of triggering given the observation of manifestation is equal to the red area divided by the sum of the areas of the red and blue zones. For P[*T*] = 0.7, P[*M*|*T*] = 0.9, and P[*M*|*NT*] = 0.2 (approximately the values in the figure), P[*T*|*M*] = 0.913, which means that the historical inference that manifestation = triggering is relatively good in this case.

The historical interpretation of case histories also makes use of observations of no manifestation and has implicitly assumed that no manifestation means that liquefaction was not triggered. This case can also be visualized graphically as shown in Figure 4-3. In this case, the purple zone represents the probability of no manifestation when the liquefiable layer does not trigger. The green zone indicates the probability of no manifestation if liquefaction is triggered. As indicated in this example, there is a relatively high probability of liquefaction (loose soil), a low probability of manifestation given triggering (the loose layer is deep and/or thin), and a very low probability of manifestation given no triggering – therefore, the probability that liquefaction actually triggered should be high if manifestation was observed. For P[*T*] = 0.7, P[*M*|*T*] = 0.1, and P[*M*|*NT*] = 0.02 (approximately the values shown in Figure 4-3), P[*T*|*M*] = 0.921 which, as expected, is quite high. However, the probability that liquefaction would not have triggered if manifestation was not observed, i.e., P[*NT*|*NM*], would only have been 0.318. In this case, the historical inference that manifestation = triggering is reasonable (the thin, deep layer would almost certainly have had to trigger in order for surface manifestation to have been observed). However, the assumption that no manifestation means no triggering is not very good, because the probability of triggering given no manifestation P[*T*|*NM*] is 0.682, so P[*NT*|*NM*] = 1 - 0.682 = 0.318. Because of the hydraulic component of manifestation, an observation of no manifestation only supports a relatively low probability that liquefaction was not triggered.

These concepts have implications for how case histories should be interpreted, particularly with respect to the “critical layer” concept in cases that appear as apparent false positives (that have thin and/or deep critical layers) and false negatives (that may generate surface evidence without actually liquefying the soil). If no surficial evidence of liquefaction was observed for the case illustrated in Figure 4-3, the values of P[*T*|*NM*] and P[*NT*|*NM*] mean that there is a 0.682 probability that liquefaction *was* triggered even though no manifestation was observed. In the common graphical display of closed and open circles, this case could then be treated with two data points – an open circle with a weighting factor of 0.318 and a co-located closed circle with a weighting factor of 0.682.

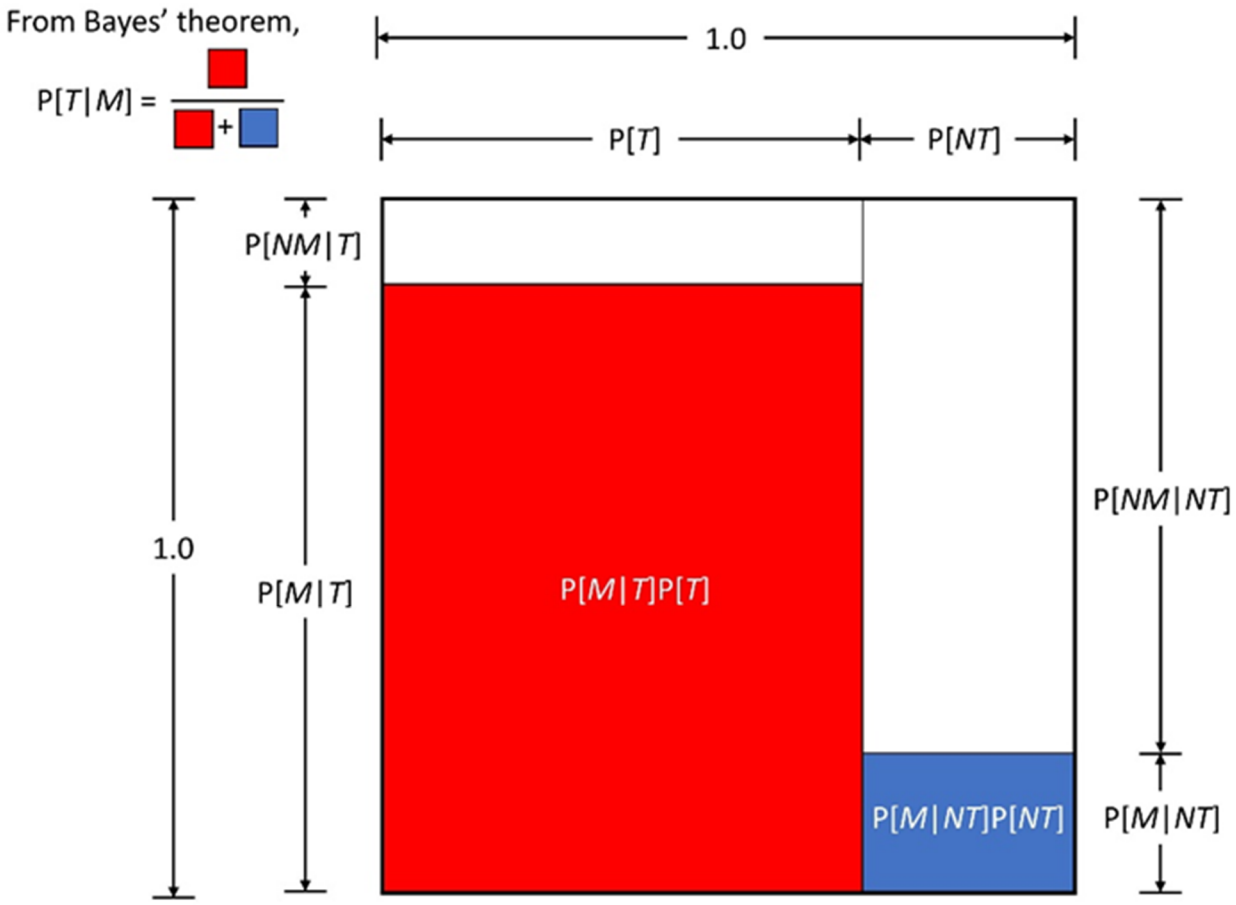

Figure 4-2 Graphical illustration of Bayes' theorem calculation to compute probability of triggering given observation of manifestation

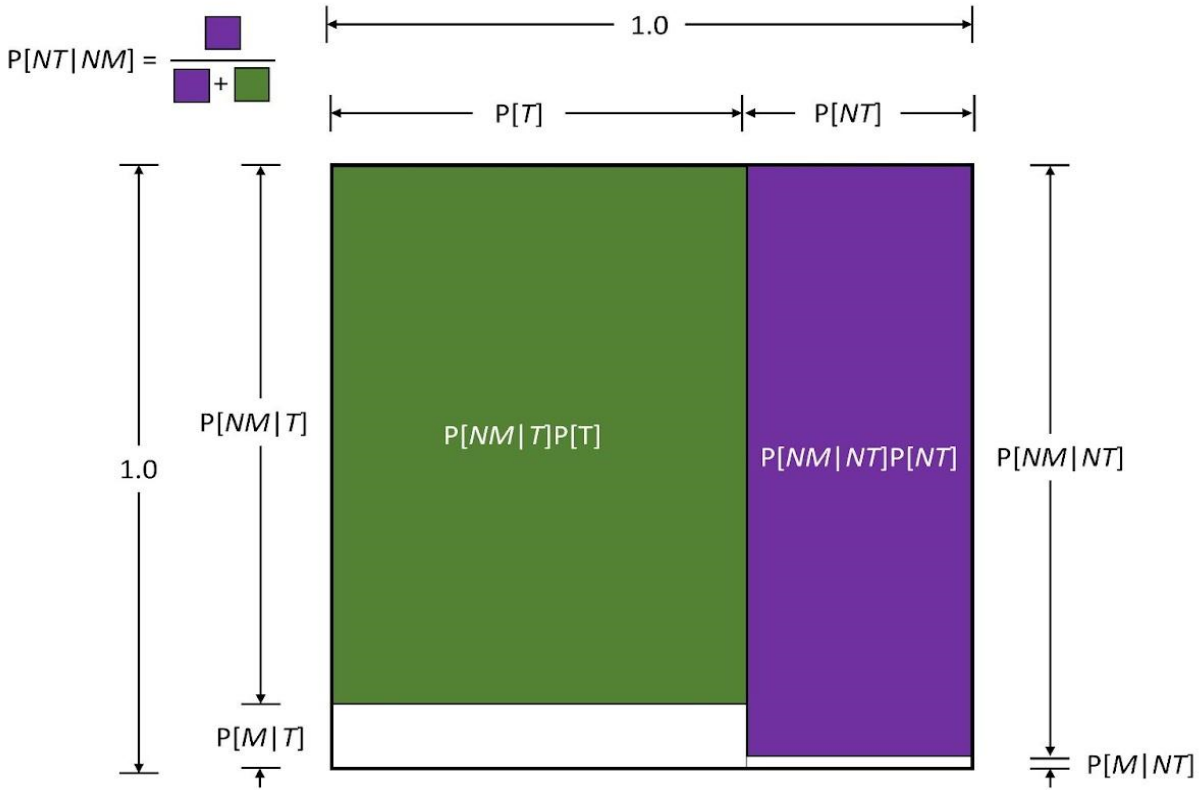

Figure 4-3 Graphical illustration of Bayes' theorem calculation to compute probability of no triggering given the lack of observed manifestation

4.1.4 Example

As a specific example, consider the Wufeng A, WAC-2 CPT site (NGL site ID = 364, test ID = 1585) where no evidence of surface manifestation was observed following the 1999 Chi-Chi earthquake despite the presence of a loose, susceptible layer being exposed to a very high *CSR*. Figure 4-4 shows a CPT profile for the site with the layering detected by an agglomerative clustering algorithm (details in Section 5.3). Of particular interest is Layer 7, which is 35 cm thick and is overlain by a 5.3 m thick crust, which could reasonably be interpreted as a critical layer for this profile. With q_{c1Ncs} ~ 80 and I_c ~ 1.9, Layer 7 is loose and susceptible and therefore should have a high probability of triggering when subjected to strong shaking. For illustrative purposes, assume P[*T*] = 0.9. Because Layer 7 is thin and under a thick crust, manifestation seems unlikely so a value of P[*M*|*T*] = 0.15 will be assumed. Finally, the chance that manifestation could be produced by this layer with pore pressures insufficient to trigger liquefaction seems miniscule, a value of P[*M*|*NT*] = 0.005 will be assumed. These values produce P[*NT*|*NM*] = 0.115, which indicates that little confidence should be placed in a "no liquefaction" interpretation of this case history. Instead, the case history could be interpreted as two co-located data points on a classic *CSR* vs. q_{c1Ncs} curve – a solid circle indicating triggering with a weighting factor of 0.885 and an open circle indicating no triggering with a weighting factor of 0.115. Using these weights, instead of a single open circle with an implied weighting factor of 1.0, we more realistically characterize the response of this soil profile in the triggering model development process.

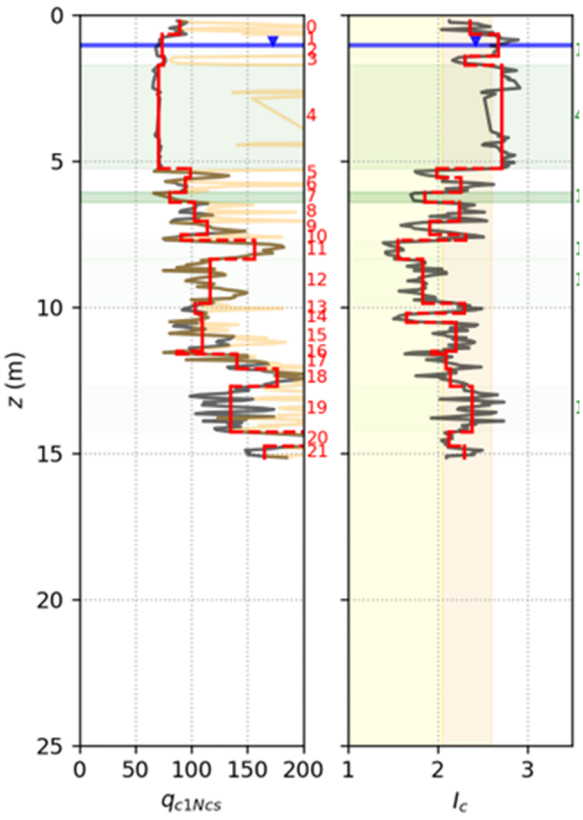

Figure 4-4 CPT profile for Wufeng A WAC-2 site (NGL site ID = 364, test ID = 1585)

4.2 Required Components

Separating triggering from manifestation using the Bayesian framework has potential to reduce bias in our SMT triggering model. It also appears that some, and perhaps a significant amount, of the uncertainty in our model could be associated with "false positive" cases like Wufeng A WAC-2 that show up as a "no liquefaction" with critical layers that have low penetration resistance and a high *CSR*.

In contrast, prior compilations of liquefaction case histories show data that appear to be outliers in the form of "false positives" (cases where manifestation was not observed for conditions under which triggering was expected) and "false negatives" (cases in which manifestation was observed for conditions under which triggering was not expected). By more appropriately interpreting the case histories in terms of probabilities of triggering (or non-triggering) given the observation (or non-observation) of surface manifestation, what appear to be outliers may not actually be outliers. The Bayesian framework described here allows prior knowledge of liquefaction behavior, as informed by principles of soil mechanics and laboratory test data, to be utilized to advantage in the process of case history interpretation. The types of calculations described in this chapter can address these situations, but they need inputs that are not currently available. These include:

P[S]: Probability of susceptibility. This is based on mineral composition as inferred from soil behavior type index, I_c.

P[*T*]: Probability of triggering. For our SMT model, it is the probability of triggering itself in a particular layer of soil (not accounting for overlying crusts or other profile-related hydraulic factors). We herein utilize a laboratory-based "prior" to assess triggering.

P[*M*|*T*]: Probability of manifestation if triggering occurs. This probability has been inferred from observations of manifestation using procedures described in Section 4.3 of this report. Triggering is first assessed using the laboratory model, and probability of manifestation of the profile is subsequently assessed conditional on probability of triggering, and other factors such as the penetration resistance, depth, thickness, and soil behavior type index for each layer.

P[*NM*|*T*]: Probability of no manifestation if triggering occurs. This is the complement of the probability of manifestation if triggering occurs (i.e., P[*NM*|*T*] = 1 - P[*M*|*T*]), which inherently assumes that there is no "marginal" manifestation category.

P[*M*|*NT*]: Probability of manifestation if triggering does not occur. This may arise when soils develop significant enough excess pore pressure to produce sand boils or other observations that are usually interpreted as manifestation of liquefaction, even at excess pore pressure ratios lower than unity.

The SMT has opted to rely on laboratory test data as an estimation of the prior probability for this purpose. We have collected data for a wide range of sands and established the within- and between-sand variability in *CRR* given some loading and D_r, which has been used to estimate P[*T*]. The lab-based expression for P[*T*] is then updated based on observations of manifestation after developing an initial model using the laboratory-based relationship. This approach is described in Section 6.2. We also considered creating a case history database that excluded cases where impedance of drainage was a significant factor affecting manifestation potential, and then developing a triggering model based on that database. This approach was ultimately not pursued because (1) it is difficult to ascertain with a high level of confidence whether triggering would for sure result in a manifestation at a particular site, and (2) the resulting database would be very small and potentially not statistically reliable.

The existence of P[*M*|*NT*] and P[*NM*|*T*], i.e., manifestation without triggering and triggering without manifestation, can be shown by examination of the data of Hutabarat and Bray (2021, 2022), which shows that the model itself has quite a bit of uncertainty in it. There are, for example, cases of minor, moderate, and severe manifestation that plot within the "None" zone (7 out of 96) for the thick sand sites (left side) and minor and moderate points (3 of 80) within it for the stratified sites (right side). There are also cases of no manifestation that plot above the "None" zone (6 of 96 for the thick sand sites and 3 of 80 for the stratified sites).

Figure 4-5 shows data extracted from the Supplemental Data file of the Hutabarat and Bray (2022) paper, hereafter abbreviated "HB2022". In Figure 4-6, we combined and plotted the data using solid circles for cases with manifestation (Minor, Moderate, Severe, or Extreme) and open circles for cases without manifestation. The data is shown with linear and logarithmic L_D scales (L_D = 0.01 was assigned to all cases that HB22 identified as having L_D = 0, which implies no triggering anywhere within the profile). In both plots, the boundary between the None and Minor states of manifestation severity are shown in red. Of the 176 case histories in the HB22 database, 55 showed some evidence of manifestation and 121 showed no evidence.

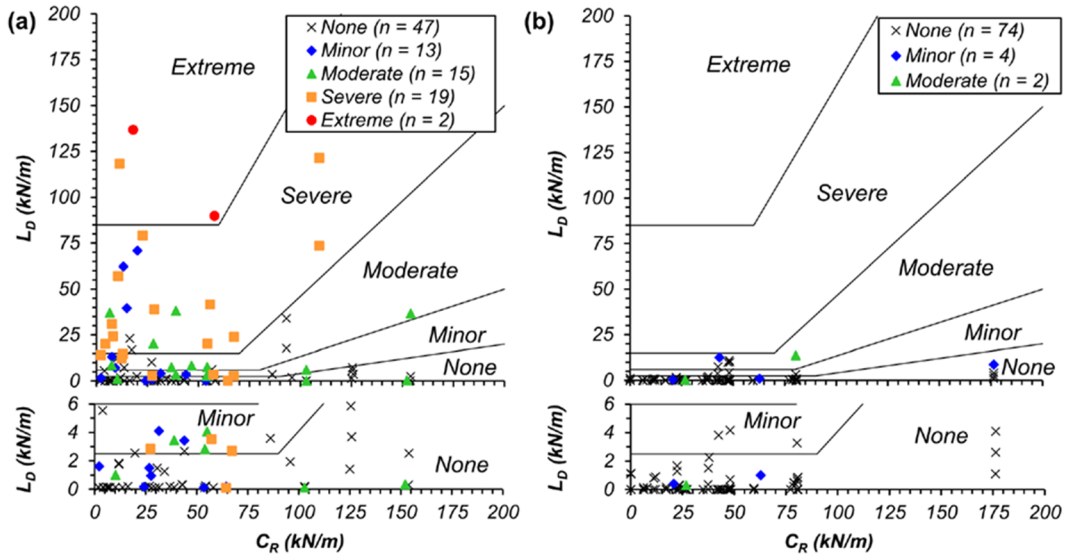

Figure 4-5 Plots of L_D vs C_R (from Hutabarat and Bray, 2022)

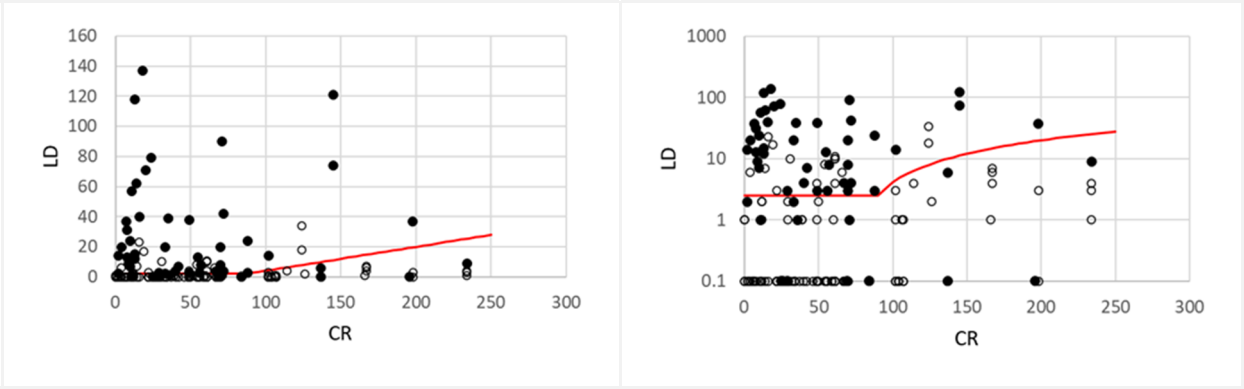

Figure 4-6 Plots of L_D vs C_R in linear-linear and log-linear scales

HB22's bilinear boundary between None and Minor can be viewed as the minimum value of L_D required to produce (any degree of) manifestation for a given C_R, which can be referred to as $L_{D,min}$. To accommodate the sloping part of the boundary, values of L_D for actual case histories can be normalized as $\alpha = L_D / L_{D,min}$. In this form, α can be thought of as something like the reciprocal of a factor of safety against manifestation. While HB22 did not attempt to characterize uncertainty in his manifestation model, it can be at least crudely approximated by considering the distribution of "missed" predictions of the occurrence of manifestation. Missed predictions can be considered as cases in which an observation of None (marked by an 'x' in Figure 4-5 and an open circle in Figure 4-6) plots above the $L_{D,min}$ boundary and cases in which observations of Minor, Moderate, Severe, or Extreme plot below that boundary. By digitizing the HB22 data and assigning "observation values" of 0 to cases in which manifestation was not observed and 1 to cases in which it was (i.e., Minor, Moderate, Severe, or Extreme), the observation values can be plotted versus the parameter α, as shown in Figure 4-7. Ideally, all points with $\alpha > 1.0$ would show some degree of manifestation and all points with $\alpha < 1.0$ would not. However, Figure 4-7 shows that there are points with $\alpha > 1.0$ for which no manifestation was observed (zero values on y-axis) and points with $\alpha < 1.0$ for which manifestation was

observed (1 values on y-axis). The latter of these are cases in which manifestation occurred where HB22 would predict none.

In Figure 4-7, 12 of the 176 case histories (6.8%) have α < 1.0 but showed some degree of manifestation (note that some points plot on top of each other). Of these 12, three have α = 0, which means that FS_L > 1.0, i.e., no triggering, over the entire depth of the profile – one with moderate manifestation and two with minor. The fact that three of the 55 sites with manifestation did not show triggering, suggests that P[*M*|*NT*] = 5.5% for this small sample set – while this percentage is not large, it does suggest that surface manifestation may develop at sites where triggering did not occur. The HB22 database includes 121 cases where no manifestation was observed. 16 of these cases had α > 1.0 but no observations of surface manifestation. Assuming an average α value of at least 4.0 indicates a very high probability of some manifestation developing, six of the 121 manifestation cases had α > 4.0 but no manifestation was observed. These "outliers" represent cases where liquefaction was triggered but manifestation was not observed, suggesting that P[*T*|*NM*] = 5.0% for this small sample set, again showing that surface manifestation can be absent for cases where liquefaction was almost certainly triggered. Thus, the data and analyses developed by HB22 suggest that both P[*T*|*NM*] and P[*M*|*NT*] are greater than zero.

We have assumed P[*M*|*NT*] = 0 in this report because we have not yet achieved consensus on whether sufficient evidence is currently available to support a different value. We recommend exploring this possibility as part of future work.

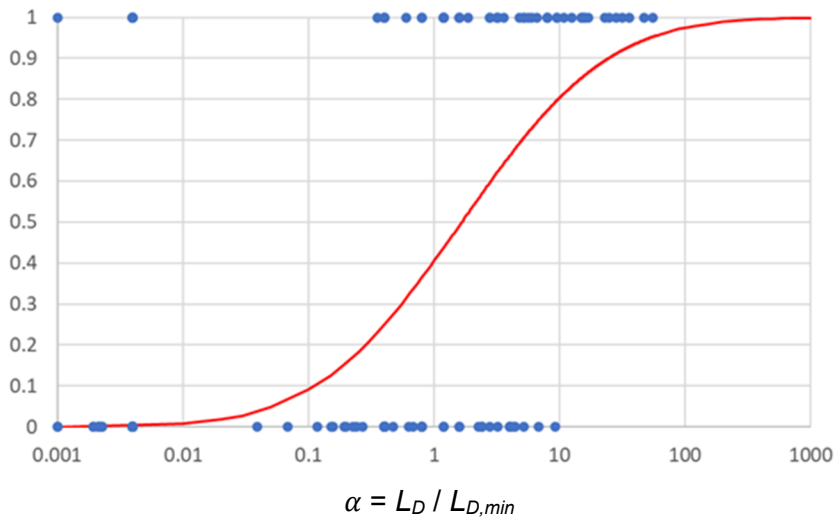

Figure 4-7 P[M] vs α using data from Hutabarat and Bray (2022). For observations, P[M] = 1 for "yes" and P[M] = 0 for "no."

4.3 Modeling of Critical Layer Triggering

The Bayesian framework can also be used with the case history database to develop a model for triggering in critical layers, which is analogous to the approach used in legacy models (Section 3.2). This form of model development requires a prior model for P[*T*], assumed manifestation models (P[*M*|*T*], and P[*M*|*NT*]), and assumed non-manifestation models (P[*NM*|*NT*] and P[*M*|*NT*]). Those models would then be applied to all case histories.

Consider for example a case history where surface manifestation was observed. Eq. (4-5) would be used to establish P[*T*|*M*] and the complement would be computed as P[*NT*|*M*] =1-P[*T*|*M*]. This would lead to two weighted and co-located points. For a case history without surface manifestation, Eq. (4-6) would be used to compute P[*NT*|*NM*] and its complement would be P[*T*|*NM*] =1-P[*NT*|*NM*]. In an extended multiple-critical-layer approach, each weighted critical layer data point would consist of two co-located points with its weighting factor multiplied by the same conditional probabilities.

The suite of *M* and *NM* weighted data points would then be used in a regression analysis to establish the boundary curve, which would update the prior P[*T*] model. This outcome would naturally depend on the assumed manifestation models, which are the subject of the next section, and the assumed non-manifestation models. As discussed in Section 6.3, we chose to update the prior P[*T*] model using Bayesian inference rather than a frequentist approach. This is because a frequentist approach requires many iterations of developing a P[*M*] model and updating P[*T*], which may converge but is inefficient and open to instability. The Bayesian inference essentially performs the same steps simultaneously and is much more stable.

4.4 Modeling of Profile Manifestation

This section describes the framework we adopted to compute the probability of manifestation of a profile. The probability that a particular layer will manifest depends on factors beyond penetration resistance and cyclic stress ratio. Additional factors include the depth and thickness of the layer, the presence of a thick and/or strong crust layer, whether the layer is interbedded or uniform, soil composition, and impeded drainage conditions. Previous models may have included these factors as part of the judgment utilized to select the critical layer. However, those judgments are subjective and were not explicitly documented, and we seek an objective method for assessing P[*M*|*T*] here. Rather than selecting a single critical layer to be representative of the profile, we evaluate the probability that each layer within a profile will cause surface manifestation, P[M_L|T_L], where the subscript "*L"* denotes manifestation or triggering of a specific layer. We then aggregate the contributions from all of the layers to define the probability of profile manifestation P[M_P], where the subscript "*P*" denotes profile. We have previously not utilized subscripts to differentiate triggering or manifestation of profiles from layers but introduce them throughout this section for clarity.

4.4.1 Manifestation Probability for Single Layer

There are many variables that could be influential in the prediction of P[M_L|T_L]. In legacy models, *CSR* and penetration resistance are used to evaluate whether a layer will produce surface manifestation, but other factors such as layer thickness, depth, soil composition, crust thickness, and impeded drainage may also play a role. The variables we considered in our model are provided in Table 4-2.

Table 4-2 List of variables considered in manifestation model.

Variable	Description
q_{c1N}	Overburden corrected cone tip resistance
I_c	Soil behavior type index
z_{top}	Depth to top of layer
$\sigma'_{v,0}$	Initial vertical effective stress
t	Layer thickness
CSR	Cyclic stress ratio
τ_{cyc}/s_u	Cyclic shear stress divided by undrained shear strength
$L_{D,l}$	Liquefaction eject demand of a layer (Hutabarat and Bray 2022)
$C_{R,l}$	Crust resistance above a layer (Hutabarat and Bray 2022)

Note that L_D and C_R (introduced in Section 2.1.3) have been converted from profile parameters to layer properties in **Error! Reference source not found.**. This is achieved by integrating from the top to bottom of each layer for the case of $L_{D,l}$ and from the ground surface to the top of the layer for $C_{R,l}$ rather than the full profile.

These variables must be combined in a mathematical framework in a manner that separates "yes" from "no" manifestation cases based on the properties of the variables. A common functional form utilized in binary classification problems is the logistic function, as shown in Eq. (4-7),

$$p = \frac{1}{1 + exp(-\beta^T x)} \quad \text{4-7}$$

where p is the probability of an outcome, β is an array of coefficients, and x is an array of variables.

The logistic function has several desirable features that make it useful for binary classification problems. First, p is constrained in the range between 0 and 1, which is the valid range of probabilities of an outcome. Second, $\beta^T x$ is a linear combination of the input variables. Although the resulting logistic function is nonlinear, logistic regression is often considered to be a linear separator because $\beta^T x$ is a linear function.

The variables in Table 4-2 can potentially be combined in many different ways using many different functional forms. The simplest approach would be to combine all the variables in Table 4-2 together in a single logistic function. However, doing so would group together variables that are unrelated to each other. For example, q_{c1N} and I_c are soil properties, and it makes sense to group them together, whereas z_{top} and t are geometric properties that should be grouped together. We therefore opted to group variables into distinct classes and multiply the

logistic functions for each grouping together. However, this caused large instabilities in the regression of model coefficients so we opted for the simpler framework with grouping all the chosen variables into one logistic function. An example is provided by Eq. (4-8).

$$P[M|T] = \frac{1}{1 + exp\left[-\left(\beta_0 + \beta_1 q_{c1N} + \beta_2 I_c + \beta_2 z_{top}\right)\right]} \quad \text{4-8}$$

Eq. (4-8) forms a four-dimensional surface in P[$M_L|T_L$], q_{c1N}, I_c, z_{top} space that is impossible to visualize in three-dimensional space. Thus, the components are illustrated schematically in Figure 4-8. The probability factor depends jointly on all three features (q_{c1N}, I_c, z_{top}), so multiple plots are required to demonstrate key aspects of the function. As evidenced in the top left subplot of , a layer at the ground surface (z_{top} = 0m) with I_c = 1 (represented as the darkest blue curve) has P[$M|T$] ~ 1 at q_{c1N} < 75. As q_{c1N} increases, P[$M|T$] decreases until it is approximately 0 at q_{c1N} = 300. As I_c increases (the color of the curve gets warmer), for the same z_{top} and q_{c1N}, the P[$M|T$] decreases. Moving to different subplots from left to right and top to bottom, as z_{top} increases P[$M|T$] decreases for the same q_{c1N} and I_c values.

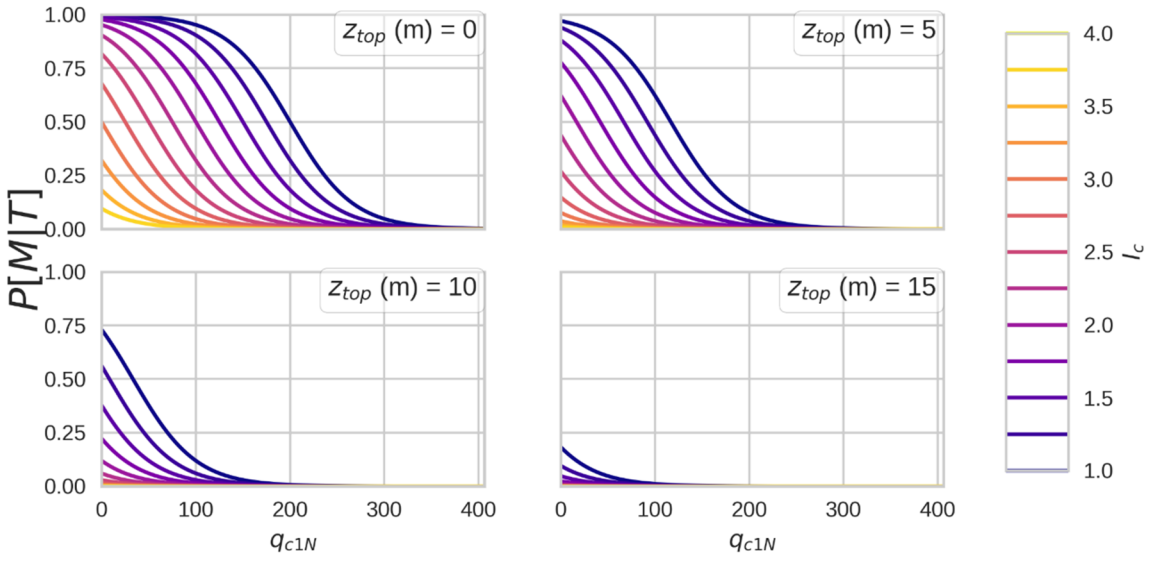

Figure 4-8 Example probability factors for layer manifestation conditioned on (a) q_{c1N} and I_c, and (b) z_{top}

As presented in Section 4.1.1, probabilities of manifestation that occur due to no triggering (P[$M|NT$]) can be separated into probability of manifestation given no triggering of a susceptible layer (r_u < 1.0 but producing large strains) and manifestation in a non-susceptible layer (cyclic softening). Each are given their own set of logistic functions and combined to produce the total probability of manifestation of a layer P[M_L] in Eq. (4-9).

$$P[M_L] = 1 - (1 - P[M|T]P[T|S]P[S]K_{Sat}) * (1 - P[M|NT]P[NT|S]P[S]K_{Sat}) * (1 - P[M|NS]P[NS]K_{Sat}) \quad \text{4-9}$$

where P[$T|S$], P[S], P[$NT|S$], and P[NS] are all obtained from probabilistic model priors. P[$M|T$], P[$M|NT$], and P[$M|NS$] are each logistic functions similar to Eq. (4-8) but with variables important for the respective scenarios (e.g., q_{c1N} for P[$M|T$] and τ_{cyc}/s_u for P[$M|NS$]). K_{Sat} is a term introduced to take into account the saturation of the soil. In future work, a K_{Sat} model could be developed using information such as P-wave velocity and partial saturation zones around the groundwater table. For this report, however, we use a binary value: K_{Sat} = 0 above the groundwater table and K_{Sat} = 1 below the groundwater table. Saturation has been shown to affect triggering; specifically as saturation decreases from S = 1, the CRR for a given D_R increases (Arab et al., 2011; Okamura and Soga 2006; O'Donnell et al. 2017; Tsukamoto et al. 2002; Yang et al. 2004). Rather than including a K_{Sat} term as done in Eq. (4-9), a saturation effect could be applied to the P[$T_L|S_L$] function using an estimated saturation that could be derived from proximity to the groundwater table and/or measured P-wave velocity (V_p). The framework presented in this report uses a simplified, binary saturation effect, therefore it is applied to the P[M_L] equation rather than the P[$T_L|S_L$] function because it would cause the same effect. Future work needs to be done on saturation effects within the presented framework.

4.4.2 Manifestation Probability for a Profile

The probability of manifestation of a profile P[M_P] is computed using Eq. (4-10),

$$P[M_P] = 1 - \prod_{i=1}^{N_L} \left(1 - PF_{M_L|T_L} PF_{T_L} K_{Sat}\right)^{t_i/t_c} \quad \text{4-10}$$

where N_L is the number of layers in the profile, t_i is the thickness of the i^{th} layer, and t_c is a constant characteristic thickness. Eq. (4-10) is a simplified case that only considers contribution to manifestation from liquefaction triggering and ignores cyclic softening and non-triggering manifestations. Eq. (4-10) consists of multiple pieces that warrant separate discussions.

First, $PF_{ML|TL}$ is the *probability factor* of manifestation of a layer given triggering of the layer, defined exactly as P[$M_L|T_L$] in Eq. (4-8). PF_{TL} is the probability factor of triggering which is the product of the probabilistic triggering and susceptibility prior models (P[$T|S$]*P[S]). The reason these are denoted as probability factors rather than probabilities now is because in the profile manifestation framework with the t/t_c exponent (explained later in this Section), these quantities are not the true probabilities of manifestation or triggering of a layer.

Second, the expression $\left(1 - PF_{M_L|T_L} PF_{T_L}\right)^{t/t_c}$ is equal to the probability that the layer will not manifest liquefaction, P[NM_L] = 1 - P[M_L]. If none of the layers manifest liquefaction, then the profile does not manifest liquefaction. Therefore, P[NM_P] is computed as a product sum of P[NM_L]. However, a direct product sum (i.e., without the t/t_c term in the exponent) inherently assumes that P[NM_L] for each layer is statistically independent from all other layers. This is generally not true. The t/t_c exponent has removed the influence of discretization by tying layer thickness to the characteristic length. The characteristic thickness is the layer thickness for which $PF_{ML|TL}$ is statistically independent of the other layers. If all layers have a thickness equal to the characteristic thickness, then Eq. (4-10) reduces to a simple product sum. If a layer is thicker than the characteristic thickness, it becomes more likely to manifest, and vice versa, as illustrated in Figure 4-9. We considered using thickness as a variable within the logistic regression instead of as an exponent, but ultimately included as an exponent instead for this reason.

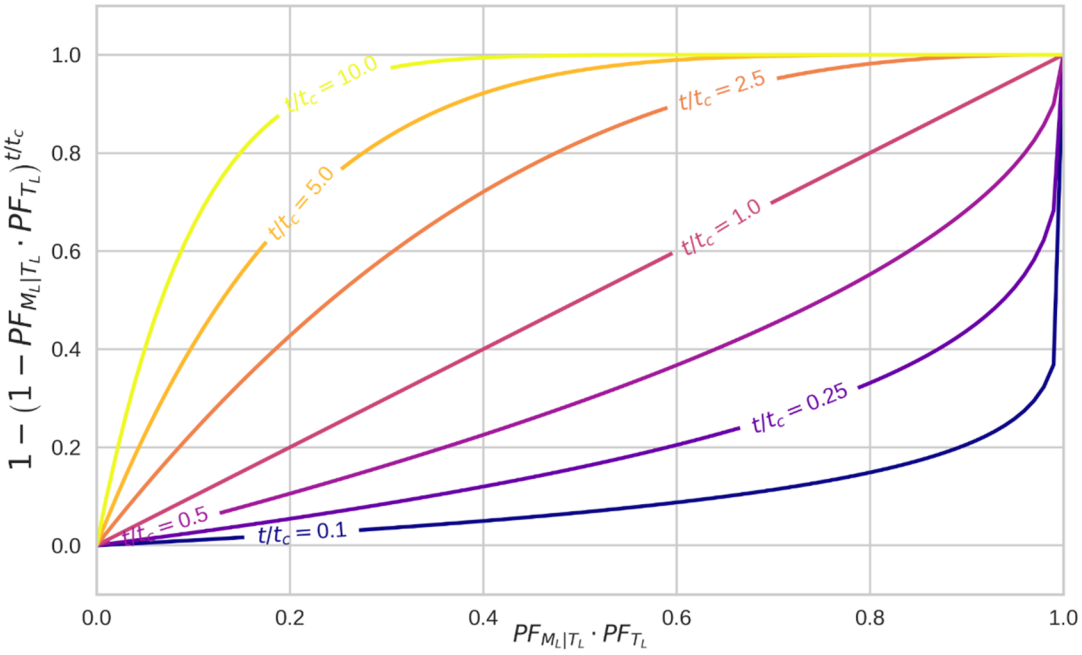

Figure 4-9 Influence of t/t_c exponent on probability of layer manifestation

Consider the example profile in Figure 4-10, which has three layers with thicknesses of 3 m (also using t_c = 3m for simplicity), and groundwater table at the ground surface. Layer 1 has a high q_{c1N} and I_c (300 and 3.2, respectively), layer 2 has a low q_{c1N} and high I_c (50 and 3.2, respectively), and layer 3 has low q_{c1N} and low I_c (50 and 1.5, respectively). A strong ground motion with CSR=0.6 is assumed. The first step is to compute P[$T|S$] for each layer; layer 1 has P[$T|S$]~0 due to its high q_{c1N}, whereas layers 2 and 3 have relatively low q_{c1N} and high CSR, therefore P[$T|S$]~1. The P[S] is low for layers 1 and 2 due to high I_c. The product of P[$T|S$] and P[S] is PF_{TL}, which is 0, 0, and 1 for layers 1, 2, and 3 respectively. The logistic functions in Figure 4-6 and Eq. (4-8) are used with the profile data to compute $PF_{ML|TL}$. Layer 1 has $PF_{ML|TL}$ = 0, layer 2 has $PF_{ML|TL}$ = 0, and layer 3 has $PF_{ML|TL}$ = 0.5. These results are combined in Eq. (4-10) to provide profile manifestation probability P[M_P] = 0.5, which is entirely caused by layer 3.

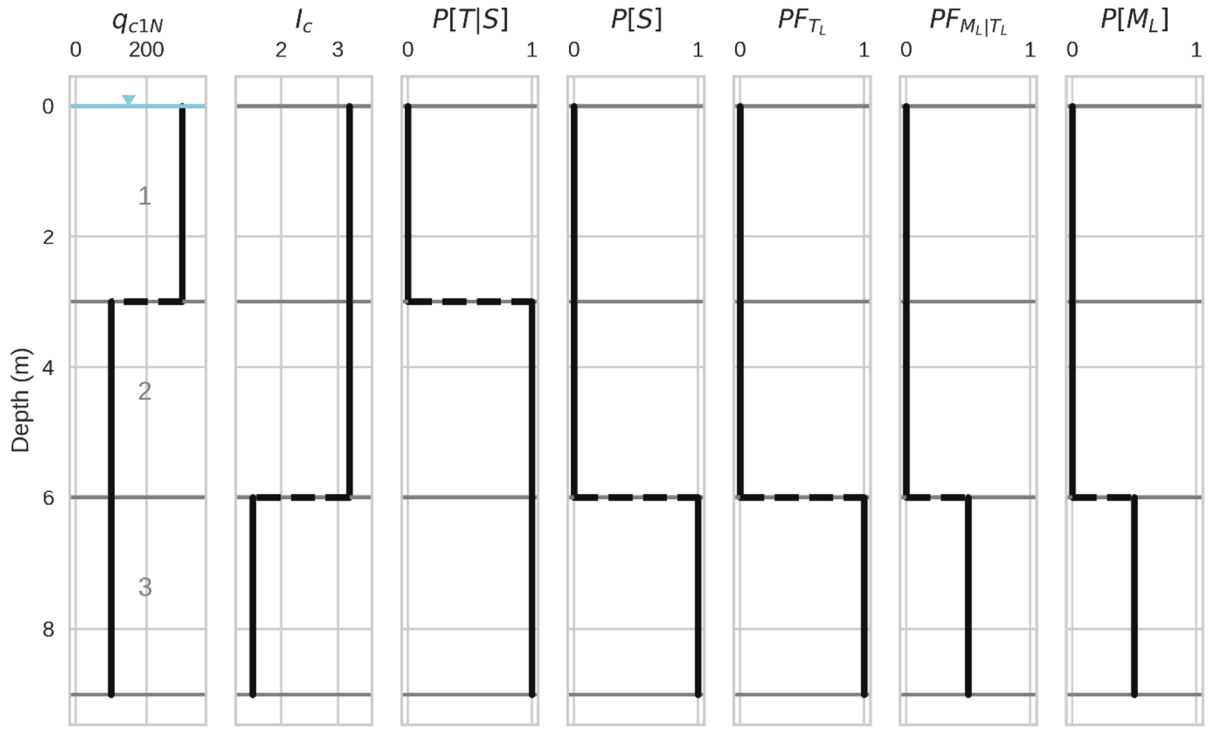

Figure 4-10 Simplified CPT profile demonstrating the computation of P[M_P]

In addition to layer properties, there may be profile properties that could improve a manifestation model's predictive accuracy such as ground motion intensity measures other than *PGA* or variables such as H_1 and *LPI* which are computed for an entire profile rather than an individual layer. These could help capture system effects or ground motion properties that are not reflected in layer properties or *CSR*. Therefore, P[M_P] can be expanded from the form presented in Eq. (4-10) to the following:

$$P[M_P] = 1 - \left(\prod_{i=1}^{N_L} \left(1 - PF_{M_L|T_L} PF_{T_L} K_{Sat}\right)^{\frac{t_i}{t_c}} \right) * (1 - PF_P) \quad \text{4-11}$$

where PF_P is the probability factor for the profile-scale manifestation effects defined using the same logistic functional form as Eq. (4-7). Any combination of profile variables can be included in PF_P. Table 4-3 lists the different profile variables that were considered during formulation of the manifestation model.

Table 4-3 List of profile variables considered in manifestation model

Variable	Description
H_1	Non-liquefiable crust thickness
C_R	Crust strength
L_D	Liquefaction Demand
PGV	Peak Ground Velocity
CAV	Cumulative Absolute Velocity
I_a	Arias Intensity
LPI	Liquefaction Potential Index
LSN	Liquefaction Severity Number

4.4.3 Profile-Based Regression Framework

Computing P[M_P] requires specification of the prior distributions for the coefficients in the *PF*s, $PF_{T|S}$, and $PF_{M|T}$ functions, and the characteristic thickness, t_c. Independently regressing all of these based on case history data is infeasible and undesirable because (i) the amount of field case history data is inadequate to isolate so many different variables with nonlinear relationships, and (ii) there is a body of knowledge from laboratory testing that help constrain PF_S and $PF_{T|S}$. This approach is therefore to develop prior distribution functions for PF_S and $PF_{T|S}$ from laboratory data and then use Bayesian regression to update uninformed $PF_{M|T}$ and PF_P coefficients and the more strongly informed PF_S and $PF_{T|S}$ coefficients. This section presents the framework utilized to infer the coefficients based on observations of manifestations at NGL sites. The functional forms of the probability factors and results of the inferences are presented in Chapter 6.

In Bayesian regression, coefficients are characterized with prior distributions and then guesses of posterior distributions are sampled using a Hamiltonian Monte Carlo algorithm (Hoffman and Gelman 2011, 2014) along with the distribution of data and Bayes theorem to produce a posterior belief about the coefficients (Gelman et al. 2014). This regression seeks coefficients within the components of Eq. (4-11) that maximize the Bernoulli log-likelihood function given by Eq. (4-12), where y_k is a binary indicator of whether manifestation was observed at the k^{th} site (y_k = 1 if manifestation was observed, y_k=0 if it was not), and N_P is the number of profiles in the database. This likelihood function is similar to those used in other probabilistic liquefaction models (e.g., Cetin et al. 2018; Moss et al., 2006).

$$L = \frac{1}{N_P}\sum_{k=1}^{N_P}[y_k \ln(P[M_P]_k) + (1 - y_k)\ln(1 - P[M_P]_k)] \quad 4\text{-}12$$

The likelihood function exhibits several notable properties. First, if y_k=1, only the first part of the expression within the square brackets on the right side of Eq. (4-12) contributes to the cost

function for profile k, whereas only the second expression contributes if y_k=0. Second, if the prediction is a true positive (i.e., if y_k=P[M_P]$_k$ = 1), or a true negative (i.e., if y_k=P[M_P]$_k$ = 0), the contribution to the cost function from that profile is zero. Only values of P[M_P] that do not match the observed manifestation contribute to the cost function. The ideal scenario would therefore be to select an optimal set of coefficients that render P[M_P] values that are either 0 or 1, and perfectly match the observations. In that case, the selected variables perfectly separate the data into distinct domains, and the cost function would be L = 0. For real datasets, this is generally not feasible, and the value of L will therefore be less than zero.

When a single logistic function is utilized to define the probability of occurrence of an event (i.e., in traditional logistic regression), the cost function given by Eq. (4-12) is convex, meaning that its second derivative is always positive. Logistic regression is therefore a convex optimization problem that is guaranteed to find the absolute minimum (within a specified threshold) using techniques like the gradient descent method (Cauchy, 1847). However, the P[M_P] function is more complicated, involving products of logistic functions raised to an exponent. As a result, the cost function is not convex, and can contain local minima. Furthermore, we wish to constrain values of certain variables. As a result, we are solving a non-convex constrained optimization problem, which is more complicated than logistic regression. Our approach is to adopt a No-U-Turn Hamiltonian Monte Carlo sampling (NUTS) algorithm (Hoffman and Gelman 2011, 2014). NUTS uses a recursive algorithm to build a set of likely candidate points that spans a wide swath of the target distribution, stopping automatically when it starts to double back and retrace its steps. The Python package PyMC is used to perform NUTS and Bayesian regression (Wiecki et al., 2023).

5 CASE HISTORY PROCESSING

Case history processing is required to convert data (e.g., CPT profiles, groundwater table measurements, ground motion measurements, observations of liquefaction manifestation) into metrics that facilitate model development (e.g., *CSR*, q_{c1Ncs}). As outlined in Section 2.2.2 and Figure 2-7, our approach to case history processing combines automated procedures with human inspection and judgment to assign liquefaction observations to nearby in situ tests, identify layers, and process the characteristics of these layers. Whenever feasible, we codify our judgments so they are objective and reproducible by other analysts. The development of calibrated automated processes is crucial for analyzing a database as large as the NGL database, and provides a repeatable, consistent, and objective initial view of the data.

This chapter describes the steps required to process liquefaction case histories as contained in the NGL database and to assign layer properties for use in model development. These steps include several advances of the state-of-the-art in liquefaction evaluation, such as a revisited relationship between I_c and *FC*, improved estimation of ground motion intensity, and an automated layer detection algorithm.

5.1 Assigning Observations to In Situ Tests

Observations of surface manifestation (or lack thereof) and site investigations are not necessarily collocated in the NGL database so it is necessary to decide which observation is to accompany which test (i.e., what in situ test data should be used in evaluating the soil layers that contributed to the surficial manifestation of liquefaction or lack thereof). Observations and in situ tests are associated through a link to a common site in the SQL data structure, but within a site there are often multiple observations and multiple in situ tests. Furthermore, there are often "yes" and "no" observations of manifestations within the same site. To make initial assignments of observations to in situ tests, we developed the following algorithm using Python code in Jupyter Notebooks.

1. Select a site and identify all the in situ tests and observations that are associated with that site.

2. Compile the latitude and longitude values for the tests and observations and compute an array containing the distance in meters between every observation and test at the site.

3. Separate the observations by events (some sites have observations from more than one earthquake event).

4. Assign the closest in situ test to each observation for each event so that every observation has an in situ test assigned to it.

This is an initial automated process to make these assignments, followed by a human review by SMT members examining each test-observation pair. To conduct the review, the SMT developed a Jupyter notebook to visualize and summarize the available data for each site and event combination. A screenshot of the notebook is shown in Figure 5-1. Red markers indicate "yes" manifestation cases, black markers are "no" manifestation, and green markers are CPT locations. Note that when an observation and CPT sounding are collocated, some information can be obscured in the map (e.g., the green CPT pins or red/black observation pins may be obscured). A circle is drawn around the observation pins that are reasonably close to a CPT and

Figure 5-1 **A screenshot of the Jupyter notebook that the SMT designed for reviews of individual case histories. Black markers represent observations of "no manifestation", red markers represent "yes manifestation", green markers represent CPTs, red/black lines connect CPTs and observations that the SMT grouped together, and red/black circles indicate a co-located CPT and observation pair.**

are therefore candidates for inclusion in the SMT's case history dataset. The purpose of this review was to:

1) Confirm the appropriate assignments of "yes manifestation" and "no manifestation" to an individual CPT or groups of CPTs when more than one CPT could be reasonably assigned to the same field observation.

2) Identify and exclude case histories where the distance between a CPT and an observation of "yes manifestation" or "no manifestation" is too great to reasonably adopt (despite being the closest CPT identified by the initial algorithm). This evaluation is dependent on the site geology and the type and spatial distribution of field observations, and there is no single cutoff distance that is appropriate in every situation. For example:

    a) A lateral spread feature extending over an area of many square meters is represented in the NGL database by a single latitude/longitude coordinate, usually near the center. The feature may contain several boreholes within its lateral extent, but the distance between the center point and the boreholes could be several meters. In this case, the appropriate maximum acceptable distance between an observation and a borehole may be greater than in another case where only a single sand boil is observed. Figure 5-1 shows a lateral spread feature that extends along the north bank of the river shown in the image, with multiple FLDM observation notes in several locations.

b) In other cases, it is important to evaluate how close a borehole is to a "yes manifestation" observation and a "no manifestation" when there are multiple observations in a single site.

c) Some sites may have more variable conditions, and the appropriate maximum acceptable distance between an observation and a borehole may be less than what is considered acceptable at a site where the soil profiles are more constant over horizontal distances. This evaluation is dependent on the site geology and available subsurface data.

3) Identify CPT data that should be disqualified for reasons not readily detected by the algorithms (e.g., unreliable CPT equipment).

4) Identify case histories where the presence of nearby structures could potentially affect the manifestation of liquefaction.

5) Assign weights to CPTs when multiple soundings are assigned to the same observation. In this manner, multiple CPT's may be paired with a single observation to form a single case history.

At least one member of the SMT and often two or more used this tool to review each case history that the algorithms initially identified. This process yielded 546 total case histories, each with a CPT associated with an observation of "yes" or "no" manifestation. The median distance between site investigation locations and observations is 0m (i.e., over half of the manifestation observations are collocated with a CPT sounding), and the mean distance is 13.7m.

5.2 Ground Motion Intensity Measures

Accurate estimates of GMIMs, such as *PGA*, at liquefaction case history sites are crucial as IMs are used on the demand side of the equation for developing liquefaction triggering and consequence models. Current liquefaction triggering models are formulated using *PGA* values developed from various approaches often based on now-dated GMMs or engineering judgment. The existence of new GMMs based on current datasets of uniformly processed ground motion recordings [e.g., the NGA ground motions (Ancheta et al., 2014; Contreras et al. 2022)] offers a tremendous opportunity to improve the accuracy and reliability of GMIMs from old as well as new liquefaction case histories.

This section describes a consistent approach developed to estimate GMIMs at NGL liquefaction case history sites and is a continuation of the work described by Hudson et al. (2023b). The method is demonstrated using *PGA* values from the 1989 Loma Prieta earthquake. The procedure has been applied to the vast majority of events in the NGL database for *PGA*, *PGV*, *CAV*, and Arias intensity (I_a). These intensity measures have been added to the GMIM table in the database to support the development of predictive models based on alternative IMs. More information on the procedures presented here is provided in Pretell et al. (2024).

5.2.1 GMIMs Used in Legacy Datasets

Traditionally, the GMIM required for liquefaction evaluations in the stress-based framework is *PGA* (e.g., Section 2.1.2). *PGAs* for legacy liquefaction case histories (e.g., Moss, 2003; Boulanger and Idriss, 2014; Cetin et al., 2018) were estimated using a variety of approaches (Table 5-1). In a handful of cases, sites with liquefaction observations (or lack thereof) had

Table 5-1 Summary of approaches used to estimate IMs in legacy datasets

Approach	Description	Comments
1	Measured at the site (collocated)	Direct measurements at location of interest but can be complicated by pore pressure, dilation effects
2	Interpolated from nearby stations	Removal of the event term allows event-specific spatial variations to be isolated. Event term subsequently added to obtain interpolated IM. Requires nearby stations surrounding site
3	Based on ShakeMaps	Initial versions are less accurate than Approach 2 (level of care adopted in ground motion processing, e.g., assignment of V_{S30}, is less rigorous), but often updated as better data become available
4	Estimated from site response analysis	Can be highly accurate at sites with strong impedance contrasts and could be utilized to inform the nonlinear site response parameters, but uncertainty in the input motion makes this approach less favorable
5	Recorded at nearest station	Relatively common in past practice, but stations are often many km from the case history site
6	Estimated from ground motion models	High degree of uncertainty because they are conditioned on data from many earthquakes
7	Based on judgment	Not well documented, difficult to reproduce
8	Unknown	No documentation available

collocated ground motion stations (Approach 1 in Table 5-1) and thus a measured value of *PGA* at the location of the observations is available. Although directly measured at the sites of interest, these *PGAs* are often affected by factors such as shaking-induced excess pore water pressure and dilation-induced acceleration spikes, and thus their direct use in triggering model development is not straightforward. In other cases, ground motion recordings were available within a few kilometers or more of the liquefaction observations (Approach 5) and were used to approximate the *PGA* at the location of the observations. These estimates were sometimes modified to account for specific site conditions via site response analyses (Approach 4). In cases where recordings were not sufficiently close to the location of the liquefaction observations, *PGAs* were estimated using region-specific or ergodic GMMs. Other *PGA*s in legacy datasets were estimated from ShakeMaps (Worden et al., 2018), which provide a weighted average estimate of the *PGA* and other IMs using multiple data sources such as interpolations between ground motion recordings, intensity reports, and GMMs. These inconsistencies lead to a potentially inappropriate seismic demand that could limit the predictive ability of liquefaction triggering models.

The approaches in Table 5-1 are presented in our perceived order of decreasing accuracy. For example, collocated measurements are most accurate, though excess pore pressure development can complicate their use. Next best is interpolation of residuals from a dense grid of measured ground motions, as done in Approaches 2 and 3. Residuals, and specifically within-event residuals, are preferred to the IMs themselves because they are specific to the event that produced the motions, the IMs themselves are not spatially stationary, and differences in site conditions can be considered when interpreting within-event residuals. Approach 2 is distinguished from ShakeMap products (Approach 3) because the goal of ShakeMap is to produce near real-time indicators of shaking intensity, which means that the level of care adopted in ground motion processing, e.g., assignment of V_{S30}, is less rigorous. Approach 2 utilizes uniformly processed ground motion records, site-specific data, site-specific spatial correlation relationships, and is therefore considered more accurate. ShakeMaps for important events are often updated as better data become available. In those cases, ShakeMap products are considered as accurate as Approach 2. Site response analysis (Approach 4) can be highly accurate at sites with strong impedance contrasts where the motion is known at the impedance contrast (e.g., the “rock” motion). However, rock motions are generally not known with a high degree of accuracy and tend to carry higher uncertainty than motions at softer sites. Even in cases where a nearby rock outcrop motion is measured, the distance is generally far enough that the rock motion is likely not characteristic of the incident motion at the site. While we do not dispute the value of site response analysis methods for many sites, uncertainty in the input motion has led us to favor interpolated motions. However, site response analysis could potentially be utilized to inform the nonlinear site response parameters used in the GMMs adopted to interpolate residuals.

Approach 5 was relatively common in past practice, in which the *PGA* from the nearest ground motion recording was adopted as the value at the site of interest. In many cases, that station was many km from the site, and significant differences in *PGA* values may arise from differences in site and path effects, and spatial correlation of residuals. Ground motion models carry a high degree of uncertainty because they are conditioned on data from many earthquakes. If ground motion measurements are available for a particular event, they should be used to refine GMM estimates. Hence, Approach 6 is considered less accurate than 1-5. In some cases, PGA values were estimated from judgment. The judgment was not well documented and is difficult to reproduce. We therefore consider this to be the least accurate approach. Furthermore, sometimes the manner in which a *PGA* value was estimated is unknown.

Legacy datasets relied solely on *PGA* as a proxy to quantify the seismic demand leading to soil liquefaction, but there is potential for using other GMIMs to characterize demand. For instance, Kayen and Mitchell (1997) proposed a liquefaction triggering procedure that uses the Arias intensity (I_a) to represent seismic demand. Kramer and Mitchell (2006) evaluated several GMIMs in their efficiency, sufficiency and predictability and found that the *CAV* estimated for time histories with a minimum acceleration cutoff of 5 cm/s^2 (i.e., CAV_5) is a good predictor of excess pore water pressure ratio (r_u) and thus liquefaction triggering. In a similar study, Karimi and Dashti (2017) found *CAV* and CAV_5 at the base rock as the best GMIMs to predict liquefaction-induced permanent settlements. The previous and other similar studies (e.g., Bullock et al., 2019, 2022; Sideras, 2019) and the recent development of GMMs for I_a and *CAV* based on current ground motion databases (e.g., Campbell and Bozorgnia, 2019, 2023) allow for the investigation of GMIMs other than *PGA* as proxies for seismic demand in liquefaction triggering models.

The work described in this section aims to address the previously described limitations of legacy datasets: (1) the inconsistency in the approaches used for GMIM estimation, and (2) the lack of availability of GMIMs other than *PGA*.

5.2.2 Consistent Method for Estimating GMIMs: Interpolation from Nearby Stations

GMIMs at liquefaction case history sites are estimated using Kriging[2] interpolation to adjust GMM predictions with data from neighboring ground motion stations. The interpolation is not performed directly on GMIM values because ground motion tends to decrease with source-to-site distance and is therefore not anticipated to be a stationary random field. Rather, the interpolation is conducted on within-event residuals. GMIM residuals for a given event "*i*" at a site "*j*" (R_{ij}) are calculated as the difference between the recorded GMIM (Y_{ij}), and the GMIM estimated using GMMs ($\hat{Y}_{ij}$), as indicated in Eq. (5-1). The GMMs used to estimate *PGAs* are the ones proposed by Boore et al. (2014) for crustal earthquake events, and by Parker et al. (2022) for subduction earthquake events. In seismic hazard analysis it is common to use multiple ground motion models to quantify epistemic uncertainty in the predictions. However, when interpolating ground motions this selection is less important because we subtract the event terms before interpolating within-event residuals. Different ground motion models have different event terms, which is a source of epistemic uncertainty, but the interpolated residuals are insensitive to these event terms. Selection of the nonlinear site response model is a more important consideration due to differences in site conditions between measured ground motion locations and liquefaction locations. We have not explored epistemic uncertainty in this area.

$$R_{ij} = ln\left(Y_{ij}\right) - ln\left(\hat{Y}_{ij}\right) \quad \text{5-1}$$

The event term η_E is approximated as the average value of the total residuals, as follows:

$$\eta_{E,i} \approx \underline{R}_{ij} = \frac{1}{N_{rec}} \sum_{j=1}^{N_{rec}} R_{ij} \quad \text{5-2}$$

The uncertainty in η_E increases as N_{rec} decreases. This uncertainty is accounted for in the correlation model estimation, described in the following section. In the context of GMM development, η_E for each event is estimated using mixed-effect regressions. However, this approximation is necessary because events for which we desire to interpolate ground motions are not always included in the datasets from which the GMMs were derived.

Within-event residuals for a given event *i* at a site *j* (δW_{ij}) are then computed as:

$$\delta W_{ij} = R_{ij} - \eta_{E,i} \quad \text{5-3}$$

Figure 5-2 shows the within-event residuals estimated at ground motion station locations for the 1989 Loma Prieta earthquake. The within-event residuals are then normalized by the within-event standard deviation ϕ_i calculated from the data. The normalized within-event residuals ($\delta\grave{W}$) are used to develop correlation models, as explained in the next section.

[2]Kriging is a method of spatial interpolation named after Danie Krige, a South African mining engineer.

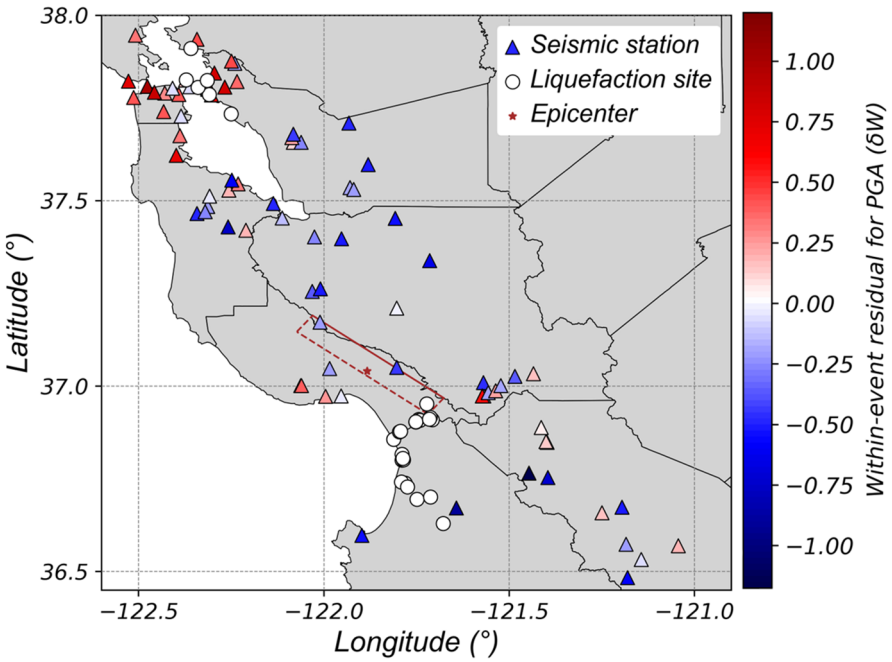

Figure 5-2 Map of interpolated within-event residuals for the 1989 Loma Prieta earthquake at strong motion recordings stations

5.2.3 Correlation Model Development

Correlation models for *PGA* and the other GMIMs were developed for each earthquake as a function of the Euclidean and angular separation distances amongst the ground motion stations. Bodenmann et al. (2023) showed that within-event residuals are not stationary random fields whose correlation depends solely on separation distance, but also on (1) the difference in the azimuth between each site location and the earthquake epicenter, and (2) the difference in the V_{S30} amongst stations. Such approach accounts for source and path effects, and also regional similarities in V_{S30} and thus site effects that are not captured by the GMM for a particular event. We herein adopt the approach of Bodenmann et al. (2023) except that we exclude the V_{S30} component since we often lack this information at points of interest, and because the additional influence of V_{S30} on *PGA* within-event residuals, beyond the site conditions already considered in the site response models in the GMMs, was found to be very small by Bodenmann et al. (2023). The correlation model is defined by Eq. (5-4), where ρ_E is correlation due to Euclidean separation distance (Eq. 5-5) and ρ_A is correlation due to azimuthal separation distance Eq. (5-6).

$$\rho_{EA}(d_E, \gamma_E, d_A) = \rho_E(d_E, \gamma_E) \cdot \rho_A(d_A) \quad 5\text{-}4$$

$$\rho_E(d_E, \gamma_E) = exp\left[-1 \cdot \left(\frac{d_E}{L_E}\right)^{\gamma_E}\right] \quad 5\text{-}5$$

$$\rho_A(d_A) = \left(1 + \frac{d_A}{L_A}\right) \cdot \left(1 - \frac{d_A}{180}\right)^{180/L_A} \quad 5\text{-}6$$

where d_E is the Euclidean distance between a ground motion station and the interpolation point in km, γ_E is a model parameter, L_E is the Euclidean length parameter in km, d_A is the difference in the azimuth between the epicenter and ground motion station and the epicenter and interpolation point in degrees, and L_A is the azimuthal length parameter in degrees.

Bayesian inference is used to estimate the model parameters L_E, γ_E, and L_A. Prior distributions for the model parameters are first established following the recommendations by Bodenmann et al. (2023). Realizations of the posterior joint distribution of the model parameters are then computed based on the $\delta\grave{W}$. The realizations of the model parameters are sampled using a Markov Chain Monte Carlo simulation method using the PyMC (Salvatier et al., 2016) Python package. A benefit of Bayesian inference over the more commonly used least squares regression in correlation model estimation is that prior beliefs about the model parameters stabilize the regressions for events that do not have a large number of ground motion records. We found that spurious models often arose from data-driven frequentist regression due to lack of adequate data. Herein, 1000 Monte Carlo samples of the posterior joint distribution are used, thus resulting in 1000 correlation models. Figure 5-3 shows the correlation models for the 1989 Loma Prieta earthquake. The model with the highest likelihood, denoted maximum a posteriori, and its parameters are also presented. Figure 5-4 shows a map of interpolated within-event residuals for the 1989 Loma Prieta earthquake developed using the maximum a posteriori correlation model.

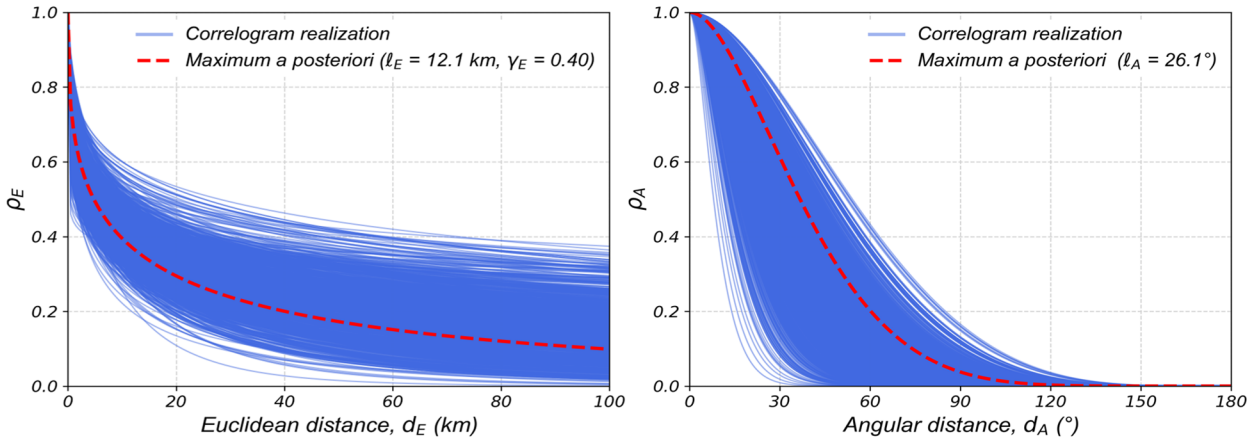

Figure 5-3 Correlation models for the 1989 Loma Prieta earthquake: (a) correlation model as a function of Euclidean distance, (b) correlation model as a function of angular distance

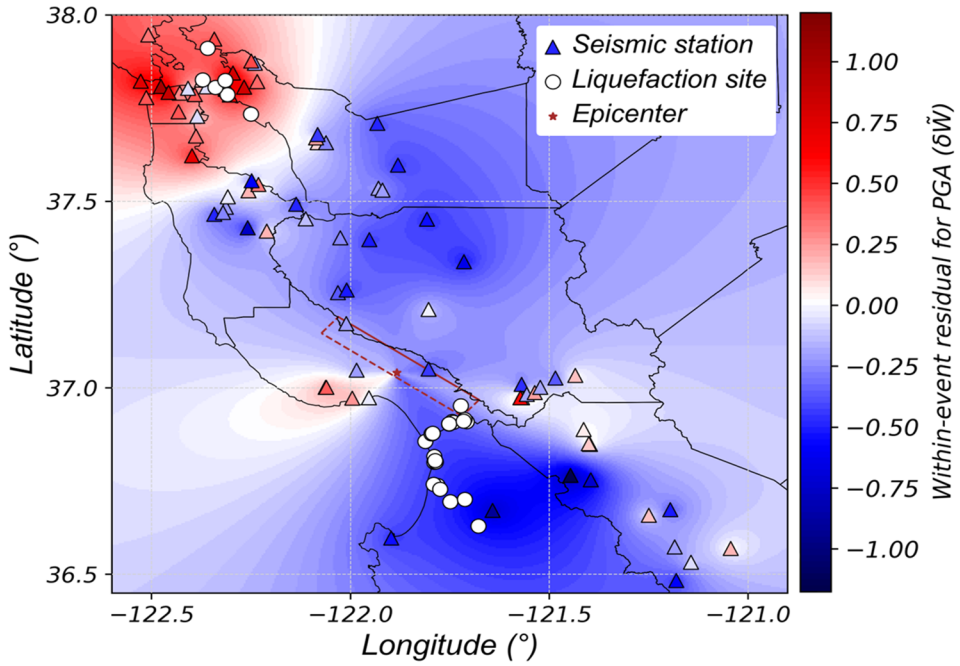

Figure 5-4 Map of interpolated within-event residuals for the 1989 Loma Prieta earthquake developed using the maximum a posteriori correlation model

5.2.4 Kriging Interpolation

Within-event residuals are interpolated at liquefaction case history sites using ordinary Kriging and the Bayesian correlation models. Ordinary Kriging estimates a given variable of interest at unsampled locations as the weighted average of data from sampled locations, as follows:

$$\begin{bmatrix} \widehat{W} \\ \mu \end{bmatrix} = \begin{bmatrix} \boldsymbol{Var} & 1 \\ 1 & 0 \end{bmatrix} \cdot \begin{bmatrix} \boldsymbol{Cov} \\ 1 \end{bmatrix} \tag{5-7}$$

where $\widehat{W}$ are the weights, μ is the Lagrange multiplier, ***Var*** is the covariance matrix among ground motion measurement points, and ***Cov*** is the covariance matrix between measurement points and interpolation points. The element values of the ***Var*** and ***Cov*** matrices are estimated using the following relation:

$$C = C_1 \cdot \rho_{EA} \tag{5-8}$$

where C is the covariance and C_1 is the semivariance of within-event residuals, estimated as:

$$C_1 = {\phi_i}^2 + \frac{\tau^2}{\sqrt{N_{rec}}} \tag{5-9}$$

In this equation, τ is the between-event standard deviation calculated from the GMMs. The rightmost term in Eq. (5-9) is intended to capture the uncertainty in the estimated event term Eq. (5-2). The mean GMIM within-event residual $\mu_{\delta\widetilde{W}}$ and corresponding Kriging interpolation error, quantified as the standard deviation $\sigma_{\delta\widetilde{W}}$, are estimated at each liquefaction case history site using all the 1000 correlation models. All the mean and standard deviation values are

combined using the following closed-form solution to obtain a single global normal distribution with mean and standard deviation defined as:

$$\mu_{\delta\tilde{W}} = \frac{1}{N_{models}} \sum_{k=1}^{N_{models}} \mu_{\delta\tilde{W},k} \quad 5\text{-}10$$

$$\sigma_{\delta\tilde{W}} = \sqrt{\left(\frac{1}{N_{models}} \sum_{k=1}^{N_{models}} \sigma_{\delta\tilde{W},k}^2\right) + \left[\frac{1}{N_{models}-1}\right] \sum_{k=1}^{N_{models}} \left(\mu_{\delta\tilde{W},k} - \mu_{\delta\tilde{W}}\right)^2} \quad 5\text{-}11$$

The mean within-event residual can then be used to estimate the mean GMIM at interpolation locations as follows:

$$\ln\left(\tilde{Y}_{ij}\right) = \ln\left(\hat{Y}_{ij} + \eta_{E,i} + \mu_{\delta\tilde{W}}\right) \quad 5\text{-}12$$

The $\sigma_{\delta\tilde{W}}$ is a measure of uncertainty in the estimated ground motion GMIM. Both the mean and standard deviation are included in the NGL database for each interpolated motion.

5.2.5 Comparison with Legacy *PGA*s

The newly estimated *PGAs* are compared against those from previous studies (e.g., Moss, 2003; Boulanger and Idriss, 2014; Cetin et al., 2018) to assess the influence in the new approach to estimating ground motions. Figure 5-5 shows a comparison for *PGA*s at the liquefaction case history sites of the 1989 Loma Prieta earthquake available on the NGL database (Brandenberg et al., 2020). In this figure, the markers are differentiated by the approach used to estimate the legacy *PGAs*, following the categories indicated in Table 5-1. The RotD50 component is considered for the newly estimated *PGAs*, given it is based on GMMs, while the geomean component is considered for the legacy *PGAs*, as it is more generally available.

Some discrepancies are observed between the legacy and the newly estimated *PGAs* for case histories. Legacy *PGAs* are based on three approaches: site response analysis, recorded from the nearest ground motion station, or based on GMMs. Overall, the newly estimated and legacy *PGAs* are within a factor of 2, as indicated by the 1:2 and 2:1 ratio lines. However, a tendency is observed for legacy *PGAs* based on GMMs to be lower, particularly for *PGA* values higher than 0.3g. This discrepancy could be attributed to differences in the site response models embedded in the old vs. the modern GMMs used for this work. Modern GMMs are based on larger ground motion databases, therefore they are expected to have more accurate site response models. In the case of legacy *PGAs* based on the nearest station (Approach 5), Figure 5-5 shows eight cases, seven of them for sites in the Moss Landing area. These sites adopted a value of 0.28g based on the *PGA* recorded at Salinas - John & Work ground motion station, adjusted based on GMMs to account for differences in path and site effects. The resulting legacy *PGA* is higher than the estimated *PGA* in this work. The remaining site is the Alameda Bay Farm Island, whose legacy *PGA* was informed by the *PGA* recorded at the Alameda Naval Air seismic station, a softer site that combined with the relatively long distance to the earthquake fault could explain the observed discrepancy. Finally, legacy *PGAs* based on site response analysis (Approach 4) are relatively close to the 1:1 line without any clear tendencies.

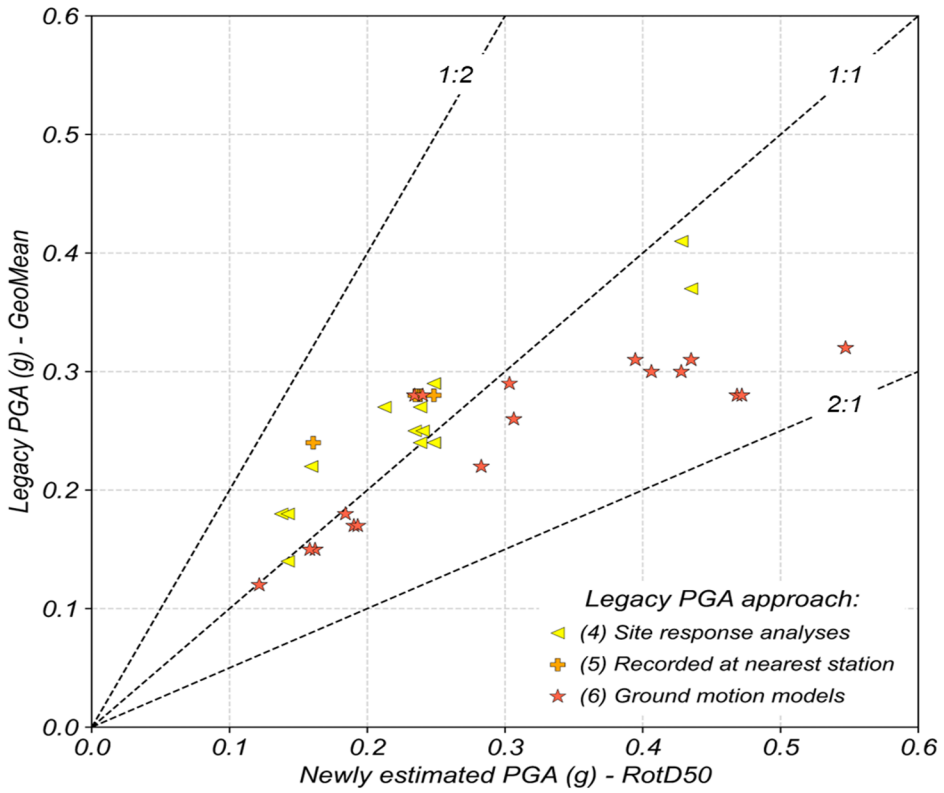

Figure 5-5 Comparison of the legacy vs. newly estimated *PGA* estimates at liquefaction case history sites from the 1989 Loma Prieta earthquake. Markers indicate the approach used for the estimation of the legacy *PGAs* (Table 5-1).

5.3 Layer Detection

Liquefaction triggering analyses are typically performed considering the representative properties of each soil layer rather than a point-by-point basis within a CPT profile. This is because liquefaction occurs as a process of pore pressure generation that typically is only meaningful if it occurs across a large enough depth range to produce manifestations. Furthermore, the CPT measurement represents an average of soil properties within a zone of influence around the cone tip, and measurements at points near layer boundaries may therefore not be representative of the soil properties at that point.

An individual CPT sounding may contain thousands of data points that provide an essentially continuous profile of tip resistance (q_c) and sleeve friction (f_s) with depth over the length of the CPT sounding. An engineer or geologist will generally use judgment to assign layer boundaries based on the CPT sounding, and subsequently select representative properties. Different analysts may make different judgments, and therefore assign layer boundaries differently. The process is therefore non-unique and unlikely to be repeatable. Furthermore, manual layer selection becomes inefficient when sufficiently large numbers of soundings require interpretation. Therefore, it is desirable to establish an algorithm that can efficiently assign layers to CPT data with repeatable, objective results that are compatible with sound human

judgment to the greatest extent possible. A repeatable algorithm can also reduce bias that can be introduced by a sole analyst or small group of analysts.

A number of different techniques have been developed to create simplified profiles from CPT data. For example, Wang et al. (2013) developed a Bayesian approach to assign layer boundaries and assign a probability that soil within a particular layer falls within a soil behavior type category. Ching et al. (2015) developed a procedure that utilizes the wavelet transform method to distinguish sudden changes in CPT tip resistance from smaller amplitude changes due to within-layer soil variability. Ntritsos and Cubrinovski (2020) developed an algorithm that minimizes the within-layer coefficient of variation of q_{c1Ncs} and I_c for the purpose of developing finite element meshes for one-dimensional ground response analysis. The first two of these three methods are rather complicated and require a significant number of calculations. The third is conceptually and computationally simpler and was shown to produce similar results to analyzing the full profile with respect to liquefaction potential. However, Ntritsos and Cubrinovski caution that the algorithm may result in fictitious layers at layer boundaries and indicate that their algorithm is not intended to replace engineering judgment.

We describe below an algorithm that utilizes a machine learning technique called agglomerative clustering to identify layer boundaries and representative layer properties. This method shares some conceptual features with Ntritsos and Cubrinovski (2020) (the methods were developed nearly simultaneously but independently); preliminary comparisons indicate that the clustering technique is more efficient. The following subsections describe the agglomerative clustering algorithm and illustrate its use on a CPT sounding from Moss Landing, an important liquefaction site in California. The method described here has been submitted as a paper (Hudson et al., 2023a).

Clustering is an unsupervised machine learning technique that separates data into different groups, often based on distance between data points and the clusters in a desired multi-dimensional parameter space (Pedregosa et al., 2011). The simplest clustering algorithm is called K-means, which groups data based on the aggregate distance between the data point and the centroid of each cluster. Gaussian mixture models assign probabilities that each data point belongs within each cluster based on the cluster statistics and may be thought of as an extension of K-means clustering that also considers covariance. Prior to clustering, variables are generally standardized, meaning that the mean is subtracted, and the resulting quantity is divided by the standard deviation.

Here, we use an example problem to illustrate various approaches for clustering to identify layers. Figure 5-6 displays profiles of q_c, f_s, I_c, and q_{c1Ncs} for CPT UC-4 that was obtained at Moss Landing near Sandholdt Road, a location that had severe liquefaction manifestation observations due to the 1989 **M**6.9 Loma Prieta earthquake (Boulanger et al., 1995, 1997). Visual inspection of the data makes it obvious that there are alternating layers of fine-grained and coarse-grained materials that compose this site's stratigraphy. Standardized versions of the variables are denoted $\hat{I}_c$ and $\hat{q}_{c1Ncs}$ and are plotted in Figure 5-7.

K-means and Gaussian mixture model clustering is applied in $\hat{I}_c$ and $\hat{q}_{c1Ncs}$ using the Scikit-learn Python package (Pedregosa et al., 2011), and plotted in Figure 5-8. The number of clusters is specified to be 14 here. Both algorithms do indeed group data points based on their proximity to each other. However, a problem arises when the clustered data are plotted as profiles with depth. As shown in Figure 5-9, non-contiguous data points may be assigned to the same cluster despite spatial separation. Figure 5-9 shows the results of K-means clustering, and Gaussian mixture model clustering suffers the same problem.

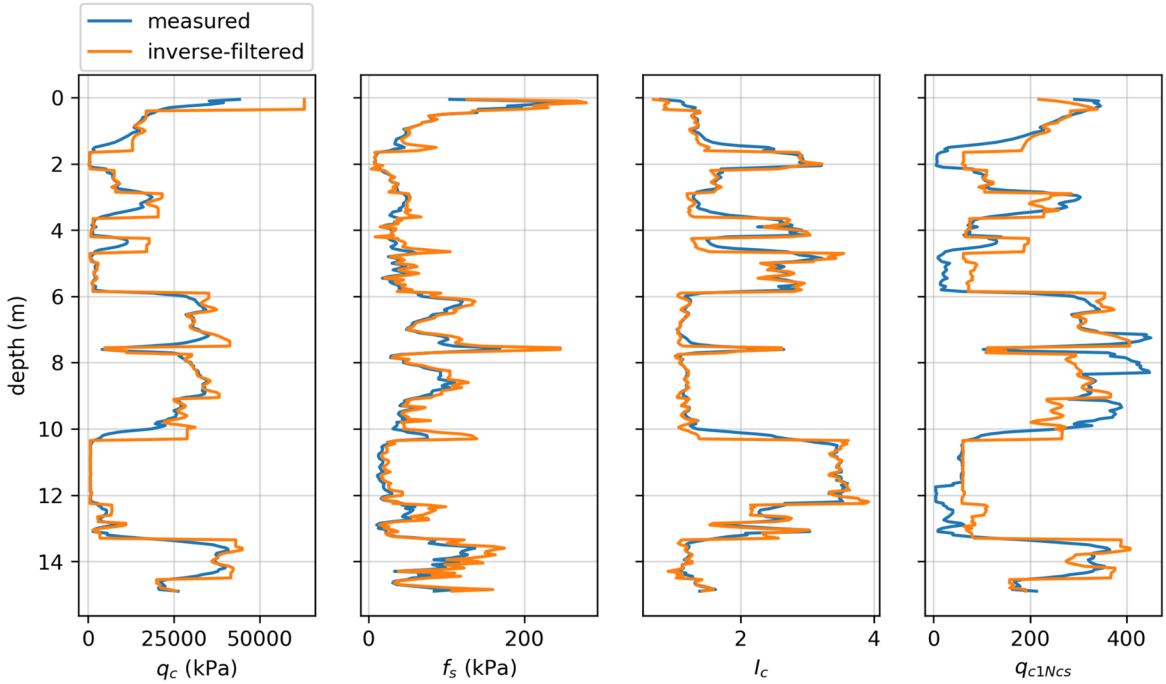

Figure 5-6 **CPT data from UC-4 at Moss Landing–Sandholdt Road (original data from Boulanger et al., 1995, 1997)**

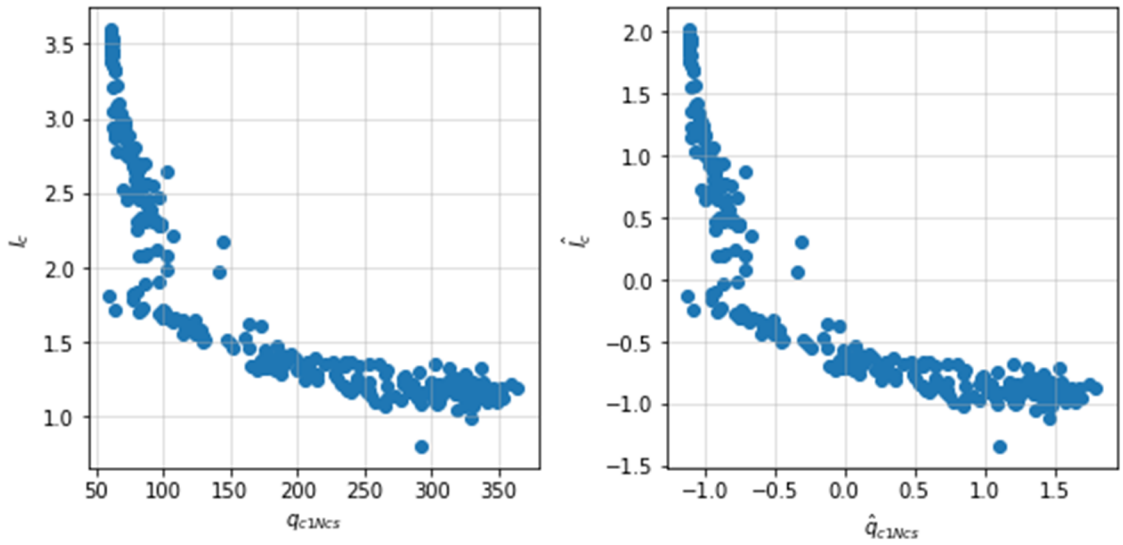

Figure 5-7 **Cross plots of I_c vs q_{c1Ncs} and $\hat{I}_c$ vs $\hat{q}_{c1Ncs}$ for UC-4 at Moss Landing–Sandholdt road**

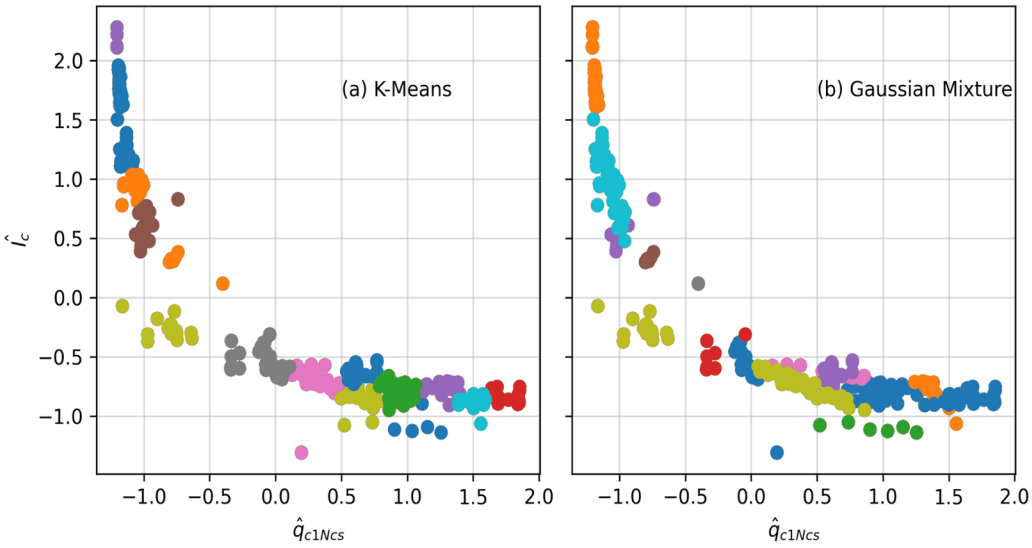

Figure 5-8 **(a) K-means and (b) Gaussian mixture clustering algorithm results for UC-4 CPT profile**

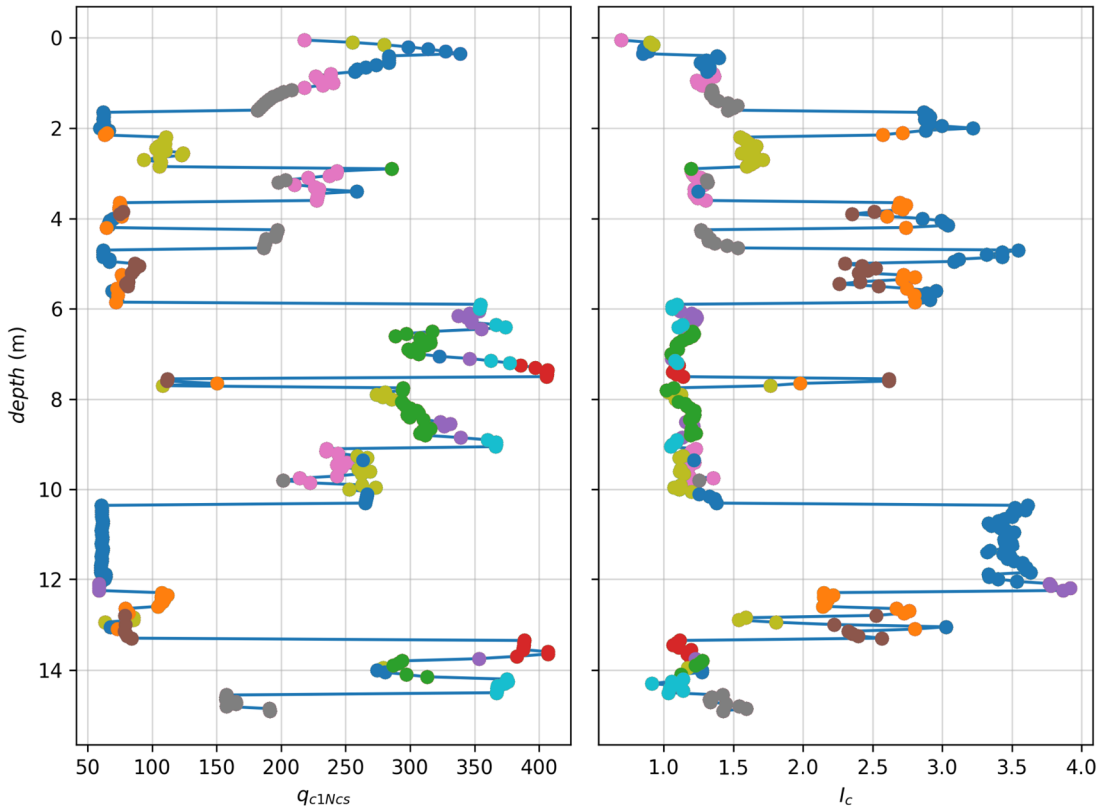

Figure 5-9 **Depth profiles for K-means clustering algorithm results for UC-4 CPT profile**

One possible solution would be to include depth as a 3rd variable in the clustering algorithm. While that solution improves continuity with depth, it does not solve the problem. To overcome this problem and obtain vertically contiguous clusters, we turn to agglomerative clustering, which is a form of hierarchical clustering that groups data based on a cascading "tree" of clusters computed using distances between points (Nielsen, 2016). A nearest neighbor matrix is provided to the clustering algorithm to specify which points are permitted to be considered when assigning clusters. For ordered data, the nearest neighbor matrix is tri-diagonal with ones on the diagonal and the two adjacent diagonals, and zeros elsewhere. This matrix forces the clusters to be contiguous. The algorithm then clusters data by minimizing the within-cluster variance for the total number of clusters specified. The resulting data is plotted in Figure 5-10, which illustrates that the layers are now vertically contiguous. Some clusters clearly correspond to transition zones (e.g., the cluster beginning at 10m depth) while others clearly belong within a stratum (the cluster immediately below the previously mentioned transition layer).

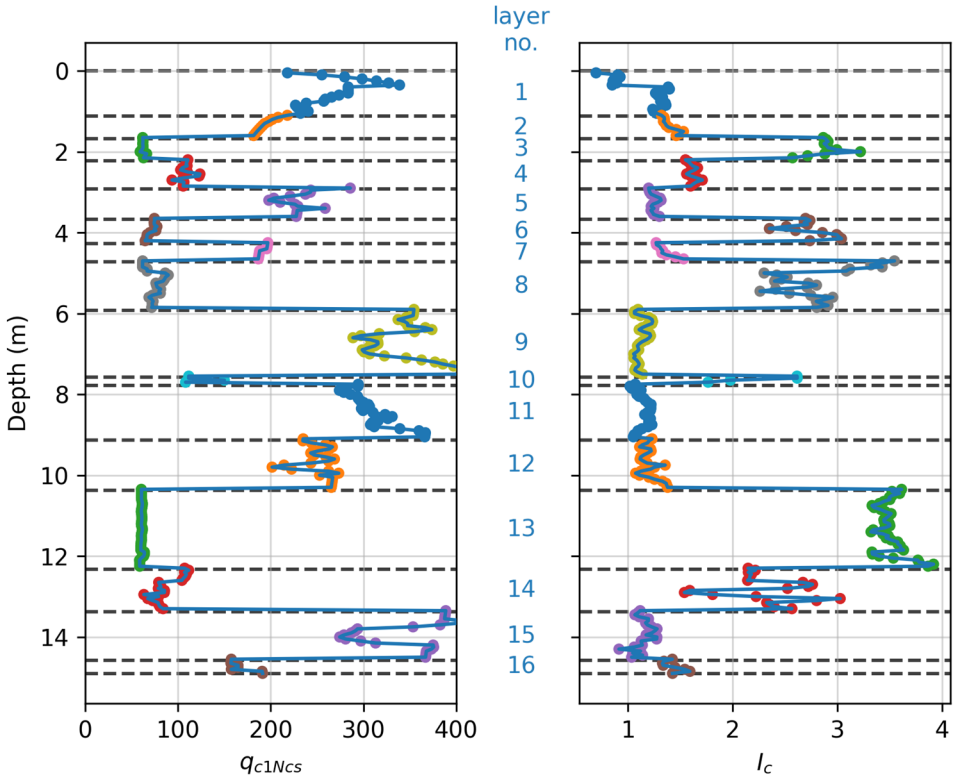

Figure 5-10 Depth profiles for agglomerative clustering algorithm with nearest neighbor Matrix for UC-4 CPT profile

Success of this method is highly dependent on the number of clusters specified, which is not known a priori because different CPT soundings require different numbers of clusters due to differences in total length and spatial variability of the soil deposit. Selecting the optimal number of clusters must balance two competing factors: (i) increasing the number of clusters reduces within-cluster variance, and (ii) to avoid over-fitting, the fewest possible number of clusters that reasonably divide the profile into layers should be provided.

In agglomerative clustering, a distortion score, J_D, is often utilized to identify the optimal number of clusters, and is defined for the two-standardized-variable case considered here in Eq. (5-13),

$$J_D = \frac{\sum_{i=1}^{N}\left[\left(\hat{q}_{c1Ncs} - \mu_{\hat{q}_i}\right)^2 + \left(\hat{I}_c - \mu_{\hat{I}_{c_i}}\right)^2\right]}{\sum_{i=1}^{N}\left[\left(\hat{q}_{c1Ncs_i}\right)^2 + \left(\hat{I}_{c_i}\right)^2\right]} \quad \text{5-13}$$

where $\mu_{\hat{q}_i}$ and $\mu_{\hat{I}_{c_i}}$ are the mean values of $\hat{q}_{c1Ncs}$ and $\hat{I}_c$, respectively, for the i^{th} cluster (i.e., subscript i is the index for clusters and identifies values of these parameters for each individual cluster), and N is the total number of data points in the profile. Note that J_D decreases as the number of clusters, K, increases, and by definition is equal to zero when K=N because every point would constitute its own cluster and the numerator would be zero. The optimal number of clusters therefore cannot be computed by minimizing the distortion score, but rather is a compromise between reducing the distortion score while retaining the smallest possible number of clusters that adequately categorizes the data.

5.3.1 Thickness-Dependent Cost Function and Combined Cost Function

We define a cost function, J_T, that penalizes the average layer thickness within a profile using Eq. (5-14).

$$J_T = 0.2\left(\frac{0.5m}{t_{avg}}\right)^3 \quad \text{5-14}$$

The average thickness is defined as $t_{avg} = z_{max}/K$, where z_{max} is generally the total depth of the CPT profile. Note that predrilling is sometimes necessary for CPT profiles, in which case the first depth at which data is recorded is non-zero. In those cases, z_{max} is the difference between the deepest and shallowest CPT measurement. The purpose of Eq. (5-14) is to penalize selection of a high value of K if it results in average layer thicknesses that are too small to be considered geotechnically significant. Based on inspections and analyses of hundreds of CPT profiles in the NGL database, we believe that 0.5 m is a fairly thin stratum, and we set the coefficients in Eq. (5-14) such that $J_T = 0.2$ for this condition. The cubic form of Eq. (5-14) was adjusted until the achieved average layer thickness accorded well with our judgment. A combined cost function is then defined in Eq. (5-15), where w_D and w_T are weights assigned to the components of the cost function. We herein utilize $w_D = w_T = 1.0$, but these weights can be adjusted based on user judgment in a site- or region-specific manner.,

$$J = w_D.J_D + w_T.J_T \quad \text{5-15}$$

5.3.2 Elbow and min(J) Methods

We consider two methods for utilizing the distortion score and the combined cost function to select the optimal number of layers. First, the “elbow” method graphically interprets a plot of J_D vs. K, which has a negative curvature over the full range of K, but flattens as K increases (Figure 5-11). The optimum value of K (9 in the case of Figure 5-10) is identified on the basis of curvature having decreased to a sufficiently low level, which is subjective. As such, the elbow

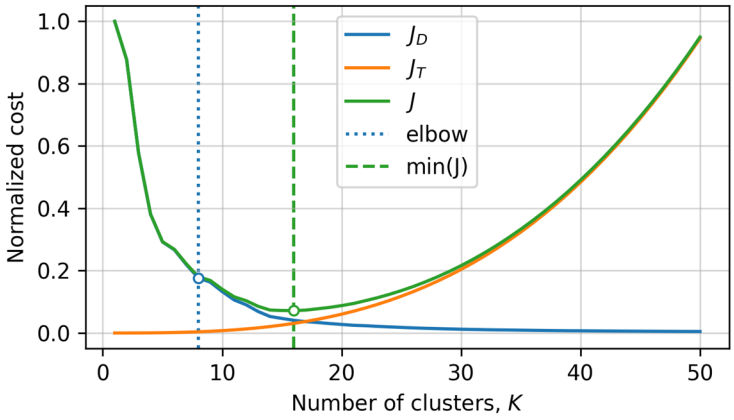

Figure 5-11 Cost functions and layer selection for CPT profile UC-4

method is based only on J_D and not on J_T. We utilize the Yellowbrick (Bengfort et al., 2022) Python package to implement the elbow method which identifies the point of maximum curvature of the J_D vs. K curve and assigns that as the optimum number of layers. The silhouette method (Bengfort et al., 2022) is also often utilized to identify the optimal number of clusters. This method is based on a so-called "silhouette" value that measures the similarity of data points within a cluster compared to other clusters. We found it to produce similar results to the elbow method. Thus, results from this method are not reported in Figure 5-11. Molina-Gómez et al. (2022) utilize the silhouette method to define the number of clusters in their algorithm. We also apply an alternative method in which K is selected as the point where J [from Eq. (5-15)] is minimized. For this reason, we call this the min(J) method. The combined cost function is minimized for K = 16 clusters for the example of CPT UC-4 in Figure 5-11.

Profiles of 16 and 9 layers are shown in Figure 5-12, where (a) and (b) have 16 layers by using the min(J) method, whereas (c) and (d) have 9 layers by using the elbow method. The primary differences between these two profiles are in layers number 3, 4, and 6 for the 9-layer profile. These layers clearly contain within-layer regions that are vertically contiguous with different q_{c1Ncs} and I_c values (e.g., the layer for the 2.2-3.8 m depth range), yet they are clustered together in the 9-layer profile. By contrast, they are separated into different layers in the 16-layer profile. The 16-layer profile accords better with our judgment, and similar observations observed across diverse profiles with a wide range of depths (as described in the next section) causes us to prefer use of the min(J) approach over the elbow method when selecting the number of layers. We recognize that a different curvature threshold in the application of the elbow method would have produced a different number of layers and, possibly, a solution that accords better with our judgment. However, the superiority of the min(J) method is related to the fact that it is based on layer thickness, which is a physically meaningful quantity, whereas the gradient of J_T vs. K used in the elbow and silhouette methods does not have a clear physical meaning.

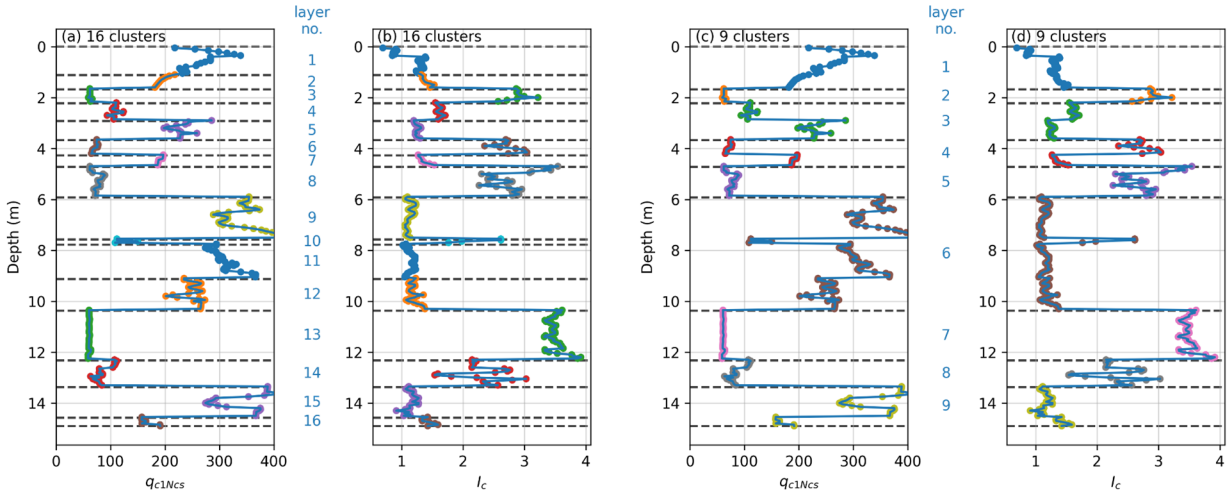

Figure 5-12 Profiles of q_{c1Ncs} and I_c with 16 layers by using the min(J) method (a and b) and 9 layers by using the elbow method (c and d)

5.3.3 Calculations for Many CPT Profiles

Calculations of the optimal numbers of layers were performed for a total of 272 CPT profiles contained in the NGL database. Both the elbow method and the min(J) method were utilized to select the optimal number of layers. We expect that t_{avg} should be independent of z_{max} because t_{avg} depends upon vertical heterogeneity of the soil profile, which is controlled by the geological processes that formed the soil deposit, whereas z_{max} arises from a decision controlled by the objectives of the site investigation. For example, z_{max} may be higher for a site investigation for a pile-supported tall building with a corresponding deep zone of influence than for a single-story building supported by spread footings with a corresponding shallow zone of influence.

Values of t_{avg} vs. z_{max} are plotted in Figure 5-13. The elbow method exhibits a strong positive correlation in which t_{avg} increases essentially linearly with z_{max}. This is an undesirable outcome since we anticipate t_{avg} to be independent of z_{max}. By contrast, values of t_{avg} are essentially independent of z_{max} using the min(J) method, particularly for values of z_{max} > 12m. For liquefaction triggering evaluation, profiles shorter than about 15m may miss layers that could potentially liquefy and produce surface manifestation. In this regard, the slight bias in the min(J) method for shallow profiles has little practical impact because evaluations of liquefaction for a profile need to extend deeper than 12m to reasonably capture all the layers that may influence manifestation, and there should not be instances where the bias on short CPTs is present.

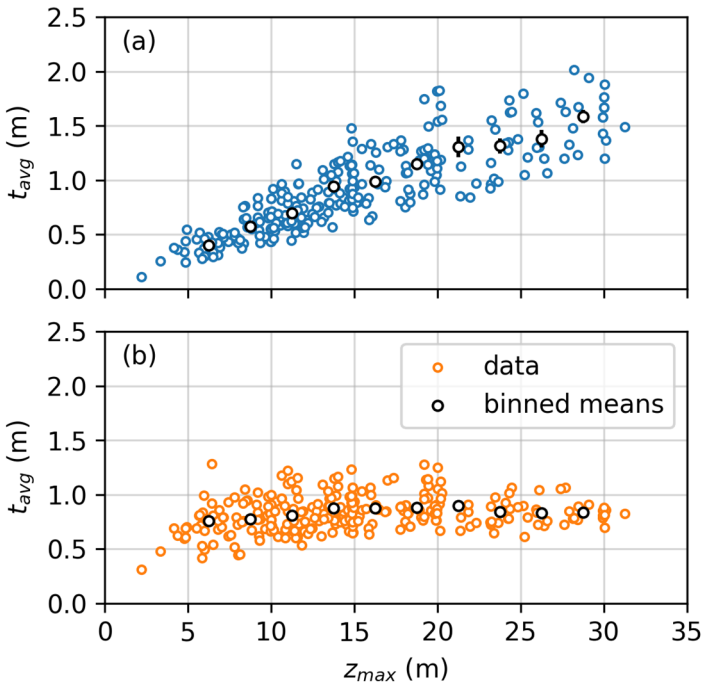

Figure 5-13 Average layer thickness, t_{avg}, versus total CPT profile length, z_{max} for (a) elbow method and (b) min(J) method.

The influence of maximum depth on average layer thickness is further explored in Figure 5-14, which illustrates normalized cost versus number of clusters for (a) a shallow profile with z_{max} = 5.1m from CPT_8933 at Site 76 in Edgecumbe, New Zealand, and (b) a deep profile with z_{max} = 31.3m from CPT001 at the Inage site in Urayasu City, Japan (CPT names are those reported in the NGL database). Note that the J_T functions are significantly different for these two profiles because the same average thickness in Eq. (5-14) produces fewer layers for the shallow profile than for the deep profile. For the shallow profile, the elbow method indicates that 8 sublayers is ideal (t_{avg} = 0.64m), while the min(J) approach provides 7 layers (t_{avg} = 0.73m). These results are very similar. By contrast, for the deep profile, the elbow method indicates that 8 layers is ideal (t_{avg} = 3.9m), while min(J) provides 36 sublayers (t_{avg} = 0.87m). These results are significantly different, and the average layer thickness using the elbow method is too large to capture potential critical layers of sand-like soil with low q_{c1Ncs}.

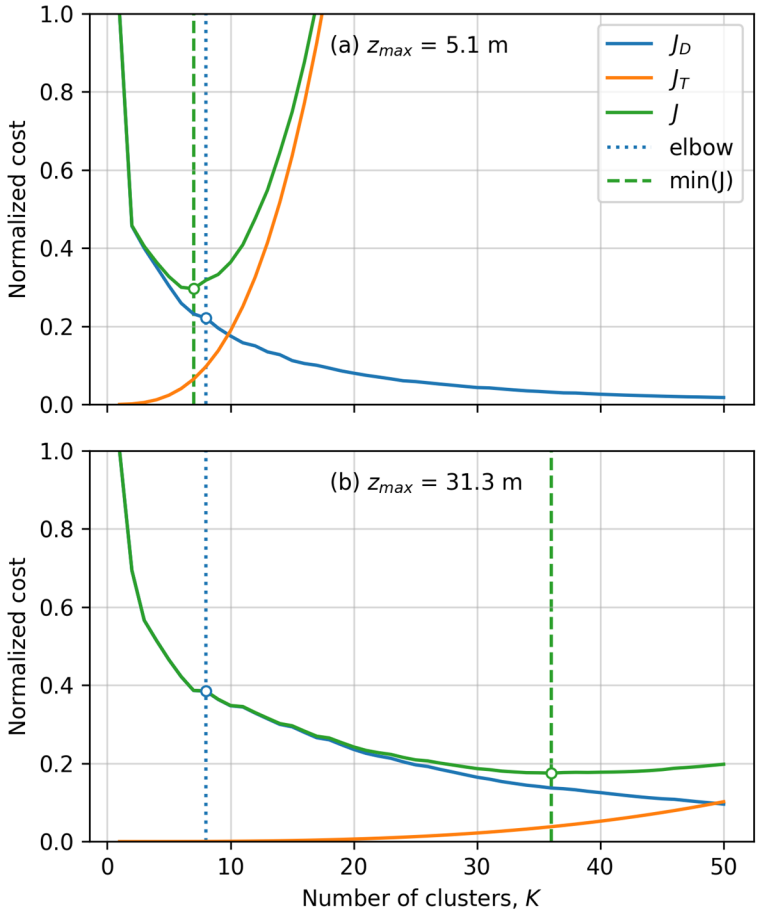

Figure 5-14 Normalized cost versus number of clusters for (a) a shallow profile with z_{max}=5.1m corresponding to CPT_8933 at Site 76 in Edgecumbe, New Zealand and (b) a deep profile with z_{max}=31.3m corresponding to CPT001 at the Inage site in Urayasu City, Japan

Note that when K=8, J_D is near 0.2 for the shallow profile and near 0.4 for the deep profile. A fundamental limitation of the elbow method is that it considers only the curvature of the cost function, and not the value of the cost function itself.

The two profiles are illustrated in Figure 5-15 with a common depth axis to illustrate the clear differences in the maximum penetration depth. The average layer thicknesses determined using the min(J) method are similar for these two profiles despite the different total depths. Furthermore, it is clear that reducing the number of layers for the deeper site from 36 [using the min(J) method] to only 8 (using the elbow method) would result in significantly higher average layer thickness and would miss much of the stratigraphic detail within that profile.

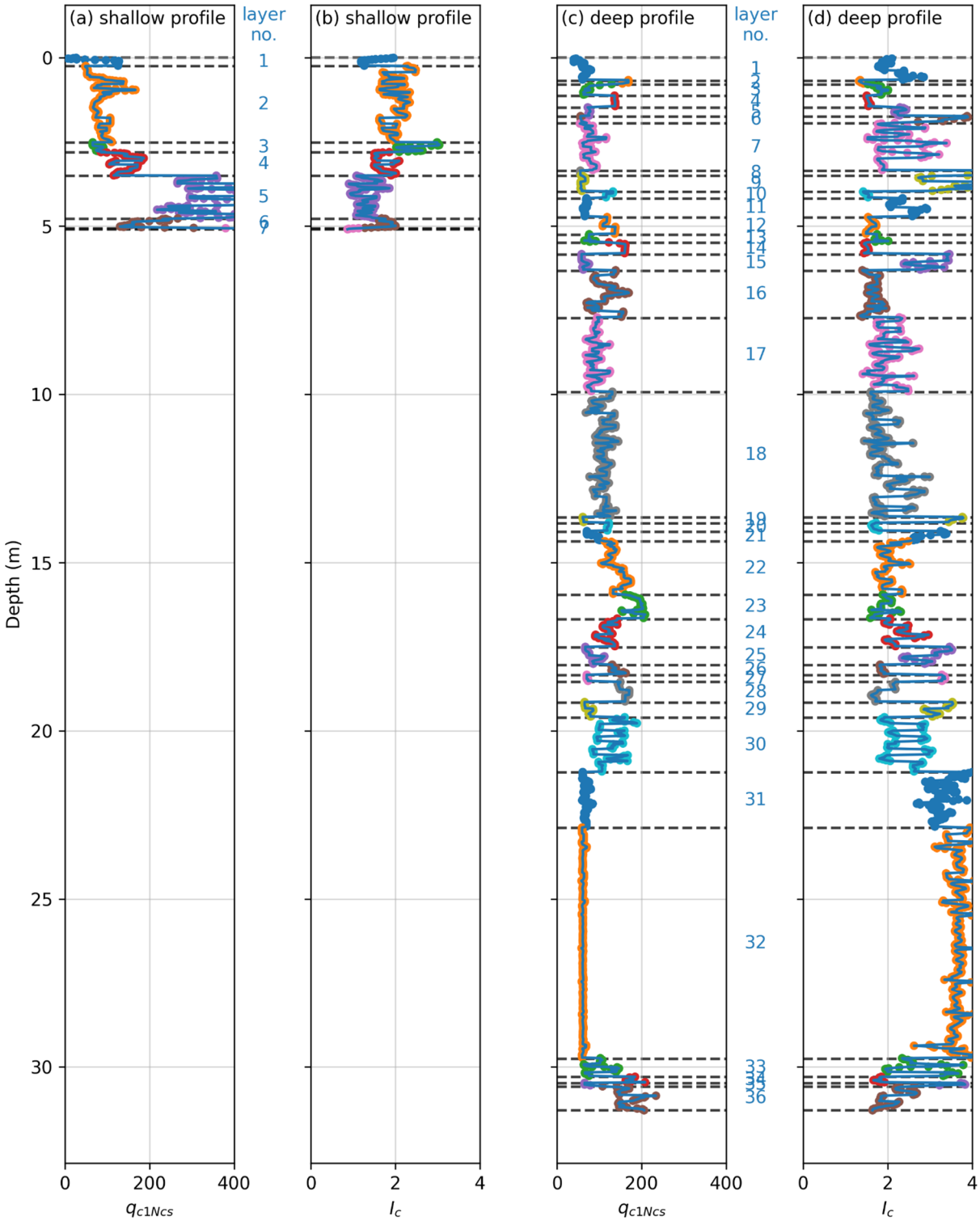

Figure 5-15 **Profiles of q_{c1Ncs} and I_c for (a) and (b) a shallow profile corresponding to CPT_8933 at Site 76 in Edgecumbe, New Zealand, and (c) and (d) a deep profile corresponding to CPT001 at the Inage site in Urayasu City, Japan**

5.4 Assigning Layer Properties

After identifying layers using the agglomerative clustering algorithm, we compute a number of different attributes for each layer in the profiles. Some attributes are computed directly from the CPT data, while others are computed using a combination of CPT data and demand for the purpose of identifying the critical layer within the profile. Section 5.4.1 describes attributes obtained directly from CPT data and stress normalization. Section 5.4.2 describes a new relationship for estimating *FC*. Section 5.4.3 describes the calculation of *CSR*.

5.4.1 Basic Layer Properties and Stress Normalization

Attributes computed directly from the CPT data are listed in Appendix A. We computed a total of 16 different layer parameters for the case history dataset for consideration in model development, including layer depth, layer thickness, cone tip resistance, overburden- and fines-corrected cone tip resistance, sleeve friction, soil behavior type index, modified soil behavior type index, vertical total stress, vertical effective stress, groundwater table depth, cyclic stress ratio, magnitude scaling factor, K_σ, strength of non-liquefied layers above the layer, and ejecta severity index within the layer. These attributes are computed in Python and stored in a pickle file format (with a .pkl file extension) that is well suited to being read into a Pandas dataframe. We will publish these data as part of this project to facilitate use by other model development teams. One pickle file has been created for the measured CPT data, and another has been created for CPT data that has been inverse-filtered using the algorithm by Boulanger and DeJong (2018).

To calculate q_{c1Ncs} for a profile, the total and effective stress profiles are needed. An estimate of the unit weight profile is created using the specific gravity (G_s) and water content (w_c) measurements from the nearest boring to the CPT. If one or neither of these values are present at a particular depth range or in the closest boring, then the G_s and w_c are assumed to be 2.7 and 35%, respectively. Assuming saturation, the unit weight is computed as $9.81\text{kN/m}^3(e+G_s)/(1+e)$ where e is the void ratio equal to $G_s(w_c/100\%)$. If there is an associated groundwater table depth in the WATR table assigned to the CPT, we select that value for case history processing. If there is no associated entry in the WATR table assigned to the CPT, we assign the closest groundwater table depth at any in situ test at the site (e.g., a borehole). These quantities are all used to compute the total and effective stress profile for the CPT.

The equations to compute q_{c1N} as recommended by Boulanger and Idriss (2014) are:

$$q_{c1N} = C_N \frac{q_c}{p_a} \tag{5-16}$$

$$C_N = \left(\frac{P_a}{\sigma'_v}\right)^m \leq 1.7 \tag{5-17}$$

$$m = 1.338 - 0.249(q_{c1Ncs})^{0.246} \tag{5-18}$$

where q_c is the cone tip resistance and p_a is atmospheric pressure (i.e., 1 atm = 101.325 kPa). Equations used to compute q_{c1Ncs} as recommended by Boulanger and Idriss (2014) are

$$q_{c1Ncs} = q_{c1N} + \Delta q_{c1N} \quad \text{5-19}$$

$$\Delta q_{c1N} = \left(11.9 + \frac{q_{c1N}}{14.6}\right) exp\left(1.63 - \frac{9.7}{FC + 2} - \left(\frac{15.7}{FC + 2}\right)^2\right) \quad \text{5-20}$$

where *FC* is fines content. The crust thickness (H_1) is taken as the sum of the thickness of layers with I_c greater than or equal to 2.6 above the water table.

5.4.2 Estimation of Fines Content from CPT Data

The liquefaction potential of an element of soil is related to its degree of contractiveness, which is a function of its state. At a given effective stress level, the state of a particular soil is a function of its relative density, which can be measured in the laboratory. The in situ relative density, however, is difficult to measure directly and typically inferred from penetration resistance. The CPT provides an effectively continuous profile of tip resistance (q_t), sleeve friction (f_s), and sometimes pore pressure (u_2), and is commonly utilized to assess soil liquefaction (e.g., Robertson and Wride, 1998; Moss et al., 2006; Boulanger and Idriss, 2016) because q_t correlates well with relative density of clean sands. However, q_t alone is inadequate to assess relative density of sandy soils with appreciable fines because the amount and plasticity characteristics of fines present in the sand influence its compressibility and drainage characteristics, and therefore influences the q_t for a given relative density. For these reasons, CPT soundings should be accompanied by sampling and laboratory testing when feasible to measure fines content and plasticity characteristics, either using a collocated borehole or by using sampling equipment that can be affixed to the CPT rods. However, many projects proceed without soil sampling, in which case susceptibility and fines content are inferred from CPT measurements. The presence and plasticity characteristics of fines also influence liquefaction susceptibility and cyclic resistance ratio (e.g., Park and Kim, 2013), albeit in a different manner from their effect on CPT measurements (investigated by Carraro et al., 2003 and Ecemis and Karaman, 2014). The fines correction applied in liquefaction evaluation does not distinguish these two effects, but rather jointly captures both effects in a combined manner. This section focuses on the influence of fines on CPT measurements, and not on the influence of fines on liquefaction susceptibility or resistance. The method described here has been submitted as a technical note (Hudson et al., 2023d), and the dataset is available on DesignSafe (Hudson et al., 2023c).

Soil behavior type index, I_c, is an indicator of the manner in which a particular soil behaves and is defined by Eq. (5-21). Robertson (1990) developed relationships between I_c and soil behavior type in which fine-grained soils tend to have I_c>2.6, sand-like soils with appreciable fines (i.e., silty sand to sandy silt) tend to have I_c = 2.05 to 2.6, and clean sand to silty sand tends to have I_c = 1.31 to 2.05. Soil behavior type is different from soil classification because the Unified Soil Classification System uses fines content (*FC*) of 50% to distinguish fine-grained soils from coarse-grained soils, whereas the mechanical behavior of soils with *FC* as low as 35% is generally considered to be dominated by the fines (Thevanayagam, 1998).

$$I_c = \sqrt{(3.47 - logQ_{tn})^2 + (logF_r + 1.22)^2} \quad \text{5-21}$$

Robertson and Wride (1998) developed a relationship between “apparent fines content” and I_c as specified by Eq. (5-22). Furthermore, they indicated that *PI* influenced the relationship

between I_c and *FC* and specified separate relationships for high plasticity fines (*PI* > 20%) and non-plastic fines (*PI* < 5%). For a given I_c, *FC* tended to be lower for high plasticity fines. They utilized the phrase “apparent fines content” rather than “fines content” as an acknowledgment that the relationship between I_c and *FC* was approximate, and influenced by plasticity, mineralogy, sensitivity, and stress-history. They indicated that the approximate relationship provided by Eq. (5-22) may nevertheless be useful for small projects.

$$FC(\%) = \begin{cases} 0 \; for \; I_c < 1.26 \\ 1.75 I_c^{3.25} - 3.7 \; for \; 1.26 \le I_c \le 3.5 \\ 100 \; for \; I_c > 3.5 \end{cases} \quad \text{5-22}$$

Robinson et al. (2013) developed a relationship between I_c and *FC* for soils in Christchurch and found that the apparent fines content was 10% for soils with I_c<1.7, and reasonably followed the Robertson and Wride (1998) relationship for non-plastic fines for soils with I_c>1.7.

Boulanger and Idriss (2016) developed a relationship between I_c and *FC* based on approximately 200 I_c-*FC* pairs from Suzuki et al. (1998) supplemented with approximately 120 I_c-*FC* pairs from liquefaction case histories. They regressed their relationship using *FC* as the independent variable, and I_c as the dependent variable, and subsequently inverted the equation to obtain the relationship given by Eq. (5-23), where C_{FC} is a parameter that may be calibrated on a site-specific basis. The mean value of C_{FC} from their dataset is 0.0, and the standard deviation is 0.29. Note that the standard deviation reflects uncertainty in I_c for a given *FC* because they regressed the model with *FC* as the independent variable.

$$FC = 80(I_c + C_{FC}) - 137 \; 0\% \le FC \le 100\% \quad \text{5-23}$$

Cetin and Ozan (2009) compiled a dataset containing 484 measurements of *FC*, CPT measurements, and plasticity indices. A total of 474 pairs have *FC* and CPT measurements, while 388 have Atterberg limits. They do not report I_c, but rather utilized Bayesian methods to estimate *FC* directly from measured cone tip resistance and sleeve friction. We sought to develop a new probabilistic relationship for *FC* conditioned on I_c using CPT and *FC* data from the NGL dataset.

5.4.2.1 Dataset

At the time the NGL database was queried to develop this relationship, a total of 2,714 layers with I_c computed using CPT soundings were associated with a measured *FC* from a sample at the same depth in a nearby boring. These data come from 111 different sites and 227 different collocated CPT/boring log pairs. All data used herein were reviewed by two independent reviewers to check for accuracy of information in the database relative to source documents. This association of a CPT sounding with a boring was applied to pairings separated by 10m or less, with most separated by less than 3m. Each CPT sounding was inverse-filtered to account for layer effects using the procedure by Boulanger and DeJong (2018), and strata from the inverse-filtered profiles were identified using an agglomerative clustering method (Hudson et al., 2023a). The representative value of I_c for each stratum was then computed as its median value over the length of the specimen used to measure *FC* computed as the percent passing the No. 200 sieve (75 μm).

An example boring log and I_c profile is shown in Figure 5-16 for Adapazari Site B (PEER 2000, Bray et al., 2004), which has 13 measured FC values. For example, *FC* in the upper 4 m of Adapazari Site B (Figure 1) is generally higher than 50% with a median I_c of 2.7 whereas I_c = 1.3 with *FC* = 5% in the sand layer from about 4 to 9 m depth. In some cases, *FC* was measured for multiple specimens within a sample, and the *FC* values varied significantly. This is consistent with interbedding in the upper 4m of this profile. We considered computing I_c as the average value over the layer thickness or the sample length. We opted to average over the specimen length because the layer thickness is often quite large and might miss important stratigraphic details, and because multiple specimens are often tested from a single sample, often with significantly different *FC* and I_c within the specimen depth range.

The processing illustrated in Figure 5-16 was repeated for all collocated CPT soundings and boring logs, resulting in the values plotted in Figure 5-17, along with binned means that illustrate trends in the data. I_c-*FC* pairs were obtained from sites in California (1928), Turkey (319), Taiwan (191), New Zealand (94), Japan (88), China (60), and Mexico (34), and reflect geological conditions including Holocene and Pleistocene aged alluvial, beach, eolian, estuarine, floodplain, fluvial, lacustrine, and marine deposits as well as artificial fill. A general trend of increasing *FC* with increasing I_c is evident from the data. Standard errors of the binned means are smaller than the icons used to plot them. When I_c=2.6, the mean value of *FC* is about 60%, which is consistent with Robertson's (1990) soil behavior type concept because soil with *FC* this high is dominated by the fine fraction. When I_c=2.0, the mean value of *FC* is about 35%, often considered the transition where the soil becomes fines-dominated. Furthermore, the mean *FC* drops to about 10% for I_c<1.5, which is also consistent with Robertson (1990). Significant scatter exists in the data, which indicates that I_c is not a unique indicator of *FC*. The model shown in Figure 5-17 is described subsequently.

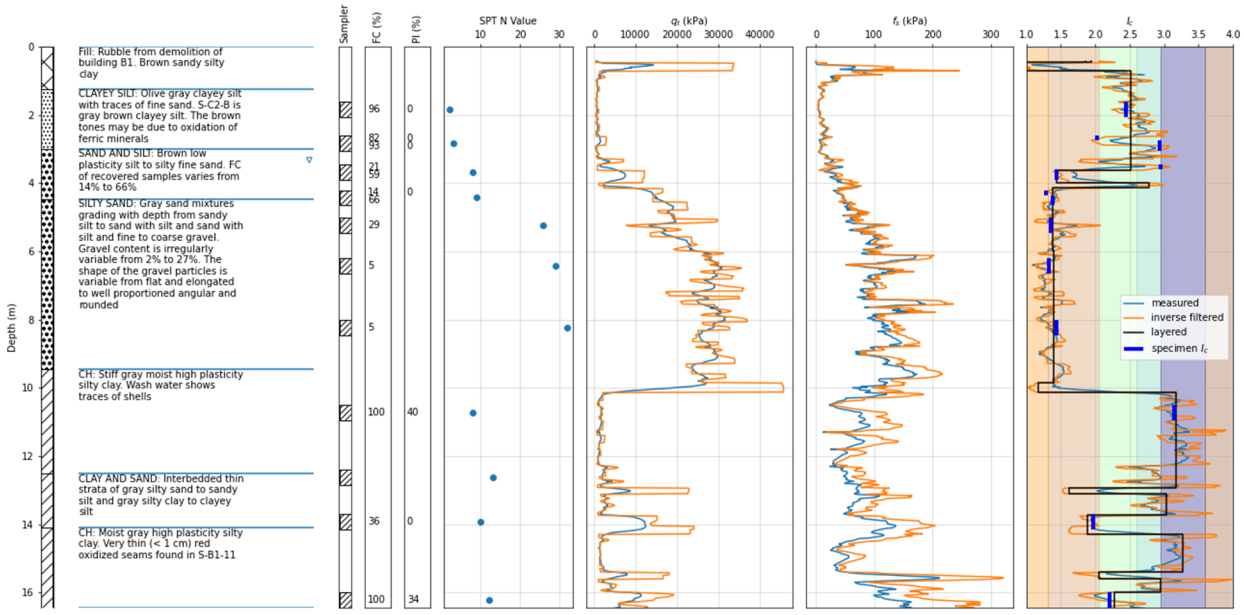

Figure 5-16 Boring log and CPT data from Adapazari Site B illustrating how *FC* values are related to I_c

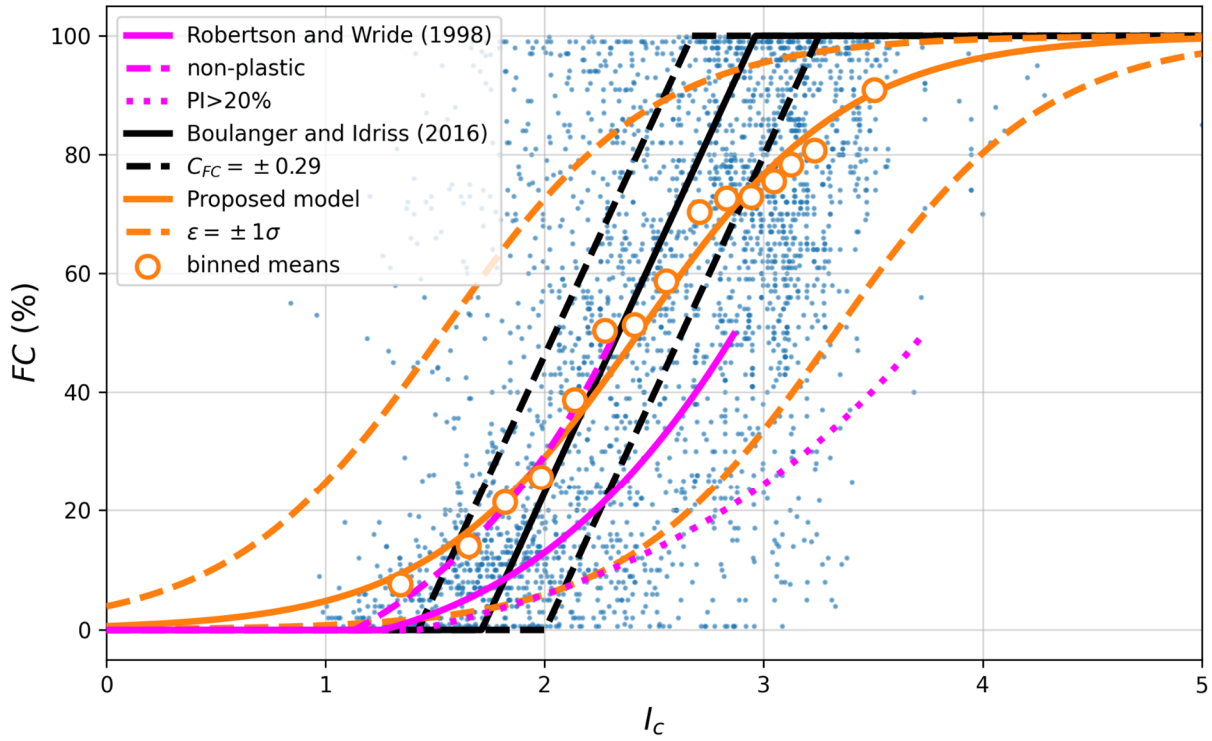

Figure 5-17 Fines content (*FC*) vs. soil behavior type index (I_c) for collocated CPT soundings and boring logs in NGL database compared with proposed model, Robertson and Wride (1998), and Boulanger and Idriss (2016). Each bin contains an equal number of data points.

5.4.2.2 Proposed FC-I_c Model

FC is bounded between 0 and 1, which poses a complication for least squares regression because the functional form must enforce these boundary conditions, which precludes linear regression. Rather than formulate a complicated functional form, we instead impose a logistic transform (Johnson, 1949) on the data as indicated by Eq. (5-24). Note that $\widehat{FC}$ is unbounded, and becomes infinity when *FC* = 1.0, and negative infinity when *FC* = 0.0. To avoid infinite values, we set the data to the nearest measured value that is not 0 or 1 (i.e., 0's are set to 0.6% and 1's are set to 99.8%).

$$\widehat{FC} = \ln\left[\frac{FC}{1-FC}\right] \qquad 5\text{-}24$$

We subsequently standardize $\widehat{FC}$ and I_c by subtracting the mean and dividing by the standard deviation of each quantity, prior to performing ordinary least squares regression (Table 5-2). The result is shown in Figure 5-18. The linear fit passes through the origin since the data were standardized prior to regression. The slope is 0.566, and the standard deviation of the residuals is 0.825. Although not shown here for brevity, residuals of the fit in transformed variable space approximately follow a normal distribution.

Table 5-2 Mean and Standard Deviation of I_c and $\widehat{FC}$

Variable	Mean	Standard Deviation
I_c	2.5	0.615
$\widehat{FC}$	0.15	2.267

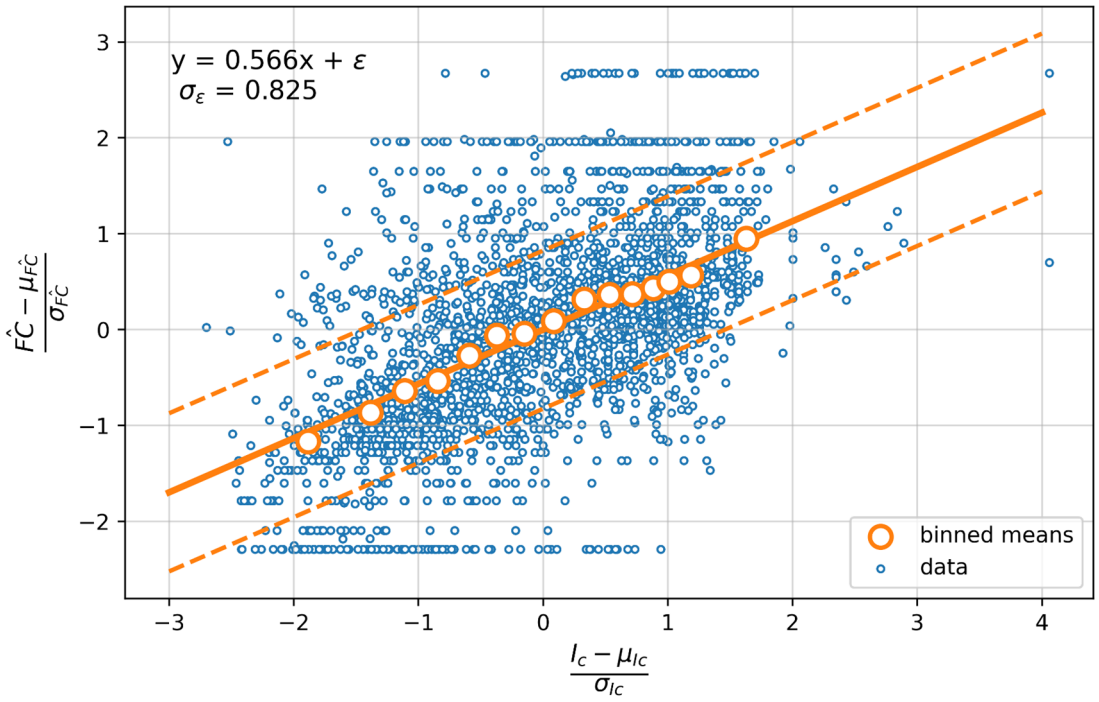

Figure 5-18 Linear least squares regression of standardized quantities

The regression results must be de-standardized and must be de-transformed to obtain a form of the equation in I_c – *FC* space. The result is provided by Eq. (5-25).

$$FC = \frac{\exp(2.084I_c - 5.066 + 1.869\epsilon)}{1 + \exp(2.084I_c - 5.066 + 1.869\epsilon)} \qquad 5\text{-}25$$

where ϵ is a random variable with mean zero and standard deviation of 1.0. The proposed relationship is plotted in Figure 5-17 in I_c – *FC* space for the mean relationship and ϵ = ±1 values. The mean curve agrees well with the binned means of the data, indicating that the fit is reasonable. The ϵ = ±1 relationships reflect the significant scatter in the data.

The relationships of Robertson and Wride (1998) and Boulanger and Idriss (2016) are also plotted in Figure 5-17. The recommended Robertson and Wride (1998) model is lower than the binned means, indicating under-prediction of *FC* for this dataset. The Robertson and Wride

(1998) model for non-plastic fines, however, is very close to the binned means of our dataset, which is consistent with the findings of Robinson et al. (2013) for the soils in Christchurch. The model of Boulanger and Idriss (2016) tends to under-predict *FC* for values of I_c < 2.0 and over-predict *FC* for values of I_c > 2.0 and does not represent the smooth variation of *FC* with I_c indicated by the binned means for the NGL dataset. Furthermore, the range corresponding to C_{FC} ± 0.29 is rather small, and significantly smaller than the range for our proposed model corresponding to ± 1σ.

5.4.2.3 Influence of Plasticity

Robertson and Wride (1998) found that plasticity index (*PI*) influenced the relationship between I_c and *FC*. Specifically, *FC* was noted to decrease as *PI* increased for a given I_c. This trend is intuitive because a small amount of plastic fines would be expected to exert more influence on soil behavior than the same amount of non-plastic fines. Of the 2,714 I_c-*FC* pairs in the NGL dataset, 1,063 have measured Atterberg limits. An additional 299 samples were inferred as non-plastic based on stratigraphic layer descriptions containing the words “non-plastic”, “sand”, and/or “gravel” and not containing any of the following words: “plastic”, “clay”, “silt”, “fat”. To investigate potential effects of soil plasticity, residuals were computed as:

$$R_{FC} = \ln(FC) - \ln\left(\frac{\exp(2.084I_c - 5.066)}{1 + \exp(2.084I_c - 5.066)}\right) \quad \text{5-26}$$

The binned means of the residuals are negative (model overpredicts) for *PI* < 20%, and positive (model underpredicts) for *PI* > 20%. This implies that, for a given I_c, the fines content is higher for high *PI* soils, which is the opposite of the trend presented by Robertson and Wride (1998). To investigate the cause of this finding, Figure 5-19b shows a positive correlation between *FC* and *PI*; i.e., higher *FC* soils are more likely to have high *PI*. As a result, an I_c-*FC* pair with an unusually high *FC* (thus producing a positive residual) is likely to also have a high *PI*, whereas a pair with an unusually low *FC* (producing a negative residual) is likely to have a non-zero but low *PI*. This parameter correlation is not surprising because Atterberg limits are tested on specimens passing the #40 sieve, which therefore include sand-size particles and fines. Accordingly, low *FC* materials likely have large granular fractions in plasticity test specimens, reducing *PI*, whereas high *FC* materials will have limited granular fractions, increasing *PI*. We recognize that incomplete sampling could also affect the results in unknown ways – perhaps Atterberg limits tests on low *FC* soils are more likely to be performed if the plasticity is low (because such samples are more likely susceptible to liquefaction). If so, this would represent a type of sampling bias. Another potential sampling bias would occur if Atterberg limits on high *PI* soils with low *FC* are underrepresented relative to the frequency of their occurrence in nature, which is a possibility we cannot exclude. Given these uncertainties, we have not attempted to adjust the relationship to recover the trend we believe would exist in the absence of correlation between *FC* and *PI*. Furthermore, the influence of *PI* on the I_c-*FC* relationship has little practical impact because in cases where *PI* is measured, *FC* should also be measured and therefore should not be inferred from I_c.

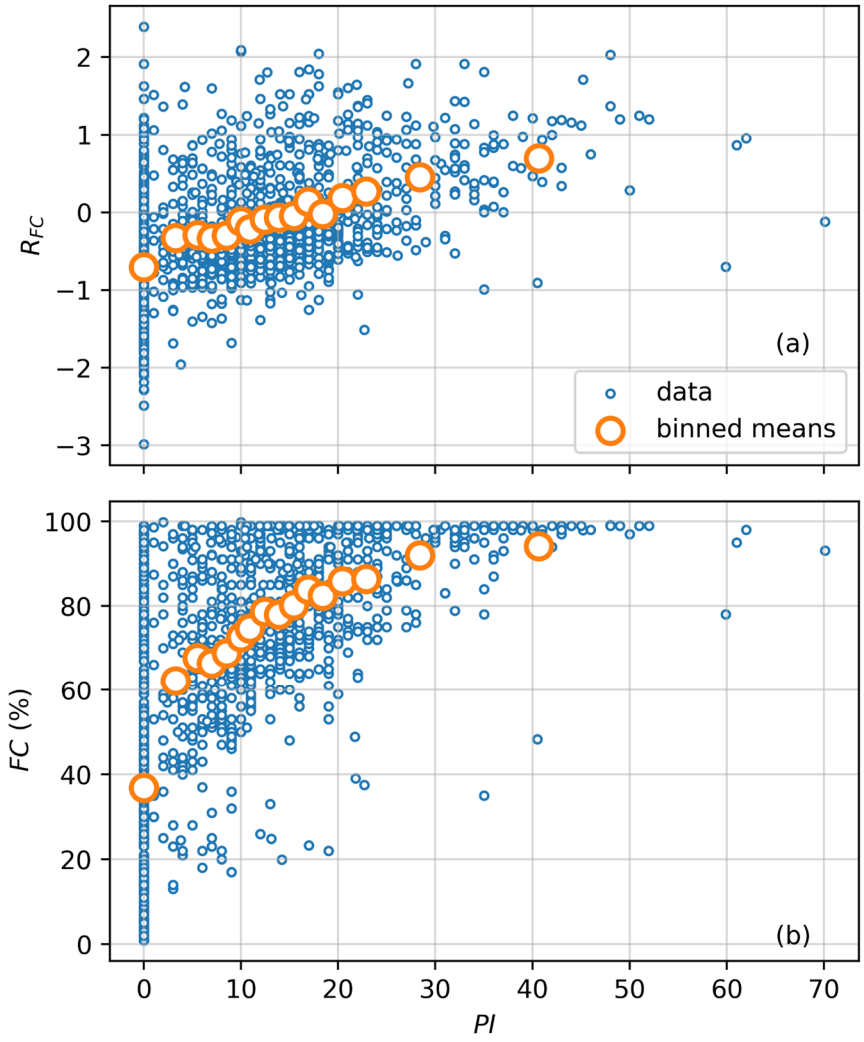

Figure 5-19 (a) Residuals of proposed model Eq. (5-26) versus *PI*, (b) positive correlation of *FC* with *PI* in database

5.4.3 Cyclic Stress Ratio

We compute seismic demands on soil layers in the form of a cyclic stress ratio, $CSR_{\mathbf{M}7.5,1atm}$ [Eq. (2-2) with adjustments *MSF* and K_σ]. $CSR_{\mathbf{M}7.5,1atm}$ is computed for a given earthquake event and ground motion that has been associated with an observation of surface manifestation (or lack thereof) at or near the location of the CPT sounding. Some locations have been shaken by multiple earthquakes; in which case the CPT data is repeated in the summary pkl file (see Appendix A for full list of quantities in the pkl file). The quantities that describe the earthquake event are summarized in Table 5-3. For each field observation, the nearest CPT sounding within the site is selected as being representative of that observation. The distance between the observation location and CPT sounding is recorded and stored in the pkl file.

Table 5-3 Summary of values queried or computed for each layer based on quantities from the database or derived from CPT data

Variable Name	Description
EVNT_ID	The primary key from the NGL database for the earthquake associated with this observation/CPT pair
EVNT_NAME	The event name from the NGL database for the earthquake associated with this observation/CPT pair
EVNT_MAG	The event magnitude from the NGL database for the earthquake associated with this observation/CPT pair
PGA	The *PGA* from the NGL database for the observation location (FLDO location)
FLDM_ID	The primary key from the NGL database for the observation of manifestation
FLDM_SFEV	The flag from the NGL database for the observation of manifestation (1 if manifestation observed, 0 if not)
FLDM_DIST	The distance between the CPT/observation pair
CSR	Cyclic stress ratio

$CSR_{\mathbf{M}7.5,1atm}$ values computed at the center of each layer are taken to be representative of the layer. As shown by the equations below, $CSR_{\mathbf{M}7.5,1atm}$ is computed using the *PGA* stored in the GMIM table associated with the observation (using the estimates from the Kriging approach outlined in Section 5.2.4, where possible), the moment magnitude of the event associated with the observation, the total and effective stress profiles computed for use in the q_{c1N} calculation, the *MSF* and N_{eq} equations by Lasley et al. (2017), and the r_d relationship presented in Lasley et al. (2016). The K_σ model is from Section 6.2.4 of this report.

$$CSR_{M7.5,1atm} = 0.65 \cdot \frac{PGA}{g}\frac{\sigma_v}{\sigma_v'}r_d\frac{1}{MSF}\frac{1}{K_\sigma} \quad 5\text{-}27$$

$$r_d = (1-\alpha)exp\left(\frac{-z}{\beta}\right) + \alpha \quad 5\text{-}28$$

$$\alpha = exp(-4.373 + 0.4491M_w) \quad 5\text{-}29$$

$$\beta = -20.11 + 6.247 * M_w \quad 5\text{-}30$$

$$ln(N_{eq}) = 0.4605 - 0.4082ln(a_{max}) + 0.2332M_w \quad 5\text{-}31$$

$$MSF = (14/N_{eq})^{0.2} \quad \text{5-32}$$

$$K_\sigma = \begin{cases} \left(\frac{\sigma'_{v0}}{p_a}\right)^{a_1} & for\ \sigma'_{v0} < p_a \\ \left(\frac{\sigma'_{v0}}{p_a}\right)^{a_2} & for\ \sigma'_{v0} \geq p_a \end{cases} \quad \text{5-33}$$

$$a_1 = \frac{-0.49}{1 + \exp[0.121(11.67 - FC)]} \quad \text{5-34}$$

$$a_2 = \begin{cases} -3.8 \times 10^{-6}(FC)^3 + 4.88 \times 10^{-4}(FC)^2 - 1.358 \times 10^{-2}(FC) - 0.13\ for\ FC < 70 \\ -0.148\ for\ FC \geq 70 \end{cases} \quad \text{5-35}$$

where ***z*** is the depth in meters, p_a is atmospheric pressure (1 atm) in the same units as σ'_v, and **M** is the moment magnitude.

6 CPT-BASED MODELS

As described in Chapter 4, the necessary components of the SMT's conditional probabilistic approach include estimates of P[*T*] = P[*T*|*S*]*P[*S*], P[*M*|*T*], and P[*M*|*NT*]. The following sections outline the preliminary approaches adopted by the SMT to estimate these probabilities. These results constitute the culmination of the model development process described in Section 2.2.2 and illustrated in Figure 2-7. The content presented in this chapter is subject to change as we refine the methodologies, input parameters, and framework, and based on the review comments from the MRT received prior to March 22, 2024.

Section 6.1 presents the SMT's selected model to estimate the probability of susceptibility P[*S*] based on existing models in the literature. Section 6.2 describes an initial (prior) model for triggering that is derived from laboratory cyclic test results. This model is needed as part of the overall model development process for reasons explained in Section 4.2. Section 6.3 presents the updated model for manifestation using the profile-based regression framework described in Section 4.4. Finally, Section 6.4 illustrates additional sensitivities of the P[*M*] model that have been investigated as part of the model development process.

6.1 Probability of Susceptibility, P[*S*]

Based on the definition of susceptibility in Section 2.1.1, our susceptibility model considers a soil's mineral composition as inferred from *PI* or I_c, and excludes non-compositional factors like state, saturation, and manifestation potential. Note that in our approach, saturation is considered as part of the P[*T*] relationship, as discussed in Section 4.4.1. Our susceptibility model is probabilistic to reflect natural variability of soil behavior and to quantify epistemic uncertainty. Following a public workshop on the topic (Stuedlein et al., 2023b), a framework for creating new susceptibility models using the laboratory component of the NGL database was formulated. However, the implementation of this framework is in its beginning stages and has not yet been adopted by the broader liquefaction research community. Therefore, we are using currently available models, namely Maurer et al. (2017) in which the authors used borings and co-located CPTs in New Zealand to correlate I_c to Atterberg limits which in turn is converted to a probability of susceptibility as defined by four criteria: Polito (2001), Seed et al. (2003), Bray and Sancio (2006), and Boulanger and Idriss (2006). The Maurer et al. (2017) adaptations of the four models are shown in Figure 6-1, and use the following functional form:

$$P[S] = 1 - \frac{1}{1 + exp\left(-\frac{1.702}{\sigma_m} * \left(\frac{I_c}{x_m} - 1\right)\right)} \quad \text{6-1}$$

The range of results in Figure 6-1 constitute a partial representation of epistemic uncertainty. We decided to treat this uncertainty using a logic tree approach to obtain I_c-conditioned probabilities of susceptibility, using equal weighting between the models. This approach produces the combined model shown in Figure 6-1, which has x_m = 2.635, and σ_m = 0.115. To incorporate the susceptibility model into the Bayesian inference framework utilized to obtain the manifestation model coefficients, a distribution function must be assigned to each model parameter. The uncertainty in these parameters was quantified by taking the standard deviation of the x_m and σ_m values from the four criteria, yielding 0.0204 and 0.0865, respectively. The Bayesian prior distributions were assumed to be normal with the means and the standard

deviations of the x_m and σ_m values as given above. The sensitivity of the P[*M*] model (Section 6.3) to variations across the different P[*S*] models is discussed in Section 6.4.3.

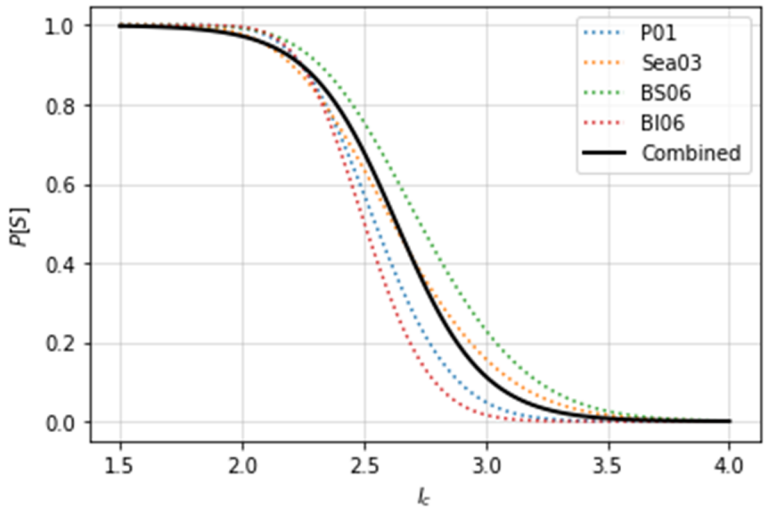

Figure 6-1 Probability of susceptibility models as a function of I_c as defined by Maurer et al (2017)

6.2 Probability of Triggering, P[*T*|*S*]

As described in Chapter 4, the SMT's approach for developing coupled probabilistic models for triggering and manifestation requires a "prior" model for the probability of triggering, which would then be potentially modified from interpretation of case history data. We develop a prior model for P[*T*|*S*] using *CRR* from cyclic tests performed on soil specimens in the laboratory. Many researchers over the last several decades have performed such tests under a wide range of conditions (e.g., cyclic stress amplitudes, soil densities, effective stress levels) and made their findings available in the published literature through journals, reports, and data repositories. These data provide meaningful insights into the mechanics of triggering and a given soil's resistance to liquefaction triggering for a broader range of conditions than exist in field case histories and without the influence of manifestation that is inherent in those case histories. We acknowledge the traditional argument that laboratory tests are performed on samples with varying levels of disturbance, and as a result, triggering under field conditions could differ from those in the laboratory. However, we seek to mitigate these concerns by considering in our model development results from intact specimens and by incorporating field performance data into the manifestation analysis. As a result, we consider a P[*T*|*S*] relationship derived from laboratory data to provide a reasonable prior. The following discussion outlines how P[*T*|*S*] was estimated from laboratory data.

6.2.1 Data Sources

As part of Task 5 of the current NRC/USBR-SwRI project, many published studies with *CRR* values from laboratory data were compiled and digitized into a single dataset to investigate the effects of overburden and initial static shear stresses on liquefaction triggering (Ulmer et al., 2022a, Ulmer et al., 2023a; Carlton et al., 2023). This dataset represented predominantly reconstituted soil specimens as opposed to intact specimens retrieved from the field with minimal disturbance and tested in the laboratory. The process of reconstituting specimens removes the effects of aging processes that occur in the field and the selection of a

reconstitution method (e.g., tamping, pluviation) can have a significant effect on the fabric of the soil. These modifications can influence the liquefaction response and triggering resistance of the soil (Seed, 1979).

We then proceeded to gather data from 19 studies in which intact specimens were sheared in CTRX or CDSS tests (CDWR, 1985; 1989; Hatanaka et al., 1995; Huang et al., 2009, 1999, 2004; Idriss et al., 1975; Ishihara et al., 1978, 1979; Ishihara and Koga, 1981; Kokusho et al., 2012; Kokusho and Tanimoto, 2021; Okamura et al., 2003; Pillai and Byrne, 1994; Pillai and Stewart, 1994; Porcino and Diano, 2016; Sancio, 2003; Sanín, 2010; Sanín and Wijewickreme, 2006; Seed et al., 1973; Suzuki et al., 1993, 1995; Wijewickreme, 2010; Wijewickreme et al., 2005; Yoshimi et al., 1989, 1994). This dataset of intact specimens represents predominantly clean sands with a few fine-grained specimens (*FC* up to 100%).

Nearly all of the intact specimen testing was performed as CTRX, although some was CDSS. The tests were typically consolidated in the laboratory to the in situ σ'_{v0} prior to cyclic loading, with some exceptions. The types of sampling methods from these studies that were considered by the respective authors to be relatively undisturbed or intact vary widely. The ability of each method to obtain undisturbed samples is not discussed in this report, but they generally fall into three categories based on their general procedures:

1) Soil is frozen in situ and subsequently sampled
2) Soil is sampled using high quality samplers and then subsequently frozen
3) Soil is sampled without freezing, e.g.:
    a) Block sampling technique
    b) Fixed piston sampler
    c) Rotary triple-tube sampler
    d) Large diameter sampler

Although intact specimens are preferable because they are more likely to retain their in situ soil fabric, reconstituted specimens have some advantages. For example, there is more opportunity for repeated tests to check for within-soil variability, whereas an intact specimen provides only one *CRR* value. Thus, in the following sections, we present and analyze results from both intact and reconstituted specimens.

The data for reconstituted specimens come from the dataset compiled for Task 5 and those data sources are discussed in detail in the Task 5 report (Ulmer et al., 2022a; Ulmer et al., 2023a; Carlton et al., 2023). We supplement the Task 5 dataset with two additional datasets containing data from other studies that investigated liquefaction resistance of various soils but that did not include a range of initial overburden stress or static shear stress values (thus disqualifying them from the Task 5 database). One of these additional datasets contains results from tests on intact specimens, while the other contains results from reconstituted specimens. Thus, three datasets were used to guide the development of a P[*T*|*S*] model as summarized below.

1. Task 5 dataset specifically compiled to investigate the effects of overburden and initial static shear stresses on liquefaction triggering (Ulmer et al., 2022a; Ulmer et al., 2023a; Carlton et al., 2023)

2. Additional data from studies of intact specimens to supplement the Task 5 dataset in developing a P[*T*|*S*] model

3. Additional data from studies on reconstituted specimens to supplement the Task 5 dataset in developing a P[*T*|*S*] model

All data in these datasets were processed in the same manner, as described in the following section.

6.2.2 Methodology

The specific process of estimating *CRR* from cyclic tests is documented in the Task 5 report (Ulmer et al., 2022a), but is also briefly summarized here. To estimate *CRR* from laboratory tests, a series of laboratory tests [e.g., CTRX, CDSS, or CTS] is conducted to develop relationships between the applied loading stress amplitude (*CSR*) and the number of cycles to reach liquefaction (N_L) as defined by a pre-defined liquefaction criterion for a given soil under a set of conditions [e.g., same D_r and σ'_{v0}]. Assuming a reference value of N_{ref} associated with a given magnitude event (e.g., 15 cycles for **M**7.5 in this study), $CSR_{M7.5}$ can be computed from a power law fit of the *CSR* versus *N* relationship. This $CSR_{M7.5}$ is the *CRR* from lab data, denoted as CRR_{lab}, which is typically adjusted to better reflect field conditions using correction factors for bi-directional shaking and mean effective stress. The following corrections were made to the CRR_{lab} values as recommended by Montgomery et al. (2012) to compute the field-corrected *CRR* (CRR_{field}):

$$CRR_{field} = 0.9\left(\frac{1+2(K_0)_{field}}{1+2(K_0)_{lab}}\right)CRR_{lab} \qquad 6\text{-}2$$

where CRR_{lab} is the *CRR* estimated from *CSR* vs *N* curves using lab data and $(K_0)_{field}$ and $(K_0)_{lab}$ are the at-rest lateral earth pressure coefficients in the field and in the lab, respectively. The 0.9 value in Eq. (6-2) is traditionally used to adjust unidirectional loading in laboratory tests to bi-directional loading in the field (e.g., Pyke, 1975). The value of $(K_0)_{lab}$ in a CTRX or CTS test is equal to the ratio of the radial to axial stress [e.g., $(K_0)_{lab}$ = 1.0 for isotropically consolidated CTRX tests] . The value of $(K_0)_{field}$ is typically unknown, but can be approximated to be between 0.5 to 1.0 for most applications related to liquefaction (Montgomery et al., 2012). In our study, we approximated the value of $(K_0)_{field}$ for each soil using reported values of the drained friction angle (ϕ') as $(K_0)_{field}$ = 1-sin(ϕ'). If ϕ' was unknown, then we assumed ϕ' = 30 degrees [i.e., $(K_0)_{field}$ = 0.5].

The value of N_{ref} and thus CRR_{lab} and CRR_{field} depends on the liquefaction criterion assumed to indicate triggering of liquefaction in the lab. As discussed in Chapter 2, the formal definition of initial liquefaction indicates that it occurs when r_u = 1.0 (i.e., a condition, usually momentary, of zero effective stress). In a number of experimental studies, liquefaction is considered to be triggered when r_u is very close to 1.0 because 1.0 is not always achieved. In many other studies, however, strain criteria are used as a substitute for pore pressure-based criteria. In some cases this is because the researchers were more interested in identifying the onset of significant shear strains rather than initial liquefaction. The conventional assumption has been that r_u reaches 1.0 at about the same time as specimens exhibit 2.5% single-amplitude axial strain (ε_{SA}) or 5% double-amplitude axial strain (ε_{DA}) in CTRX tests, or 3.75% single-amplitude shear strain (γ_{SA}) in CDSS tests. However, this is not always the case. A recent laboratory study (Stuedlein et al., 2023a), for example, has shown that soils can exhibit clay-like hysteretic behavior at moderate strain levels (γ_{SA} ~ 3%) that transitions to sand-like behavior when additional cycles of loading produce higher strains. Thus, in several figures that follow, the *CRR* values we computed in this study are separated by liquefaction criterion type to identify trends specific to each criterion.

Using this approach, we computed 215 CRR_{field} values from intact specimens and 1154 CRR_{field} values from reconstituted specimens. In most cases, values of D_r were reported for each specimen. In some cases, estimates of SPT blow count and/or estimates of q_c were also reported. Figure 6-2 shows histograms of the combined datasets in terms of test type, intact vs. reconstituted, D_r, FC, σ'_{v0}, and liquefaction criterion type.

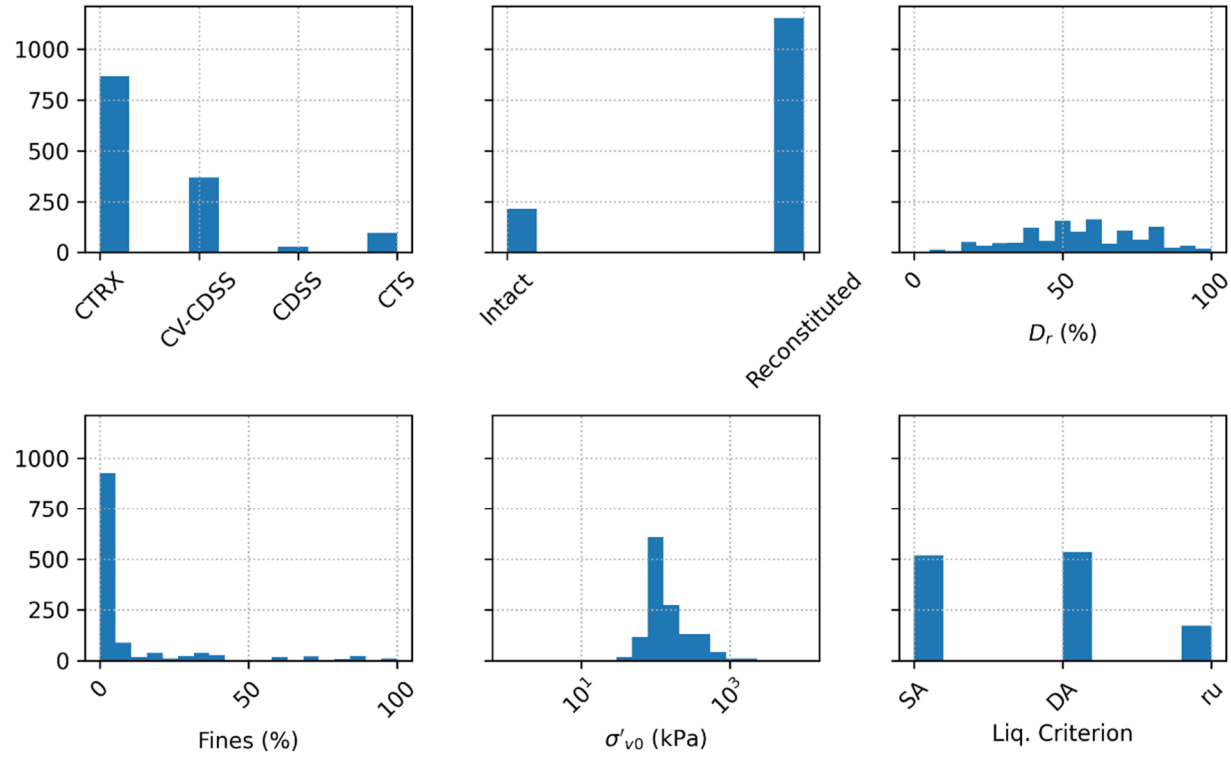

Figure 6-2 Histograms of *CRR* values obtained from the combined datasets in terms of test type, reconstituted vs. intact specimens, D_r, FC, σ'_{v0}, and liquefaction criterion

6.2.3 Data Coverage

As part of our analysis, we attempted to discern whether there were any significant differences in *CRR* values between intact vs reconstituted specimens, CTRX vs CDSS tests, and strain-based vs r_u-based liquefaction criteria. Our findings along this line are discussed in this section and in the figures below. However, despite gathering published data from a wide variety of sources, there are some underrepresented scenarios within our database that lead to some sampling bias, as will be discussed.

Figure 6-3 shows the variation of CRR_{lab} with D_r for the entire dataset used for estimating P[T|S], split up by intact vs. reconstituted specimens. The trendlines through each subset of the data are of a simple exponential functional form used for purposes of illustration. For D_r less than approximately 50%, the *CRR* for intact specimens is generally indistinguishable from the *CRR* for reconstituted specimens. However, as D_r increases beyond 50%, the *CRR* for intact specimens appears to be greater than that of reconstituted specimens. This may be the result of the age of the intact specimens making them more resistant to liquefaction, and perhaps in part due to other effects as discussed subsequently.

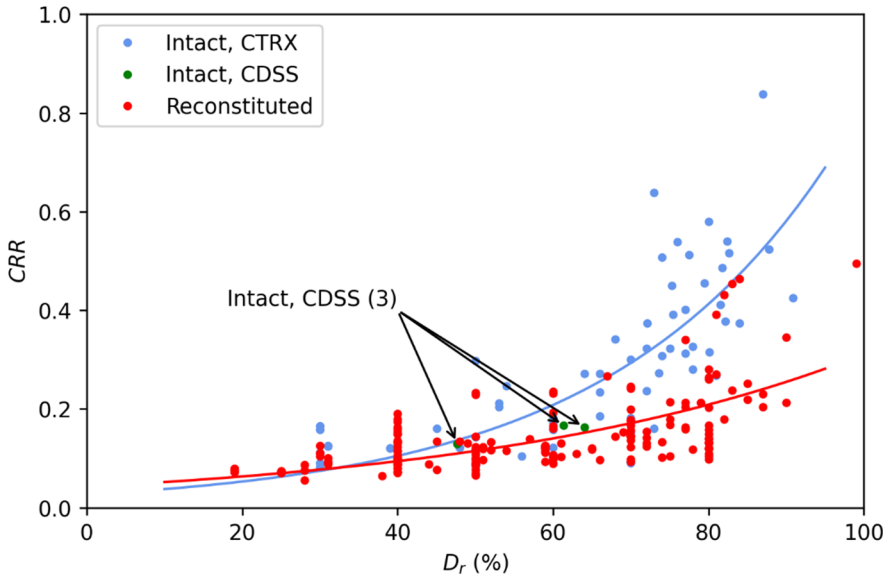

Figure 6-3 *CRR* vs D_r showing differences in intact and reconstituted datasets

Figures 6-4 to 6-6 partition the data to investigate various effects. Figure 6-4 shows that the *CRR* values from CDSS tests tend to be less sensitive to D_r than those from CTRX tests within the reconstituted data alone; this effect may be influenced by necking that often occurs in CTRX tests. Figures 6-5 and 6-6 illustrate the effects of different failure criteria (strain- vs. r_u-based). Figure 6-5 focuses on this comparison using CDSS tests, which show that *CRR* values from strain-based criteria are slightly higher than those from r_u-based criteria, but that the shapes of the *CRR* vs D_r curves for the two data sets generally match. Figure 6-6 makes the same comparison using *CRR* values from CTRX tests and shows that *CRR* values from strain-based criteria are much more sensitive to D_r than the *CRR* values from r_u-based criteria are. Granted, the number of *CRR* values from tests that use r_u-based criteria is limited compared to the number of *CRR* values from tests that use strain-based criteria, so this finding could be refined with more data. However, current trends indicate that the use of strain-based criteria can influence the shape of the *CRR* vs D_r curve more for CTRX tests than for CDSS tests. Thus, the difference between *CRR* values from intact specimens compared to *CRR* values from reconstituted specimens could be explained by the almost exclusive use of CTRX tests and strain-based criteria within the intact subset of the database, and there is no conclusive evidence to state whether intact specimens do indeed yield higher *CRR* values.

In general, we believe that triggering behavior in the field, (represented by the P[*T*|*S*] curve) is most consistent with CDSS stress paths, which are more representative of in situ loading conditions during seismic events. We also believe that r_u-based criteria are more closely related to the actual triggering of liquefaction than strain-based criteria, which are considered to be more of a consequence (e.g., manifestation) issue. However, we recognize that limiting our P[*T*|*S*] regression to this scenario alone would represent a small fraction of our current database and would not likely reflect our current uncertainty in the actual *CRR* curve for forward analysis (i.e., an unspecified soil that may not be represented in the current *CRR* database). Thus, we decided to use the entire dataset with the basic data filters discussed subsequently in Section 6.2.6 when regressing the P[*T*|*S*] curve to provide a realistic level of uncertainty based on currently available data.

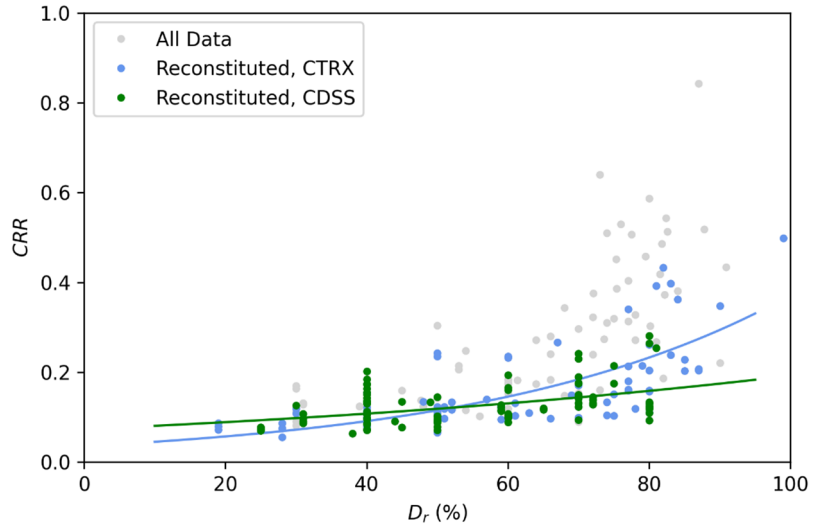

Figure 6-4 ***CRR*** **vs** ***D_r*** **showing differences in CTRX and CDSS tests within the laboratory results from reconstituted specimens**

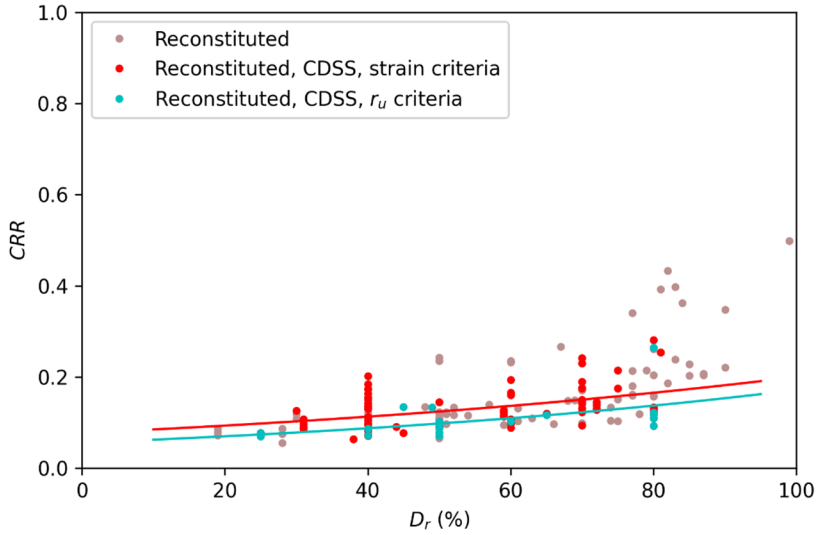

Figure 6-5 ***CRR*** **vs** ***D_r*** **showing differences in r_u- and strain-based liquefaction criteria within the laboratory results from CDSS tests performed on reconstituted specimens**

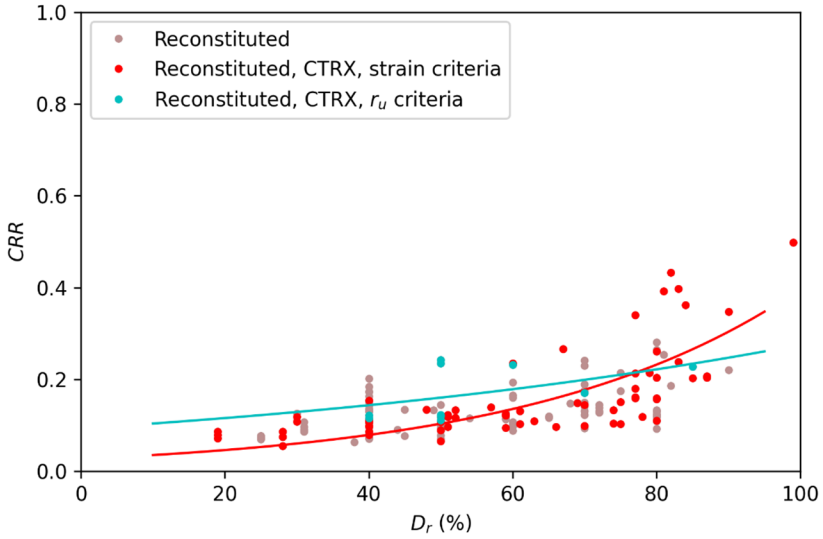

Figure 6-6 ***CRR* vs D_r showing differences in r_u- and strain-based liquefaction criteria within the laboratory results from CTRX tests performed on reconstituted specimen**

6.2.4 K_σ Model

The liquefaction behavior of a soil is influenced by its initial stress conditions because of the dependence of state on stress (Vaid et al., 2001). Laboratory tests have shown that the *CRR*, a normalized measure of a soil's cyclic resistance to liquefaction, decreases as the effective confining pressure (e.g., σ'_{v0}) increases (e.g., Seed et al., 1973). In addition, the presence of a non-zero initial static shear stress (τ_s) can either increase or decrease a soil's *CRR*, depending on the state of the soil and its contractive or dilative nature (Boulanger, 2003b). In cyclic stress-based liquefaction triggering evaluations (Seed and Idriss, 1971), the overburden stress correction factor (K_σ) is used to modify the *CRR* to account for σ'_{v0} differing from 1 atm, and the initial shear stress correction factor (K_α) is used to modify the *CRR* to account for τ_s not equal to zero (Seed, 1983).

There are two well-known approaches to developing models for K_σ and K_α: 1) constrain the relationship as part of regressing an empirical *CRR* model using a database of field case histories (e.g., Moss et al., 2006; Cetin et al., 2018); or 2) use laboratory data and soil mechanics concepts to develop a model (e.g., Boulanger, 2003a, 2003b; Bilge and Cetin, 2011). The challenge of the first approach is collecting case histories with a wide enough range of σ'_{v0} and τ_s to sufficiently constrain K_σ and K_α. Historically, this has been difficult to achieve. The use of surface manifestation as a criterion for triggering in the field has limited the case history database to cases with critical layers at depths generally less than 8 m and far less than the depths of interest in many important applications. In the second approach, the results of laboratory tests [e.g., CTRX, CDSS, or CTS] are used to develop relationships between cyclic stress ratio ($CSR = \tau_{cyc} / \sigma'_{v0}$ where τ_{cyc} is the applied cyclic loading stress) and the number of cycles to liquefaction (N) for a given soil under a set of conditions [e.g., same relative density (D_r), σ'_{v0}, and τ_s]. Typically, this is done first using a reference condition such as σ'_{v0} = 1 atm or τ_s = 0. Assuming a value of N associated with a given magnitude event (e.g., M_w7.5), *CRR* can be computed from the reference *CSR* versus N relationship. To compute K_σ or K_α, the same soil is tested using the same set of conditions but with a change in either σ'_{v0} or τ_s. The K_σ or K_α

correction factor is then defined as the ratio of the *CRR* of the second set of tests to the *CRR* of the reference condition tests.

To develop a comprehensive generic (i.e., not material-specific) model to account for the effects of σ'_{v0} and τ_s in liquefaction triggering evaluation procedures, the aggregated results of cyclic tests performed on many different soils over a wide range of states and stresses are required. There have been prior efforts to compile datasets of K_α values (e.g., Harder and Boulanger, 1997) and K_σ values (Montgomery et al., 2012, 2014) and to develop ergodic models (Boulanger, 2003a, 2003b; Bilge and Cetin, 2011). However, these datasets and models are still limited in scope (e.g., for clean sands only) and there have been a significant number of laboratory studies that greatly expanded the range and quantity of soil state and stress parameters (Ulmer et al., 2023a) since the time when the earlier compiled datasets were published.

As discussed in Section 6.2.1, the SMT compiled a database of results from laboratory tests that could elucidate the effects of initial overburden (σ'_{v0}) or static shear stresses (τ_s) over the broad range of conditions encountered in practice. Where possible, we computed K_σ from *CSR* vs *N* data as discussed in Section 6.2.2 or from reported *CRR* data. However, in some instances, K_σ values were directly reported without *CSR* vs *N* or *CRR* data. Our approach yielded hundreds of K_σ and K_α factors for a broad range of soils. A summary plot of the K_σ values is shown in Figure 6-7. Figures 6-8 and 6-9 compare the K_σ values from the laboratory tests with existing relationships (e.g., Idriss and Boulanger, 2008; Bilge and Cetin, 2011) and demonstrates that there are potential misfits of these existing models to the data when considering a broader range of D_r (D_r >70% and D_r <30%) and *FC* (*FC* >10%). The SMT concluded that it is possible to regress updated K_σ and K_α relationships that would better fit the data over a wider range of D_r and *FC*.

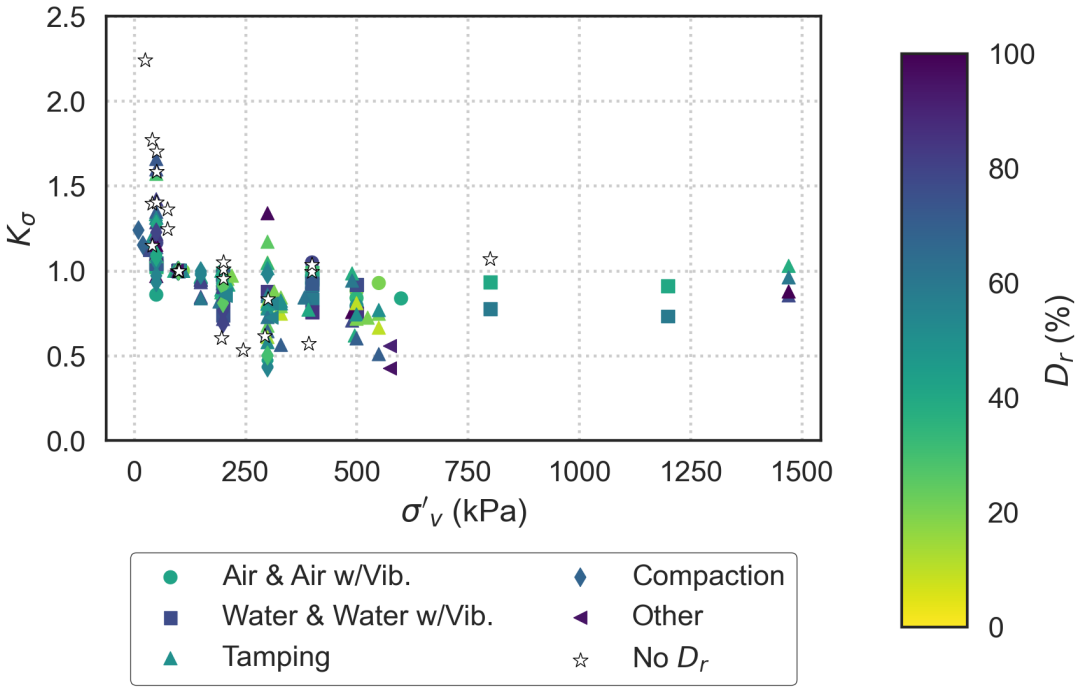

Figure 6-7 **K_σ vs σ'_{v0} from the Task 5 laboratory results dataset. Symbols for different preparation methods and colors based on D_r.**

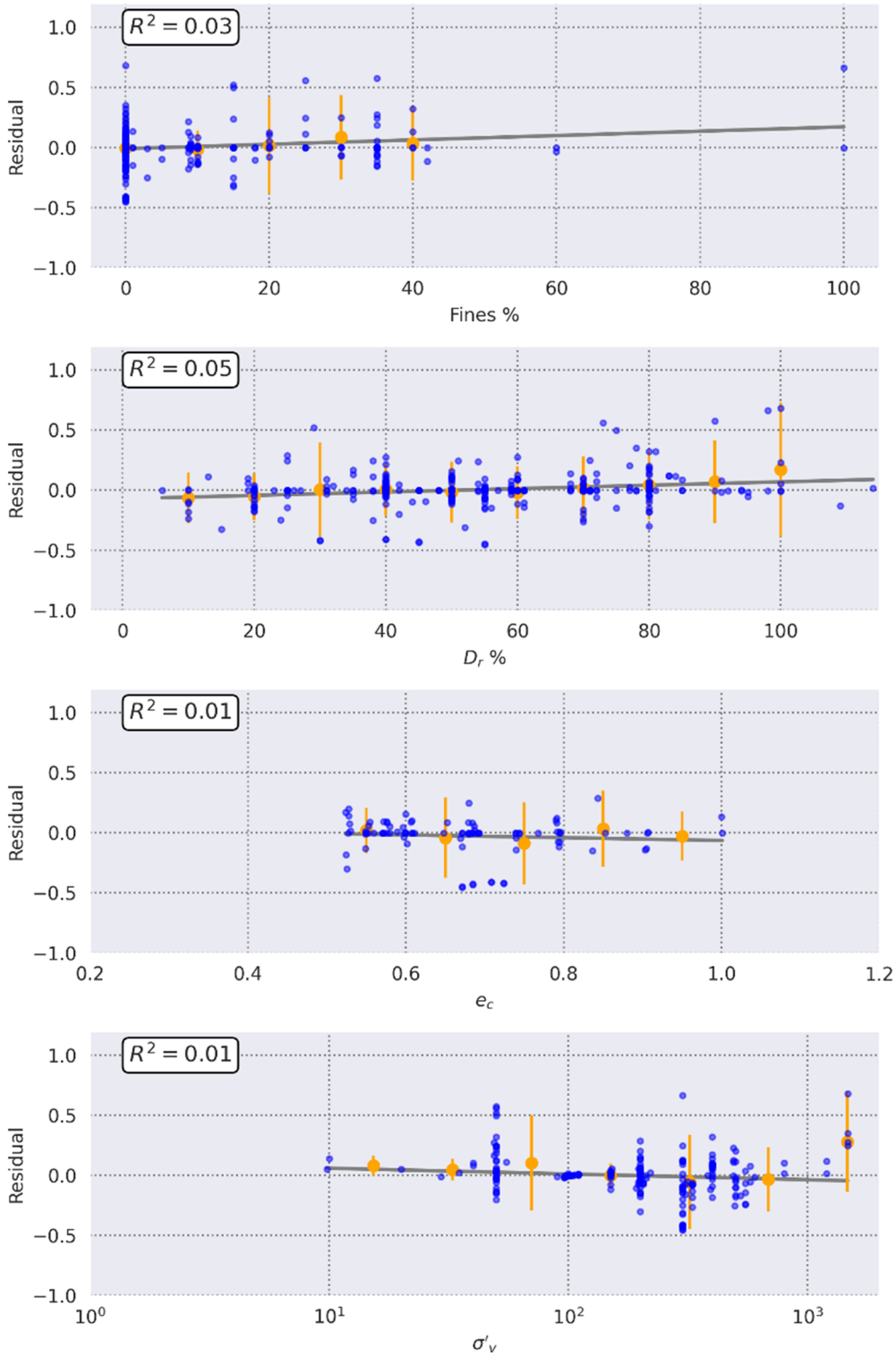

Figure 6-8 **Residuals of K_σ vs *FC*, D_r, void ratio post-consolidation (e_c), and σ'_{v0} using the Idriss and Boulanger (2008) K_σ model**

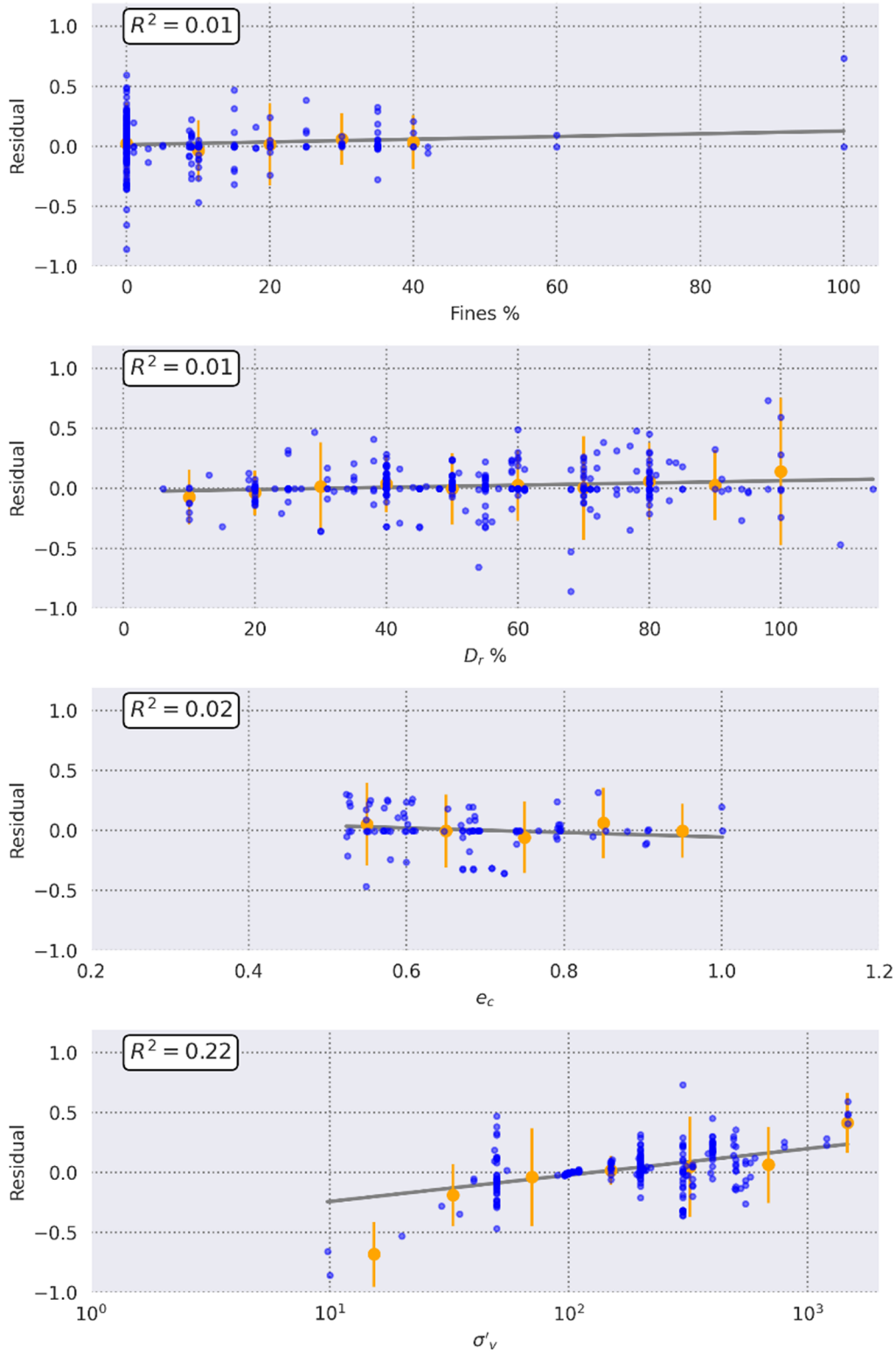

Figure 6-9 **Residuals of K_σ vs *FC*, D_r, void ratio post-consolidation (e_c), and σ'_{v0} using the Bilge and Cetin (2011) K_σ model**

As part of an NGL supporting study (Section 2.2), the SMT worked with Brian Carlton to regress updated K_σ and K_α relationships using the Task 5 dataset (Ulmer et al., 2022a; Ulmer et al., 2023a; Carlton et al., 2023). Given that the majority of the case histories in the NGL database are on relatively level ground (~80% with less than 1 degree ground slope) and free of significant initial shear stress, the SMT agreed that updating the K_σ relationship was a higher priority than updating K_α. Using 230 K_σ values that span a wide range of soil types, D_r, initial stresses, fines content, and specimen preparation methods, the SMT developed two options for modeling K_σ as functions of either (i) σ'_{v0} or (ii) σ'_{v0} and *FC*. Preliminary results showed a relatively weak dependence of K_σ on D_r, which is contrary to the assumptions used by some existing K_σ models that depend on D_r (e.g., Boulanger, 2003b) but agreed with other models that do not include D_r (e.g., Cetin et al., 2018). K_σ was shown to be sensitive to *FC,* which warranted its inclusion as an independent variable.

The SMT adopted the following relationship based on σ'_{v0} and *FC*:

$$K_\sigma = \begin{cases} \left(\frac{\sigma'_{v0}}{p_a}\right)^{a_1} & for\ \sigma'_{v0} < p_a \\ \left(\frac{\sigma'_{v0}}{p_a}\right)^{a_2} & for\ \sigma'_{v0} \geq p_a \end{cases} \quad \text{6-3}$$

$$a_1 = \frac{-0.49}{1 + \exp[0.121(11.67 - FC)]}$$

$$a_2 = \begin{cases} -3.8 \times 10^{-6}(FC)^3 + 4.88 \times 10^{-4}(FC)^2 - 1.358 \times 10^{-2}(FC) - 0.13 \; for\ FC < 70 \\ -0.148 \; for\ FC \geq 70 \end{cases}$$

where *FC* is in percent and p_a is one standard atmospheric pressure in the same units as σ'_{v0}. This K_σ relationship assumes a different exponent (a_1 or a_2) depending on whether σ'_{v0} is less than or greater than 1 atm (100 kPa). This relationship was adopted to adjust *CSR* to $CSR_{M7.5,1atm}$ (see Section 5.4.3) and to adjust *CRR* for laboratory tests performed at levels of σ'_{v0} other than 1 atm (discussed subsequently in Section 6.2.6).

In existing K_σ relationships, there is typically an upper limit imposed on K_σ to avoid very high values at low σ'_{v0} to avoid being unconservative in a forward analysis. For example, Boulanger and Idriss (2014, 2016) recommend an upper limit of 1.1. Based on the laboratory data collected for our study, there are examples of soils with K_σ greater than 1.1, particularly for soils with high *FC*. In our effort to develop an unbiased (i.e., neither conservative or unconservative) model, we chose to limit our model to the range of σ'_{v0} represented in our laboratory data (greater than about 20 kPa). Thus, the upper limit of K_σ in Eq. (6-3) is associated with σ'_{v0} = 20 kPa (0.2 atm), which is roughly 1.17 for *FC* = 0% up to 2.2 for *FC* > 50%. This is illustrated in Figure 6-10. Reasons for the increase in K_σ at low σ'_{v0} with increasing *FC* is not yet clear, but could be investigated in follow-on studies (e.g., over consolidation effects).

Figure 6-11 shows a comparison between the SMT's selected K_σ model and other published relationships (Idriss & Boulanger, 2008; Bilge & Cetin, 2011; Cetin et al., 2018). The SMT's K_σ relationships for a range of *FC* nearly captures the range of K_σ values from these published relationships.

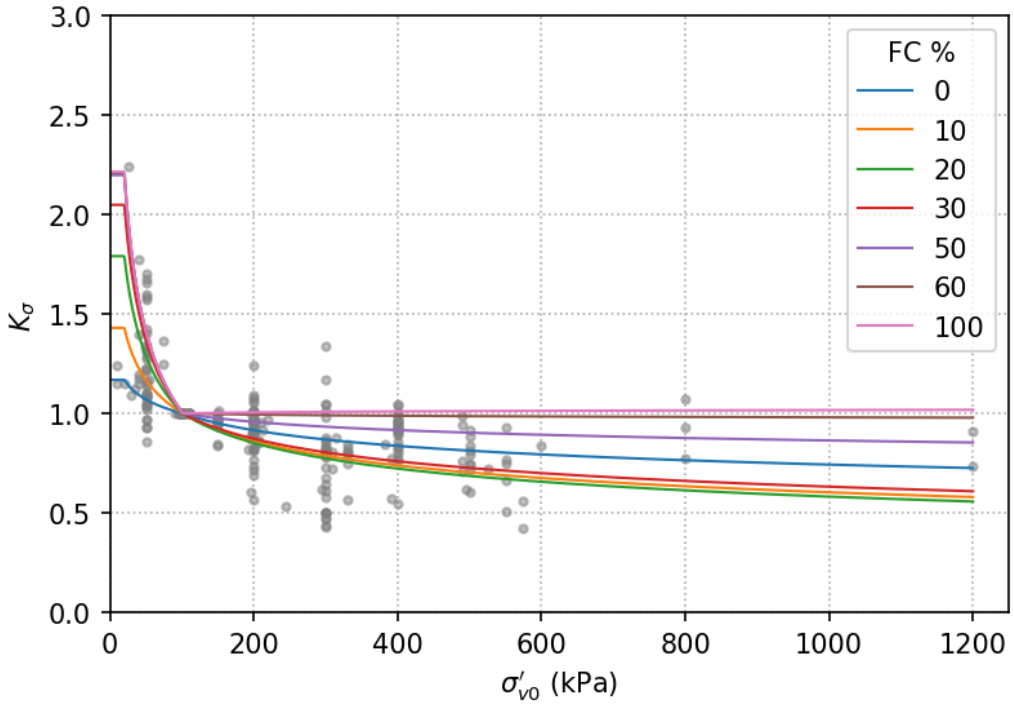

Figure 6-10 ***K_σ* vs *σ'_{v0}* from the Task 5 laboratory results dataset with the proposed SMT model based on *σ'_{v0}* and *FC*. Upper limits of *K_σ* represented by σ'_{v0} = 20 kPa (0.2 atm).**

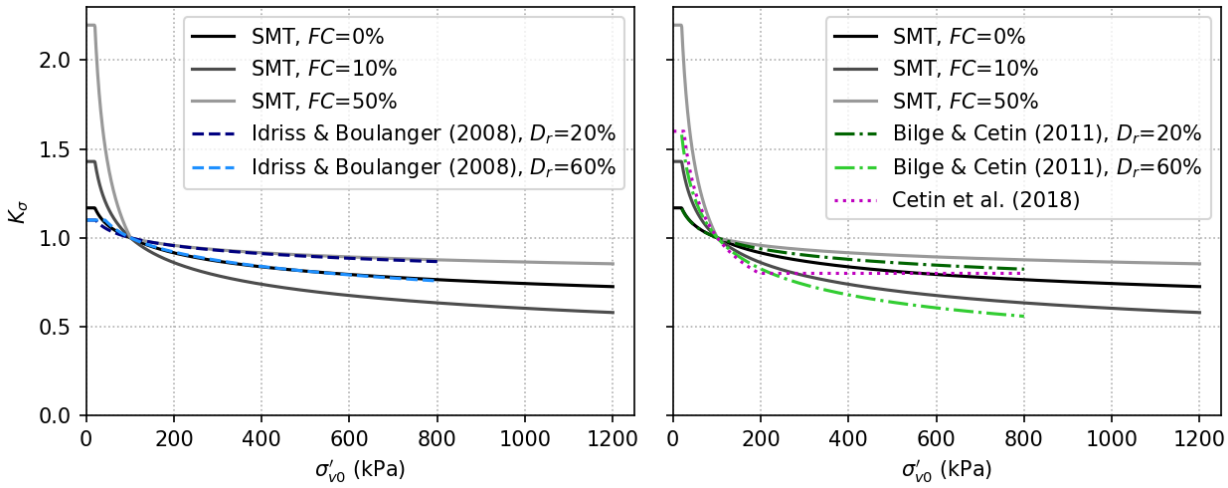

Figure 6-11 **Comparison of several *K_σ* models based on either *FC* and *σ'_{v0}* (SMT model), *D_r* and *σ'_{v0}* (Idriss & Boulanger, 2008; Bilge & Cetin, 2011), or *σ'_{v0}* alone (Cetin et al., 2018)**

6.2.5 Functional Form of *CRR* vs *D_r*

To establish a reasonable functional form for *CRR* vs. D_R, we first developed *CRR* curves using a relatively complete dataset for a single soil from tests performed on reconstituted specimens over wide ranges of D_r and σ'_{v0} values. We found such a dataset published by Vaid and

Sivathayalan who performed constant-volume CV-CDSS tests on water-pluviated specimens of FRS (Sivathayalan 1994; Vaid and Sivathayalan, 1996). FRS is a medium-grained sand predominantly composed of quartz with some unstable volcanic rock fragments. Prior to testing, the fine particles were removed so that the FRS specimens tested were clean sands (i.e., *FC* less than 5%). Vaid and Sivathayalan prepared specimens using air pluviation and investigated the effects of varying σ'_{v0}. In a parallel study, Vaid and Thomas tested the same sand under CTRX conditions (Vaid and Thomas, 1995; Vaid and Thomas 1994; Thomas, 1992). For CV-CDSS tests, they used γ_{SA} = 3.75% to define liquefaction and for CTRX tests they used ε_{SA} = 2.5%.

Using the FRS data, we computed *CRR* at multiple values of D_r. The resulting *CRR* vs D_r curves are shown in Figure 6-12. The curves were established by fitting the following equation to the data:

$$\ln\left(CRR_{field}\right) = c_1 + c_2 D_r + c_3 {D_r}^3 \qquad 6\text{-}4$$

where c_1, c_2 and c_3 are regressed coefficients and D_r is in percent. Coefficients of Eq. (6-4) for an FRS combined curve (CTRX & CV-CDSS) are provided in Table 6-1.

Also shown in Figure 6-12 is the Boulanger and Idriss (2016) (denoted BI16) deterministic triggering curve (shown in gray). The curve for $P_L \approx 15\%$ is used for this purpose, with q_{c1Ncs} converted to D_r for the plot using their relationship. At values of D_r < 40%, the laboratory CV-CDSS curve generally aligns with the BI16 curve. However, both the CV-CDSS and CTRX curves are substantially lower than the BI16 curve at higher D_r. The BI16 curve, being based solely on case histories of surficial manifestation, reflects both triggering and manifestation effects whereas the laboratory data reflects triggering alone. Although there are other field-related factors that could be influencing this difference (e.g., aging, previous seismic history, over consolidation), these results suggest the influence of manifestation is especially impactful at higher penetration resistances, and thus the BI16 curve is not expected to perfectly match the laboratory-based curve, which represents triggering alone.

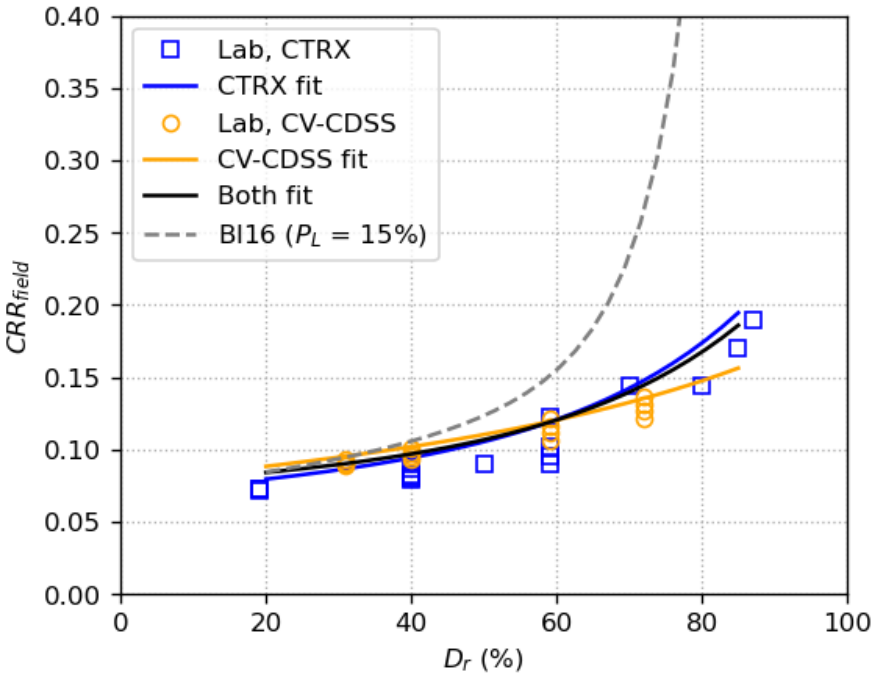

Figure 6-12 ***CRR*** **curve regressed using proposed functional form and** ***CRR*** **values computed from CV-CDSS and CTRX tests on water-pluviated specimens of Fraser River sand. CV-CDSS data are from Sivathayalan (1994) and Vaid and Sivathayalan (1996), whereas CTRX data are from Vaid and Thomas (1995), Vaid and Thomas (1994), and Thomas (1992)**

Table 6-1 Regressed coefficients for *CRR* curves using Eq. (6-4)

Scenario	c_1	c_2	c_3
FRS CTRX & CV-CDSS	-2.578	4.881e-3	7.830e-7
CRR based on Intact and Reconstituted Specimens	-2.473	3.335e-3	1.509e-6

6.2.6 Preliminary ***CRR*** vs D_r Model

Given the functional form of *CRR* vs D_r as established based on an individual soil shown previously Eq. (6-4), we seek to establish a generic (multi-material) probabilistic *CRR* vs D_r model. A key modeling decision for development of the triggering prior was whether to produce separate models for CTX and CDSS conditions. Had this been done, as suggested by the results shown in Figure 6-5 and Figure 6-6, the CDSS model would produce relatively low resistances without appreciable increases at large D_R. This feature was considered unrealistic. Thus, to develop the prior laboratory-based model, we broadened our analysis to include *CRR* values from both CTRX and CDSS tests on both intact and reconstituted specimens from multiple references as outlined in Section 6.2.1.

The database of *CRR* values from the literature represents a range of reconstitution methods, initial loading conditions, liquefaction criteria, and other testing parameters as determined by the researchers for each individual study. To focus our prior model on the data that are most

relevant to this project, we screened the total dataset of *CRR* values using data that met the following criteria:

- $\alpha \leq 0.02$ or anisotropic consolidation ratio (K_c) = 0.9-1.1
- Reasonable liquefaction criteria assumed to be associated with triggering based on precedent in the literature:
  - $r_u \geq 0.95$
  - CTRX: ε_{DA} = 4 - 6%, ε_{SA} = 2 - 3%
  - CDSS: γ_{DA} = 7 - 8%, γ_{SA} = 3.5 - 4%
- $FC \leq 30\%$
- Specimen reconstitution methods not involving tamping or compaction.

We then regressed a *CRR* vs D_r relationship using a cubic polynomial [Eq. (6-4)] and the screened database of *CRR* values, with the results shown in Figure 6-13 and coefficients provided in the previously introduced Table 6-1 for comparison with FRS results. Also shown in Figure 6-13 are the binned means of the data with 95% confidence intervals to confirm that the cubic polynomial adequately captures the data. The regressed *CRR* vs D_r relationship is accompanied by dotted lines representing the mean +/- $\sigma_{\ln(CRR)}$ where $\sigma_{\ln(CRR)}$ is the standard deviation of the residuals of ln(*CRR*). Figure 6-14 shows the binned means of the residuals and the $\sigma_{\ln(CRR)}$ against D_r. This figure indicates that the residuals are not sensitive to D_r. However, the uncertainty (i.e., $\sigma_{\ln(CRR)}$) does appear to increase as D_r increases.

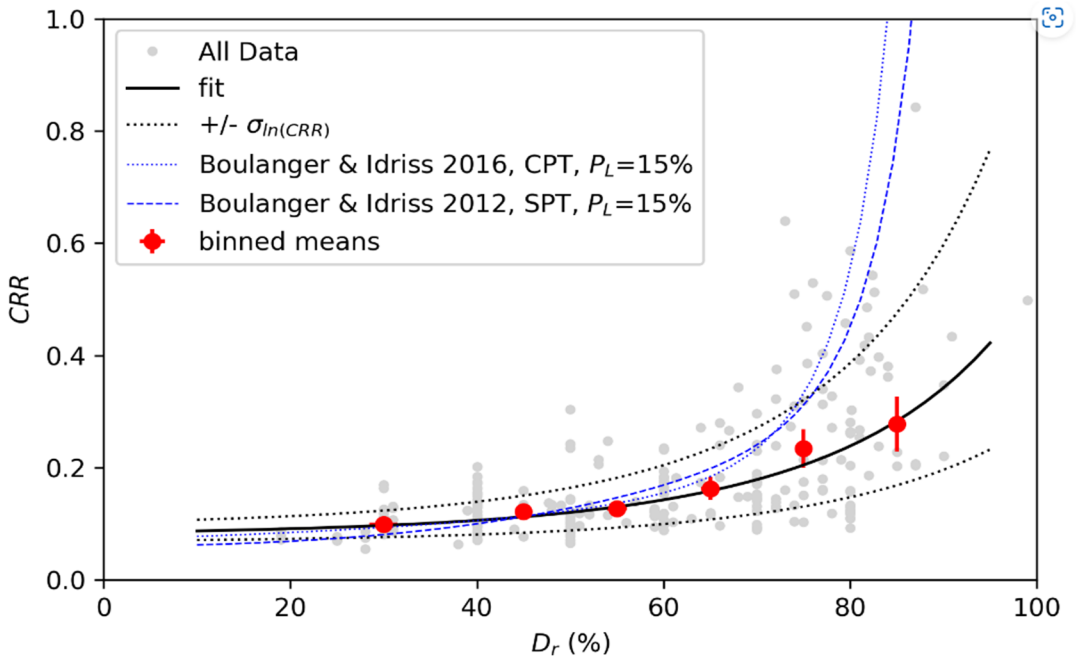

Figure 6-13 Summary of CRR_{field} vs D_r results from laboratory tests on intact and reconstituted specimens (using basic filters outlined in Section 6.2.6) and the median *CRR* curve proposed in this report [i.e., Eq. (6-4) with coefficients from row 2 of Table 6-1] compared to BI12 and BI16 CRR curves

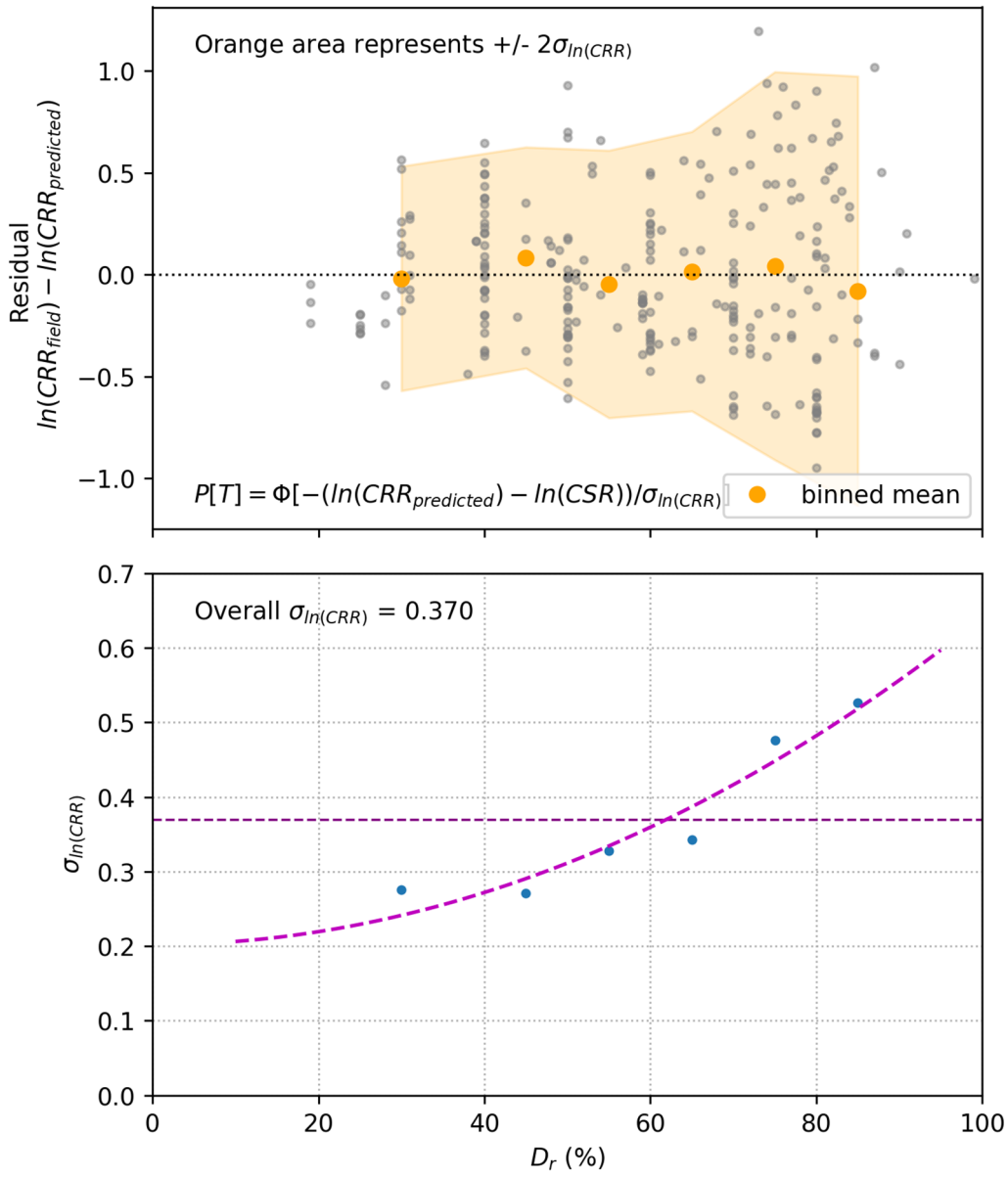

Figure 6-14 (a) model residuals computed as ln(CRR_{field})–ln($CRR_{predicted}$) vs D_r with binned mean values shown in orange; (b) standard deviation of model residuals, $\sigma_{ln(CRR)}$, vs D_r

After developing this initial *CRR* vs D_r relationship, we identified the need to account for a non-uniform distribution of D_r values in our dataset that effects the results of model fitting. Figure 6-15 shows the distribution of D_r values in bins of [0-40%], (40-60%], (60-80%], and (80-100%] {note that a square bracket is inclusive such that (40-60%] is equivalent to 40% < D_r <= 60%}. The sampling bias reflects more laboratory tests performed between 40-80% D_r compared to D_r<40% and D_r>80%. In order to reduce the sampling bias, each data point is weighted by the inverse of the number of points within its D_r bin (and normalized by the mean weight). Figure 6-16 replots the dataset with coloration based on assigned weights.

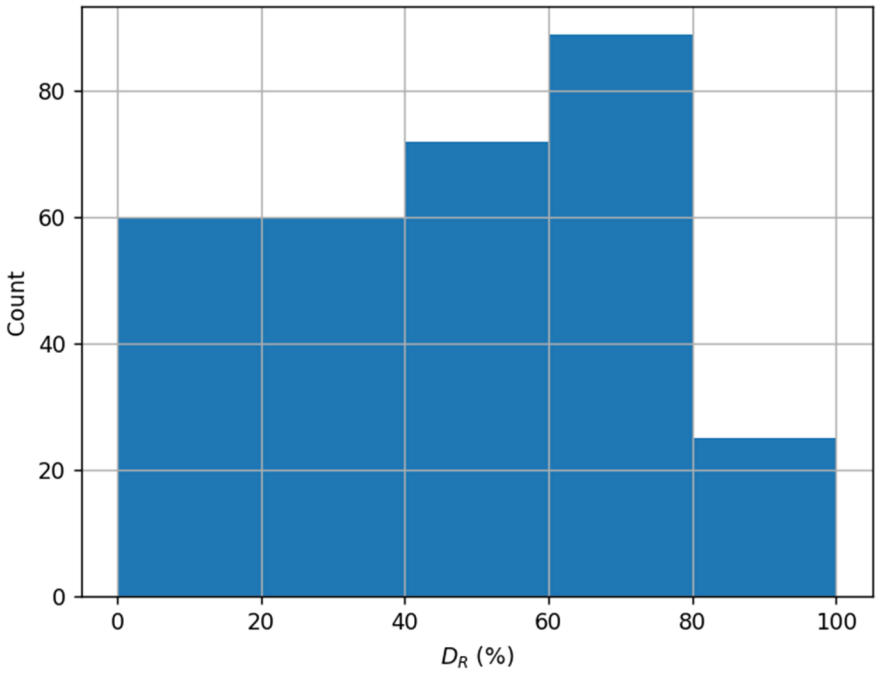

Figure 6-15 **Histogram of the triggering dataset D_r values with bin edges defined at [0,40], (40,60], (60,80], and (80,100]. The proportion of counts within each bin was applied as weight for regressing the triggering prior.**

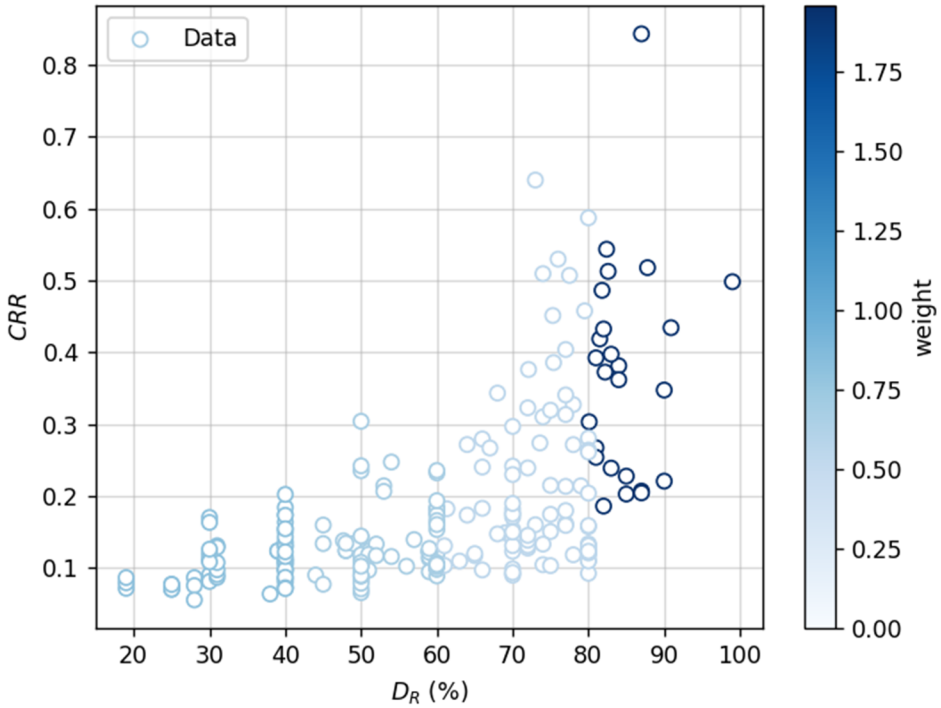

Figure 6-16 **Dataset used for determining triggering prior. Datapoints are weighted by the inverse proportion of points within histogram bins presented in Figure 6-16.**

We then updated the initial *CRR* vs D_r model to address two issues: (i) account for the weights shown in Figure 6-15 and (ii) to stabilize the regression using a simpler linear model in transformed parameter spaces in which the data distribution is approximately normal and homoscedastic, i.e., with a consistent level of dispersion across the range of the independent variable. This model is referred to as a linear P[*T*|*S*] model subsequently. The transformation of the dataset was accomplished by applying a Box-Cox transformation (Box & Cox, 1964; Eq. 6-5) to both the D_r and *CRR* values, as follows,

$$\hat{x} = \frac{x^{\lambda} - 1}{\lambda} \qquad 6\text{-}5$$

where λ is taken as the value that transforms the dataset as close as possible to a normal distribution. The λ values for D_r and *CRR* (λ_{D_r} and λ_{CRR}, respectively) were determined to be 1.202 and -0.657, respectively, calculated using the SciPy Python package (Virtanen et al. 2020). The dataset in the transformed $\widehat{CRR}$-$\widehat{D_r}$ space is presented in Figure 6-17.

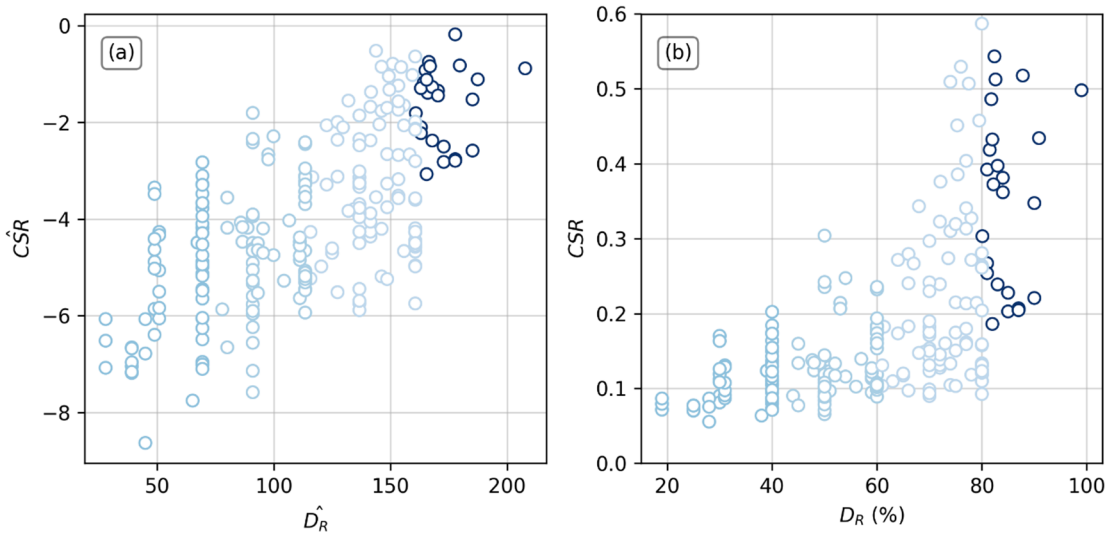

Figure 6-17 Dataset for triggering model development in (a) Box-Cox transformed ($\widehat{CRR}$-$\widehat{D_R}$) space and (b) *CSR*-D_R space. The data points are colored by the weights in Figure 6-16.

Following this transformation, the dataset was fit using a linear model:

$$\widehat{CRR} = \zeta_0 + \zeta_1 * \widehat{D_R} + \varepsilon * \sigma_\zeta \qquad 6\text{-}6$$

where ζ_0, ζ_1, and σ_ζ are model coefficients to be regressed as described in the next section and ε is the standard normal variate (zero mean and unit standard deviation). Alternatively, the equation can be rewritten in the untransformed space as:

$$CRR = \left(\frac{D_r^{\lambda_{Dr}} \lambda_{CRR} \zeta_1}{\lambda_{Dr}} + \lambda_{CRR} \sigma_\zeta \varepsilon + \lambda_{CRR} \zeta_0 - \frac{\lambda_{CRR} \zeta_1}{\lambda_{Dr}} + 1 \right)^{\frac{1}{\lambda_{CRR}}} \quad 6\text{-}7$$

6.2.7 P[T|S] Model Prior

We performed Bayesian inference using the PyMC Python package (Wiecki et al. 2023) to determine prior distributions of the coefficients in Eq. (6-6). Bayesian inference was used instead of a typical least squares regression because of the advantages gained in determining distribution of the coefficients so that uncertainty can be quantified for later updates to the model in the form of posterior coefficient distributions (Section 6.3.2). An "uninformed" prior distribution was adopted for each coefficient from Eq. (6-6) using a normal distribution with mean of zero and standard deviation of ten. The weighted dataset (Figure 6-16) was used in the inference. Four Markov chains (Gagniuc 2017; Markov 2006) with 1000 samples drawn from each chain and the resulting distribution of parameters and drawn samples are presented in Figure 6-18. Note that each distribution seems homogeneous and stationary (there are no large drifts or other odd patterns) indicating a stable regression.

The posterior distributions of the triggering model coefficients reflect uncertainty in how well the model represents the laboratory data. Additional uncertainty that is not reflected in the coefficient uncertainty is caused by (i) sample disturbance that creates uncertainty regarding applicability of laboratory data to field conditions and (ii) uncertainty in the correlation between q_{c1Ncs} and D_r. For these reasons, we decided to increase the standard deviation of each model coefficient in the posterior laboratory-based triggering model by a factor of 4, and to use the results of this adjusted model as the prior triggering model in developing the manifestation model, as described later. To account for correlations between the three coefficients, the covariances were computed (Table 6-3). The covariance matrix was used to create multivariate normal distribution priors for updating the triggering model as described in Section 6.3. The correlation matrix (a transformation of the covariance matrix) is presented in Table 6-4 to present the correlation coefficients between the three $PF_{T|S}$ coefficients; note there is a strong negative correlation between ζ_0 and ζ_1 and weak correlations between both the slope and intercept to σ_ζ.

The regressed model (shown in Figure 6-19) is linear and the error term, defined by σ_ζ, is normally distributed within Box-Cox space ($\widehat{CSR}$). The probability density for the regressed model, shown in Figure 6-20, is a normal distribution in Box-Cox space, but skewed in *CSR* space. The skewed distribution is similar in shape to a log-normal distribution; however, it is not identical because the Box-Cox transformation is not logarithmic. Instead, it can be called a "Box-Cox normal" distribution.

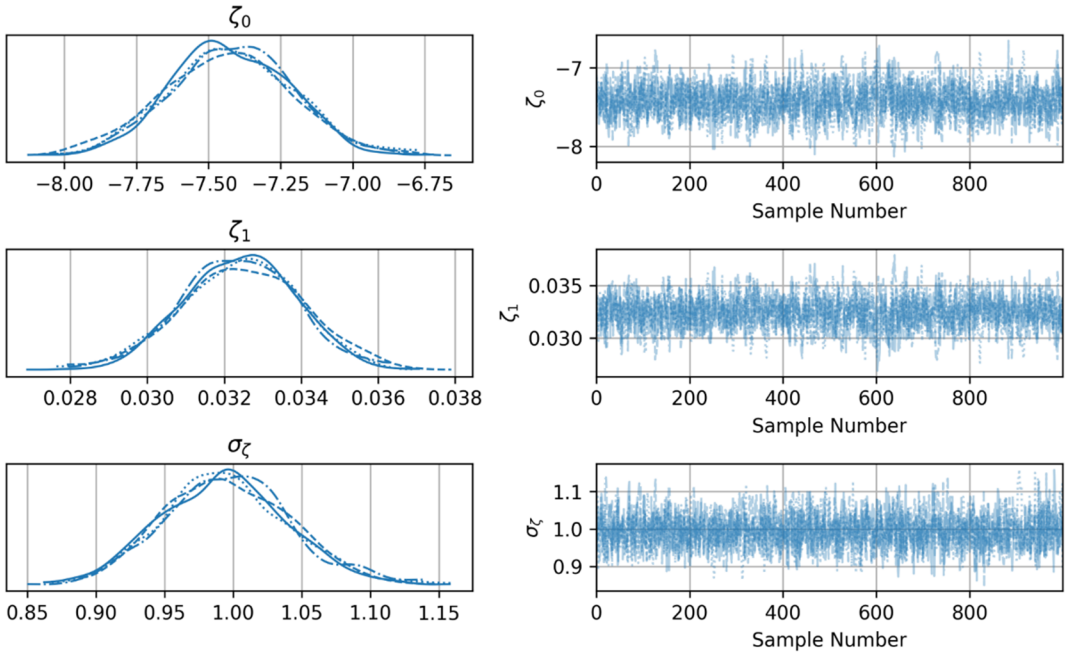

Figure 6-18 **Distribution of triggering model coefficients (left column) and sampling draws for each coefficient (right column). The four distributions with different line styles shown in the left column are the four Markov chains that are sampled.**

Table 6-2 **Means and standard deviations for the coefficients in Eq. 6-6 taken from Bayesian inference**

Variable	Value
μ_{ζ_0}	-7.43
σ_{ζ_0}	0.196
μ_{ζ_1}	0.0325
σ_{ζ_1}	0.00141
μ_{σ_ζ}	0.994
σ_{σ_ζ}	0.0459

Table 6-3 **Covariance matrix of the three $PF_{T|S}$ coefficients after Bayesian inference sampling. Note the diagonals are squared standard deviations from Table 6-2.**

	ζ_0	ζ_1	σ_ζ
ζ_0	3.844e-02	-2.597e-04	-6.792e-04
ζ_1	-2.597e-04	2.007e-06	5.106e-06
σ_ζ	-6.792e-04	5.106e-06	2.102e-03

Table 6-4 Covariance matrix of the three $PF_{\eta S}$ coefficients in the after Bayesian inference sampling

	ζ_0	ζ_1	σ_ζ
ζ_0	1	-0.935	-0.0755
ζ_1	-0.935	1	0.0786
σ_ζ	-0.0755	0.0786	1

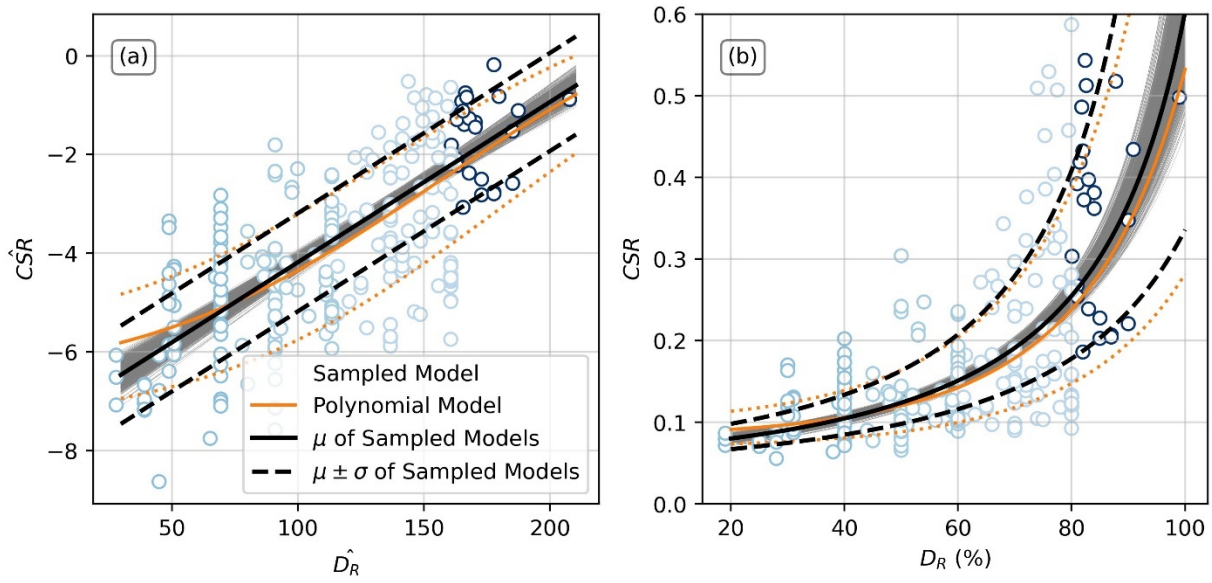

Figure 6-19 Triggering model fit shown in (a) Box-Cox transformed space and (b) untransformed parameter space. Samples of the mean model are shown as light gray lines and the recommended mean and mean plus or minus one standard deviation are plotted as solid and dashed black lines, respectively. Orange line represents preliminary polynomial fit (Eq. 6-4).

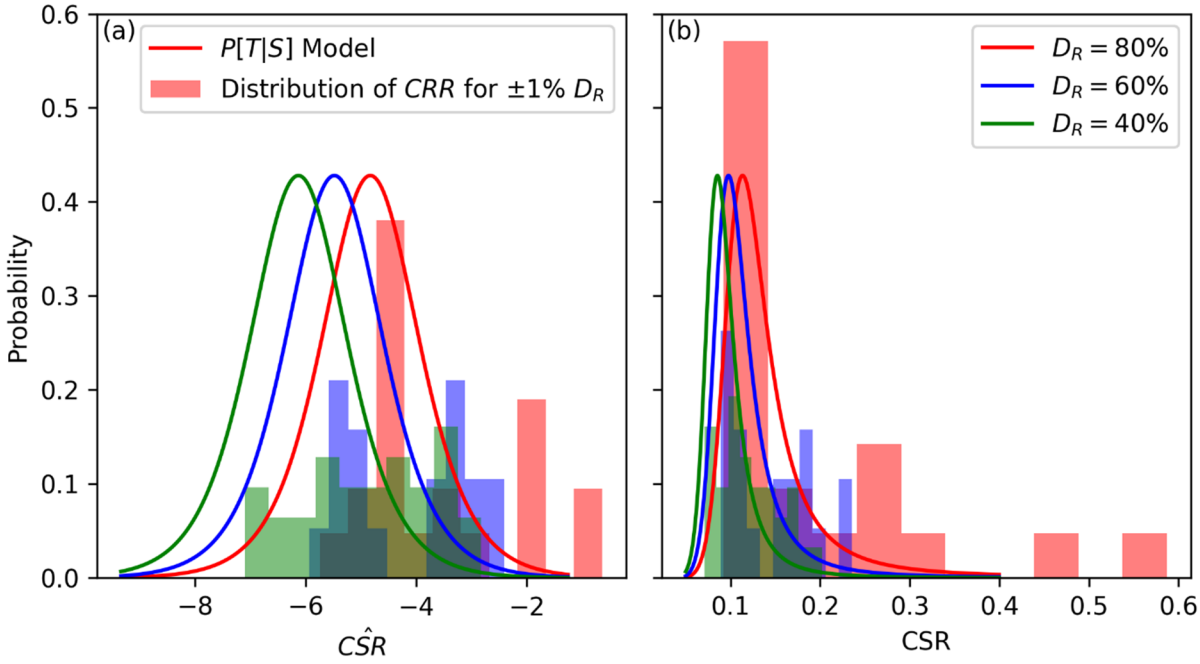

Figure 6-20 Probability density of the regressed triggering model for D_R = 80, 60, and 40% and histograms of laboratory *CRR* data within $\pm$ 1 of the target D_R. Plotted in (a) Box-Cox transformed space and (b) CSR space. The distributions in CSR space can be described as "Box-Cox normal".

6.2.8 Magnitude Scaling Factor

As discussed in Section 2.1.2, liquefaction triggering depends not only on the *CSR* but also on the number of loading cycles or duration of shaking. To account for the influence of the number of loading cycles on cyclic strength, *CSR* is typically adjusted using a *MSF* to compute an equivalent *CSR* for a reference **M**7.5 using Eq. (2-3). Historically, *MSF* has been derived from cyclic laboratory test results as:

$$MSF = \left(\frac{N_{eq,Mw}}{N_{eq,Mw7.5}}\right)^{-b} \qquad 6\text{-}8$$

where $N_{eq,Mw}$ and $N_{eq,Mw7.5}$ are the equivalent number of cycles associated with **M** and **M**7.5, respectively, and *b* (herein called the b-value) represents the relationship between the number of cycles to liquefaction and *CSR* in log-log space. This MSF relationship comes from the general assumption that the log(*CSR*) vs log(*N*) relationship is linear. Estimates of $N_{eq,Mw}$ and $N_{eq,Mw7.5}$ can be obtained from published correlations (e.g., Lasley et al., 2017). The b-value is often estimated from laboratory data by using a power law fit of the *CSR* versus *N* relationship as discussed in Section 6.2.2. A b-value can be estimated for a given soil using laboratory tests performed on specimens of that soil but would only be applicable for that soil. An alternative is to develop a generic b-value that is reasonably representative of many soils, thus the resulting *MSF* could be generally applied to soils that for various reasons cannot, or have not, been sampled and tested in the laboratory. This is a necessary approximation in our case history processing as discussed in Section 5.4.3.

However, there is no current consensus on the appropriate b-value to use for establishing the *MSF* relationship. Historically, b-values have been interpreted as being functions of **M** alone (i.e., independent of environmental factors such as soil state). Some studies recommend that the b-value increases with increasing D_r (e.g., Boulanger and Idriss, 2014, 2016), which results in a density-dependent *MSF* relationship. Subsequent studies have shown that the b-value vs D_r relationship is more ambiguous, and is potentially unnecessary (e.g., Ulmer et al., 2018; 2022b). Table 6-5 summarizes the recommended b-values from several published studies, which range from 0.178 to 0.417. We used the compiled datasets as outlined in Section 6.2.1 to select a recommended b-value for computing *MSF* and to highlight some trends in b-value vs. D_r, *FC*, and σ'_{v0}.

Table 6-5 Recommended b-values for computing MSF

Reference	Recommended b-value	Alternative b-values
Liu et al. (2001)	0.37	0.5
Idriss & Boulanger (2008)	0.35	N/A
Kishida and Tsai (2014)	0.35 (adopted from I&B08)	0.1-0.4
Boulanger & Idriss (2014)	0.178 (D_r = 10%) 0.200 (D_r = 44%) 0.350 (D_r = 76.65%) 0.417 (D_r = 90%)	N/A
Green et al. (2019)	0.34	N/A
Ulmer et al. (2022)	0.28	0.20
SMT	0.20 (σ_b =0.069)	N/A

Figures 6-21, 6-22 and 6-23 plot the trends of b-values with D_r, σ'_{v0}, and *FC*, respectively. In general, there is no strong relationship between the b-values and D_r, *FC*, and σ'_{v0}. However, the scatter in b-values is significant, particularly when no constraints are placed on the values of initial static shear stress ratio (i.e., $\alpha = \tau_s/\sigma'_{v0}$) and uncertainties in the b-value estimates (i.e., the standard error of the b-value, ε_b) are not used for screening purposes. Figure 6-24 shows the relationship between b-value and D_r after restricting α to be approximately 0 and ε_b to be less than 0.15. In general, the data supports an assumption that a b-value of approximately 0.20, with a standard deviation σ_b of 0.069, is representative of many soil types, regardless of D_r, *FC*, and σ'_{v0}. This value is also aligned with one of the recommended b-values from Ulmer et al. (2022b) based on an interpretation of constant dissipated energy using published modulus reduction and damping relationships. Therefore, the SMT elected to use a constant b-value of 0.20 combined with the Lasley et al. (2017) N_{eq} relationship to compute *MSF* as shown below (see also Section 5.4.3).

$$\ln(N_{eq}) = 0.4605 - 0.4082\ln(a_{max}) + 0.2332M_w \qquad 6\text{-}9$$

$$MSF = (14/N_{eq})^{0.2} \quad \text{6-10}$$

To investigate whether the lack of D_r-dependence and lack of σ'_{v0}-dependence also applies to individual soils, we looked for these dependencies using the FRS data as shown in Figure 6-25. Note that the b-value for FRS is generally insensitive to both D_r and σ'_{v0}, with the exception of the D_r = 60% group which has a slightly different b-value for the highest σ'_{v0} tested within that D_r group. Note also that the b-values from CTRX tests (0.09-0.12) are different than those from CDSS tests (0.20-0.22). Such comparisons are also discussed for other soil types by Ulmer et al. (2018), showing that D_r-dependencies exist for some soils, but not all. In some cases, the apparent D_r-dependency in a given soil disappears after ensuring that the log(*CSR*) vs log(*N*) relationship is indeed linear, as is generally assumed. Given this ambiguity, more complex, material-specific models for b-values could be considered in a forward analysis.

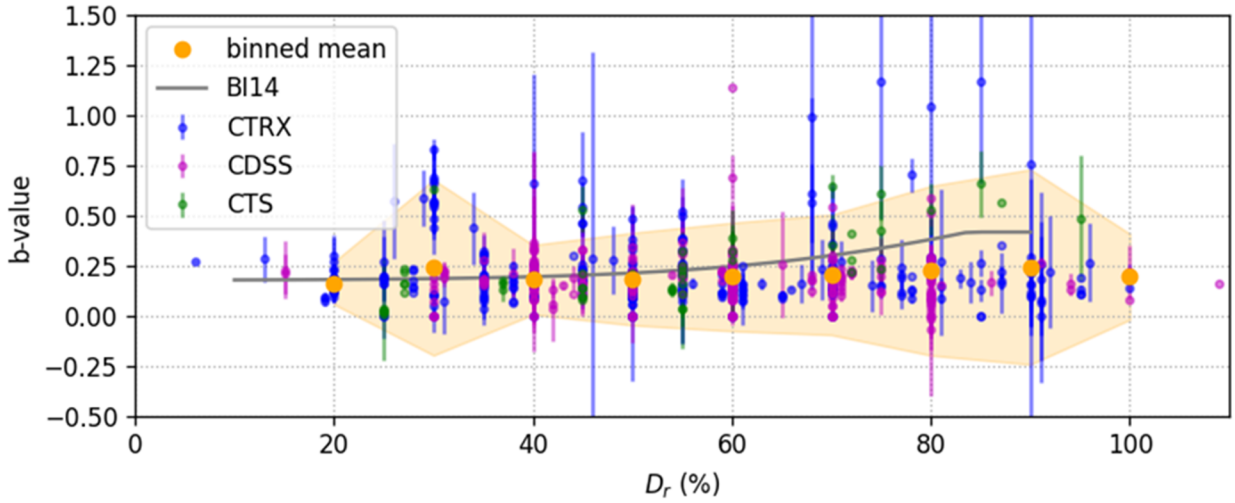

Figure 6-21 Computed b-values vs. D_r using the SMT's compiled dataset of laboratory data. Orange shaded area represents +/- the standard deviation of the b-values for each D_r bin. The gray line represents the implied b-values associated with the BI14 MSF relationship.

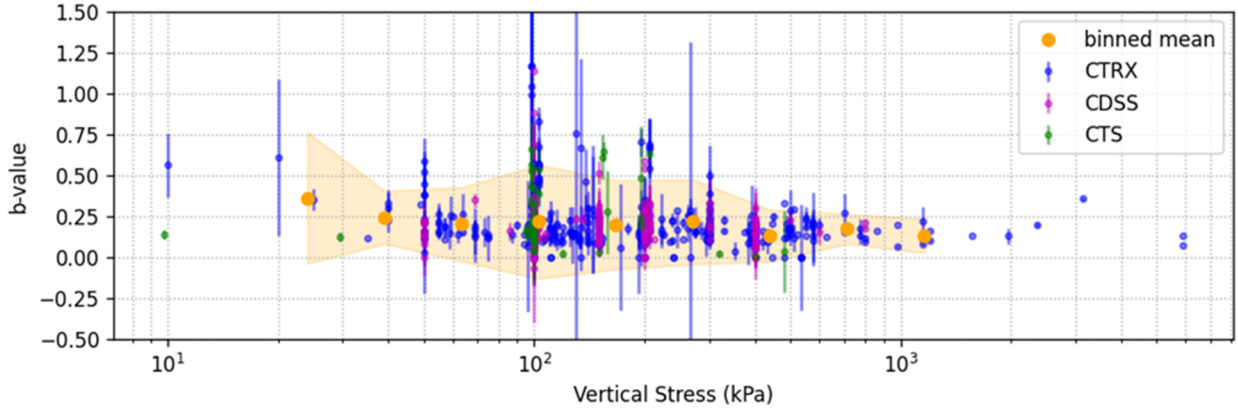

Figure 6-22 Computed b-values vs. σ'_{v0} using the SMT's compiled dataset of laboratory data. Orange shaded area represents +/- the standard deviation of the b-values for each σ'_{v0} bin.

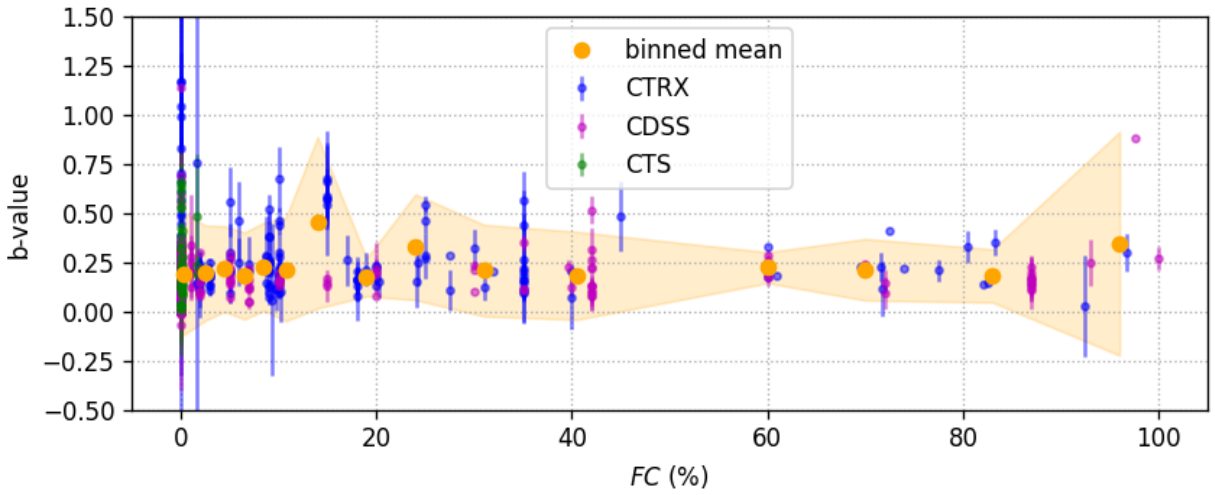

Figure 6-23 **Computed b-values vs. *FC* using the SMT's compiled dataset of laboratory data. Orange shaded area represents +/- the standard deviation of the b-values for each *FC* bin.**

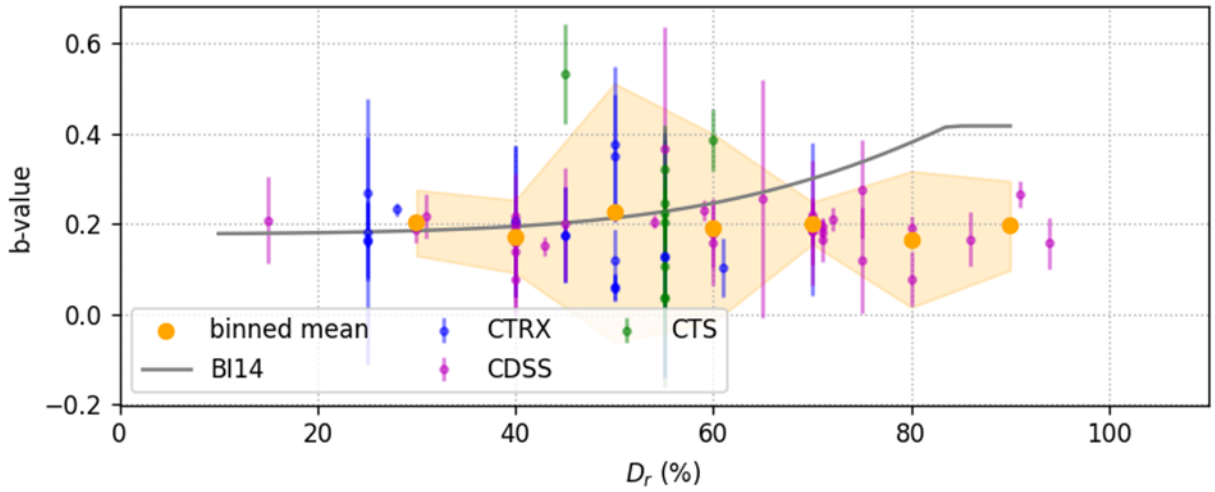

Figure 6-24 **Computed b-values vs. D_r using the SMT's compiled dataset of laboratory data with some filters applied (σ'_{v0} approximately 1 atm, α = 0, FC less than or equal to 10%, and standard error of b-value less than or equal to 0.15). Orange shaded area represents +/- the standard deviation of the b-values for each D_r bin. The gray line represents the implied b-values associated with the BI14 MSF relationship.**

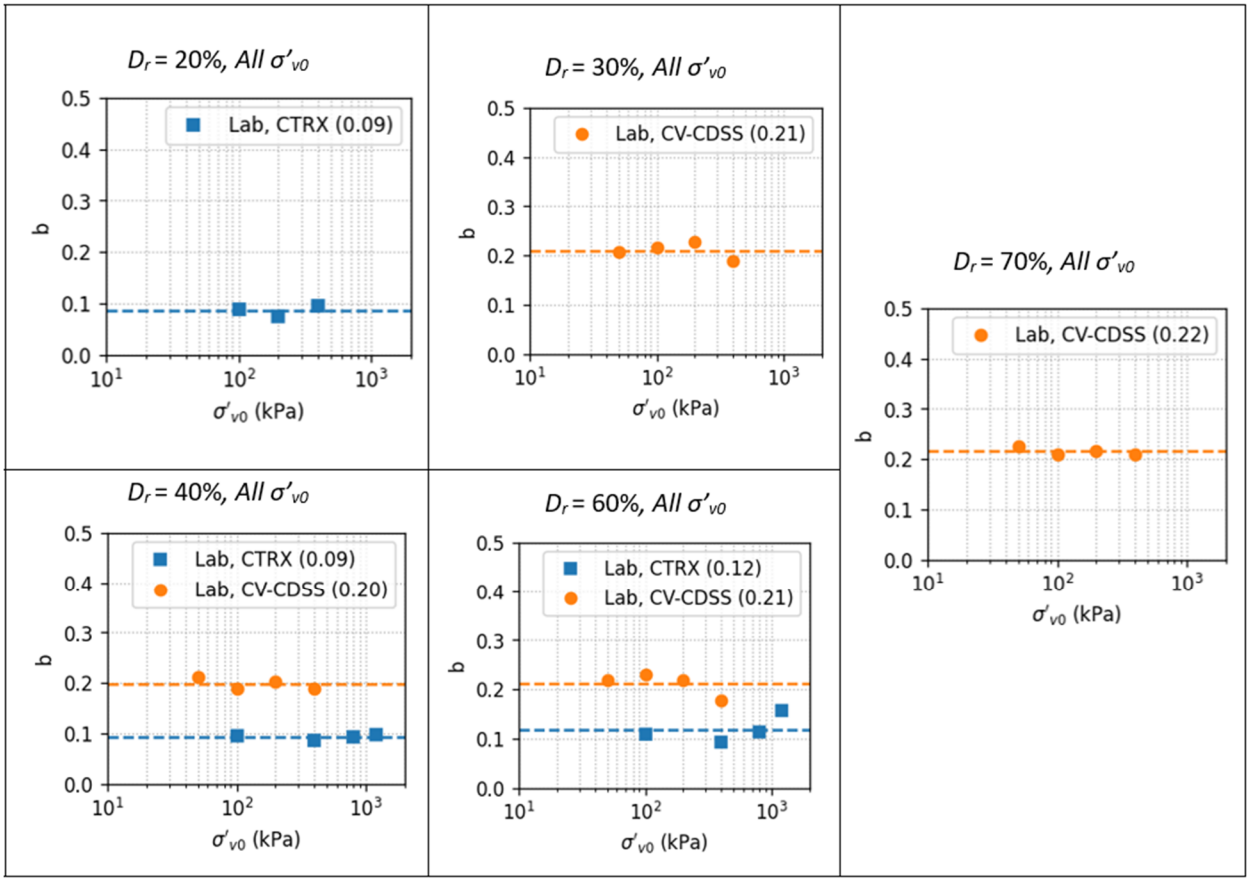

Figure 6-25 Computed b-values vs. σ'_{v0} for a range of D_r using FRS data (water-pluviated specimens)

6.3 Probability of Manifestation P[M] Model

The model formulation applied in this research includes manifestation given triggering but does not include manifestation given no triggering nor manifestation given no susceptibility (Section 4.4.2). Potential contributors to surface manifestations of ground failure aside from liquefaction triggering were not included in the final model because:

- Versions of models that include effects such as substantial strains related to cyclic softening of clays did not improve predictive power significantly compared to models that neglected such effects.
- Members of the NGL Advisory Board voiced skepticism about manifestation in the absence of triggering.
- By not including these other mechanisms, the resulting model is simpler to adopt for end users.

The model that only considers manifestation caused by triggering therefore involves three models that each have coefficients that can be updated: susceptibility, triggering given susceptibility, and manifestation given triggering. The formulation in Eq. (4-10) can be expanded

to show the susceptibility, triggering, and manifestation models that go into the profile manifestation prediction as follows:

$$P[M_P] = 1 - \prod_{l=1}^{N_L} \left(1 - PF_{M|T_l} PF_{T|S_l} PF_{S_l} K_{Sat_l}\right)^{t_l/t_c} \quad 6\text{-}11$$

Variable t_c is the characteristic thickness as introduced in Section 4.4.2. This variable could potentially be treated as a model coefficient in the Bayesian inference, but we found that it causes instability in the results. Several t_c values ranging from 0.5m to 5m were tested in the regression, and the likelihood, L, was maximized at $t_c \sim$ 2m. The value was thereafter fixed at 2m.

The development of the manifestation model is presented in a step-by-step approach in the following subsections to clarify the model development process. First, a simple manifestation model conditioned on one parameter is presented. That relationship was developed only allowing the manifestation model ($PF_{M|T}$) priors to update to posteriors while fixing the triggering ($PF_{T|S}$) and susceptibility (PF_S) priors. Next, both the manifestation and triggering priors were updated simultaneously within the single parameter model. Finally, other manifestation model parameters were explored, and a two-parameter version of the manifestation model was selected as the recommended model.

6.3.1 $PF_{M|T}$ Inference with Single Parameter Model

The modeling began with a one-dimensional logistic function in which the single independent variable was the depth to the top of the potentially liquefiable layer z_{top}. The conditional probability factor is then described by

$$PF_{M|T} = \frac{1}{1 + \exp\left(-\left(\beta_0 + \beta_1 \cdot z_{top}\right)\right)} \quad 6\text{-}12$$

As discussed in Section 6.2.7, the coefficients updated through Bayesian inference needed to be assigned prior distributions. It was not desired to impose any prior belief about the relationships for manifestation given triggering, therefore β_0 and β_1 were initialized as having normal distributions with mean (μ) = 0 and standard deviation (σ) = 1000 (Gelman 2006 recommend a normal distribution centered at zero with a standard deviation set to a very high value for a noninformative prior distribution). The other models, $PF_{T|S}$ and PF_S, are given the mean prior model coefficients presented in Sections 6.1 and 6.2 but are not given the opportunity to update so that they remain fixed while the $PF_{M|T}$ coefficients update.

The model was developed using a dataset reduced from the full dataset described in Section 5 to a subset that only contained CPT profiles with total lengths of at least 15m. This filter was applied because shorter profiles were observed to cause significantly reduced model performance since the short profiles did not represent all of the soil layers that could contribute to surface manifestation. The threshold of 15m was selected based on a series of tests in which different depth thresholds were used and manifestation models developed. Review of the model coefficients and performance produced the conclusion that 15m gave a practical balance between the size of the dataset and the performance of the model. Application of the >15m threshold reduces the case history dataset to 204 profiles that include 5091 soil layers. Each

case history is also weighted to account for cases in which multiple CPTs are associated with a single observation, as described in Section 5.1.

The results of the $PF_{M|T}$ model coefficient inference are presented in Figure 6-26. For this and the following inferences, a local MAP estimate (i.e., mode of the a posteriori distribution) (Bassett and Deride 2016) is evaluated to approximate the mean for each coefficient rather than sampling which would produce posterior distributions of each coefficient. The MAP provides a point estimate using the dataset and the priors and was used during exploratory analyses (and for this simplified illustrative model) for computational efficiency. The final recommended model will present the results of sampling the full distributions of the model coefficients.

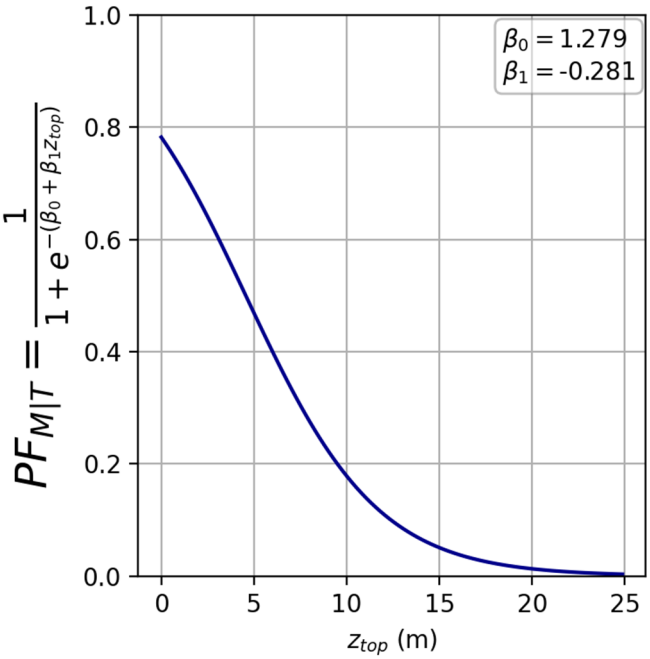

Figure 6-26 Computed b-values vs. σ'_{v0} for a range of D_r using FRS data (water-pluviated specimens)

The MAP estimates for β_0 and β_1 are 1.279 and -0.281, respectively. The negative coefficient on β_1 ensures that $PF_{M|T}$ decreases as the depth of a layer increases. It is also noted that $PF_{M|T}$ never reaches a value of 1, even at z_{top}=0 it only reaches ~0.8.

The probability factor model (Eq. 6-12) only produces an equivalent probability $P[M_L|T_L]$ for a layer of thickness t_c. Recall that $P[M_L]$ is influenced by the layer thickness (Section 4.4.2), so while a layer with t=t_c produces $P[M|T]$=0.8, a layer with t somewhat larger than t_c could produce $P[M|T]$~1. Therefore, the model is predicting that a layer at the ground surface that has liquefaction triggered will have an ~80% chance of manifesting if it is 2m thick. If t < 2m, $P[M]$ will decrease and if t > 2m, $P[M]$ will increase. This is also intuitive: a thin layer, even if it is shallow, will be less likely to manifest surface evidence if liquefaction is triggered compared to a thick layer.

To track performance of the regressed models, a cost function (J) is introduced that is very similar to the likelihood function presented in Eq. 4-12 except that it incorporates a negative sign

so that values are positive. As model performance improves, the value of the cost function decreases, with 0 representing a perfect model.

$$J = -\frac{1}{N_P}\sum_{k=1}^{N_P}[y_k \ln(P[M_P]_k) + (1-y_k)]\ln(1-P[M_P]_k) \quad \text{6-13}$$

When the model is run on the training dataset using the above MAP estimates of the $PF_{M|T}$ coefficients, the cost is J=0.566.

6.3.2 Single Parameter $PF_{M|T}$ Model with $PF_{T|S}$ Inference

Whereas in the previous section the triggering and susceptibility prior models were fixed (not adjusted by Bayesian regression), in this section the Bayesian inference is allowed to simultaneously update both the $PF_{M|T}$ and $PF_{T|S}$ coefficients while the PF_S priors remain fixed. The $PF_{M|T}$ priors were again set at μ=0 and σ=1000. The $PF_{T|S}$ priors were set using the μ inferred from the laboratory test dataset in Section 6.2 (Table 6-2) while the covariance coefficients were increased (multiplied by four) from those directly inferred from the laboratory-based data to incorporate a larger level of uncertainty. As discussed in Section 6.2.7, the σ values determined from the laboratory test dataset represent uncertainty with laboratory tests, but do not incorporate additional uncertainty that comes from a lack of knowledge of how representative of field conditions these specimens are. This is a somewhat arbitrary modification, but the sensitivity to inference results is explored in Section 6.4.4 where a multitude of different σ multipliers are tested. The 4x multiplier was deemed appropriate to maintain confidence in the laboratory-based triggering prior while accounting for uncertainty for the laboratory tests representing field conditions.

Bayesian inference is performed using the case history dataset and MAP estimates of the $PF_{M|T}$ and $PF_{T|S}$ coefficients were evaluated, with the results shown in Figure 6-27 and Figure 6-28. The $PF_{M|T}$ posterior (Figure 6-27) remains very similar to the posterior inferred in Section 6.3.1 but the $PF_{T|S}$ posterior (Figure 6-28) changes significantly, reducing the CSR required to trigger liquefaction at high D_r/q_{c1Ncs}. These posterior models produce J=0.558 which is only a small reduction in cost (small increase in model predictive performance) compared to the model that fixed the $PF_{T|S}$ prior and inferred the $PF_{M|T}$ posterior.

The shift in the $PF_{T|S}$ posterior is potentially important and warrants discussion. While the Bayesian inference shifts down the triggering relationship, this produces only marginal improvement, suggesting that it is only weakly supported by the data. To more carefully evaluate this effect, the shift is re-examined using different assumptions regarding the $PF_{M|T}$ conditioning variables and updating of the PF_S in subsequent sections.

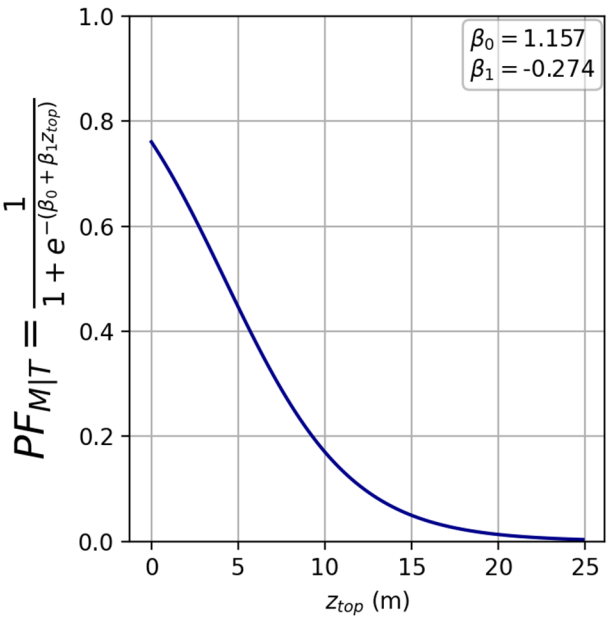

Figure 6-27 ***PF*$_{M|T}$ function conditioned on z_{top} based on MAP estimates of model coefficients in which *PF*$_{T|S}$ was also updated. The *PF*$_S$ priors were fixed.**

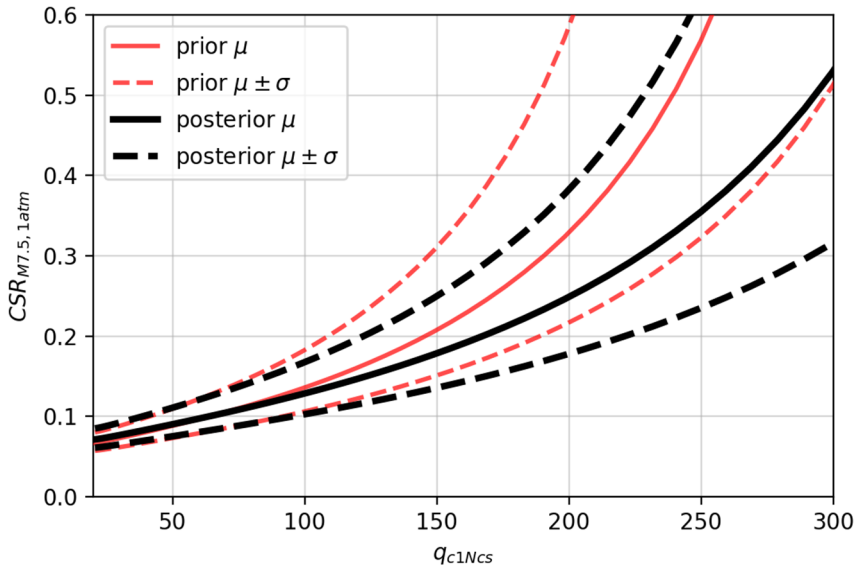

Figure 6-28 ***PF*$_{T|S}$ function conditioned on q_{c1Ncs} based on MAP estimates of model coefficients. The *PF*$_S$ priors were fixed.**

6.3.3 Single Parameter *PF*$_{M|T}$ Model with *PF*$_{T|S}$ and *PF*$_S$ Inference

In this section the Bayesian inference was extended to include the susceptibility prior, which updated the posterior PF_S model. The two PF_S model coefficients, x_m and σ_m, had prior μ and σ values that were described in Section 6.1; those coefficients' priors were assumed to be

normally distributed. The Bayesian inference updated these along with the $PF_{M|T}$ and $PF_{T|S}$ coefficient priors. The inference was performed using the same dataset as described previously (Section 6.3.1). MAP estimates of coefficients were obtained and the results are shown in Figure 6-29, Figure 6-30, and Figure 6-31.

The $PF_{M|T}$ updated posterior was generally similar to the previous two posteriors; however, it reached higher probabilities at shallow depths. The $PF_{T|S}$ posterior shifted to lower *CSR* at high D_R again, but to a lesser extent, indicating that some of the change may have actually been due to susceptibility effects rather than triggering. The PF_S posterior decreased across the entire range of I_c values, meaning that the susceptibility prior was not adequately decreasing P[*M*] for fine-grained soils with moderate to high I_c. This inference produced J=0.515, which is a significant improvement compared to the prior two iterations, indicating that the susceptibility function update is important for improving manifestation prediction.

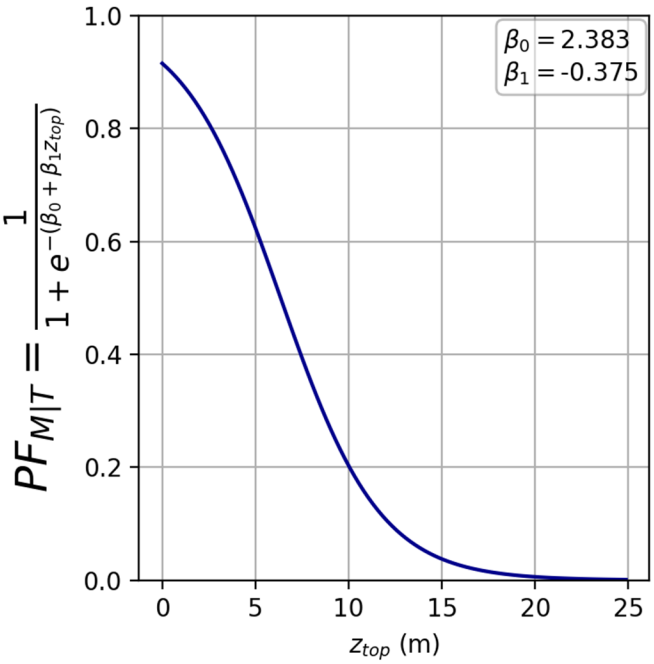

Figure 6-29 **$PF_{M|T}$ function conditioned on z_{top} based on MAP estimates of model coefficients in which $PF_{T|S}$ and PF_S were also updated**

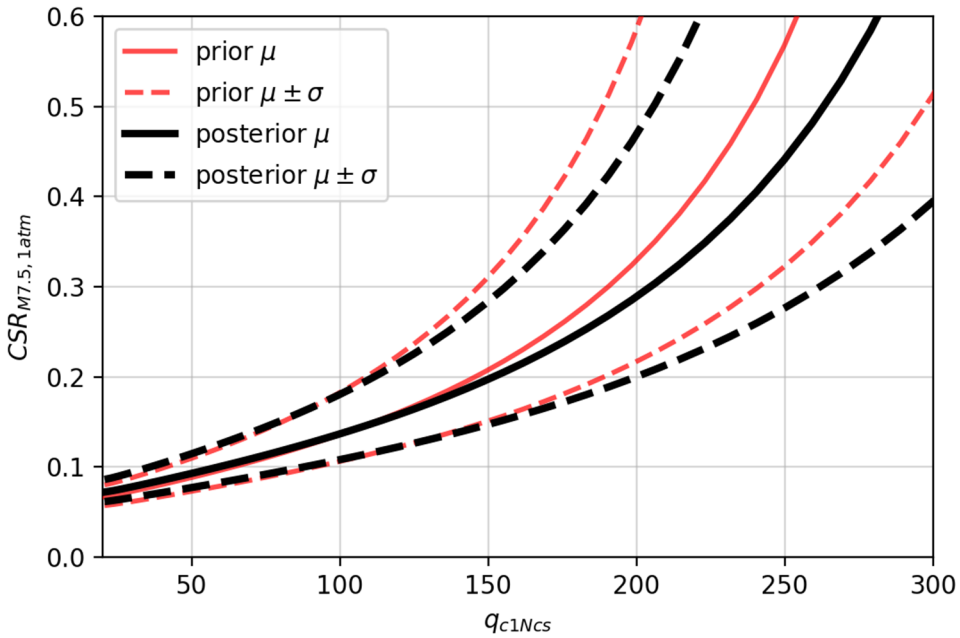

Figure 6-30 $PF_{\eta|S}$ **function conditioned on** q_{c1Ncs} **based on MAP estimates of model coefficients. The** PF_S **priors were also adjusted.**

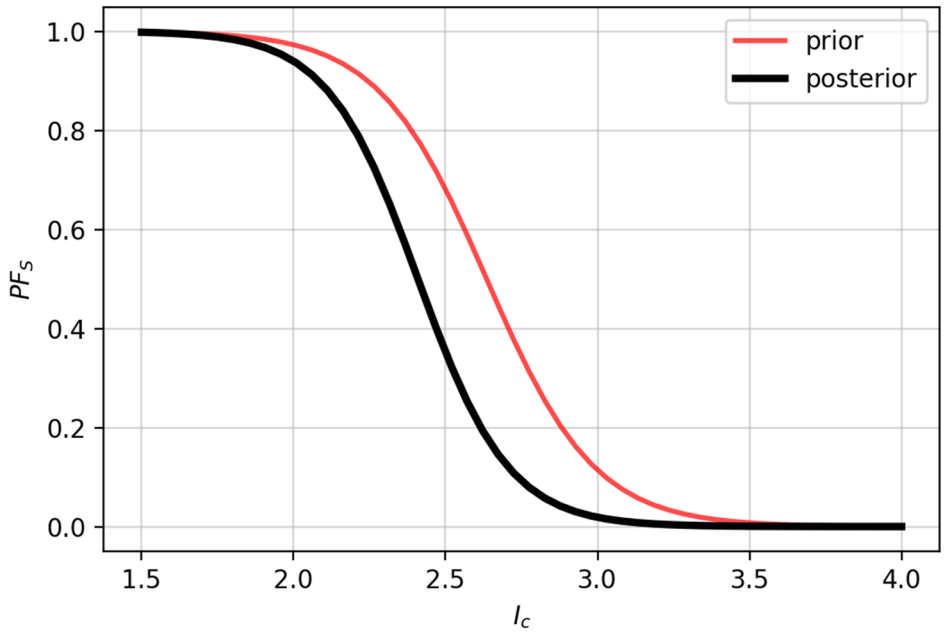

Figure 6-31 PF_S **function conditioned on** I_c **based on MAP estimates of model coefficients**

6.3.4 P[***M***] Inference Using Multi-Parameter $PF_{M|T}$ Models

Up to this point, the manifestation given triggering function has only included z_{top} as a predictive feature but other features and combinations of multiple features could help further improve manifestation prediction. Additional layer attributes that could potentially improve the $PF_{M|T}$ function are listed in Table 4-2. Soil layer thickness, t, is not listed in Table 4-2 because it is already included in the t/t_c exponent. MAP estimates that describe the posterior $PF_{M|T}$, $PF_{T|S}$, and PF_S coefficients were obtained for all parameter combinations; a total of 127 combinations of potential predictive features were investigated.

Several feature combinations in the $PF_{M|T}$ function produced physically unrealistic trends (i.e., $PF_{M|T}$ increases as z_{top} increases or $PF_{M|T}$ decreases as CSR increases). For each feature, a sign for its multiplying coefficient can be anticipated, representing the physically expected trend (i.e., β_i for z_{top} should be a negative number and β_i for CSR should be a positive number). While the Bayesian inferences were not constrained to conform with the expected coefficient signs, any model with at least one coefficient opposite to the anticipated sign was discarded and not listed in Table 6-6. Of the 127 possible $PF_{M|T}$ combinations, 87 were rejected using this process. The 40 remaining models are listed in Table 6-6. The table is sorted first by ascending number of features, and then by ascending J. Note that J generally decreases as the number of features increases; this trend is shown in Figure 6-32.

Table 6-6 Accepted P[M_P] models with MAP estimated coefficients

$PF_{M\|T}$ Features	$PF_{M\|T}$, coefficients ($\beta_0, \beta_1, \ldots, \beta_i$)	$PF_{T\|S}$ coefficients (ζ_0, ζ_1, σ)	PF_S coefficients (σ_m, x_m)	J
z_{top}	-1.3429, -2.8025	-7.004, 0.0285, 0.9377	0.1054, 2.4093	0.5148
$C_{R,I}$	-1.6795, -3.4581	-6.9896, 0.0287, 0.9597	0.1068, 2.5014	0.5243
σ_v'	-0.8982, -1.1557	-7.0584, 0.0274, 0.9549	0.1041, 2.4394	0.5512
$L_{D,I}$	-1.7139, 1.1218	-7.5775, 0.0258, 1.0229	0.114, 2.566	0.5557
I_c	-2.4065, -3.5026	-7.3687, 0.0331, 0.99,	0.115, 2.6414	0.5658
$CSR_{M7.5,1atm}$	-1.2846, 0.0276	-7.2739, 0.0249, 0.9465	0.1063, 2.4554	0.6004
z_{top}, $L_{D,I}$	-1.9695, -2.4715, 1.2552	-7.4491, 0.0301, 1.0108	0.1097, 2.5266	0.4907
$L_{D,I}$, σ_v'	-1.5557, 1.3474, -1.5057	-7.5004, 0.0296, 1.0285	0.1113, 2.5599	0.499
$C_{R,I}$, $L_{D,I}$	-1.9662, -2.9421, 0.9195	-7.2948, 0.0299, 1.0246	0.1099, 2.5807	0.5051
I_c, z_{top}	-2.1977, -2.6584, -2.0155	-7.3037, 0.0328, 0.9408	0.1148, 2.6223	0.5072
z_{top}, $C_{R,I}$	-1.556, -1.4489, -1.9446	-6.9953, 0.0286, 0.9485	0.1057, 2.4469	0.5154
I_c, $C_{R,I}$	-2.0743, -1.8466, -2.6926	-7.1716, 0.0325, 0.9524	0.1137, 2.6292	0.517
$CSR_{M7.5,1atm}$, $C_{R,I}$	-1.6998, 0.1085, -3.4694	-7.1344, 0.0294, 0.9643	0.1064, 2.5005	0.5241
I_c, σ_v'	-1.8673, -2.7136, -0.9504	-7.3221, 0.0333, 0.9529	0.1147, 2.6313	0.533
I_c, $L_{D,I}$	-2.2372, -2.1159, 0.8318	-7.5346, 0.0317, 1.0475	0.1151, 2.6446	0.5422
$CSR_{M7.5,1atm}$, $L_{D,I}$	-1.7140e+00, 1.3000e-03, 1.1217e+00	-7.5789, 0.0258, 1.0229	0.114, 2.5659	0.5557
$CSR_{M7.5,1atm}$, I_c	-2.4201, 0.0548, -3.5239	-7.4249, 0.0335, 0.9932	0.1149, 2.6416	0.5656
q_{c1N}, I_c	-2.435, -0.3291, -3.4513	-7.3235, 0.0324, 0.9863	0.1151, 2.6412	0.5659
I_c, z_{top}, $L_{D,I}$	-2.3693, -1.6522, -2.2252, 1.0134	-7.4738, 0.0323, 0.9968	0.1147, 2.6284	0.4822
I_c, $L_{D,I}$, σ_v'	-1.9027, -1.3049, 1.1658, -1.4059	-7.4995, 0.0318, 1.0223	0.1145, 2.6313	0.4921
$C_{R,I}$, $L_{D,I}$, σ_v'	-1.6673, -0.8586, 1.2296, -1.1256	-7.4425, 0.0298, 1.0274	0.1108 2.5661	0.4982

$PF_{M\|T}$ Features	$PF_{M\|T}$, coefficients (β_0, β_1, …, β_i)	$PF_{T\|S}$ coefficients (ζ_0, ζ_1, σ)	PF_S coefficients (σ_m, x_m)	J
$CSR_{M7.5,1atm}$, $L_{D,I}$, σ_v'	-1.5559e+00, 5.0000e-04, 1.3481e+00, -1.5064e+00	-7.5014, 0.0296, 1.0285	0.1113, 2.5599	0.499
I_c, $C_{R,I}$, $L_{D,I}$	-2.143, -1.0562, -2.6921, 0.7581	-7.3044, 0.0319, 1.0139	0.113, 2.6335	0.5016
$CSR_{M7.5,1atm}$, $C_{R,I}$, $L_{D,I}$	-1.9755, 0.0935, -2.9593, 0.9174	-7.3971, 0.0304, 1.0276	0.1096, 2.5778	0.5045
q_{c1N}, I_c, z_{top}	-2.3555, -0.6257, -2.7786, -1.93,	-7.2198, 0.0315, 0.9318	0.115, 2.6218	0.5063
I_c, z_{top}, $C_{R,I}$	-2.1904, -2.5977, -1.9204, -0.1612	-7.2935, 0.0327, 0.9414	0.1147, 2.6217	0.5071
$CSR_{M7.5,1atm}$, z_{top}, $C_{R,I}$	-1.5865, 0.0727, -1.3552, -2.0807	-7.0821, 0.029, 0.9527	0.1054, 2.4501	0.5159
$CSR_{M7.5,1atm}$, I_c, $C_{R,I}$	-2.0901, 0.1001, -1.8697, -2.6906	-7.2762, 0.0331, 0.9568	0.1136, 2.629	0.5164
I_c, $C_{R,I}$, σ_v'	-1.6799, -1.493, -1.9084, -0.0509	-6.8722, 0.03, 0.9195	0.1136, 2.6303	0.5206
q_{c1N}, I_c, σ_v'	-2.0166, -0.6511, -2.7446, -0.9263	-7.2146, 0.0315, 0.9467	0.1149, 2.6293	0.5323
$CSR_{M7.5,1atm}$, I_c, σ_v'	-1.8707, 0.015, -2.7199, -0.9498	-7.3363, 0.0334, 0.9537	0.1147, 2.6312	0.533
q_{c1N}, I_c, $L_{D,I}$	-2.2913, -0.3738, -2.1058, 0.8085	-7.4667, 0.0302, 1.0355	0.1155, 2.6453	0.5416
$CSR_{M7.5,1atm}$, I_c, $L_{D,I}$	-2.2551, 0.0465, -2.1721, 0.8291	-7.5802, 0.0321, 1.0484	0.1151, 2.6446	0.542
q_{c1N}, $CSR_{M7.5,1atm}$, I_c	-2.6119, -1.4734, 0.1968, -3.4726	-7.126, 0.0289, 0.9553	0.119, 2.6262	0.5621
$CSR_{M7.5,1atm}$, I_c, z_{top}, $L_{D,I}$	-2.3816, 0.0369, -1.6528, -2.2449, 1.0197	-7.5292, 0.0326, 0.9972	0.1147, 2.6271	0.4821
$CSR_{M7.5,1atm}$, I_c, $L_{D,I}$, σ_v'	-1.9096, 0.0308, -1.3145, 1.1663, -1.4064	-7.5305, 0.0319, 1.0231	0.1144, 2.6312	0.4921
$CSR_{M7.5,1atm}$, $C_{R,I}$, $L_{D,I}$, σ_v'	-1.6714, 0.043, -0.8765, 1.2254, -1.1205	-7.4869, 0.03, 1.029	0.1106, 2.5646	0.4981
$CSR_{M7.5,1atm}$, I_c, $C_{R,I}$, $L_{D,I}$	-2.1604, 0.1102, -1.0864, -2.6979, 0.7595	-7.4149, 0.0325, 1.0184	0.1129, 2.6323	0.5007
q_{c1N}, $CSR_{M7.5,1atm}$, I_c, z_{top}	-2.4281, -0.8623, 0.0664, -2.8546, -1.8899	-7.253, 0.0315, 0.9311	0.1151, 2.6217	0.5062
q_{c1N}, $CSR_{M7.5,1atm}$, I_c, z_{top}, $C_{R,I}$	-2.4258, -0.8583, 0.0674, -2.834, -1.8717, -0.0398	-7.2538, 0.0315, 0.9328	0.115, 2.6214	0.5062

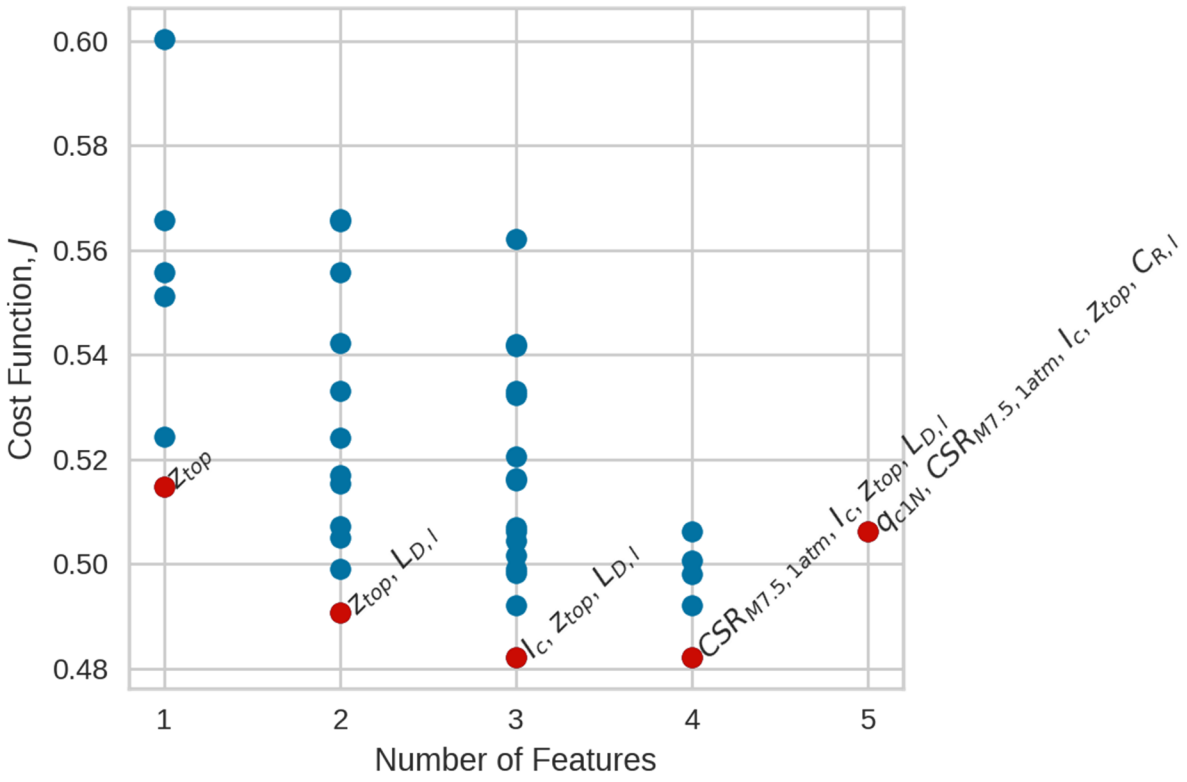

Figure 6-32 Cost (*J*) of accepted P[M_P] models with MAP estimated coefficients compared with number of features in the $PF_{M|T}$ function. The lowest *J* model for each number of feature group is highlighted red and the feature(s) in that model's $PF_{M|T}$ function is printed next to it.

The best performing $PF_{M|T}$ model with a single independent variable used z_{top} (the model presented in Sections 6.3.1-6.3.3). The z_{top} parameter also appears in each of the top performing multi-variable models. Based on these results, z_{top} is considered to be the single most important layer parameter for analysis of profile manifestation given triggering. The $L_{D,I}$ parameter also frequently appears in top performing models, indicating it is a useful predictor. However, it incorporates FS_L in its calculation and so requires use of a prior liquefaction model for *CRR*. This complicates the analyses because triggering is incorporated into multiple analysis phases, which may introduce correlation issues (if the same triggering model is used in $PF_{M|T}$ and $PF_{T|S}$) or incompatibility issues (if different triggering models are used in $PF_{M|T}$ and $PF_{T|S}$). For this reason, $L_{D,I}$-conditioned models were not selected. Ultimately, the two-parameter model that includes z_{top} and I_c was selected as the recommended model. Models with three parameters did not significantly reduce the cost function relative to the selected two-parameter model.

6.3.5 Recommended P[*M*] Model

The recommended model is Eq. (6-11) with t_c=2m and the $PF_{M|T}$, $PF_{T|S}$, and PF_S, functions presented in Eq. 6-14 through Eq. 6-20 and visualized in Figure 6-33 through Figure 6-38. This model combines z_{top} and I_c in the manifestation given triggering model. The reasoning behind

including I_c is that it serves as a proxy of hydraulic conductivity and erodibility of a layer. A soil with low hydraulic conductivity could generate large excess water pressures but not be able to expel water quickly enough to contribute to surface manifestation. This is reflected in Figure 6-33 by reductions of $PF_{M|T}$ as I_c increases, with probability factors approaching zero for I_c >~ 2.5. Similarly, Figure 6-34 shows how fixed values of $PF_{M|T}$ (0.16, 0.5, 0.84) vary with z_{top} and I_c, illustrating the decay of manifestation likelihood as depth increases or I_c increases. This model produces J=0.508, which is notably reduced from the 0.515 value for the single parameter model (Section 6.3.3).

By including I_c in the $PF_{M|T}$ function with a very weak prior, the model recovers a strong dependence on I_c in the manifestation component (Figure 6-33 and Figure 6-34) and the susceptibility posterior is very similar to the prior (Figure 6-37). This contrasts with the results in Section 6.3.3 when I_c was not considered in the manifestation model; by allowing I_c to affect manifestation, adjustments of the susceptibility prior are no longer suggested. As shown in Figure 6-35, the triggering model posterior shifts up modestly relative to the prior for this model, which is in contrast to no change (Section 6.3.3) or a downward shift (Section 6.3.2). The upward shift with the present model makes the most physical sense, due to the unaccounted for effects of sample disturbance in the prior, which would be expected to increase resistance for a given D_r. However, it is worthwhile to acknowledge that the improvement in fit produced by these shifts in the triggering model is small. The $PF_{T|S}$ model is visualized with continuous plots against z_{top} for bands of I_c in Figure 6-36.

Because this is the recommended model, in this section we provide not only MAP estimates of coefficients, but also sample parameter distributions with four Markov chains (Section 4.4.3), each composed of 1000 samples. Recommended coefficients are taken as the mean across the four sampling chains, and thus are not exactly equal to the MAP estimates in Table 6-6, although they are very similar. The distributions of the posterior coefficients are shown in Figure 6-38.

$$PF_{M|T} = \frac{1}{1 + \exp\left(-\left(8.206 - 0.342 \cdot z_{top} - 3.461 \cdot I_c\right)\right)} \quad 6\text{-}14$$

$$PF_{T|S} = \frac{1}{1 + \exp\left(\frac{-1.702 \cdot \left(\widehat{CSR} - \widehat{CRR}\right)}{0.985}\right)} \quad 6\text{-}15$$

$$\widehat{CSR} = \frac{\left({CSR_{M7.5,1atm}}^{-0.6566} - 1\right)}{-0.6566} \quad 6\text{-}16$$

$$\widehat{CRR} = -7.427 + 0.0338 \cdot \widehat{D_r} \quad 6\text{-}17$$

$$\widehat{D_r} = \frac{\left({D_r}^{1.2022} - 1\right)}{1.2022} \quad 6\text{-}18$$

$$D_r(\%) = 47.8 \cdot {q_{c1Ncs}}^{0.264} - 106.3 \; (0 \le D_r \le 100\%) \qquad \text{6-19}$$

$$PF_S = 1 - \frac{1}{1 + \exp\left(\frac{-1.702 \cdot \left({I_c}/{2.614} - 1\right)}{0.116}\right)} \qquad \text{6-20}$$

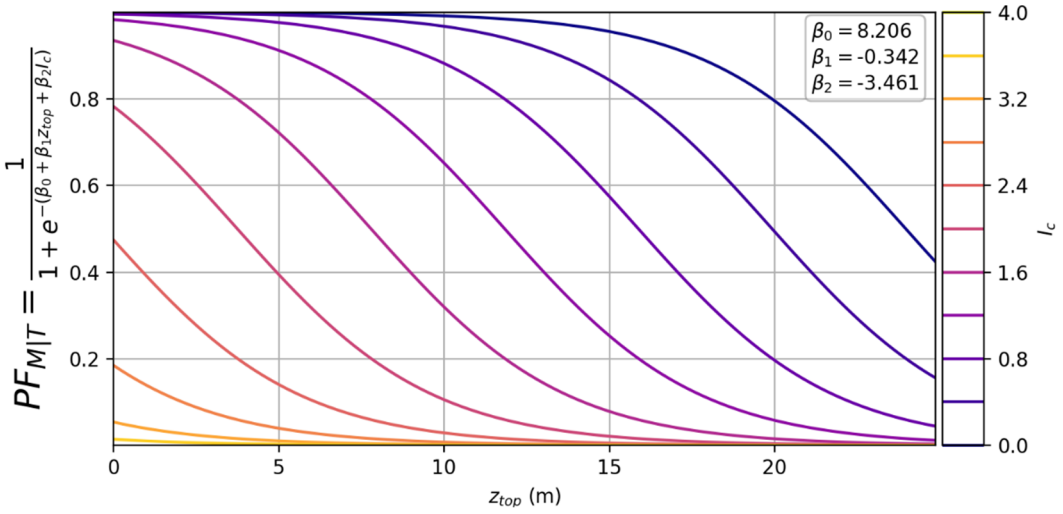

Figure 6-33 ***PF*$_{M|T}$ function conditioned on z_{top} and I_c based on MAP estimates of model coefficients in which *PF*$_{T|S}$ and *PF*$_S$ were also updated**

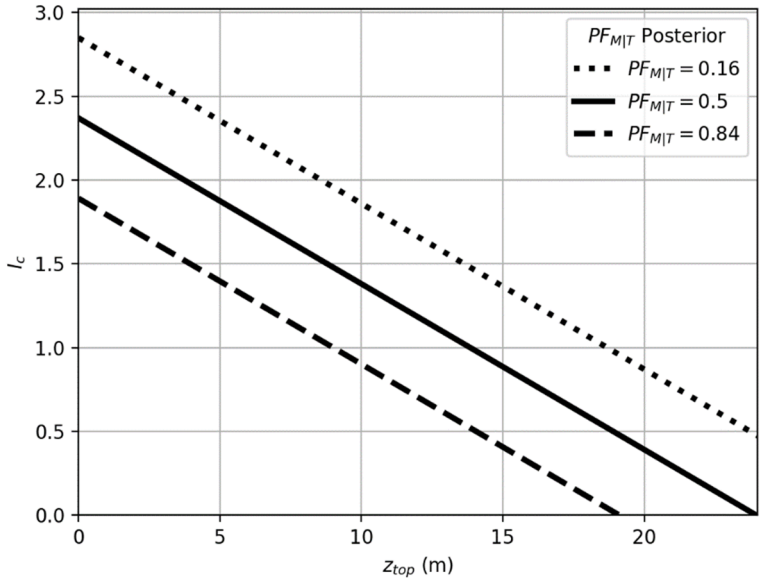

Figure 6-34 **Values of z_{top} and I_c that produce probability factors of 0.16, 0.5, and 0.84. As z_{top} increases and I_c increases, the probability of manifestation given triggering decreases.**

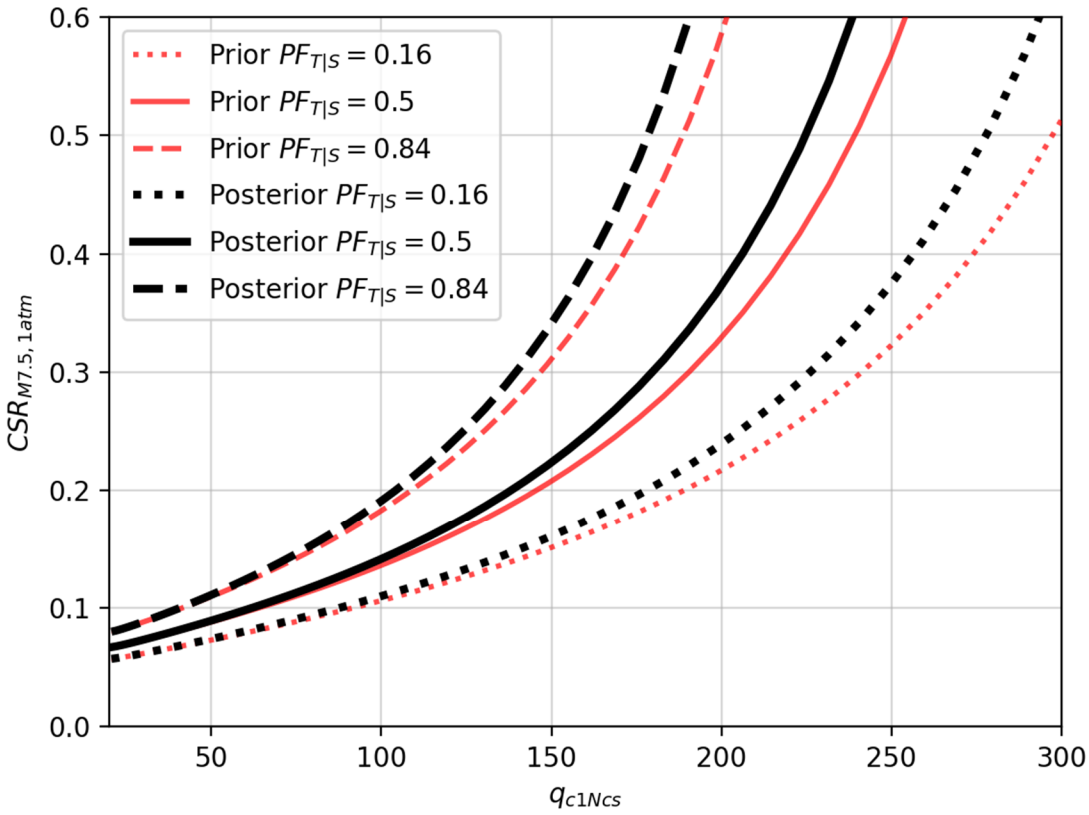

Figure 6-35 Recommended $PF_{T|S}$ function conditioned on q_{c1Ncs} based on MAP estimates of model coefficients. The PF_S priors were also adjusted.

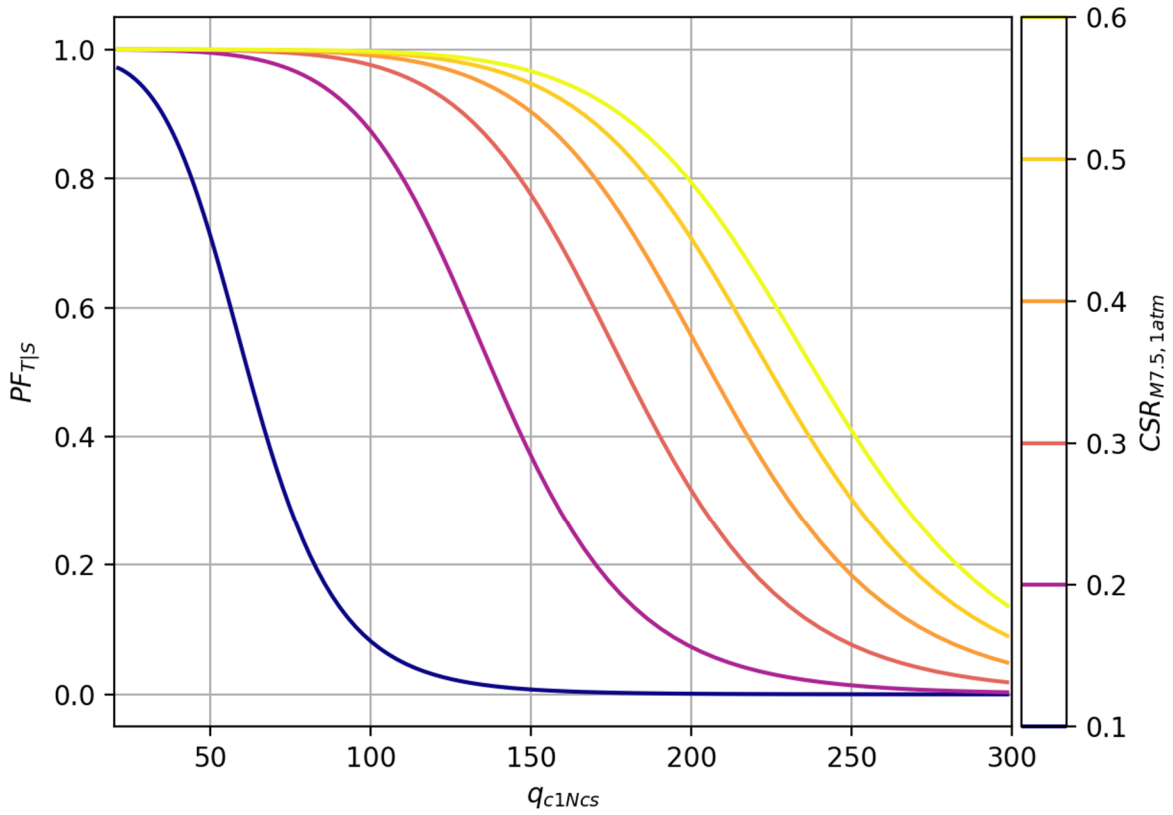

Figure 6-36 $PF_{T|S}$ **values for the recommended P[**M_P**] model for varying** q_{c1Ncs} **and** $CSR_{M7.5,1atm}$ **values**

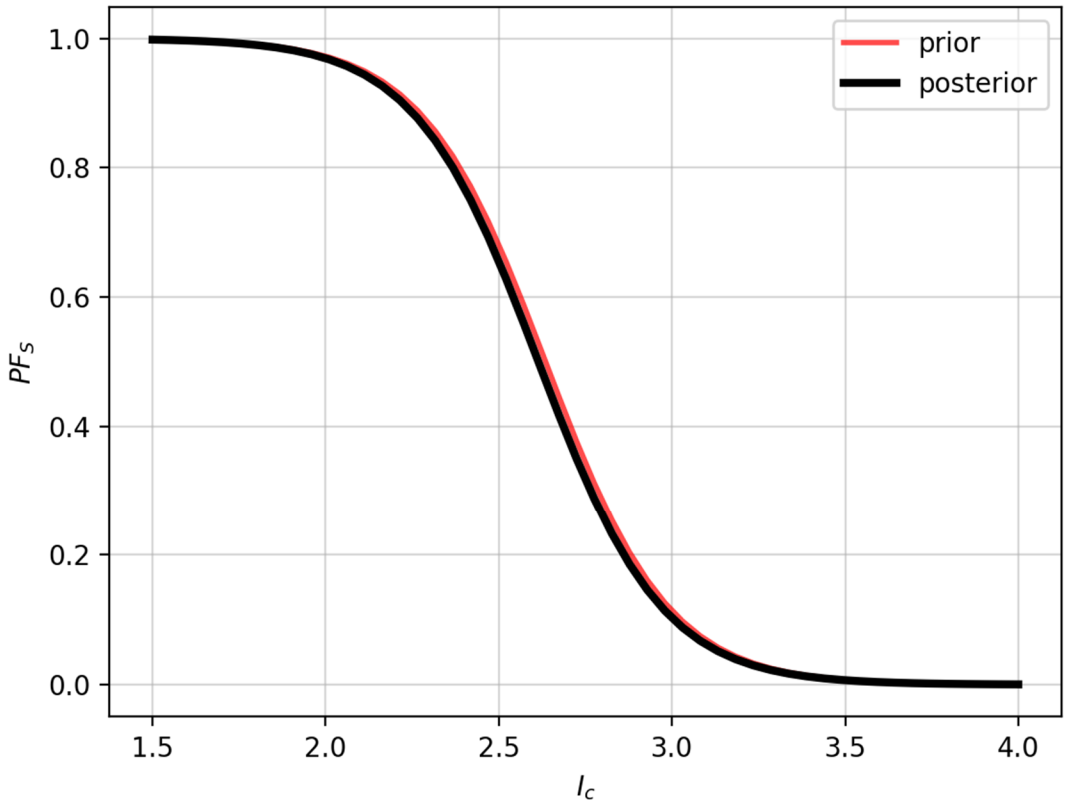

Figure 6-37 ***PF*$_S$ function from recommended model conditioned on I_c based on MAP estimates of model coefficients**

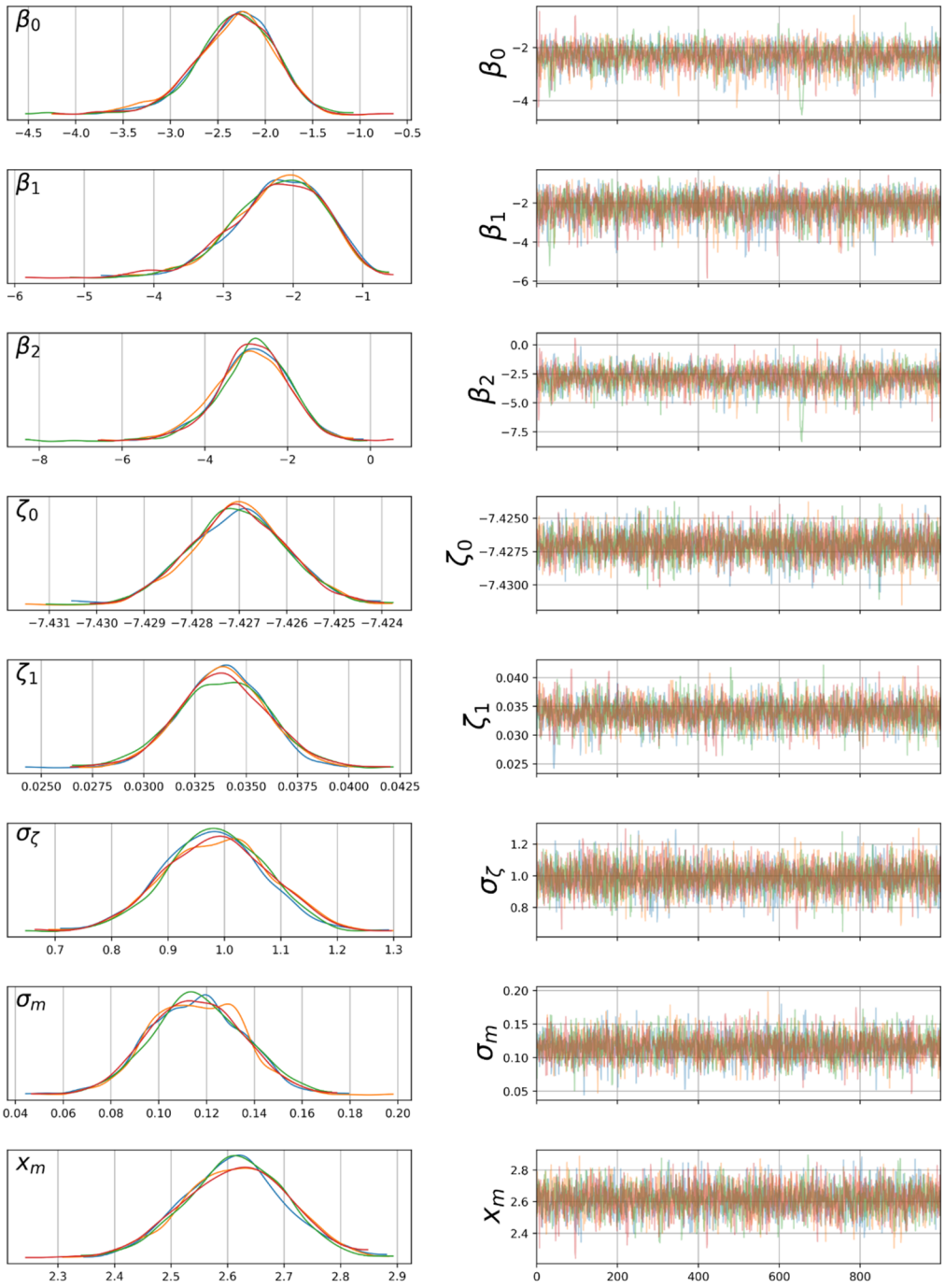

Figure 6-38 **Posterior distributions of the coefficients updated with Bayesian inference for the recommended P[*M*] model. The first three coefficients are for $PF_{M|T}$, the next three are for $PF_{T|S}$, and the final two are for PF_S. Note the $PF_{M|T}$ coefficients are in normalized I_c-z_{top} space and therefore do not match the unnormalized coefficients in Eq. 6-14.**

6.3.6 P[***M***] Discussion

The manifestation model presented in Section 6.3.5 operates on an entire profile rather than a critical layer, which is a significant break from past practice in liquefaction model development. As noted in Chapter 3, while legacy models are generally considered to predict triggering, because they are based on case histories of surface manifestation (or lack thereof), the manifestation effects considered in this chapter must affect those models to some extent. For this reason, I compare here the predicted probabilities of profile manifestation with predictions from a legacy triggering model.

There are several metrics in statistics for quantifying the predictive accuracy of a model. The recommended model produces a probability of observable surface manifestation of liquefaction, but the physical outcome is always a binary outcome: no manifestation (y_{obs}=0) or manifestation (y_{obs}=1). The P[M_P] value can be categorized as either a yes (y_{pred}=1) or no (y_{pred}=0) prediction if it is above or below a threshold probability. An obvious threshold probability to use would be 0.5, and a confusion matrix using that threshold with the dataset that the model was trained on is presented in Figure 6-39. A confusion matrix shows the proportion of correctly and incorrectly predicted “yes” and “no” cases for binary outcomes; there are four categories: true positives (TP) are correctly predicted “yes” cases, false positives (FP) are incorrectly predicted “no” cases, true negatives (TN) are correctly predicted “no” cases, and false negatives (FN) are incorrectly predicted “yes” cases. The percentages shown are the true positive rate(TPR=TP/(TP+FN)), false positive rate (FPR=FP/(FP+TN)), false negative rate (FNR=FN/(TP+FN)), and true negative rate (TNR=TN/(FP+TN)) Both the TP and TN categories have more cases than their FN and FP counterparts, indicated by the TPR and TNR percentages higher than 50%. If the model were random, the TPR, TNR, FPR, and FNR values would each be approximately 50% and if the model was able to perfectly predict the outcome for every case, then it would show TPR = TNR = 100% and FPR = FNR = 0%. Figure 6-39 also presents several statistical metrics and their definitions including accuracy, precision, recall, and F1 score.

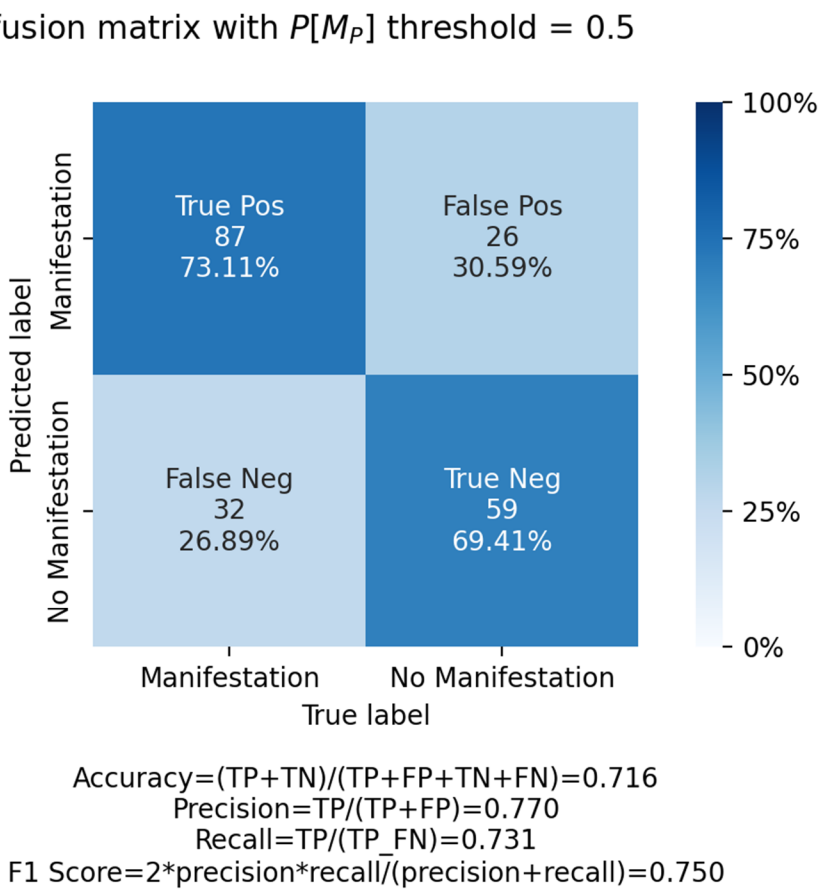

Figure 6-39 Confusion matrix using a P[M_P] threshold = 0.5 for model training dataset

Instead of looking at predictions based on one P[M_P] threshold, the probability threshold for assigning manifestation to a site can be varied from 0 to 1 and the TPR and FPR calculated for each probability threshold to create a ROC curve as shown in Figure 6-40. As the threshold increases from 0 to 1, the TPR and FPR decrease from 100% to 0% and there is a threshold that balances the two values relative to each other called the OOP, defined as the point that minimizes FPR + (1 – TPR) (Figure 6-41). For this dataset, the OOP=0.51, and the confusion matrix using the OOP as the P[M_P] threshold is displayed in Figure 6-42. The slight change from 0.5 to 0.51 in the threshold changes one TP to a FN and three FPs to TNs, meaning that there were a total of four case histories with P[M_P] between 0.5 and 0.51.

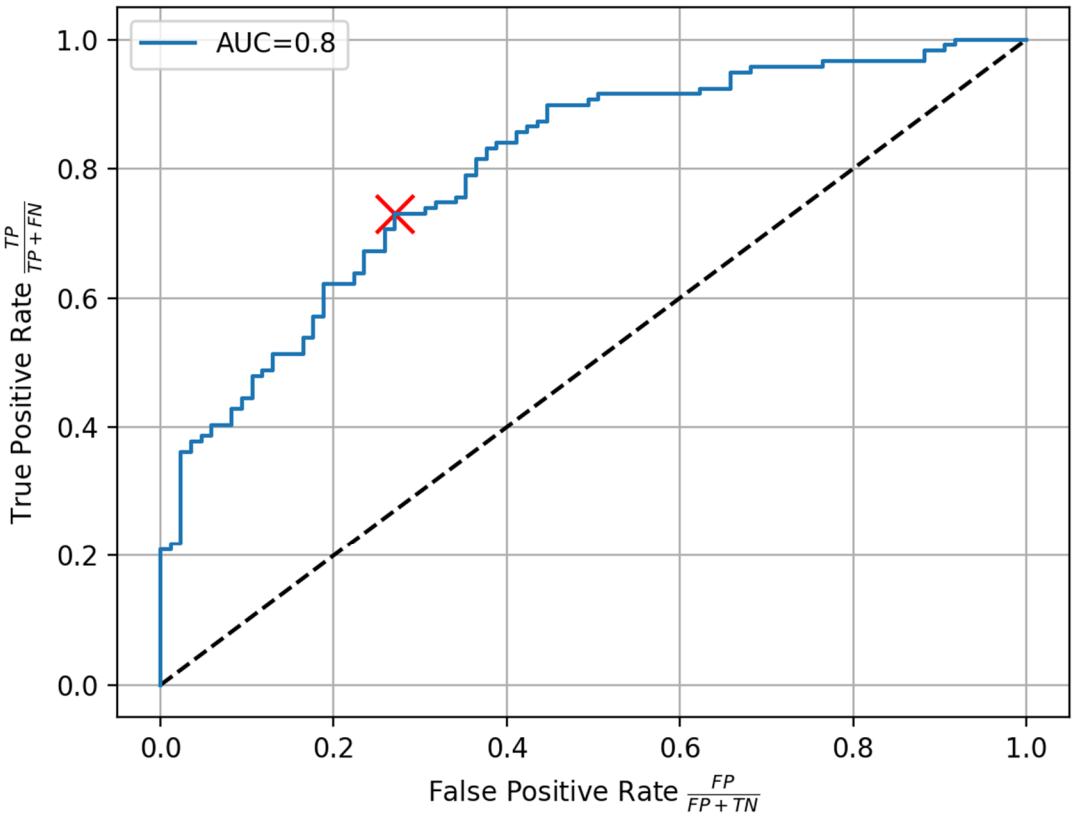

Figure 6-40 ROC curve for the model training dataset. The OOP is shown as the red "x", and the AUC is printed in the legend.

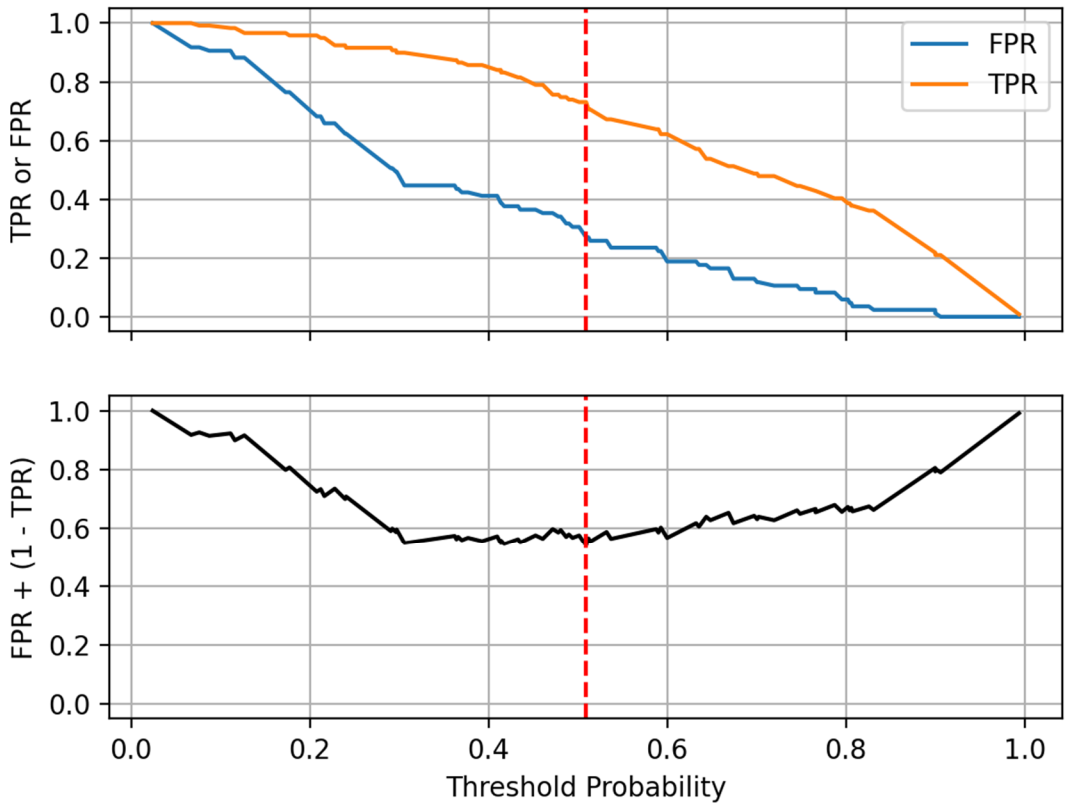

Figure 6-41 Trend of TPR and FPR with threshold probabilities and identification of the OOP

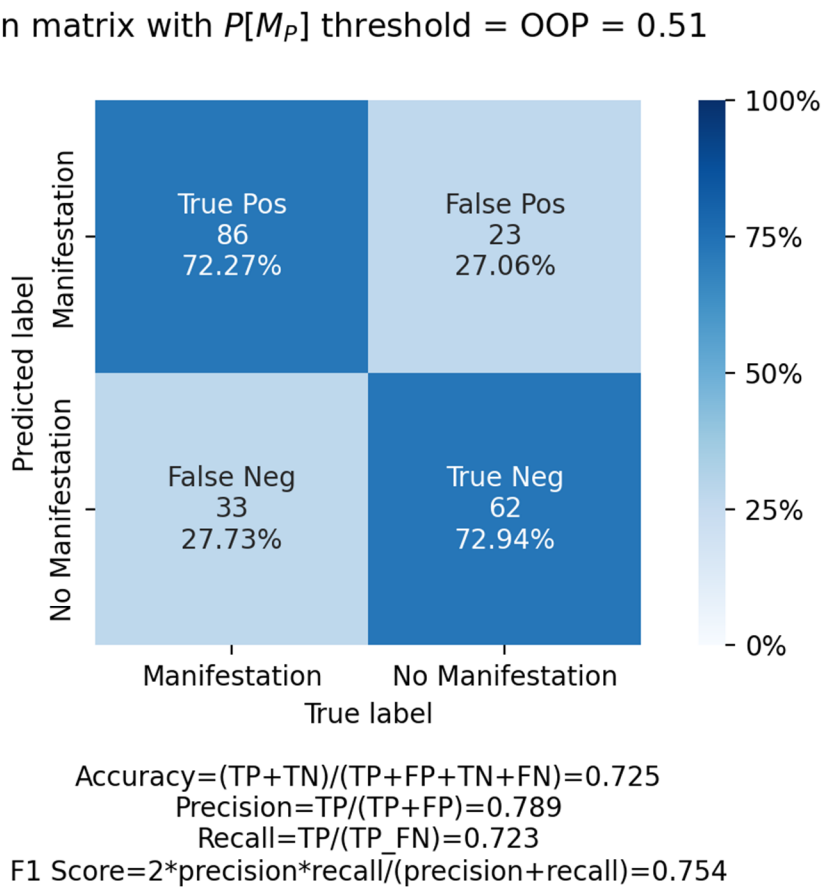

Figure 6-42 Confusion matrix using a P[M_P] threshold = OOP = 0.51 for model training dataset

A model is expected to perform well on the dataset it is trained on, therefore it is useful to see how the model applies to a test dataset that is independent of the training dataset. A dataset of CPTs and surface manifestation of liquefaction observations from the Canterbury earthquake sequences was published in DesignSafe (Geyin et al. 2020b). All the CPTs with length greater than 15m were obtained from this dataset and used with the recommended model to predict P[M_P]. The resulting ROC curve and confusion matrix are presented in Figure 6-43 and Figure 6-44. All the statistical metrics for the Canterbury liquefaction dataset are very similar to the model training dataset even though it is a much larger number of case histories exemplifying that the model is not overfit to the training dataset.

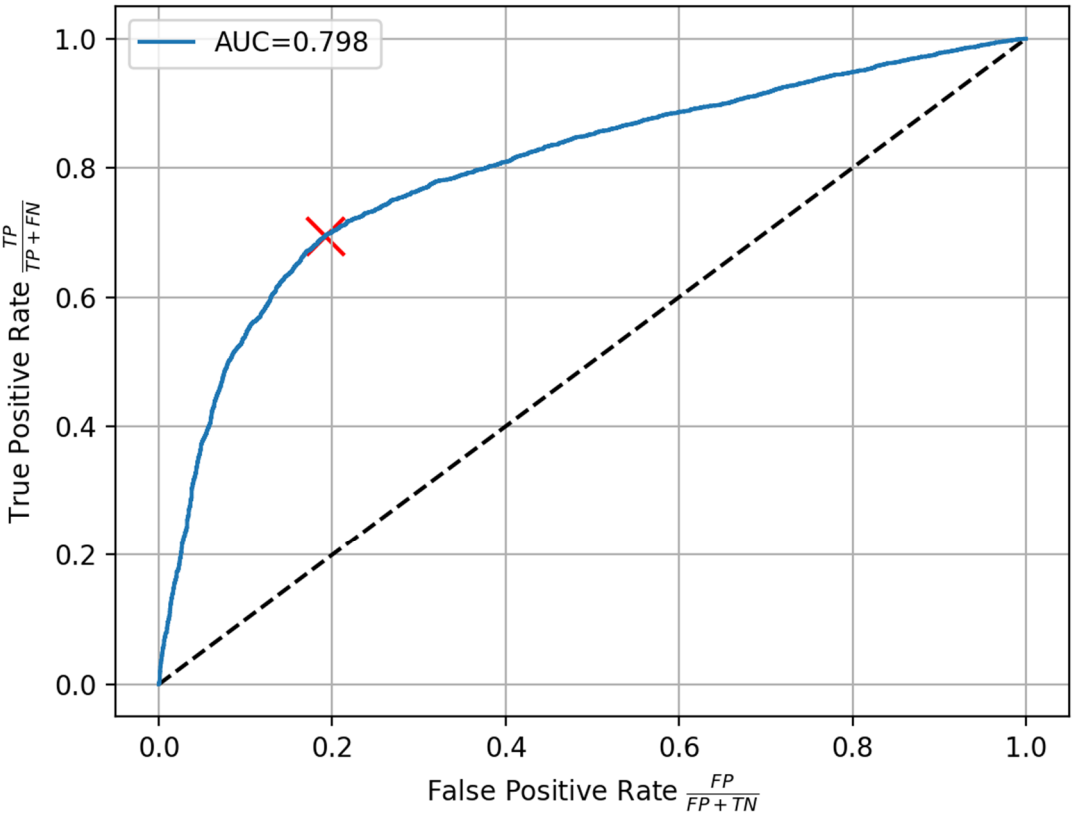

Figure 6-43. ROC curve for the Canterbury liquefaction dataset. The OOP is shown as the red "x", and the AUC is printed in the legend.

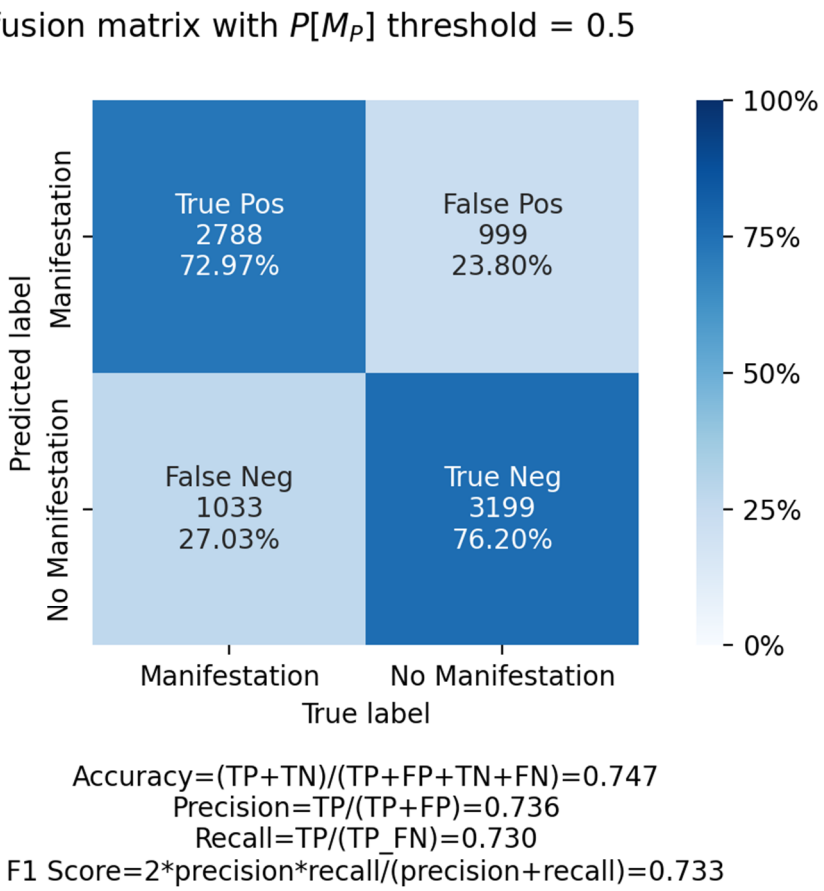

Figure 6-44. Confusion matrix using a P[M_P] threshold = 0.5 for the Canterbury liquefaction dataset.

6.3.7 Recommended P[$T|S$] Model and its Epistemic Uncertainty

We anticipate that applications of the P[$T|S$] models developed in this report will be of two types: (1) applications for which the desired end product is a prediction of manifestation and (2) applications for which only P[T] is of interest (i.e., the manifestation components of the model will not be used). For the first application type, the P[$T|S$] model that should be used is the posterior model associated with the manifestation model (details in Section 6.3.5). Our recommendation for the second application type is the subject of the remainder of this section.

The second type of application would presumably be used to assess whether triggering will occur at a site. However, we contend that a triggering analysis by itself should not be used to make mitigation decisions. It is quite possible that layers will trigger without causing any adverse consequences to infrastructure, and this can only properly be assessed using a manifestation model. The manifestation models presented in this report pertain to surface evidence in the form of ground cracks, sand boils, etc. under essentially free-field conditions (no large driving static shear stresses). Separate manifestation models may be required for different conditions, especially those involving large overburden or shear stresses (e.g., settlement of a shallow foundation, end bearing at the tip of a deep foundation, slope instability of dams, etc.).

We considered two alternative recommendations when P[T|S] is the terminal model result that is desired (application 2). The first alternative is to use the posterior P[T|S] associated with the preferred P[M_L] model, which is the model conditioned on z_{top} and I_c. The rationale for selecting this alternative is that the posterior distribution is a modification of the laboratory-based prior that is constrained by case history data, and as such overcomes the well-known limitations of a solely laboratory-based model (i.e., sample disturbance effects, fabric effects, etc.). The second alternative is to use the P[T|S] prior, which is based on laboratory data (Section 6.2.7). The rationale for considering this alternative is that different manifestation models (i.e., those summarized in Table 6-6) produce different P[T|S] posterior distributions, as shown in Figure 6-45a, some of which are above the prior and some of which are below. Three posterior distributions are highlighted in Figure 6-45a, which are associated with manifestation models conditioned on z_{top} only, z_{top} and I_c, and z_{top}, I_c, and q_{c1ncs}. We consider these three models to be the most likely models that would be used, and they too have posteriors below, above, and nearly coincident with the laboratory prior. If future work produces a different manifestation model, another posterior P[T|S] would be produced. Given these variations, one approach is using a stable central model for P[T|S], which is provided by the laboratory prior model.

Given the current stage of model development, we prefer the second alternative, but also recommend that epistemic uncertainty in the model be considered. Epistemic uncertainties are described below, but the recommended central branch P[T|S] model when P[T] of a single layer is desired (i.e., triggering analysis only) is to compute P[T] as $PF_{T|S}$ multiplied by PF_S where $PF_{T|S}$ is defined using the same logistic functional form as Eq. (6-15) but uses the lab-based coefficients given in Table 6-2. The equations to compute P[T] are summarized below in Eq. (6-21) through Eq. (6-27).

$$P[T] = PF_{T|S} PF_S \tag{6-21}$$

$$PF_{T|S} = \frac{1}{1 + \exp\left(\frac{-1.702 \cdot \left(\widehat{CSR} - \widehat{CRR}\right)}{0.994}\right)} \tag{6-22}$$

$$\widehat{CSR} = \frac{\left(CSR_{M7.5,1atm}{}^{-0.6566} - 1\right)}{-0.6566} \tag{6-23}$$

$$\widehat{CRR} = -7.43 + 0.0325 \cdot \widehat{D_r} \tag{6-24}$$

$$\widehat{D_r} = \frac{\left(D_r{}^{1.2022} - 1\right)}{1.2022} \tag{6-25}$$

$$D_r(\%) = 47.8 \cdot q_{c1Ncs}{}^{0.264} - 106.3 \; (0 \le D_r \le 100\%) \tag{6-26}$$

$$PF_S = 1 - \frac{1}{1 + \exp\left(\frac{-1.702 \cdot \left(I_c/2.635 - 1\right)}{0.115}\right)} \quad \text{6-27}$$

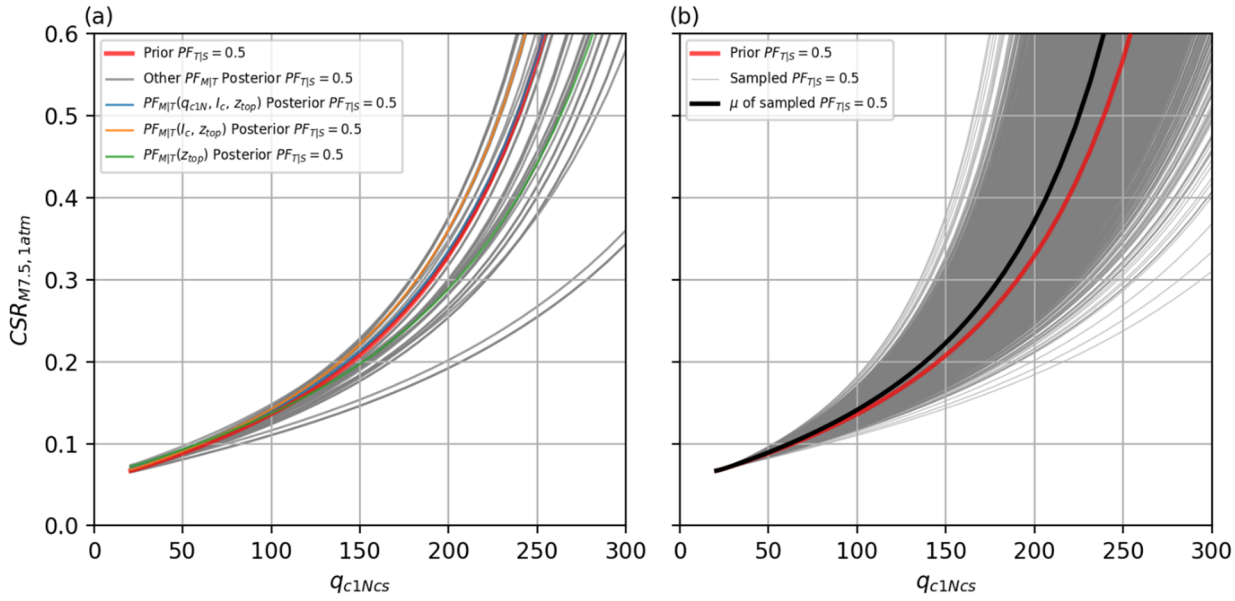

Figure 6-45. Uncertainty in posterior triggering relationships (a) across the possible manifestation models and (b) within the recommended model (distributions presented in Figure 6-38). The mean of the samples in (b) is the recommended model as presented in Section 6.3.5 for applications in which manifestation probabilities are to be predicted (black curve), whereas the prior model (red curve) is the recommended central model when the terminal analysis result is the probability of triggering.

To characterize model uncertainty in P[*T*|*S*], we consider the range of posterior distributions provided by Bayesian inference. Two components of model uncertainty can be considered. First is within-model uncertainty, as illustrated in Figure 6-45b, which shows 4000 sampled $PF_{T|S}$ = 0.5 curves within the distribution of ζ_0, and ζ_1 for the recommended manifestation model (i.e., distributions presented in Figure 6-38). There are also model uncertainties related to which set of parameters is appropriate for the manifestation model, as shown in Figure 6-45a and described previously. These two elements, intra- and inter-model uncertainty, can both be considered to represent epistemic uncertainties in the triggering model, but the inter-model uncertainty is considered to be the best representation of uncertainty in the central branch triggering model.

6.4 Sensitivity Analyses

The proposed P[M_P] model is conditioned on several variables and was derived using prior models for susceptibility and triggering. In this section, sensitivity analyses were performed to demonstrate variations of predicted outcomes from the recommended model from changes of input parameters (Section 6.4.1). Suites of alternative models are also derived using different

susceptibility and triggering priors, to investigate the relative impacts of the Bayesian inference of the data vs. the prior formulation on the characteristics of the posterior (Sections 6.4.2-6.4.3).

6.4.1 Sensitivity to Recommended Model Parameters

To compare the proposed P[M_P] model to legacy models and understand its sensitivity to model parameters, a reference *CSR*, CSR_{ref}, was computed for a target P[M_L], reference depth (z_{top}), reference I_c, and reference *t* value for a given q_{c1Ncs}. The computed value of P[M_L] was taken as equivalent to the profile manifestation P[M_P], which can be visualized as a profile composed entirely of non-susceptible material (PF_S = 0) except for a single layer with properties defined by the reference conditions (Figure 6-46). The reference properties of the soil can be adjusted to examine the effects on P[M_P] with changing layer conditions.

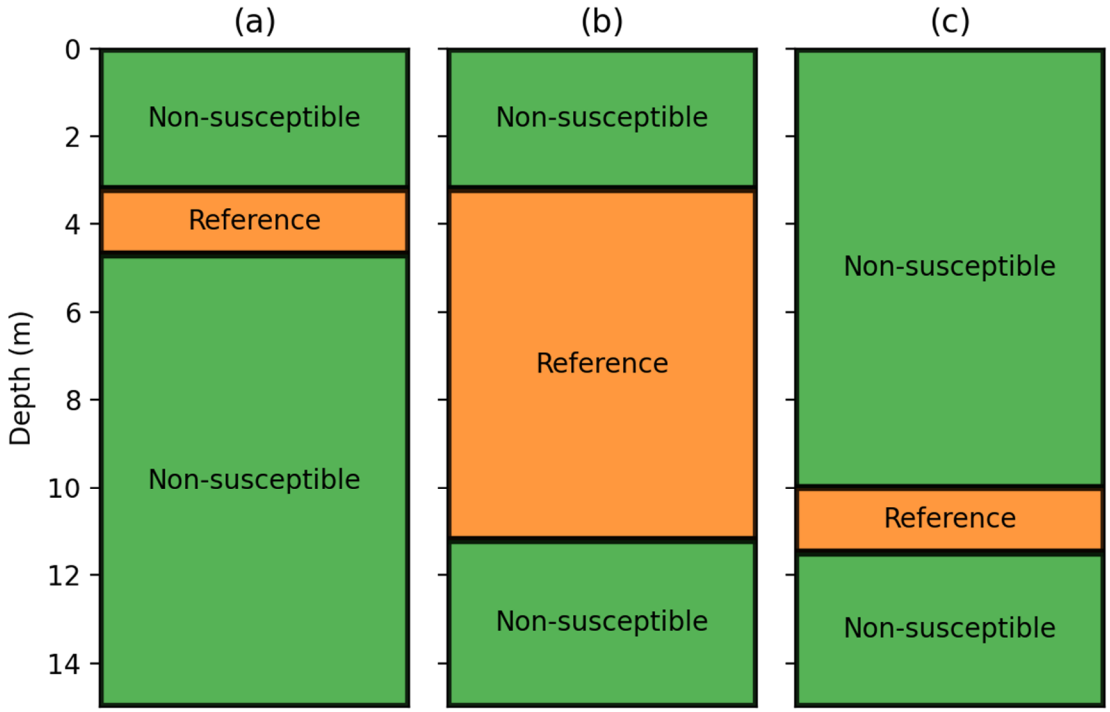

Figure 6-46. Example of profiles with different reference layer geometries that are used to evaluate P[M_P] sensitivity to model parameters: z_{top}, *t*, I_c. (a) is a relatively shallow and thin layer, (b) is a relatively shallow and thick layer, and (c) is a relatively deep and thin layer.

For a reference condition with a shallow depth, low I_c, and P[M_P]=0.16 or 0.5, CSR_{ref} was computed for a range of q_{c1Ncs} values and shown relative to the $PF_{T|S}$=0.16 and 0.5 curves in Figure 6-47. The CSR_{ref} curve is located above and to the left of the triggering curve, meaning that for a given tip resistance a higher *CSR* is needed for manifestation than for triggering. The difference is modest at low penetration resistances but significant for stiffer soils.

Figure 6-48 to Figure 6-50 show sensitivities of $CSR_{ref} - q_{c1Ncs}$ curves to variations in z_{top}, I_c, and t, respectively. These plots were prepared for a relatively low probability level of P[M_L]=0.16. The rationale for selecting this low probability is because individual layer P[M_L] values are often low even for sites with high P[M_P] values, due to multiple layers contributing to P[M_P]. As shown in Figure 6-28, as z_{top} increases higher *CSR* values are required for a given q_{c1Ncs} to produce P[M_P] = 0.16, increasing the upward shift relative to the triggering curve. Similarly, as I_c increases, higher *CSR* values are required to produce P[M_P]=0.16 (Figure 6-49). For the case of variable layer thicknesses (Figure 6-50), higher *CSRs* are required for relatively thin layers ($t < t_c$) and lower *CSRs* are required for thick layers ($t > t_c$).

Figures 6-47 to 6-50 include comparisons of results from the proposed models (both triggering and manifestation) to the Boulanger and Idriss (2016) model. A direct comparison of the triggering model (labeled as $PF_{T|S}$ in the figures) with triggering models such as Boulanger and Idriss (2016) would be a false comparison. As discussed in Section 4.1, we contend that the historical reliance on manifestation as an indicator of liquefaction triggering and lack of manifestation as an indicator of a lack of triggering has led to conventional liquefaction triggering procedures producing factors of safety against manifestation rather than of liquefaction triggering. The SMT model explicitly separates triggering from manifestation, and we therefore believe it is more appropriate to compare our “triggering + manifestation” model (results labeled as P[M_P] in the figures) with legacy “triggering” models. The SMT triggering model is lower than legacy models, but that should not necessarily be interpreted as the SMT model being more conservative than legacy models. On the other hand, the SMT profile manifestation results (P[M_P]) are generally closer to the legacy model.

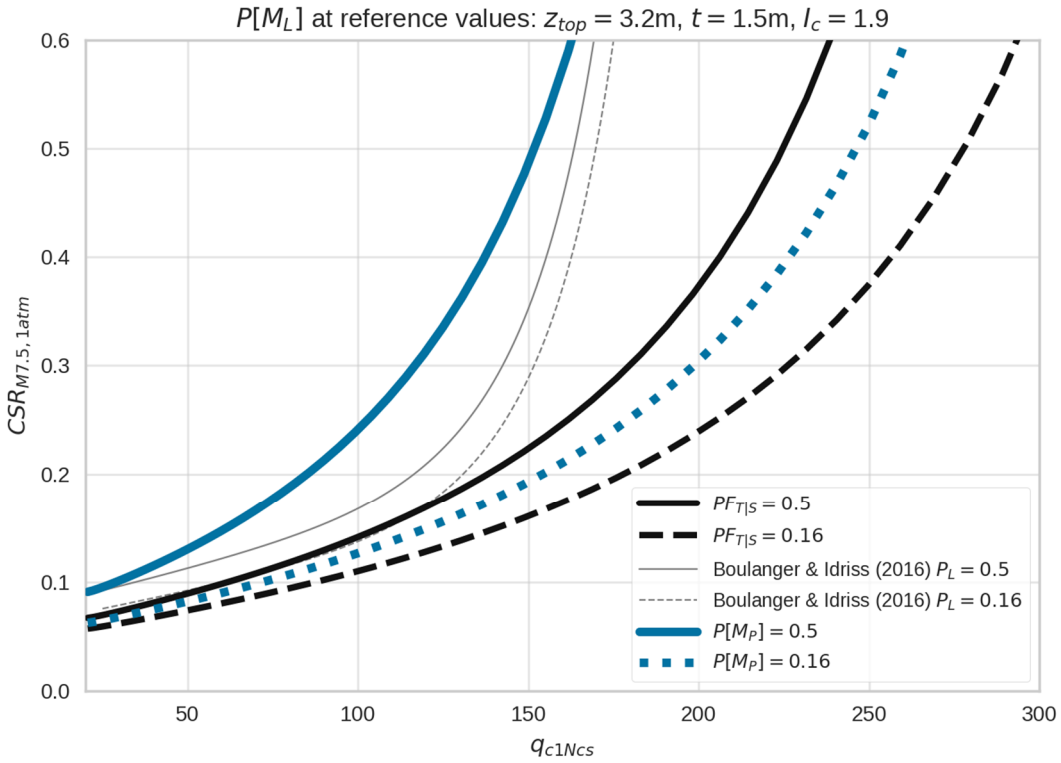

Figure 6-47. Median and 16% $PF_{T|S}$, P_L (Boulanger and Idriss 2016), and P[M_P] from the recommended model presented in this section using reference conditions for z_{top}, t, and I_c obtained as the median z_{top}, t, and I_c from critical layers selected for the Boulanger and Idriss (2016) dataset.

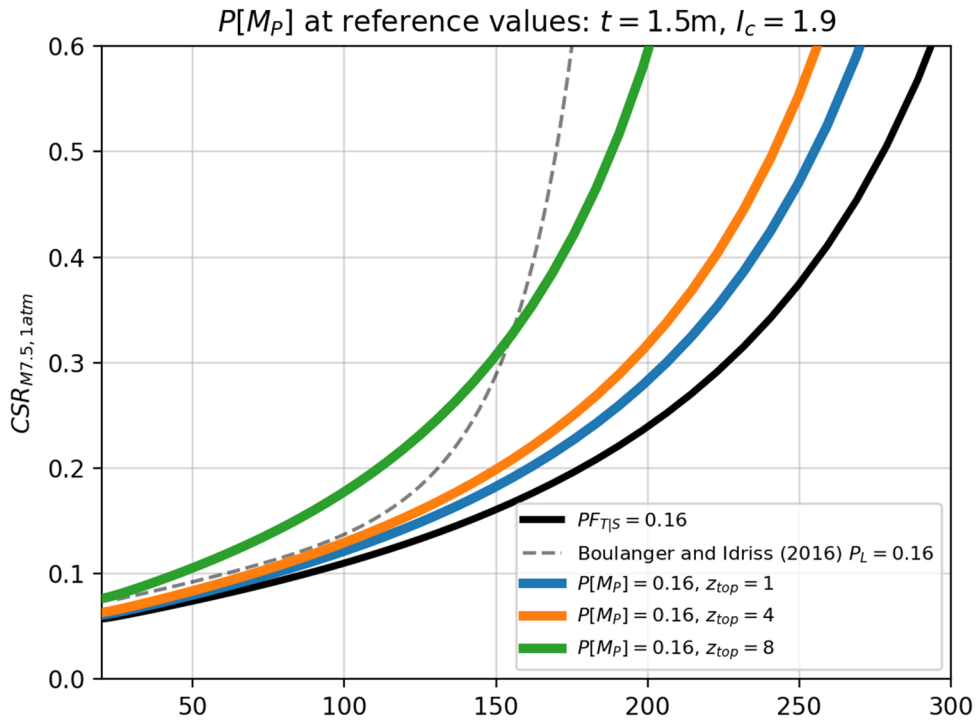

Figure 6-48. Reference condition P[M_P] = 0.16 curve with varying z_{top} values relative to the $PF_{T|S}$ = 0.16 curve

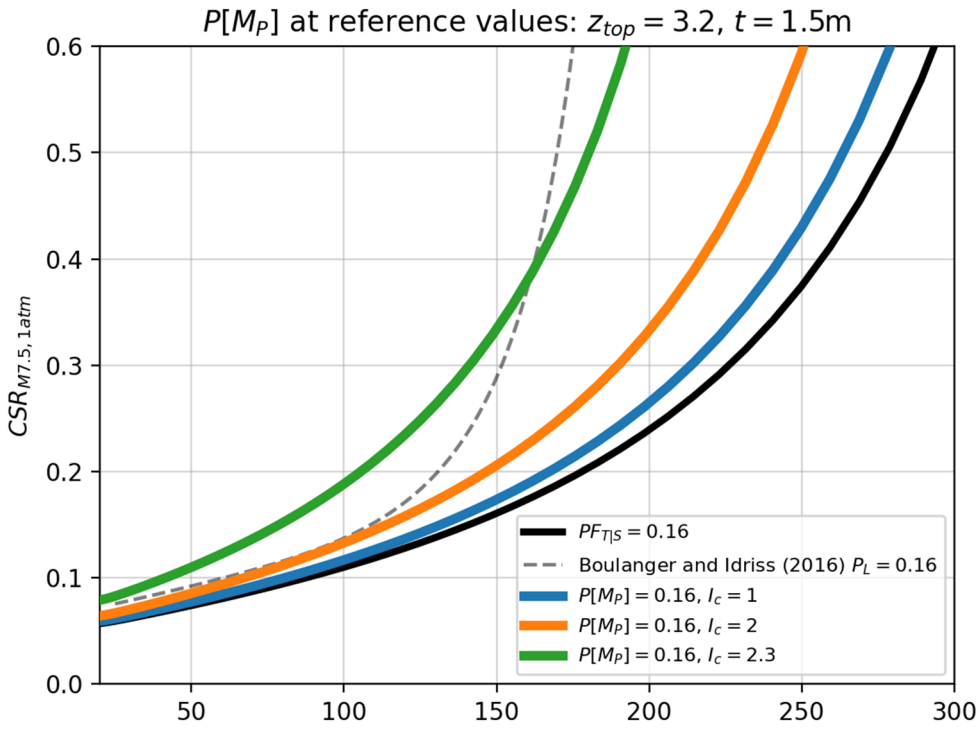

Figure 6-49. Reference condition P[M_P] = 0.16 curve with varying I_c values relative to the $PF_{T|S}$ = 0.16 curve

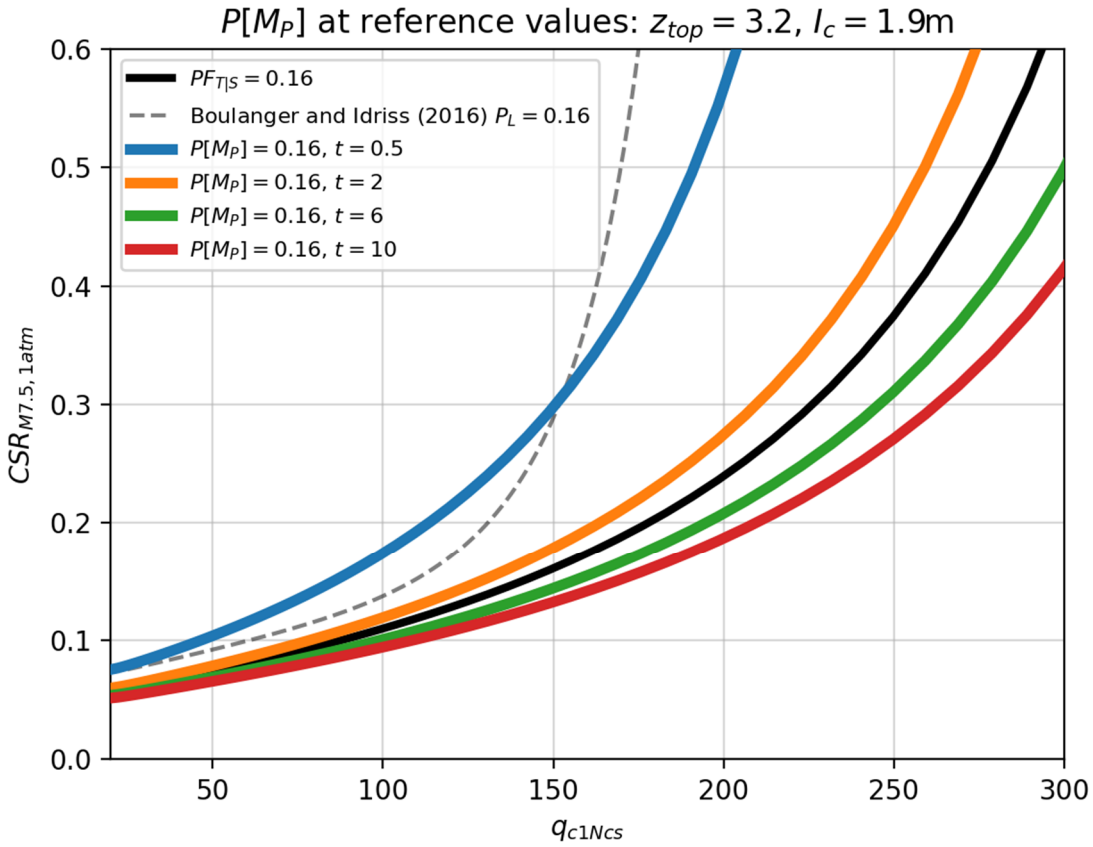

Figure 6-50. Reference condition P[M_P] = 0.16 curve with varying *t* values relative to the $PF_{T|S}$ = 0.16 curve

6.4.2 Sensitivity to PF_S Priors

In this section, the sensitivity of the P[M_P] model to susceptibility priors is tested. This sensitivity was investigated in two ways: (1) changes to the mean model, (2) changes to the uncertainty level on the mean model coefficients for the original prior (i.e., the prior presented in Section 6.1).

The first evaluation considered each of the four published susceptibility models and the combined model discussed in Section 6.1. The four susceptibility model coefficients were used as the PF_S prior in the Bayesian inference. The resulting posteriors are presented in Figure 6-51. Figure 6-51 (a) shows that the higher the PF_S relationship, the flatter the trend of the $PF_{M|T}$ lines in I_c-z_{top} space. While the manifestation model is affected, Figure 6-51 (b) shows that the susceptibility posteriors are not significantly modified from the prior. This occurs because the susceptibility prior is given relatively strong confidence (the standard deviations used in the normal distributions for the two PF_S coefficients, x_m and σ_m, are relatively small). The cost function, *J*, using these four priors were very similar (between 0.506 and 0.508).

The second evaluation modified the confidence levels placed on the PF_S coefficients for the original model (from Section 6.1). The standard deviations on the PF_S coefficients' normal

distributions (σ) were increased by factors of 2 and 4. The resulting $PF_{M|T}$ posteriors are presented in Figure 6-52. By increasing the coefficient standard deviations, Bayesian inference has greater freedom to update the posteriors, and the PF_S function shifts to the left such that a soil is less susceptible for a given I_c. However, the $PF_{M|T}$ coefficient on I_c moves in the opposite direction, eventually producing a model that shows increasing manifestation potential for increasing I_c, which is clearly non-physical. While J decreases to 0.491 for the P[M_P] model with a factor of 4 on the PF_S coefficients' normal distributions, because the $PF_{M|T}$ model has a counter-intuitive trend a strong prior for the PF_S function was retained.

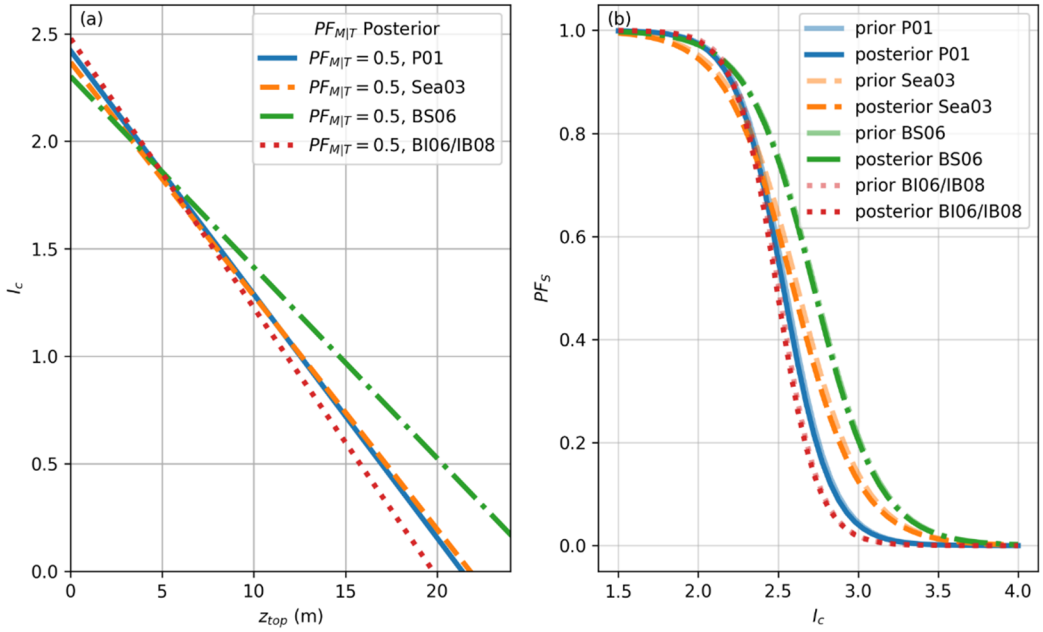

Figure 6-51. Impact of changing initial PF_S model on final P[M] model using the four models recommended in Maurer et al.(2017): P01 (Polito 2001), Sea03 (Seed et al. 2003), BS06 (Bray and Sancio 2006), and BI06/IB08 (Boulanger and Idriss 2006; Idriss and Boulanger 2008). The $PF_{M|T}$ function in (a) shows that the manifestation portion of the model that includes I_c changes to accommodate the change in susceptibility functions. The change in the $PF_{M|T}$ function allow the strongly informed prior PF_S (b) to remain almost unchanged in the posterior.

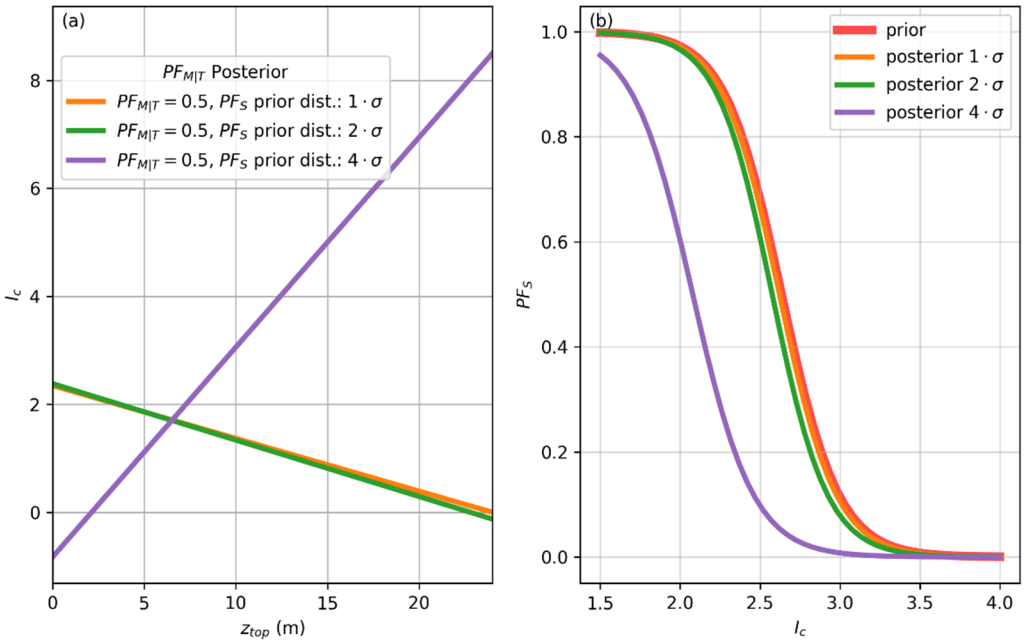

Figure 6-52. Impact of changing the confidence in the original PF_S prior on resulting P[*M*] model. The $PF_{M|T}$ function in (a) shows that the manifestation portion of the model that includes l_c changes to accommodate the change in PF_S functions posteriors (b).

6.4.3 Sensitivity to $PF_{T|S}$ Priors

In this section, the sensitivity of the P[M_P] model to variations in the triggering priors is tested. This was done by considering alternate means and standard deviations for the $PF_{T|S}$ priors' distributions. The effects of these variations on the $PF_{M|T}$ and $PF_{T|S}$ posteriors were evaluated.

First, alternate prior mean values (μ) were considered by increasing or decreasing the mean of each coefficient's prior by five times the standard deviation of that coefficient's distribution and by applying a weak confidence (100 times the standard deviations in the covariance matrix). This produces the prior $PF_{T|S}$ functions plotted in Figure 6-53. Second, different levels of confidence are explored by changing the multiplier on the standard deviations in the covariance matrix. In the first case where only the mean priors are changed, Figure 6-53 shows that the posterior does not noticeably move relative to the prior. In the second case where the standard deviations are increased, despite the posterior having more freedom to move, the posteriors all converge to curves similar to the priors (Figure 6-54).

The $PF_{M|T}$ and $PF_{T|S}$ posteriors all converge on similar values irrespective of the prior μ so long as they are given enough uncertainty on the standard deviations to find the lowest cost model. The insensitivity of the posterior distributions to changes in the mean and uncertainty of the prior indicates that the approach used in Section 6.3 is appropriate for finding a stable $PF_{T|S}$ posterior.

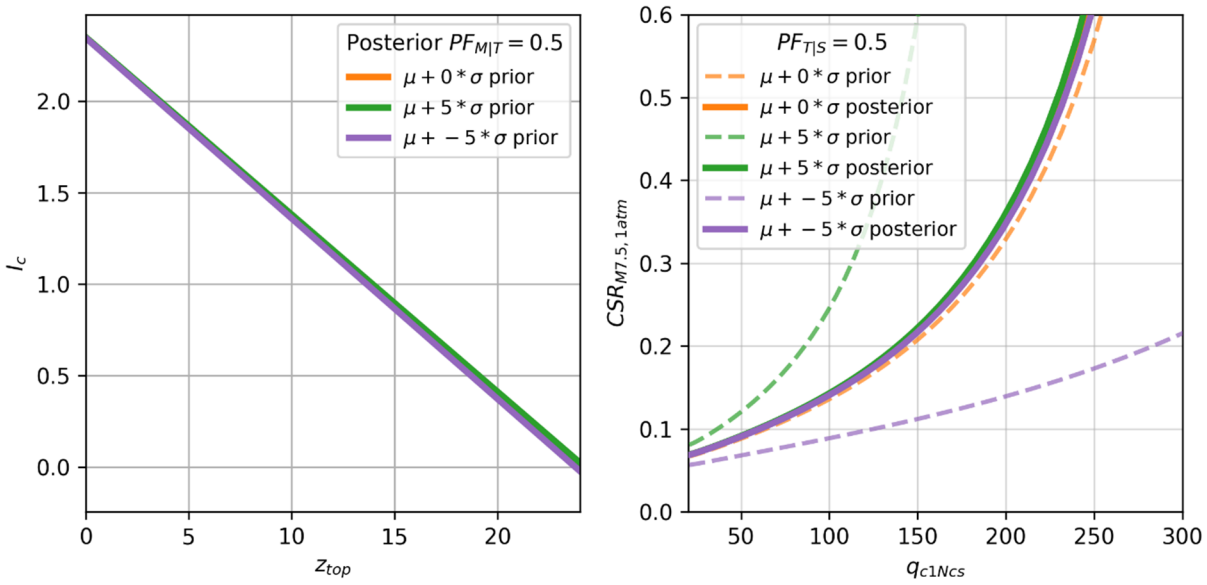

Figure 6-53. Impact of changing the $PF_{T|S}$ prior means on $PF_{M|T}$ and $PF_{T|S}$ posteriors. The posteriors converge on approximately the same values when given a sufficiently large uncertainty on the priors.

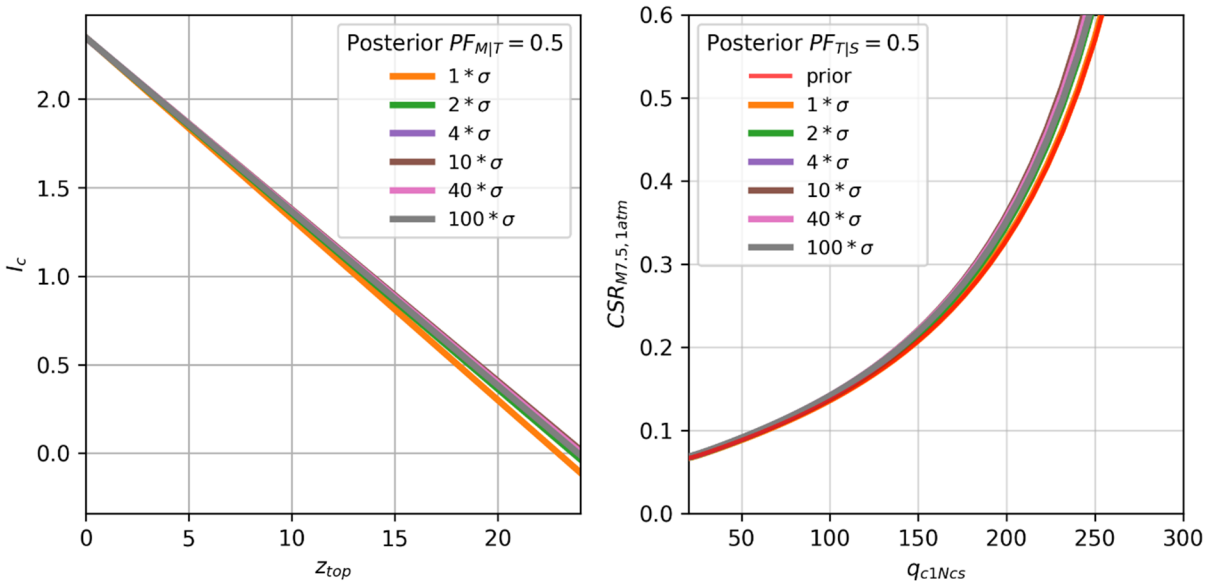

Figure 6-54. Impact of changing the $PF_{T|S}$ prior standard deviations on $PF_{M|T}$ and $PF_{T|S}$ posteriors. The posteriors converge on approximately the same values when uncertainty on the priors is increased by a factor of 2 or higher.

7 DISCUSSION

In this report, we present probabilistic models developed by the SMT for the prediction of liquefaction susceptibility, triggering, and manifestation. We used specific definitions for those terms (Section 2.1) and formulated the models in a manner that is consistent with those definitions. For a given application, particular elements of the three-part modeling framework may be critical. The clear separation of the components allows such determinations to be made, which in turn provides the opportunity to refine such elements through additional testing or data collection to reduce uncertainties for critical applications.

As discussed in Section 2.2, two important philosophies influenced how this work was performed. First, we only use data from the NGL database, and as such the information we relied upon is available to any interested researcher. This promotes transparency and repeatability. Second, while we exercised our experience and judgment throughout the learning and model building process, we translated that judgment into procedures that can be consistently applied across case histories. This too promotes transparency and repeatability, while also reducing the influence of confirmation bias and allowing the models to be used in forward applications in a manner that is consistent with how they were developed.

Our modeling process has Bayesian elements, as described in Section 4.1 and 4.2. The main objective of the modeling process is prediction of a particular effect of liquefaction, namely surface manifestation. Within the Bayesian process that leads to such predictions, several critical model elements must be formulated, which include probability of susceptibility P[S], probability of triggering given the soil is susceptible P[$T|S$], probability of profile manifestation when one or more layers within the profile trigger P[$M_P|T$] (which is conditioned on a series of variables that are not shown here for brevity), and probability of profile manifestation when no layers within it trigger P[$M_P|NT$]. This report presents models for three of these four elements – P[S] (Section 6.1), P[$T|S$] (Section 6.2), and P[$M_P|T$] (Sections 4.4 and 6.3). A model for the P[$M|NT$] component has not been developed yet; while we have ideas about how to form this modeling element, our work has not advanced to the state of a presentable model. For this report, we assumed that P[$M|NT$] = 0.

We recognize that the modeling approach here diverges from precedent in liquefaction modeling, which may be welcomed by some and viewed skeptically by others. We envision several assessments to help geotechnical engineers better understand these models, including:

1) The performance of the proposed models will be compared to the performance of legacy models when applied to the full NGL data inventory. This will allow the predictive power of the different methods to be compared, albeit with some subjectivity given the need for critical layer selection with the legacy models. This is a recommendation for future work.

2) Demonstration of the use of the models for example applications in which stability is the main concern (i.e., manifestation is secondary) vs applications where manifestation is the main concern will help engineers understand how these models would be applied to solve practical problems encountered in engineering design. This is a recommendation for future work.

3) A set of example calculations to show the step-by-step application of the P[M_P] model using data from a case history in the NGL database. This is provided in Appendix B.

Each of the models provided in this report have empirical elements. As such, they are valid only over certain parametric ranges. The P[$T|S$] model mainly applies for Holocene sediments and artificial fills that are relatively granular in composition, although *FC* can range from 0 to 100%. The D_r range for the model is considered to be 20% to 90%. The P[$M_P|T$] model is considered to be applicable for I_c = 0.2 to 6.7, D_r = 0 to 100%, z_{top} = 0 to 49m, and t = 0.01 to 14m. The model is intended to predict manifestation from liquefaction at essentially level ground sites; as such it does not apply for problems involving cyclic mobility, flow slides, or ground failure from non-susceptible soils (i.e., stability problems involving strength loss in clay).

In developing the proposed models, we have adopted some prior modeling conventions that are important, including fines corrections to convert q_{c1N} to q_{c1Ncs} (Section 5.4.1), conversions of D_r to q_{c1N} (Section 6.2.6), and plasticity-based models for liquefaction susceptibility (Section 6.1). Each of these is potentially subject to revision as research progresses. A subsequent phase of the NGL project will investigate the potential for improvement of susceptibility models (Stuedlein et al., 2023b). For fines, there is a need to separate fines effects on q_{c1N} from its effect on triggering. The fines correction to q_{c1N} is also critical, as it jointly accounts for the effects of fines on penetration resistance, and the effects of fines on liquefaction triggering resistance, given a particular state of the soil. In future work, it would be useful to separate these two factors in the model formulation.

This report focuses on using CPT data in model formulation. We have developed SPT-based models in an addendum to this report (SPT-based models, Chapters 10-14) to fulfill Task 9 of this project, as outlined in Section 1.2. Using SPT data instead of CPT data affects the P[$T|S$] model (mainly through the D_r to $N_{1,60}$ relationship) and the surface manifestation model (P[$M_P|T$]) through the use of SPT blow count and index test data in lieu of q_{c1N} and I_c to represent layer characteristics.

7.1 Triggering and Manifestation in Soils with High Relative Density

Some comments received from the MRT appear to question whether the attributes of the proposed triggering model at high relative densities (D_r near 100%) are supported by the available data. To respond to this comment, two considerations must be discussed. The first consideration is related to evidence from laboratory data at high relative densities. This topic was addressed in Section 6.2.3, where *CRR*s are reported from tests on specimens of sand with D_r values up to about 92%, with seven tests between 85-92%. The results show that liquefaction can be triggered in such materials at *CRR*s ranging from 0.25 to 0.85, with an approximate average of 0.35-0.4. Based on the extrapolation of the fitted curves, at D_r = 100% the *CRR* range is 0.35-0.85. We recognize that finite *CRR* values for these dense materials run counter to classical understandings, in which liquefaction is attributed to contraction of granular soils during undrained cyclic shear. High D_r soils dilate, thus do not contract, to reach a critical state. However, before they dilate, they temporarily contract at relatively modest strain levels, thus generating positive pore pressures as measured in these tests. We have taken this data into account in the development of the prior. An alternative approach would be to neglect the data and impose judgment by increasing *CRR* to very large values beyond some limiting D_r. We recognize that some researchers may support such model features, but this was not our choice so as to avoid inconsistency between the prior and laboratory test data.

The second consideration is related to manifestation of liquefaction, which was a major focus of the SMT modeling effort. If a high D_r material triggers, it is unlikely to manifest (incidentally, the NGL database contains no manifestation cases wherein a layer has P[M_L] greater than 0.5 and D_r near 100%). The lack of manifestation is reasoned to be a consequence of two factors:

(1) dense soil, following relatively small-strain pore pressure generation, experiences strong dilation upon straining, which limits strain accumulation in the profile and thus manifestation, and (2) dense soils have low compressibility, which limits the volume of porewater they expel when pore pressures dissipate. We anticipated that the case history data would reflect this expected feature via a strong dependence of manifestation probabilities on q_{c1Ncs}. This was investigated in Section 6.3.4, where the effects of q_{c1Ncs} were in fact rather weak. For this reason, we recommended that the manifestation model be conditioned on other parameters that exert greater influence, which were layer depth and I_c. We are currently considering whether judgment-based adjustments to the model for high D_r conditions can be implemented without compromising model performance.

7.2 Future Work

As we developed the models documented in this report, we have identified other improvements or enhancements that could be incorporated but that were not feasible within the scope and limitations of the current project. These suggestions are listed here as opportunities for future work.

- Refine the P[*S*] as discussed in Section 6.1. For the purposes of the work in this report, we adopted a combined model representing several published susceptibility models for forward analysis to reflect the lack of consensus in the community regarding susceptibility. Over the long-term, a probabilistic susceptibility model should be derived from laboratory test data that may be conditioned on parameters with more predictive power than *PI* or I_c. Ideally, this would be the subject of a dedicated NGL supporting study. A workshop supported by the PEER center and organized mainly by NGL researchers was held in September 2022, with the aim of soliciting community feedback and building consensus on the path forward for susceptibility modeling. A follow-on study after this workshop would ideally provide an improved P[*S*] relationship.

- Re-visit r_d, K_σ, and *MSF* models. In this report, we refined our selections of r_d, K_σ, and *MSF* models as outlined in Sections 5.4.3, 6.2.4, and 6.2.8, respectively, to compute *CSR* for the purposes of assigning layer properties (Section 5.4.3) and regressing preliminary models (Chapter 6). However, preliminary work using a relative importance ranking based on a random forest machine learning algorithm identified several of these parameters as most influential in our model development. This suggests that future efforts to further refine these models would be beneficial.

- Develop a saturation effect to apply to the P[T_L|*S*] function. Herein, we use a simple binary K_{Sat} value of 0 above the groundwater table and 1 below the groundwater table. Alternatively, a saturation effect could be derived from proximity to the groundwater table and/or measured P-wave velocity (V_p).

- Re-examine interpretations of select case histories. Our approach to case history processing combines automated procedures with human inspection and judgment using what we believe are reasonable first-order approximations to assign liquefaction observations to nearby in situ tests, identify layers, and process the characteristics of these layers. This automated process is crucial for analyzing a database as large as the NGL database, and provides a repeatable, consistent, and objective initial view of the data. However, there are currently unidentified nuances in each case history that could potentially affect these modeling decisions. One particularly difficult situation relates to separating instances of ground failure due to liquefaction triggering from instances of

ground failure due to cyclic softening (e.g., a non-susceptible soil as discussed in Section 2.1.1). This could be addressed through excluding such cases that are clearly cases of cyclic softening or through a combined cyclic softening and manifestation model for fine-grained soils.

- Expand the site characterization data considered in model development to include V_S data. Several legacy models mentioned in Section 3.2 are based on V_S and developing a set of V_S-based models to accompany our CPT-based (Task 7) and SPT-based (Task 9) models, or perhaps a combined model using two or more of these in situ data types, would potentially improve model performance.

- Evaluate whether some outliers in the database can be explained by factors not directly considered in the modeling approaches described herein, such as:

    - Partial drainage of susceptible and liquefiable strata

    - Aging effects that may be predictable based on geologic age or V_S

    - Effects of geologic complexity, such as horizontally discontinuous vs relatively continuous strata, which may affect manifestation

    - The effects of mechanisms other than liquefaction, such as cyclic softening of clayey soils not susceptible to liquefaction.

- Evaluate model sensitivity using seismic hazard curves. For example, Dr. Andrew Makdisi at the U.S. Geological Survey (USGS) previously developed a Python script for probabilistic liquefaction hazard analyses (PLHA) using the USGS seismic source models and designed his script to implement new triggering models as they become available, such as those resulting from NGL model development efforts (e.g., this report). This could be a productive investigation, particularly when additional NGL modeling teams have proposed models that could be used to capture epistemic uncertainty.

8 CONCLUSIONS AND NEXT STEPS

In this report, we provided a framework for liquefaction modeling that includes discrete steps for susceptibility, triggering, and manifestation. Each of these models has been updated since the presentation of preliminary models in the Task 4 report and are approaching their final form. In this report, we clarified the meaning of key terms in liquefaction analysis and provided a framework by which the different effects can be evaluated in a consistent and rational manner that is probabilistic and performance-based. In the preceding chapters, we described several significant aspects of the model development process, such as:

- using the extensive NGL case history database to perform analyses that previously would have been logistically impractical (Section 2.3),
- exploring the uncertainties in critical layer selection and finding this process to be non-repeatable within the SMT and compared to legacy models (Section 3.3-3.4),
- using algorithms to process case history data and provide a repeatable, consistent, and objective view of the data (Chapter 5),
- interpolating ground motion intensity measures at case history locations (Section 5.2),
- identifying layers within continuous CPT profiles (Section 5.3),
- estimating *FC* from CPT data using an updated relationship derived using the NGL database (Section 5.4.2) for cases where directly measured *FC* values are not available,
- interpreting susceptibility in a probabilistic manner using CPT data which captures variability and epistemic uncertainty in current models (Section 6.1),
- combining knowledge from laboratory tests and field case histories by using a rich database of laboratory data spanning a wide parameter space to define the Bayesian prior probability, P[T|S] (Section 6.2.7), and
- modeling surface manifestation conditional on liquefaction having triggered within one or more layers through probabilistic analysis of the NGL database (Section 6.3.5); this approach allows for an entire soil profile to be considered within the coupled triggering-manifestation framework (Chapter 4) and does not require identification of a specific critical layer.

The preceding chapters outline the approaches adopted by the SMT to model critical relationships including probability of susceptibility conditional on I_c (P[S]), probability of triggering for susceptible layers conditional on state and stress demand (P[T|S]), and probability of profile manifestation conditional on at least one layer within the profile having triggered (P[M_P|T]). The role of a fourth model component to estimate the probability of profile manifestation when no triggering occurs P[M_P|NT] has also been identified, although the model is not yet formulated. For this report, P[M_P|NT] was assumed to be zero.

The recommended model for estimating P[M_P] is provided in Eq. (6-14) through Eq. (6-20) in Section 6.3.5. For forward analysis where P[T] of a single layer is desired (i.e., ignoring manifestation), we recommend computing P[T] as $PF_{T|S}$ multiplied by PF_S given by Eq. (6-21) through Eq. (6-27) in Section 6.3.7, where $PF_{T|S}$ relies on laboratory data.

Although not designated as a formal Senior Seismic Hazard Analysis Committee (SSHAC) study, the approach and processes we relied on as the SMT to develop our models followed several of the basic SSHAC principles. These included evaluation and integration of available data, clearly defined roles and responsibilities of all project members, and transparent documentation of the SMT decisions needed to develop our findings. In addition, the model presented in a previous version of this report (August 2023) has been peer reviewed by the Modeling Review Team (MRT), with all comments received prior to March 22, 2024 documented in a separate report along with SMT responses (Task 8, Ulmer et al., 2024). The purpose of the MRT review was to provide feedback on the SMT's methods but does not necessarily constitute an endorsement of the SMT's methods, results, or recommendations.

Findings provided in this report are nearing their final form, although future refinements and improvements are possible. The content presented here is subject to change as we refine the methodologies, input parameters, and framework, and based on the review comments from the MRT received after March 22, 2024. Where possible, comments from the MRT have been directly addressed in this report. Comments from the MRT that were not received with sufficient time remaining in the project schedule may be addressed in derivative products (e.g., journal papers) where feasible. While the general concepts behind our approach have been shared in meetings with the NGL Advisory Board and other NGL modeling teams, this document presents these concepts in greater detail and is more up-to-date than any prior presentation. Accordingly, we look forward to receiving feedback from regulatory agencies, topical experts, practicing engineers, and others about the modeling approach and the reasonableness and practicality for application of the models that have been presented.

Although current SMT models are not yet sufficiently mature to ensure that the center body and range of technically defensible interpretations have been captured, the developments thus far advance the ultimate realization of this goal and have set up a framework for doing so. The proposed modeling framework has distinct elements, each with their own uncertainties, that can be separately evaluated in a general (ergodic) sense or for application to a specific project. An additional component of epistemic uncertainty involves the model-to-model uncertainty that will only be evident once the larger NGL modeling efforts mature. An important step in this process is soliciting feedback from the stakeholder agencies and topical experts.

9 REFERENCES

Abdoun, T., M. Ni, R. Dobry, K. Zehtab, A. Marr, and W. El-Sekelly. “Pore Pressure and Kσ Evaluation at High Overburden Pressure Under Field Drainage Conditions. II: Additional Interpretation.” *Journal of Geotechnical and Geoenvironmental Engineering*. Vol 146, No.9. 04022089. doi: 10.1061/(asce)gt.1943-5606.0002302. 2020.

Ancheta, T.D., R.B. Darragh, J.P. Stewart, E. Seyhan, W.J. Silva, B.S.-J. Chiou, K.E. Wooddell, R.W. Graves, A.R. Kottke, D.M. Boore, T. Kishida, and J.L. Donahue. “NGA-West2 Database.” *Earthquake Spectra*. Vol. 30, No. 3. p. 989–1,005. 2014.

Andrus, R.D. and K.H.I. Stokoe. “Liquefaction Resistance of Soils from Shear-Wave Velocity.” *Journal of Geotechnical and Geoenvironmental Engineering*. Vol. 126, Nol. 11. pp. 1,015–1,025. 2000.

Andrus, R.D., K.H. Stokoe, R.M. Chung, and C.H. Juang. “Guidelines for Evaluating Liquefaction Resistance Using Shear Wave Velocity Measurements and Simplified Procedures.” NIST GCR 03- 854. Gaithersburg, Maryland: National Institute of Standards and Technology. 2003.

Arab, A., I. Shahrour, and L. Lancelot. “Estudio En Laboratorio Sobre Licuefacción de Arena Parcialmente Saturada.” *Journal Iberian Geology*. Vol. 37, No. 1. pp. 29–36. https://doi.org/10.5209/rev_JIGE.2011.v37.n1.2. 2011.

Bassett, R. and J. Deride. “Maximum a Posteriori Estimators as a Limit of Bayes Estimators.” *Math Program*. Vol. 174. https://doi.org/10.1007/s10107-018-1241-0. 2016.

Bengfort, B., L. Gray, R. Bilbro, R. Prema, D. Patrick, K. McIntyre, M. Morrison, A. Ojeda, E. Schmierer, A. Morris, S. Molin, and S. Swadik. “Yellowbrick v1.5 (1.5). Zenodo. DOI 10.5281/zenodo.1206239. 2022.

Bilge, T. and K. Cetin. “Effect of Vertical Effective Stress on Liquefaction Triggering Analyses.” *Seventh National Conference on Earthquake Engineering*. May 30-June 3, Istanbul, Turkey. (in Turkish). 2011.

Bodenmann, L., J. W. Baker, and B. Stojadinovic. “Accounting for Path and Site Effects in Spatial Ground-motion Correlation Models Using Bayesian Inference. *Natural Hazards and Earth System Sciences*. Vol. 23. pp. 2,387–2,402. 2023.

Boore, D.M., J.P. Stewart, E. Seyhan, and G.M. Atkinson. “NGA-West2 Equations for Predicting PGA, PGV, and 5% Damped PSA for Shallow Crustal Earthquakes.” *Earthquake Spectra*. Vol 30, No. 3. pp.1,057–1,085. 2014.

Boulanger, R.W. “Susceptibility Criteria for Selecting Engineering Procedures.” in *PEER Workshop on Liquefaction Susceptibility*, PEER Report 2023/02, Pacific Earthquake Engineering Research Center, UC Berkeley (headquarters). 207p. 2023.

Boulanger, R.W. “Relating Kα to a Relative State Parameter Index.” *Journal of Geotechnical and Geoenvironmental Engineering*. Vol. 129, No. 10. pp. 770–773. 2003a.

Boulanger, R.W. “High Overburden Stress Effects in Liquefaction Analyses.” *Journal on Geotechnical and Geoenvironmental Engineering*. Vol. 129, No. 12. pp.1,071–1,082. 2003b.

Boulanger, R.W. and J.T. DeJong. “Inverse Filtering Procedure to Correct Cone Penetration Data for Thin-layer and Transition Effects.” Proceedings of the 4th International Symposium on Cone Penetration Testing. M. Hicks, F. Pisano, and J. Peuchen, eds. Delft University of Technology. The Netherlands. 2018. <https://par.nsf.gov/biblio/10079692> (Accessed date 27 August 2022).

Boulanger, R.W. and I.M. Idriss. “CPT-Based Liquefaction Triggering Procedure.” *Journal of Geotechnical and Geoenvironmental Engineering*. Vol. 142, No. 2. 2016.

Boulanger, R. and I.M. Idriss. “CPT and SPT Based Liquefaction Triggering Procedures.” Report No. UCD/CGM-14/01. Center for Geotechnical Modeling. University of California, Davis. 2014.

Boulanger, R.W. and I.M. Idriss. “Probabilistic Standard Penetration Test-based Liquefaction-Triggering Procedure.” *Journal of Geotechnical and Geoenvironmental Engineering*. Vol. 138, No. 10. pp.1,185–1,195. 2012.

Boulanger, R.W. and I.M. Idriss. “Liquefaction Susceptibility Criteria for Silts and Clays.” *Journal of Geotechnical and Geoenvironmental Engineering*. Vol. 132, No. 11, pp. 1,413–1,426. 2006.

Boulanger, R.W., L.H. Mejia, and I.M. Idriss. “Liquefaction at Moss Landing During Loma Prieta Earthquake.” *Journal of Geotechnical and Geoenvironmental Engineering.* Vol. 123, No. 5. pp. 453–467. 1997.

Boulanger, R.W., I.M. Idriss, and L.H. Mejia. “Investigation and Evaluation of Liquefaction Related Ground Displacements at Moss Landing During the 1989 Loma Prieta Earthquake.” Report No. UCD/CGM-95/02. Center for Geotechnical Modeling, Department of Civil & Environmental Engineering, University of California Davis. 1995.

Box, G.E.P. and D.R. Cox. “An Analysis of Transformations.” *Journal of the Royal Statistical Society Series B Methodology*. Vol. 26, No. 2. pp. 211–252. 1964.

Brandenberg, S.J., P. Zimmaro, J.P. Stewart, D.Y. Kwak, K.W. Franke, R.E.S. Moss, K.O. Çetin, G. Can, M. Ilgac, J. Stamatakos, T. Weaver, and S.L. Kramer. “Next-Generation Liquefaction Database.” *Earthquake Spectra*. Vol. 36, No. 2. pp. 939–959. 2020.

Bray, J.D., R.B. Sancio, H.T. Durgunoðlu, A. Önalp, T.L. Youd, J.P. Stewart, R.B. Seed, K.O. Cetin, E. Bol, M.B. Baturay, C. Christensen, and T. Karadayýlar. “Subsurface Characterization at Ground Failure Sites in Adapazari, Turkey. *Journal of Geotechnical and Geoenvironmental Engineering*. ASCE. Vol.130, No. 7. pp. 673–685. 2004.

Bray, J.D. and R.B. Sancio. “Assessment of the Liquefaction Susceptibility of Fine-Grained Soils.” *Journal of Geotechnical and Geoenvironmental Engineering*. Vol 132, No. 9. pp. 1,165–1,177. September 2006.

Bullock, Z., S. Dashti, A.B. Liel, K.A. Porter, and B. Maurer. “Probabilistic Liquefaction Triggering and Manifestation Models Based on Cumulative Absolute Velocity. *Journal of Geotechnical and Geoenvironmental Engineering*. Vol. 148, No. 3. 04021196. 2022.

Bullock, Z., S. Dashti, A.B. Liel, K.A. Porter, and Z. Karimi. “Assessment Supporting the Use of Outcropping Rock Evolutionary Intensity Measures for Prediction of Liquefaction Consequences.” *Earthquake Spectra*. Vol. 35, No. 4. pp. 1,899–1,926. 2019.

Campbell, K.W. and Y. Bozorgnia. “Ground-motion Model for the Standardized Version of Cumulative Absolute Velocity. *Earthquake Spectra*. Vol. 39, No. 1. pp. 634–652. 2023.

Campbell, K.W. and Y. Bozorgnia. “Ground Motion Models for the Horizontal Components of Arias Intensity (AI) and Cumulative Absolute Velocity (CAV) Using the NGA-West2 Database.” *Earthquake Spectra*. Vol. 35, No. 3. pp. 1,289–1,310. 2019.

Carlton, B., K. Ulmer, T. Nguyen, and Q. Parker. “Next Generation Liquefaction (NGL)-Supporting Studies: Overburden and Initial Shear Stress.” DesignSafe-CI. https://doi.org/10.17603/ds2-c9fr-x257 v1. 2023.

Carraro, J.A.H., P. Bandini, and R. Salgado. “Liquefaction Resistance of Clean and Non-plastic Silty Sands Based on Cone Penetration Resistance.” *Journal of Geotechnical and Geoenvironmental Engineering.* Vol. 129, No 11. pp. 408-415. 2003.

Cauchy, A. “Méthode générale pour la résolution des systèmes d'équations simultanées.” Comptes rendus de l'Académie des Sciences. Paris, Vol. 25. pp. 536–538. 1847.

CDWR. “The August 1, 1975 Oroville Earthquake Investigation.” California Department of Water Resources. Supplement to Bulletin 203-78. 1989.

CDWR. “Stability Investigation of Antelope Dam.” California Department of Water Resources. 1985.

Cetin, K.O. and H.T. Bilge. “Stress Scaling Factors for Seismic Soil Liquefaction Engineering Problems: A Performance-based Approach. In Perspectives on Earthquake Geotechnical Engineering. A. Ansal and M. Sakr, editors. Basel, Switzerland: Springer. 2014.

Cetin, K.O. and H.T. Bilge. “Performance-based Assessment of Magnitude (duration) Scaling Factors.” *Journal of Geotechnical and Geoenvironmental Engineering*. Vol. 138, No. 3. pp. 324–334. 2012.

Cetin, K.O. and C. Ozan. “CPT-based Probabilistic Soil Characterization and Classification.” *Journal of Geotechnical and Geoenvironmental Engineering.* Vol. 135, No. 1. 84-107. doi: 10.1061/(ASCE)1090-0241(2009)135:1(84). 2009.

Cetin, K.O., R.B. Seed, R.E. Kayen, R.E.S. Moss, H.T. Bilge, M. Ilgac, and K. Chowdhury. “SPT-based Probabilistic and Deterministic Assessment of Seismic Soil Liquefaction Triggering Hazard. *Soil Dynamics and Earthquake Engineering*. Vol. 115. pp. 698–709. doi:-10.1016/j.soildyn.2018.09.012. 2018.

Cetin, K.O., R.B. Seed, A. Der Kiureghian, K. Tokimatsu, L.F. Harder, R.E. Kayen, and R.E.S. Moss. “Standard Penetration Test-based Probabilistic and Deterministic Assessment of Seismic Soil Liquefaction Potential.” *Journal of Geotechnical and Geoenvironmental Engineering*. Vol. 130, No. 12. pp. 1,314–1,340. 2004.

Cetin, K.O., R.B. Seed, R.E.S. Moss, A.K. Der Kiureghian, K. Tokimatsu, L.F. Harder, Jr., R.E. Kayen, and I.M. Idriss. “Field Performance Case Histories for SPT-based Evaluation of Soil Liquefaction Triggering Hazard.” Geotechnical Research Report No. UCB/GT-2000/09. Department of Civil and Environmental Engineering. University of California, Berkeley, California. 2000.

Ching, J., J.S. Wang, H.C. Juan, and C.S. Ku. “Cone Penetration Test (CPT)-based Stratigraphic Profiling Using the Wavelet Transform Modulus Maxima Method.” *Canadian Geotechnical Journal*. Vol. 52, No. 1. pp. 1,993–2,007. 2015.

Contreras, V., J.P. Stewart, T Kishida, R.B. Darragh, B.S.J. Chiou, S. Mazzoni, R.R. Youngs, N.M. Kuehn, S.K. Ahdi, K. Wooddell, R. Boroschek, F. Rojas, and J. Ordenes. “NGA-sub Source and Path Database.” *Earthquake Spectra.* Vol. 38, No. 2. pp. 799–840. 2022.

Cubrinovski M, and K. Ishihara. “Maximum and Minimum Void Ratio Characteristics of Sands.” *Soils and Foundations*. Vol. 42, No. 6. pp. 65–78. 2002.

Cubrinovski, M., A. Rhodes, N. Ntritsos, and S. van Ballegooy. “System Response of Liquefiable Deposits.” *Soil Dynamics and Earthquake Engineering.* Vol. 124. pp. 212–229. 2019.

Dobry R., R. Ladd, F. Yokel, R. Chung, D. Powell. “Prediction of Pore Water Pressure Buildup and Liquefaction of Sands During Earthquakes by the Cyclic Strain Method.” NBS Building Science Series 138. National Bureau of Standards. Washington, DC. 1982.

Ecemis, N. and M. Karaman. “Influence of Non-low Plastic Fines on Cone Penetration and Liquefaction Resistance.” *Engineering Geology*. Vol.181. pp. 48-57. 2014.

Gagniuc, P. A. *Markov chains: from theory to implementation and experimentation*. Hoboken, New Jersey: John Wiley & Sons. 2017.

Gelman, A. “Prior Distributions for Variance Parameters in Hierarchical Models (comment on article by Browne and Draper).” *Bayesian Analysis*. Vol. 1 No. 3. https://doi.org/10.1214/06-BA117A. 2006.

Gelman, A., J.B. Carlin, H.S. Stern, D.B. Dunson, A. Vehtari, and D.B. Rubin. *Bayesian data analysis*. Texts in statistical science series. Boca Raton London New York: CRC Press, Taylor and Francis Group. 2014.

GeoLogismiki. “CLiq User’s Manual”. 61p. 2018. https://geologismiki.gr/Documents/CLiq/CLiq%20manual.pdf

Geyin, M., A.J. Baird, and B.W. Maurer. “Field Assessment of Liquefaction Prediction Models Based on Geotechnical Versus Geospatial Data, with Lessons for Each.” *Earthquake Spectra.* Vol. 36, No. 3. pp. 1,386–1,411. 2020a.

Geyin, M., B. Maurer, B. Bradley, R. Green, and S. van Ballegooy. “CPT-Based Liquefaction Case Histories Resulting from the 2010-2016 Canterbury, New Zealand, Earthquakes: A Curated Digital Dataset (Version 2).” Designsafe-CI. https://doi.org/10.17603/ds2-tygh-ht91. 2020b.

Green, R.A. and S.M. Olson. “Interpretation of Liquefaction Field Case Histories for Use in Developing Liquefaction Triggering Curves.” 6th International Conference on Earthquake Geotechnical Engineering, Christchurch, NZ. 2015.

Green, R.A., C. Wood, B. Cox, M. Cubrinovski, L. Wotherspoon, B. Bradley, T. Algie, J. Allen, A. Bradshaw, and G. Rix. “Use of DCP and SASW Tests to Evaluate Liquefaction Potential: Predictions vs. Observations During the Recent New Zealand Earthquakes.” *Seismological Research Letters.* Vol. 82, No. 6. pp. 927–938. 2011.

Harder, L.F. and R.W. Boulanger. “Application of K-Sigma and K-Alpha Correction Factors.” *Proceedings of the NCEER Workshop on Evaluation of Liquefaction Resistance of Soils, Technical Report NCEER-97-0022*. T.L. Youd and I.M. Idriss, eds. Buffalo, New York: National Center for Earthquake Engineering Research, SUNY. pp. 167–190. 1997.

Hatanaka, M., A. Uchida, and H. Oh-Oka. “Correlation Between the Liquefaction Strengths of Saturated Sands Obtained by In-situ Freezing Method and Rotary-type Triple Tube Method.” *Soils and Foundations, Japanese Society of Soil Mechanics and Foundation Engineering.* Vol. 35, No. 2. pp. 67–75. 1995.

Hirschhorn, R. and T. Schonberg. “Replication.” *Reference module in neuroscience and biobehavioral psychology*, Elsevier, 2024.

Hoffman, M. D., and A. Gelman. “The No-U-Turn Sampler: Adaptively Setting Path Lengths in Hamiltonian Monte Carlo.” *Journal of Machine Learning Research*. Vol. 15 No. 47. pp. 1593–1623. 2014.

Hoffman, M.D. and A. Gelman. “The No-U-Turn Sampler: Adaptively Setting Path Lengths in Hamiltonian Monte Carlo.” arXiv. https://doi.org/10.48550/ARXIV.1111.4246. 2011.

Holzer, T.L. and T.L. Youd. “Liquefaction, Ground Oscillation, and Soil Deformation at the Wildlife Array, California.” *Bulletin Seismological Society of America.* Vol. 97, No. 3. pp. 961–976. 2007.

Hossain, A.M., R.D. Andrus, and W.M. Kamp. “Correcting Liquefaction Resistance of Unsaturated Soil Using Wave Velocity.” *Journal of Geotechnical and Geoenvironmental Engineering*. Vol. 139, No. 2. pp. 277–287. 2013.

Huang, A.-B., Y.-Y. Tai, W.F. Lee, and Y.-T. Huang. “Field Evaluation of the Cyclic Strength Versus Cone Tip Resistance Correlation in Silty Sands.” *Soils and Foundations*. Vol. 49, No. 4. pp. 557–567. 2009.

Huang, Y.T., A.B. Huang, Y.C. Kuo, and M.D. Tsai. “A Laboratory Study on the Undrained Strength of a Silty Sand from Central Western Taiwan.” *Soil Dynamics and Earthquake Engineering*. Vol. 24, No. 9–10. pp. 733–743. 2004.

Huang, A., H.H. Hsu Bin, J.W. Chang, A.B. Huang, H.H. Hsu, and J.W. Chang. “The Behavior of a Compressible Silty Fine Sand.” *Canadian Geotechnical Journal*. Vol. 36. pp. 88–101. 1999.

Hudson, K.S., K.J. Ulmer, P. Zimmaro, S.L. Kramer, J.P. Stewart, and S.J. Brandenberg. “Unsupervised Machine Learning for Detecting Soil Layer Boundaries from Cone Penetration Test Data.” *Earthquake Engineering and Structural Dynamics*. doi: 10.1002/eqe.3961. 2023a.

Hudson, K.S., S.J. Brandenberg, P. Zimmaro, K.J. Ulmer, S.L. Kramer, and J.P. Stewart. “Kriging Interpolation of Ground Motion Residuals at Liquefaction Case History Sites.” *GeoCongress 2023*, Los Angeles, California. 2023b.

Hudson, K., K. Ulmer, P. Zimmaro, S, Kramer, J. Stewart, and S. Brandenberg. “Relationship Between Fines Content (FC) and Soil Behavior Type Index (Ic).” in Next Generation Liquefaction - Supported Modeling Team. DesignSafe-CI. 2023c. https://doi.org/10.17603/ds2-7e6k-ca26 v1.

Hudson, K.S., S.J. Brandenberg, P. Zimmaro, K.J. Ulmer, S.L. Kramer, and J.P. Stewart. “Relationship Between Fines Content and Soil Behavior Type Index at Liquefaction Sites." *Journal of Geotechnical and Geoenvironmental Engineering*. Submitted for review. 2023d.

Hutabarat, D. and J.D. Bray. “Estimating the Severity of Liquefaction Ejecta Using the Cone Penetration Test. *Journal of Geotechnical and Geoenvironmental Engineering.* Vol. 148, No. 3. doi: 2022. https://doi.org/10.1061/(ASCE)GT.1943-5606.0002744

Hutabarat, D. and J.D. Bray. “Effective Stress Analysis of Liquefiable Sites to Estimate the Severity of Sediment Ejecta. *Journal of Geotechnical and Geoenvironmental Engineering*. Vol. 147, No. 5. doi: 2021. <https://doi.org/10.1061/(ASCE)GT.1943-5606.0002503>

Idriss, I.M. “An Update to the Seed-Idriss Simplified Procedure for Evaluating Liquefaction Potential.” Proceedings, TRB Workshop on New Approaches to Liquefaction, Publication No. FHWARD-99-165, Federal Highway Administration. January. 1999.

Idriss I.M. and R.W. Boulanger. “Examination of SPT-based Liquefaction Triggering Correlations. *Earthquake Spectra*. Vol. 28, No. 3. pp. 989–1018, 2012.

Idriss, I.M. and R.W. Boulanger. “Soil Liquefaction During Earthquakes.” D. Becker, ed. *Earthquake Engineering Research Institute*. 2008.

Idriss, I.M., K. Sadigh, and A. Menoret. “Evaluation of Seismic Stability of Perris Dam.” Sacramento, California. 1975.

Ishihara, K. “Stability of Natural Deposits During Earthquakes. Proceedings of the 11th International Conference on Soil Mechanics and Foundation Engineering. San Francisco, California. USA. pp. 1, 321–1,376. 1985.

Ishihara, K. and M. Yoshimine. “Evaluation of Settlements in Sand Deposits Following Liquefaction During Earthquakes.” *Soils and Foundations*. Vol. 32, No. 1. pp. 173–88. 1992.

Ishihara, K. and Y. Koga. “Case Studies of Liquefaction in the 1964 Niigata Earthquake.” *Soils and Foundations*. Vol.21, No. 3. pp.35–52. 1981.

Ishihara, K., H. Tsuchiya, Y. Huang, and K. Kamada. “Keynote Lecture: Recent Studies on Liquefaction Resistance of Sand–Effect of Saturation.” Proceedings of 4th International Conference on Recent Advance in Geotechnical Earthquake Engineering and Soil Dynamics, San Diego, California. 2001.

Ishihara, K., M.L. Silver, and H. Kitagawa. “Cyclic Strength of Undisturbed Sands Obtained by a Piston Sampler.” *Soils and Foundations, Japanese Society of Soil Mechanics and Foundation Engineering*. Vol. 19, No. 2. pp. 61–76. 1979.

Ishihara, K., M.L. Silver, and H. Kitagawa. “Cyclic Strengths of Undisturbed Sands Obtained by Large Diameter Sampling.” *Soils and Foundations, Japanese Society of Soil Mechanics and Foundation Engineering*. Vol. 18, No. 4. pp. 61–76. 1978.

Iwasaki, T., F. Tatsuoka, K. Tokida, and S. Yasuda. “A Practical Method for Assessing Soil Liquefaction Potential Based on Case Studies at Various sites in Japan.” Proceedings of the 2nd International Conference on Microzonation, San Francisco. p. 885−896. 1978.

Jefferies, M. and K. Been. S*oil liquefaction: A critical state approach*. 2nd edition. Florida: Taylor & Francis Group. 2016.

Johnson, N. “Systems of Frequency Curves Generated by Methods of Translation.” *Biometrika*. Vol. 36, No. 1/2. pp. 149–176. doi: 10.2307/2332539. 1949.

Karimi, Z. and S. Dashti. “Ground Motion Intensity Measures to Evaluate II: The Performance of Shallow-founded Structures on Liquefiable Ground. *Earthquake Spectra*. Vol. 33, No. 1. pp. 277–298. 2017.

Kayen, R.E. and J.K. Mitchell. “Assessment of Liquefaction Potential During Earthquakes by Arias Intensity.” *Journal of Geotechnical and Geoenvironmental Engineering*. Vol. 123, No. 12. pp.1,162–1,174. 1997.

Kayen, R. E., Mitchell, J. K., Seed, R. B., & Nishio, S. Y. “Soil Liquefaction in the East Bay During the Earthquake.” *U.S. Geological Survey. Prof. Paper 1551-B*, Editor T.L. Holzer. 1998.

Kayen, R.R., R.E.S. Moss, E.R. Thompson, R.B. Seed, K.O. Cetin, A. Derkiureghian, Y. Tanaka, and K. Tokimatsu. “Shear Wave Velocity-based Probabilistic and Deterministic Assessment of Seismic Soil Liquefaction Potential. *Journal of Geotechnical and Geoenvironmental Engineering*. Vol. 139, No. 3. pp. 407–419. 2013.

Kishida, T. and C.-C. Tsai. “Seismic Demand of the Liquefaction Potential with Equivalent Number of Cycles for Probabilistic Seismic Hazard Analysis. *Journal of Geotechnical and Geoenvironmental Engineering*. Vol. 140, No. 3. doi: 10.1061/(ASCE)GT.1943-5606.0001033. 2014.

Kokusho, T. and S. Tanimoto. “Energy Capacity Versus Liquefaction Strength Investigated by Cyclic Triaxial Tests on Intact Soils.” *Journal of Geotechnical and Geoenvironmental Engineering.* Vol. 147, No.4. 04021006. 2021.

Kokusho, T., Y. Nagao, F. Ito, and T. Fukuyama, “Aging Effect on Sand Liquefaction Observed During the 2011 Earthquake and Basic Laboratory Studies.” Proceedings of the International

Symposium on Engineering Lessons Learned from the 2011 Great East Japan Earthquake, Tokyo, Japan. pp. 759–770. 2012.

Kramer, S.L. and R. A. Mitchell. “Ground Motion Intensity Measures for Liquefaction Hazard Evaluation. *Earthquake Spectra*. Vol. 22, No. 2. pp. 413–438. 2006.

Kramer, S.L., S.S. Sideras, and M.W. Greenfield. “The Timing of Liquefaction and Its Utility in Liquefaction Hazard Evaluation.” *Soil Dynamics and Earthquake Engineering.* Vol. 91. pp. 133–146. 2016.

Lasley, S.J., R.A. Green, & A. Rodriguez-Marek. “New stress reduction coefficient relationship for liquefaction triggering analyses.” *Journal of Geotechnical and Geoenvironmental Engineering*, Vol. 142, No. 11, 06016013. 2016.

Lasley, S.J., R.A. Green, & A. Rodriguez-Marek. “Number of equivalent stress cycles for liquefaction evaluations in active tectonic and stable continental regimes.” *Journal of Geotechnical and Geoenvironmental Engineering*, Vol. 143, No. 4, 04016116. 2017.

Liao, S., S.C., and R.V. Whitman. “Overburden Correction Factor for SPT in Sand.” *Journal of Geotechnical and Geoenvironmental Engineering.* Vol. 112, No. 3. pp. 373–377. 1986.

Liao, S.S.C., D. Veneziano, and R.V. Whitman. “Regression Models for Evaluating Liquefaction Probability.” *Journal of Geotechnical Engineering*. Vol. 114, No. 4. pp. 389–411. 1988.

Liu, A., J. Stewart, N. Abrahamson, and Y. Moriwaki. “Equivalent Number of Uniform Stress Cycles for Soil Liquefaction Analysis.” *Journal of Earthquake Engineering.* Vol. 127, No. 12. pp. 1,017–1,026. 2001.

Markov, A. A. “An Example of Statistical Investigation of the Text Eugene Onegin Concerning the Connection of Samples in Chains.” *Sci. Context*, Vol. 19 No. 4. pp. 591–600. https://doi.org/10.1017/S0269889706001074. 2006.

Matsuo, O. “Simplified Procedure for Assessing Liquefaction Potential of Soils in the Specifications for Highway Bridges.” *Journal of Geotechnical Engineering* JSCE 757(III-66). pp. 1-20 (in Japanese). 2004.

Maurer, B.W., R.A. Green, and O.-D.S. Taylor. “Moving Towards an Improved Index for Assessing Liquefaction Hazard: Lessons from Historical Data.” *Soils and Foundations*. Vol. 55, No. 4. pp. 778–787. 2015a.

Maurer, B.W., R.A. Green, M. Cubrinovski, and B.A. Bradley. “Assessment of CPT-based Methods for Liquefaction Evaluation in a Liquefaction Potential Index Framework.” *Géotechnique*. Vol. 65, No. 5. pp. 328–336. 2015b.

Maurer, B.W., R.A. Green, S. van Ballegooy, and L. Wotherspoon. “Assessing Liquefaction Susceptibility using the CPT Soil Behavior Type Index.” Proceedings of the 3rd International Conference on Performance-Based Design in Earthquake Geotechnical Engineering (PBDIII). 2017.

Molina-Gómez, F., D. Cordeiro, C. Ferreira, and A. Viana da Fonseca. “Soil Stratigraphy from Seismic Piezocone Data and Multivariate Clustering in Alluvial Soil Deposits: Experience in the

Lower Tagus Valley Region." Cone Penetration Testing 2022. Gottardi & Tonni (eds). doi: 10.1201/9781003308829-84. 2022.

Montgomery, J., R.W. Boulanger, and L.F. Harder Jr. "Examination of the Kσ Overburden Correction Factor on Liquefaction Resistance. Rep. No. UCD/CGM-12-02. Davis, CA: Center for Geotechnical Modeling, Dept. of Civil and Environmental Engineering, Univ. of California. 2012.

Montgomery, J., R.W. Boulanger, and L.F.J. Harder. "Examination of the $K\sigma$ Overburden Correction Factor on Liquefaction Resistance." *Journal of Geotechnical and Geoenvironmental Engineering*. Vol. 140, No. 12. pp. 04014066. 2014

Moss, R.E.S. *CPT-based probabilistic assessment of seismic soil liquefaction initiation*. Ph.D. Dissertation, University of California, Berkeley. 2003.

Moss, R.E.S., R.B. Seed, R.E. Kayen, J.P. Stewart, A. Der Kiureghian, and K.O. Cetin. "CPT-based Probabilistic and Deterministic Assessment of In Situ Seismic Soil Liquefaction Potential." *Journal of Geotechnical and Geoenvironmental Engineering*. Vol. 132, No. 8. pp. 1,032–1,051. 2006.

NASEM. "State of the Art and Practice in the Assessment of Earthquake-Induced Soil Liquefaction and Its Consequences." Washington, DC: National Academies of Sciences, Engineering, and Medicine. The National Academies Press. doi: 1017226/23474. 2021.<https://doi.org/10.17226/23474>.

NASEM. "State of the Art and Practice in the Assessment of Earthquake-Induced Soil Liquefaction and Its Consequences." Washington, DC: National Academies of Sciences, Engineering, and Medicine. The National Academies Press, prepublication copy. 2016. doi: 1017226/23474. <https://doi.org/10.17226/23474>.

NGL. "Next Generation Liquefaction Ddatabase." 2021. <https://www.nextgenerationliquefaction.org/>.

Ni, M., T. Abdoun, R. Dobry, K. Zehtab, A. Marr, and W. El-Sekelly. "Pore Pressure and Kσ Evaluation at High Overburden Pressure Under Field Drainage Conditions. I: Centrifuge Experiments." *Journal of Geotechnical and Geoenvironmental Engineering*. Vol. 146, No. 9. 04020088. doi: 10.1061/(ASCE)GT.1943-5606.0002303. 2020.

Nickerson, R.S. "Confirmation Bias: A Ubiquitous Phenomenon in Many Guises." *Review of General Psychology*. Vol. *2,* No 2. pp. 175–220. 1998.

Nielsen, F. "Hierarchical Clustering." 2016. 10.1007/978-3-319-21903-5_8.

Ntritsos, N. and M. Cubrinovski. "A CPT-based Effective Stress Analysis Procedure for Liquefaction Assessment." *Soil Dynamics and Earthquake Engineering*. Vol. 131. 2020.

_____. “Procedures and Criteria for Assessing Seismic Soil Liquefaction at Nuclear Power Plant Sites.” Regulatory Guide 1.198. Washington, DC: U.S. Nuclear Regulatory Commission. 2003. <https://www.nrc.gov/docs/ML0332/ML033280143.pdf> (Accessed date 27 August 2022).

O’Donnell, S.T., B.E. Rittmann, and E. Kavazanjian. “MIDP: Liquefaction Mitigation via Microbial Denitrification as a Two-Stage Profess. I: Desaturation.” *Journal of Geotechnical and Geoenvironmental Engineering.* Vol. 143, No. 12. doi: 10.1061/(ASCE)GT.1943-5606.0001818. 2017.

Okamura, M., M. Ishihara, and T. Oshita. “Liquefaction Resistance of Sand Deposit Improved with Sand Compaction Piles.” *Soils and Foundations*. Vol. 43, No. 5. pp. 175–187. 2003.

Okamura, M., and Y. Soga. “Effects of Pore Fluid Compressibility on Liquefaction Resistance of Partially Saturated Sand.” *Soils Found*., Vol. 46, No. 5. pp. 695–700. https://doi.org/10.3208/sandf.46.695. 2006.

Park, S.-S. and Y.-S. Kim. “Liquefaction Resistance of Sands Containing Plastic Fines with Different Plasticity.” *Journal of Geotechnical and Geoenvironmental Engineering.* Vol. 139, No, 5. pp. 825–830. 2013.

Parker, G.A., J.P. Stewart, D.M. Boore, G.M. Atkinson, and B. Hassani. “NGA-subduction Global Ground Motion Models with Regional Adjustment Factors. *Earthquake Spectra*. Vol. 38, No.1. pp. 456–493. 2022.

Pedregosa, F., G. Varoquaux, A. Gramfort, V. Michel, B. Thirion, O. Grisel, M. Blondel, P. Prettenhofer, R. Weiss, V. Dubourg, J. Vanderplas, A. Passos, D. Cournapeau, M. Brucher, M. Perrot, and E. Duchesnay. “Scikit-learn: Machine Learning in Python.” *Journal of Machine Learning Research*. Vol. 12. pp. 2,825–2,830. 2011.

PEER “Documenting Incidents of Ground Failure Resulting from the August 17, 1999 Kocaeli, Turkey Earthquake.” 2000. https://apps.peer.berkeley.edu/publications/turkey/adapazari/index.html

Pillai, V.S. and P.M. Byrne. “Effect of Overburden Pressure on Liquefaction Resistance of Sand.” *Canadian Geotechnical Journal*. Vol. 31, No. 1. pp. 53–60. 1994.

Pillai, V.S. and R.A Stewart. “Evaluation of Liquefaction Potential of Foundation Soils at Duncan Dam.” *Canadian Geotechnical Journal*. Vol. 31, No. 6. pp. 951–966. 1994.

Polito, C.P. “Plasticity Based Liquefaction Criteria.” Proceedings of the 4th International Conference on Recent Advances in Geotechnical Earthquake Engineering and Soil Dynamics, University of Missouri-Rolla, Rolla, Mo., Paper No. 1.33. 2001.

Polito, C.P. and J.R. Martin. “Effects of Nonplastic Fines on the Liquefaction Resistance of Sands.” *Journal of Geotechnical and Geoenvironmental Engineering,* ASCE. Vol 127, No. 5. pp. 408–415. 2001.

Porcino, D. and V. Diano. “Laboratory Study on Pore Pressure Generation and Liquefaction of Low-Plasticity Silty Sandy Soils During the 2012 Earthquake in Italy.” *Journal of Geotechnical and Geoenvironmental Engineering*. Vol. 142, No. 10. 2016. 04016048.

Pretell, R., S.J. Brandenberg, J.P. Stewart. "Ground motion intensity measures at liquefaction field case history sites." *Report GIRS-2024-02*, B. John Garrick Risk Institute, Natural Hazards Risk and Resiliency Research Center, UCLA (Center Headquarters), 2024.

PWRI. “Re-examination of Evaluation Method of Liquefaction Strength of Sand Containing Fine Particles.” Report #4352, Public Works Research Institute. National Research and Development Corporation. 2016.

Pyke, R.M., C.K. Chan, and H.B. Seed. “Settlement of Sands Under Multidirectional Shaking.” *Journal of the Geotechnical Engineering Division, ASCE.* Vol. 101, No. 4. pp. 379–398. 1975.

Rateria, G. and B.W. Maurer. “Evaluation and Updating of Ishihara’s (1985) Model for Liquefaction Surface Expression, with Insights from Machine and Deep Learning.” *Soils and Foundations*. Vol. 62, No. 3. 101131. 2022.

Rathje, E., C. Dawson, J.E. Padgett, J.-P. Pinelli, D. Stanzione, A. Adair, P. Arduino, S.J. Brandenberg, T. Cockerill, C. Dey, M. Esteva, F.L. Haan, Jr., M. Hanlon, A. Kareem, L. Lowes, S. Mock, and G. Mosqueda. “DesignSafe: A New Cyberinfrastructure for Natural Hazards Engineering.” *ASCE Natural Hazards Review*. Vol. 18, No. 3. doi:10.1061/(ASCE)NH.1527-6996.0000246. 2017.

Robertson, P.K. “Soil Classification Using the Cone Penetration Test.” *Canadian Geotechnical Journal*. Vol. 27, No. 1. pp.151–158. doi: 10.1139/t90-014. 1990.

Robertson, P.K. “CPT-based SBT Classification System—An Update.” *Canadian Geotechnical Journal*. Vol. 53, No. 12. pp. 1,910–1,927. 2016.

Robertson, P.K. and K.L. Cabal. “Guide to CPT for Geotechnical Engineering. Signal Hill, California: 6th ed. Gregg Drilling Testing, Inc. 2015.

Robertson, P.K. and C.E. Wride, (Fear). “Evaluating Cyclic Liquefaction Potential Using the Cone Penetration Test.” *Canadian Geotechnical Journal*. Vol. 35, No. 3. pp. 442–459. 1998.

Robinson, K., M. Cubrinovski, and B.A. Bradley. “Sensitivity of Predicted Liquefaction-induced Lateral Displacements from the 2010 Darfield and 2011 Christchurch Earthquakes.” Proceedings of the New Zealand Society for Earthquake Engineering Annual Conference, Wellington, New Zealand. 8p. 2013.

Salvatier, J., T.V. Wiecki, and C. Fonnesbeck “Probabilistic Programming in Python Using PyMC3.” *PEERJ Computer Science*. 2:e55. 2016.

Sancio, R.B. “Ground Failure and Building Performance in Adapazari, Turkey.” University of California, Berkeley. 2003.

Sanín, M.V. *Cyclic shear loading response of Fraser River delta silt*. Ph.D. The University of British Columbia, Vancouver. 2010.

Sanín, M.V. and D. Wijewickreme. “Cyclic Shear Response of Channel-fill Fraser River Delta Silt.” *Soil Dynamics and Earthquake Engineering*. Vol. 26. pp. 854–869. 2006.

Seed, H.B. “Soil Liquefaction and Cyclic Mobility Evaluation for Level Ground During Earthquakes. *Journal of Geotechnical Engineering.* ASCE. Vol. 105, No, 2. p. 201–255. 1979.

Seed, H. B. (1983). ‘‘Earthquake resistant design of earth dams.’’ *Proc., Seismic Design of Embankments and Caverns*, Philadelphia, ASCE, New York, 46–64.

Seed, H.B. and I.M. Idriss. “Simplified Procedure for Evaluating Soil Liquefaction Potential.” *Journal of Geotechnical Engineering Division*. Vol. 97, No. 9. pp.1,249–1,273. 1971.

Seed, H.B., K. Tokimatsu, L.F. Harder Jr., and R. Chung. “Influence of SPT Procedures in Soil Liquefaction Resistance Evaluations. *Journal of Geotechnical Engineering*. Vol. 111, No 12. pp. 1,425–1,445. 1985.

Seed, H.B., K. Tokimatsu, L.F. Harder, Jr., and R. Chung. “Influence of SPT Procedures in Soil Liquefaction Resistance Evaluations. Report No. UCB/EERC-84/15. Earthquake Engineering Research Center, University of California, Berkeley. 1984.

Seed, H.B., K.L. Lee, I.M. Idriss, and F. Makdisi. “Analysis of the Slides in the San Fernando Dams During the Earthquake of February 9, 1971.” Report No. EERC-73-02. Berkeley, California. 1973.

Seed, H.B. and K.L. Lee. “Liquefaction of Saturated Sands During Cyclic Loading.” *Journal of the Soil Mechanics and Foundations Division*. Vol. 92, No. 6. pp. 105–134. 1966.

Seed, R.B., K.O. Cetin, R.E.S. Moss, A.M. Kammerer, J. Wu, J.M. Pestana, M.F. Riemer, R.B. Sancio, J.D. Bray, R.E. Kayen, A. Faris. Recent advances in soil liquefaction engineering: a unified and consistent framework. In: Proceedings of the 26th annual ASCE Los Angeles geotechnical spring seminar. 30 April 2003, Long Beach, California. 2003.

Sideras, S.S. *Evolutionary intensity measures for more accurate and informative evaluation of liquefaction triggering*. Ph.D. dissertation Dept. of Civil and Environmental Engineering, University of Washington. 2019.

Sivathayalan, S. *Static, cyclic and post liquefaction simple shear response of sands*. M.S. Thesis, Department of Civil Engineering, University of British Columbia, Vancouver, B.C., Canada. 1994.

Stuedlein, A.W., A. Dadashiserej, A. Jana, and T.M. Evans. “Liquefaction Susceptibility and Cyclic Response of Intact Nonplastic and Plastic Silts.” *Journal of Geotechnical and Geoenvironmental Engineering*. Vol. 149, No. 1. pp. 04022125. doi:10.1061/(ASCE)GT.1943-5606.0002935. 2023a.

Stuedlein, A.W., B. Alemu, T.M. Evans, S.L. Kramer, J.P. Stewart, K. Ulmer, K. Ziotopoulou. “PEER Workshop on Liquefaction Susceptibility.” PEER Report 2023/02. Pacific Earthquake Engineering Research Center, UC Berkeley (headquarters). 207p. 2023b.

Suzuki Y., T. Sanematsu, and K. Tokimatsu. “Correlation Between SPT and Seismic CPT.” P.K. Robertson and P.W. Mayne, eds. Proceedings, Conference on Geotechnical Site Characterization, Balkema, Rotterdam. pp. 1,375–1,380. 1998.

Suzuki, Y., K. Tokimatsu, Y. Taya, and Y. Kubota. “Correlation Between CPT Data and Dynamic Properties of In Situ Frozen Samples.” 3rd International Conference on Recent Advances in *Geotechnical Earthquake Engineering and Soil Dynamics*. Rolla, Missouri. pp. 249–252. 1995.

Suzuki, Y., S. Goto, M. Hatanaka, and K. Tokimatsu. “Correlation Between Strengths and Penetration Resistances for Gravelly Soils.” *Soils and Foundations, Japanese Society of Soil Mechanics and Foundation Engineering*. Vol. 33, No. 1. pp. 92–101. 1993.

Thevanayagam, S. “Effects of Fines and Confining Stress on Undrained Shear Strength of Silty Sands.” *Journal of Geotechnical and Geoenvironmental Engineering*. Vol. 124, No. 6. pp. 479-491. doi: 10.1061/(ASCE)1090-0241(1998)124:6(479). 1998.

Thomas, J. *Static, Cyclic and post liquefaction undrained behaviour of Fraser River sand*. M.A.S. Thesis, Department of Civil Engineering, University of British Columbia, Vancouver, B.C., Canada. 1992.

Tokimatsu, K. and Y. Yoshimi. “Empirical Correlation of Soil Liquefaction Based on SPT N-Value and Fines Content.” *Soils and Foundations*. Vol. 23, No. 4. pp. 56–74. 1983.

Tokimatsu, K., S. Tamura, H. Suzuki, K. Katsumata. “Building Damage Associated With Geotechnical Problems in the 2011 Tohoku Pacific Earthquake.” *Soils and Foundations*. Vol. 52, No.5. pp. 956–74. 2012.

Tsukamoto, Y., K. Ishihara, H. Nakazawa, K. Kamada, and Y. Huang. “Resistance of Partly Saturated Sand to Liquefaction with Reference to Longitudinal and Shear Wave Velocities.” *Soils Found*., Vol. 42, No. 6. pp. 93–104. https://doi.org/10.3208/sandf.42.6_93. 2002

Tsukamoto, Y., S. Kawabe, J. Matsumoto, and S. Hagiwara. “Cyclic Resistance of Two Unsaturated Silty Sands Against Soil Liquefaction.” *Soils and Foundations.* Vol. 54, No. 6. pp. 1,094–1,103. 2014.

Ulmer, K.J. *Development of an energy-based liquefaction evaluation procedure*. Ph.D. Dissertation, Virginia Tech, Blacksburg, Virginia. 2019.

Ulmer, K.J., B. Carlton, T. Nguyen, and Q. Parker. “An Expanded Data Set of Overburden (Kσ) and Initial Static Shear Stress (Kα) Correction Factors from Published Cyclic Laboratory Tests for Liquefaction Triggering Analyses.” *In Geo-Congress 2023.* pp. 197–206. 2023a.

Ulmer, K.J., R.A. Green, A. Rodriguez-Marek, J.K. Mitchell. “Energy-based Liquefaction Triggering Model.” *Journal of Geotechnical and Geoenvironmental Engineering*. In press. 2023b.

Ulmer, K.J., S.J. Brandenberg, K.S. Hudson, S.L. Kramer, P. Zimmaro, J. Stamatakos, and J.P. Stewart. “Task 7a: Progress Report on Final Liquefaction Model Development.” Washington, DC: U.S. Nuclear Regulatory Commission. April 2023c.

Ulmer K.J., P. Zimmaro, S.J. Brandenberg, J.P. Stewart, K.S. Hudson, A.W. Stuedlein, A. Jana, A. Dadashiserej, S.L. Kramer, K.O. Cetin, G. Can, M. Ilgac, K.W. Franke, R.E.S. Moss, S.F. Bartlett, M. Hosseinali, H. Dacayanan, D.Y. Kwak, J. Stamatakos, J. Mukherjee, U. Salman, S. Ybarra, and T. Weaver. “Next-generation Liquefaction Database.” Version 2. Next-Generation Liquefaction Consortium. doi: 10.21222/C23P70. 2023d.

Ulmer, K.J., B. Carlton, and J. Stamatakos. “Task 5b: Focused Study on the Effects of Overburden and Initial Static Shear Stresses.” Washington, DC: U.S. Nuclear Regulatory Commission. July 2022a.

Ulmer, K.J., R.A. Green, and A. Rodriguez-Marek. “Recommended B-value for Computing Number of Equivalent Stress Cycles and Magnitude Scaling Factors for Simplified Liquefaction Triggering Evaluation Procedures.” *Journal of Geotechnical and Geoenvironmental Engineering*. Vol. 148, No. 12. 04022113. 2022b.

Ulmer, K.J., K.S. Hudson, S.J. Brandenberg, P. Zimmaro, S.L. Kramer, and J.P. Stewart. “Task 4: Technical Letter Report Documenting Preliminary Probabilistic Liquefaction Models.” Washington, DC: U.S. Nuclear Regulatory Commission. August 2022c.

Ulmer, K.J., P. Zimmaro, S.J. Brandenberg, and J. Stamatakos. “Task 2: Liquefaction Case History Database Status Report.” Washington, DC: U.S. Nuclear Regulatory Commission. February 2021.

Ulmer, K.J., S. Upadhyaya, R.A. Green, A. Rodriguez-Marek, P.J. Stafford, J.J. Bommer, and J. van Elk. “Proceedings of the Geotechnical Earthquake Engineering and Soil Dynamics V, Slope Stability and Landslides, Laboratory Testing, and In Situ Testing, GSP 293.” Austin, Texas, June 2018. pp. 112–121. 2018.

Ulmer, K.J., K.S. Hudson, S.J. Brandenberg, P. Zimmaro, S.L. Kramer, and J.P. Stewart. “Task 8: Model Review Team Comments.” Washington, DC: U.S. Nuclear Regulatory Commission. March 2024.

Vaid, Y.P. and S. Sivathayalan. “Static and Cyclic Liquefaction Potential of Fraser Delta Sand in Simple Shear and Triaxial Tests.” *Canadian Geotechnical Journal*. Vol. 33, No. 2. pp. 281–289. 1996.

Vaid, Y.P. and J. Thomas. “Liquefaction and Post-liquefaction Behavior of Sand.” *Journal of Geotechnical and Geoenvironmental Engineering*. Vol. 121, No. 2. pp.163–173. 1995.

Vaid, Y.P. and J. Thomas. “Post-liquefaction Behaviour of Sand.” Proceedings of the 13th International Conference on Soil Mechanics and Foundation Engineering, New Delhi, India. pp. 1,305–1,310. 1994.

Vaid, Y.P., J.D. Stedman, and S. Sivathayalan. "Confining stress and static shear effects in cyclic liquefaction." *Canadian Geotechnical Journal.* Vol. 38, No. 3. pp. 580-591. 2001.

van Ballegooy, S., P. Mala, V. Lacrosse, M.E. Jacka, M. Cubrinovski, J.D. Bray, T.D. O’Rourke, S.A. Crawford, and H. Cowan. “Assessment of Liquefaction-induced Land Damage for Residential Christchurch. *Earthquake Spectra*. Vol. 30, No. 1. pp. 31–55. doi: 10.1193/031813EQS070M. 2014.

Virtanen, P., R. Gommers, T.E. Oliphant, M. Haberland, T. Reddy, D. Cournapeau, E. Burovski, P. Peterson, W. Weckesser, J. Bright, S.J. van der Walt, M. Brett, J. Wilson, K.J. Millman, N. Mayorov, A.R.J. Nelson, E. Jones, R. Kern, E. Larson, C.J. Carey, İ. Polat, Y. Feng, E.W. Moore, J. VanderPlas, D. Laxalde, J. Perktold, R. Cimrman, I. Henriksen, E.A. Quintero, C.R. Harris, A.M. Archibald, A.H. Ribeiro, F. Pedregosa, P. van Mulbregt, and SciPy 1.0

Contributors. “SciPy 1.0: Fundamental Algorithms for Scientific Computing in Python.” *Nature Methods*. Vol. 17, No. 3. pp. 261–272. 2020.

Wang, Y., K. Huang, and Z. Cao. “Probabilistic Identification of Underground Soil Stratification Using Cone Penetration Tests. *Canadian Geotechnical Journal*. Vol. 50, No. 1. pp. 766–769. 2013.

Whitman, R.V. “Resistance of Soil to Liquefaction and Settlement. *Soils and Foundations*. Vol. 11, No. 4. pp. 59–68. 1971.

Wiecki, T., J. Salvatier, R. Vieira, M. Kochurov, A. Patil, M. Osthege, B. T. Willard, B. Engels, C. Carroll, O. A. Martin, A. Seyboldt, A. Rochford, L. Paz, R. Goldman, K. Meyer, P. Coyle, M. E. Gorelli, O. Abril-Pla, J. Lao, R. Kumar, V. Andreani, T. Yoshioka, G. Ho, T. Kluyver, K. Beauchamp, A. Andorra, D. Pananos, E. Spaak, B. Edwards, and E. Ma. “pymc-devs/pymc: v5.9.1.” 2023.

Wijewickreme, D. “Cyclic Shear Response of Low Plastic Fraser River Silt.” 9th US National and 10th Canadian Conference on Earthquake Engineering 2010, Including Papers from the 4th International Tsunami Symposium, Toronto, Ontario, Canada, Paper No. 1431. 2010.

Wijewickreme, D., M.V. Sanin, and G.R. Greenaway. “Cyclic Shear Response of Fine-grained Mine Tailings.” *Canadian Geotechnical Journal*. Vol. 42, No. 5. pp. 1,408–1,421. 2005.

Worden, C.B., E.M. Thompson, J.W. Baker, B.A. Bradley, N. Luco, and D.J. Wald. “Spatial and Spectral Interpolation of Ground-Motion Intensity Measure Observations. *Bulletin of the Seismological Society of America*. Vol 108, No 2. pp. 866–875. 2018.

Yang, J., S. Savidis, and M. Roemer. “Evaluating Liquefaction Strength of Partially Saturated Sand.” *J. Geotech. Geoenvironmental Eng*., Vol. 130 No. 9. pp. 975–979. https://doi.org/10.1061/(ASCE)1090-0241(2004)130:9(975). 2004.

Yoshimi, Y., K. Tokimatsu, and J. Ohara. “In Situ Liquefaction Resistance of Clean Sands Over a Wide Density Range.” *Géotechnique*. Vol. 44, No. 3. pp. 479–494. 1994.

Yoshimi, Y., K. Tokimatsu, and Y. Hosaka. “Evaluation of Liquefaction Resistance of Clean Sands Based on High-quality Undisturbed Samples.” *Soils and Foundations, Japanese Society of Soil Mechanics and Foundation Engineering*. Vol. 29, No. 1. pp. 93–104. 1989.

Youd, T.L. and S.K. Noble. “Liquefaction Criteria Based on Statistical and Probabilistic Analyses.” In Proceedings NCEER Workshop on Evaluation of Liquefaction Resistance of Soils, State University of New York, Buffalo, New York. pp. 201–205. 1997.

Youd, T.L., I.M. Idriss, R.D. Andrus, I. Arango, G. Castro, J.T. Christian, R. Dobry, W.D.L. Finn, L.F.J. Harder, M.E. Hynes, K. Ishihara, J.P. Koester, S.S.C. Liao, W.F.I. Marcuson, G.R. Martin, J.K. Mitchell, Y. Moriwaki, M.S. Power, P.K. Robertson, and K.H.I. Stokoe. “Liquefaction Resistance of Soils: Summary Report from the 1996 NCEER and 1998 NCEER/NSF Workshops on Evaluation of Liquefaction Resistance of Soils.” *Journal of Geotechnical and Geoenvironmental Engineering*. Vol. 127, No. 10. pp. 817–833. doi: 10.1061/(ASCE)1090-0241(2001)127:10(817). 2001.

Zhang, B., K.K. Muraleetharan, and C. Liu. “Liquefaction of Unsaturated Sands,” *International* Journal of Geomechanics. Vol. 16, No. 6. 2016. https://doi.org/10.1061/(ASCE)GM.1943-5622.0000605.

Zhang, G., P.K. Robertson, and R.W.I. Brachman. “Estimating Liquefaction-induced Lateral Displacements Using the Standard Penetration Test or Cone Penetration Test.” *Journal of Geotechnical and Geoenvironmental Engineering*. Vol. 130, No. 8. pp. 861–871. 2004.

Zimmaro, P., D.Y. Kwak, Y.T. Tsai, J.P. Stewart, S.J. Brandenberg, A. Mikami, and S. Kataoka. “Database on Seismic Response of Instrumented Flood Control Levees.” *Earthquake Spectra*. Vol. 36. pp. 924–938. 2020.

APPENDIX A

Table A-1 Parameters in the Summary pkl File Containing SMT's Processed Case History Data

Parameter	Description	Classification
TEST_ID	primary key in test table	metadata
dGWT	depth to groundwater table (m)	layer
ztop	depth to top of layer (m)	layer
zbot	depth to bottom of layer (m)	layer
qc min	minimum qc within-layer (kPa)	layer
qc avg	average qc within-layer (kPa)	layer
qc 30%	30th percentile qc within-layer (kPa)	layer
qc 50%	median qc within-layer (kPa)	layer
qc max	maximum qc within-layer (kPa)	layer
qc std	standard deviation of qc within-layer (kPa)	layer
fs min	minimum fs within-layer (kPa)	layer
fs avg	average fs within-layer (kPa)	layer
fs 30%	30th percentile fs within-layer (kPa)	layer
fs 50%	median qc within-layer (kPa)	layer
fs max	maximum fs within-layer (kPa)	layer
fs std	standard deviation of fs within-layer (kPa)	layer
sigma_v min	minimum vertical total stress (kPa)	layer
sigma_v avg	average vertical total stress (kPa)	layer
sigma_v 50%	median vertical effective stress (kPa)	layer
sigma_v max	maximum vertical total stress (kPa)	layer
sigmap_v min	minimum vertical effective stress (kPa)	layer
sigmap_v avg	average vertical effective stress (kPa)	layer
sigmap_v 50%	median vertical effective stress (kPa)	layer

Table A-1 Parameters in the Summary pkl File Containing SMT's Processed Case History Data (cont'd)

Parameter	Description	Classification
sigmap_v max	maximum vertical effective stress (kPa)	layer
Ic min	minimum soil behavior type index	layer
Ic avg	average soil behavior type index	layer
Ic 30%	30th percentile soil behavior type index	layer
Ic 50%	median soil behavior type index	layer
Ic 70%	70th percentile soil behavior type index	layer
Ic max	maximum soil behavior type index	layer
Ic std	standard deviation of soil behavior type index	layer
qc1Ncs min	minimum normalized clean sand cone tip resistance	layer
qc1Ncs avg	average normalized clean sand cone tip resistance	layer
qc1Ncs 30%	30th percentile normalized clean sand cone tip resistance	layer
qc1Ncs 50%	median normalized clean sand cone tip resistance	layer
qc1Ncs max	maximum normalized clean sand cone tip resistance	layer
qc1Ncs std	standard deviation of normalized clean sand cone tip resistance	layer
CSR avg	average cyclic stress ratio computed using Idriss (1999) r_d	layer
I_B	modified soil behavior type index	layer
Su	undrained shear strength (kPa)	layer
taucycsu	cyclic shear stress divided by undrained shear strength	layer
IF_layer	layer interbeddedness factor (number of double threshold crossings above the layer, where Ic_thresh1 = 2.34, Ic_thresh2 = 2.93)	layer

Table A-1 Parameters in the Summary pkl File Containing SMT's Processed Case History Data (cont'd)

Parameter	Description	Classification
H1	thickness of non-liquefiable crust (m)	profile
SITE_ID	primary key of site table	metadata
SITE_NAME	site name	metadata
TEST_NAME	test name	metadata
EVNT_ID	primary key of event table	metadata
EVNT_NAME	event name	metadata
EVNT_MAG	earthquake magnitude	profile
PGA	peak horizontal acceleration (g)	profile
FLDM_ID	primary key of fldm (field observation) table	metadata
FLDM_SFEV	surface evidence of liquefaction (0 = no, 1 = yes)	profile
FLDM_DIST	distance between observation and cone penetration test (m)	profile
TEST weights	weights for observation in regression	profile
alltriggers	Total number of double Ic threshold crossings in the profile, where Ic_thresh1 = 2.34; Ic_thresh2 = 2.93	profile
FLDM_SNBL	sand boils (0 = no, 1 = yes)	profile
FLDM Slope (deg)	slope at observation location from 3-arc second digital elevation model (deg)	profile
TEST Slope (deg)	slope at test location from 3-arc second digital elevation model (deg)	profile
LPI	liquefaction potential index	profile
LSN	liquefaction severity number	profile
CR	crust strength (kN/m)	profile
LD	liquefaction ejecta demand parameter (kN/m)	profile
PGV	peak ground velocity (m/s)	profile
CAV	cumulative absolute velocity (m/s)	profile

Table A-1 Parameters in the Summary pkl File Containing SMT's Processed Case History Data (cont'd)

Parameter	Description	Classification
I_a	Arias intensity (m/s)	profile
CSR Lasley r_d	CSR computed using stress reduction coefficient from Lasley et al. (2017)	layer
MSF B&I	magnitude scaling factor from Boulanger and Idriss (2016)	layer
MSF Green et al	magnitude scaling factor from Green et al. (2019)	layer
MSF Green et al b=0.2	magnitude scaling factor from Green et al. (2019) for b = 0.2	layer
MSF Green et al b=0.28	magnitude scaling factor from Green et al. (2019) for b = 0.28	layer
Ksig I&B	K-sigma from Idriss and Boulanger (2008)	layer
Ksig Carlton	K-sigma for SMT model	layer
LDI	Liquefaction ejecta demand parameter within the layer (kN/m)	layer
CRI	Crust resistance above a layer (kN/m)	layer
qc1N	Overburden corrected cone tip resistance (kPa)	layer

APPENDIX B – EXAMPLE APPLICATION OF PROPOSED MODEL

This appendix provides an example application of the P[M_P] model using data from a case history in the NGL database: Wufeng Site A, which had no surface manifestation despite very strong shaking during the 1999 Chi-Chi Taiwan earthquake.

The four CPT profiles shown here have false positive predictions using legacy models (critical layers above the probability of liquefaction = 0.5 curve). These analyses began at the stage where the raw CPT data had been discretized into layers (using the algorithm in Section 5.3) and converted into q_{c1Ncs} and I_c values for each layer. Another critical step is the assignment of a ground surface PGA value and earthquake magnitude; for the present analysis the conditions for the event that produced the observations were used (Section 5.2), but in general forward applications these would be derived from seismic hazard analyses. In this section, the calculations will be illustrated in detail for CPT WAC-4 and then results are provided for all four CPTs.

Eq. B-1 is used to compute the probability of manifestation for each layer, P[M_L].

$$P[M_L] = 1 - \left(1 - PF_{M|T_l} PF_{T|S_l} PF_{S_l} K_{Sat_l}\right)^{t_l/t_c} \qquad \textbf{B-1}$$

There are four model components within Eq. B-1 ($PF_{M|T_l}$, $PF_{T|S_l}$, PF_{S_l}, and K_{Sat_l}) and one variable (t_l). Each model component is computed for each layer, given the respective independent variables, with the results tabulated on the right side of Table B-1 and displayed in Figure B-1.

Table B-1. Example Computation of P[M_P] for Wufeng Site A WAC-4 for the first 20 layers in the profile.

Layer #	z_{top} (m)	z_{bot} (m)	t (m)	q_{c1Ncs}	I_c	$CSR_{M7,.5,1atm}$	PF_S	$\widehat{CSR}$	D_R (%)	$\widehat{D_R}$	$\widehat{CRR}$	$PF_{T\|S}$	PF_T	$PF_{M\|T}$	K_{Sat}	P[M_L]
1	0.05	0.5	0.45	7.7	1.96	0.26	0.98	-2.21	0.00	-0.8	-7.46	1.00	0.98	0.81	0.00	0.00
2	0.5	1.118	0.618	3.9	2.76	0.26	0.30	-2.21	0.00	-0.8	-7.46	1.00	0.30	0.18	0.00	0.00
3	1.118	1.35	0.232	3.9	2.76	0.26	0.30	-2.21	0.00	-0.8	-7.46	1.00	0.30	0.15	1.00	0.01
4	1.35	1.8	0.45	1.0	3.89	0.30	0.00	-1.86	0.00	-0.8	-7.46	1.00	0.00	0.00	1.00	0.00
5	1.8	3	1.2	5.2	2.72	0.35	0.36	-1.54	0.00	-0.8	-7.46	1.00	0.36	0.14	1.00	0.03
6	3	3.8	0.8	45.3	2.75	0.38	0.31	-1.34	24.50	38.1	-6.14	1.00	0.31	0.09	1.00	0.01
7	3.8	5.55	1.75	16.1	2.91	0.41	0.16	-1.22	0.00	-0.8	-7.46	1.00	0.16	0.04	1.00	0.01
8	5.55	5.8	0.25	108.7	2.08	0.42	0.95	-1.17	58.49	109.9	-3.71	0.99	0.94	0.29	1.00	0.04
9	5.8	6	0.2	20.8	3.06	0.42	0.08	-1.16	0.16	-0.7	-7.45	1.00	0.08	0.01	1.00	0.00
10	6	6.3	0.3	92.0	1.91	0.42	0.98	-1.15	51.43	94.1	-4.25	1.00	0.98	0.38	1.00	0.07
11	6.3	9.5	3.2	19.0	3.03	0.43	0.09	-1.12	0.00	-0.83	-7.46	1.00	0.09	0.01	1.00	0.00
12	9.5	10.4	0.9	76.9	2.37	0.43	0.80	-1.11	44.12	78.10	-4.79	1.00	0.80	0.04	1.00	0.01
13	10.4	10.65	0.25	26.0	3.09	0.44	0.06	-1.11	6.68	7.33	-7.18	1.00	0.06	0.00	1.00	0.00
14	10.65	11	0.35	101.9	2.28	0.43	0.87	-1.11	55.71	103.64	-3.92	0.99	0.86	0.03	1.00	0.01
15	11	12.1	1.1	19.1	2.99	0.43	0.11	-1.11	0.00	-0.83	-7.46	1.00	0.11	0.00	1.00	0.00
16	12.1	13	0.9	176.5	1.95	0.43	0.98	-1.12	81.01	163.04	-1.92	0.80	0.78	0.06	1.00	0.02
17	13	13.65	0.65	89.0	2.20	0.43	0.91	-1.12	50.04	90.99	-4.35	1.00	0.91	0.02	1.00	0.01
18	13.65	13.9	0.25	8.7	3.21	0.43	0.03	-1.12	0.00	-0.83	-7.46	1.00	0.03	0.00	1.00	0.00
19	13.9	14.15	0.25	91.3	2.16	0.43	0.93	-1.13	51.10	93.33	-4.27	1.00	0.92	0.02	1.00	0.00
20	14.15	14.4	0.25	13.2	3.06	0.43	0.07	-1.13	0.00	-0.83	-7.46	1.00	0.07	0.00	1.00	0.00

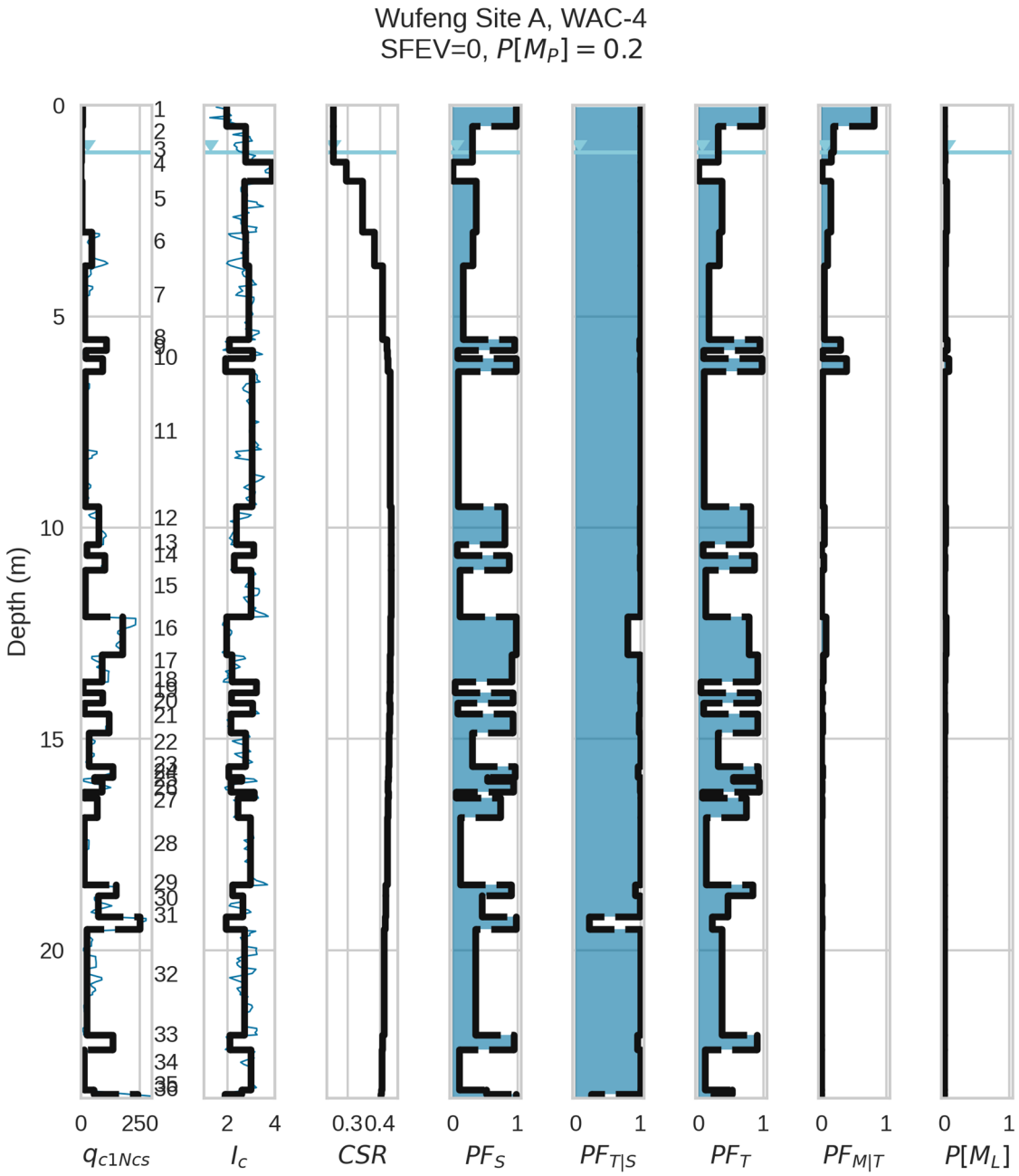

Figure B-1. CPT "WAC-4" from Wufeng Site A with *CSR* computed using a *PGA* estimate from the 1999 Chi-Chi, Taiwan earthquake and probability factors used to compute P[M_L] for each layer. The total P[M_P] prediction is printed at the top of the figure along with the observation of manifestation (SFEV=1) or lack of manifestation (SFEV=0).

Considering first the PF_S component (probability factor for susceptibility), the independent variable is I_c (Eq. 6-20). For example, the first layer that is below the ground water table and

clearly granular (Layer 8) has I_c=2.08, and produces PF_S = 0.95, indicating a highly susceptible layer.

$$PF_S = 1 - \frac{1}{1 + \exp\left(\frac{-1.702 \cdot \left({}^{I_c}/_{2.614} - 1\right)}{0.116}\right)} = 1 - \frac{1}{1 + \exp\left(\frac{-1.702 \cdot \left({}^{2.08}/_{2.614} - 1\right)}{0.116}\right)} = 0.95 \quad \textbf{B-2}$$

Next, the probability factor for triggering given susceptibility ($PF_{T|S}$) is computed. This is a function of $\widehat{CSR}$ and $\widehat{CRR}$ (Eq. 6-15) and therefore requires some transformations of the CPT data. $\widehat{CSR}$ can be computed directly from $CSR_{M7.5,1atm}$ (Eq. 6-16), which is demonstrated for layer 8 in Eq. B-3. Relative density (D_r) is estimated from the q_{c1Ncs} value of the layer (Eq. 6-19) yielding D_r=58% in Eq. B-3 which is then converted to $\widehat{D_r}$ = 109.9 (Eq. 6-18) in Eq. B-5. $\widehat{CRR}$ can then be computed (Eq. 6-17) in Eq. B-6 and combined with $\widehat{CSR}$ to produce $PF_{T|S}$ = 0.99 (Eq.B-7). This indicates that layer 8, being a low tip resistance layer shaken at a high intensity, is likely to trigger.

$$\widehat{CSR} = \frac{(CSR^{-0.6566} - 1)}{-0.6566} = \frac{(0.42^{-0.6566} - 1)}{-0.6566} = -1.17 \quad \textbf{B-3}$$

$$0 < D_r < 100\% = 47.8 \cdot {q_{c1Ncs}}^{0.264} - 106.3 = 47.8 \cdot 108.7^{0.264} - 106.3 = 58\% \quad \textbf{B-4}$$

$$\widehat{D_r} = \frac{\left({D_r}^{1.2022} - 1\right)}{1.2022} = \frac{(58^{1.2022} - 1)}{1.2022} = 109.9 \quad \textbf{B-5}$$

$$\widehat{CRR} = -7.427 + 0.0338 \cdot \left(\widehat{D_r}\right) = -7.427 + 0.0338 \cdot (109.9) = -3.71 \quad \textbf{B-6}$$

$$PF_{T|S} = \frac{1}{1 + \exp\left(\frac{-1.702 \cdot \left(\widehat{CSR} - \widehat{CRR}\right)}{0.985}\right)} = \frac{1}{1 + \exp\left(\frac{-1.702 \cdot \left(-1.17 - (-3.71)\right)}{0.985}\right)} = 0.99 \quad \textbf{B-7}$$

Taking the product of PF_S and $PF_{T|S}$ gives the probability factor of triggering (PF_T), a metric that accounts for both the susceptibility and triggering potential of the layer. The PF_T for layer 8 is computed in Eq. B-8 to be 0.94.

$$PF_T = PF_{T|S} * PF_S = 0.99 * 0.95 = 0.94 \quad \textbf{B-8}$$

The probability factor for manifestation given triggering ($PF_{M|T}$) is a function of I_c and z_{top} (Eq. 6-14) and is computed for layer 8 in Eq. B-9. $PF_{M|T}$ is nearly zero for layer 8, which is expected

because the layer is thin and deep, being overlain by predominantly clay layers. Therefore, if liquefaction were to occur in this layer, it would be unlikely to produce surface manifestations.

$$PF_{M|T} = \frac{1}{1+\exp\left(-\left(8.206 - 0.342 \cdot z_{top} - 3.461 \cdot I_c\right)\right)} = \frac{1}{1+\exp\left(-(8.206 - 0.342 \cdot 2.08 - 3.461 \cdot 5.55)\right)} = 0.29 \quad \textbf{B-9}$$

Finally, the saturation term, K_{Sat}, which is taken as a binary outcome of 0 above the groundwater table and 1 below the groundwater table, is assigned to each layer (taken as 1 for layer 8). With all model components derived, the probability of manifestation for layer 8 can be computed,

$$P[M_L] = 1 - \left(1 - PF_{M|T} PF_{T|S} PF_S K_{Sat}\right)^{\frac{t}{t_c}} = 1 - (1 - 1 * 0.29 * 0.99 * 0.94)^{\frac{0.25}{2}} = 0.04 \quad \textbf{B-10}$$

This shows that layer 8 is unlikely to manifest. Looking at the different layers in Table B-1, most have no appreciable manifestation potential. Among the different layers, layer 10 has the strongest manifestation potential (0.38), although even this result is modest, which is due mainly to its limited susceptibility potential.

The total manifestation probability for the profile, P[M_P], can now be computed as the product sum of the P[NM_L] = 1-P[M_L] values for all layers using Eq. B-11,

$$P[M_P] = 1 - \prod_{l=1}^{N_L} (1 - P[M_L]_l)^{t_l/t_c} \quad \textbf{B-11}$$

This yields P[M_P] ~ 0.2 for WAC-4, indicating a low probability of manifestation, making it a “no” surface evidence prediction. This matches the observation of no manifestation for this site in Wufeng. This prediction occurs despite there being multiple layers beneath the groundwater table that have a high probability factor for triggering, due to the features of the manifestation model.

Results similar to those for CPT WAC-4 were generated for the other CPTs at the site – WAC-5, 7, and 9. These results are plotted in Figure B-2 through Figure B-4. Each of these CPTs correctly predict no manifestation for the profile despite the presence of layers with high PF_T and “yes” manifestation predictions from legacy models. Table B-2 summarizes the probability of manifestation predicted using Boulanger and Idriss (2016) for the critical layer selected on the basis of being susceptible and having the highest predicted P_L in the profile, as well as the P[M_P] predicted using the recommended model.

Table B-2. Probability of manifestation predictions for Boulanger and Idriss (2016) and the recommended P[M_P] model compared with surface evidence of manifestations for Wufeng Site A CPTs.

CPT Number	Boulanger and Idriss (2016) P_L	P[M_P]	Surface Evidence?
4	0.99	0.20	No
5	0.99	0.41	No
7	0.99	0.17	No
9	0.99	0.21	No

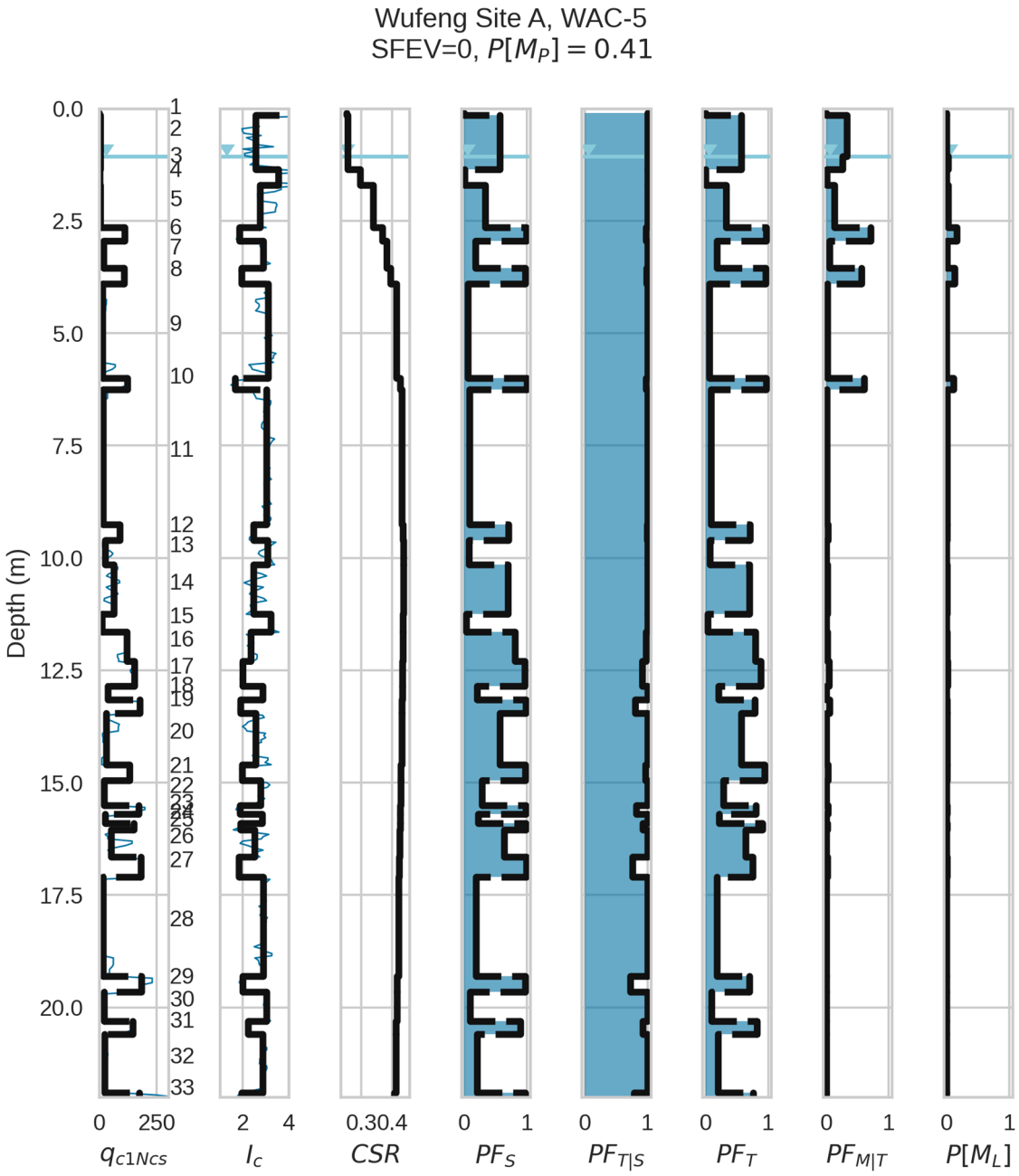

Figure B-2. **CPT "WAC-5" from Wufeng Site A with *CSR* computed using a *PGA* estimate from the 1999 Chi-Chi, Taiwan earthquake and probability factors used to compute P[M_L] for each layer. The total P[M_P] prediction is printed at the top of the figure along with the observation of manifestation (SFEV=1) or lack of manifestation (SFEV=0).**

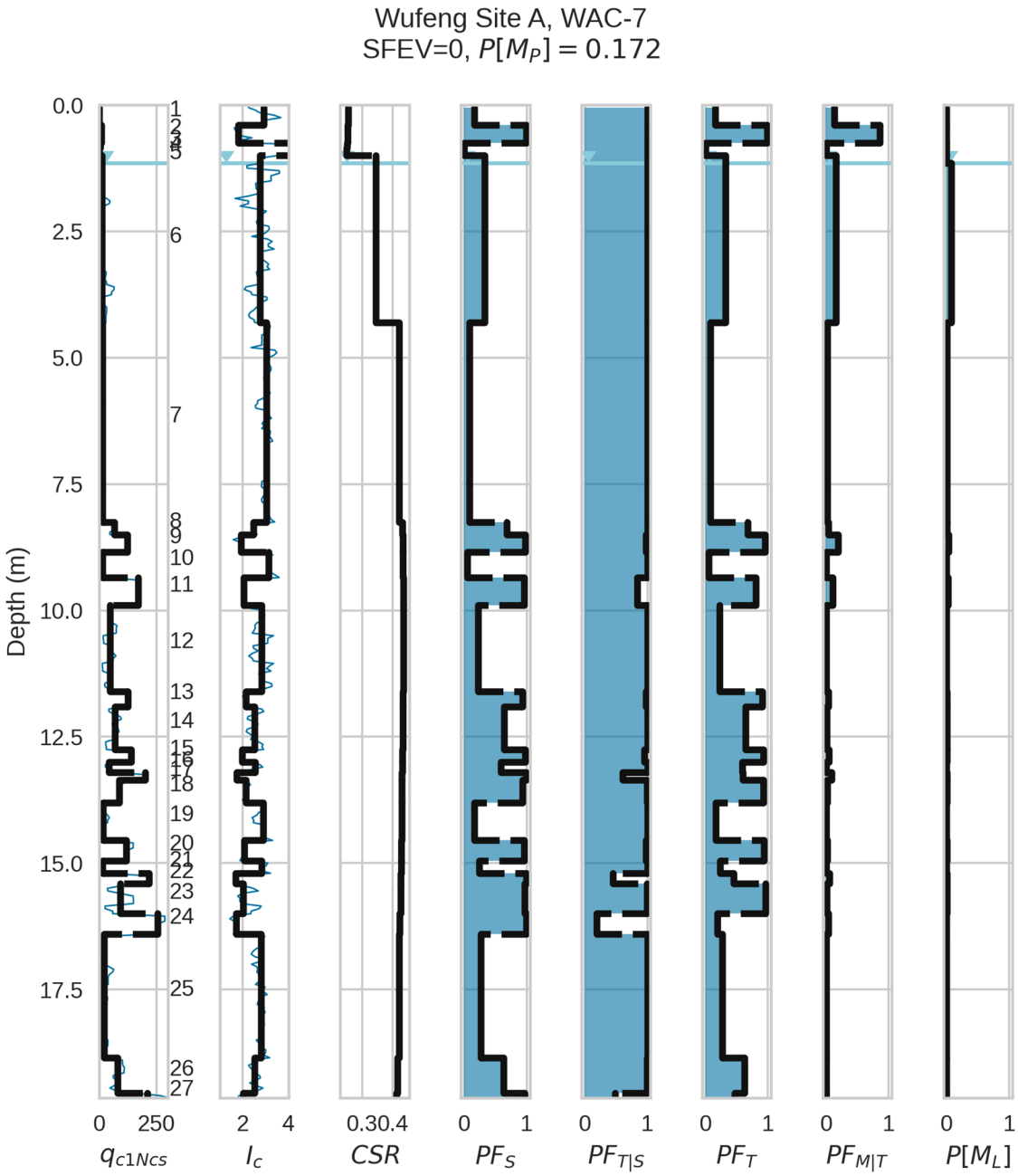

Figure B-3. **CPT "WAC-7" from Wufeng Site A with *CSR* computed using a *PGA* estimate from the 1999 Chi-Chi, Taiwan earthquake and probability factors used to compute P[M_L] for each layer. The total P[M_P] prediction is printed at the top of the figure along with the observation of manifestation (SFEV=1) or lack of manifestation (SFEV=0).**

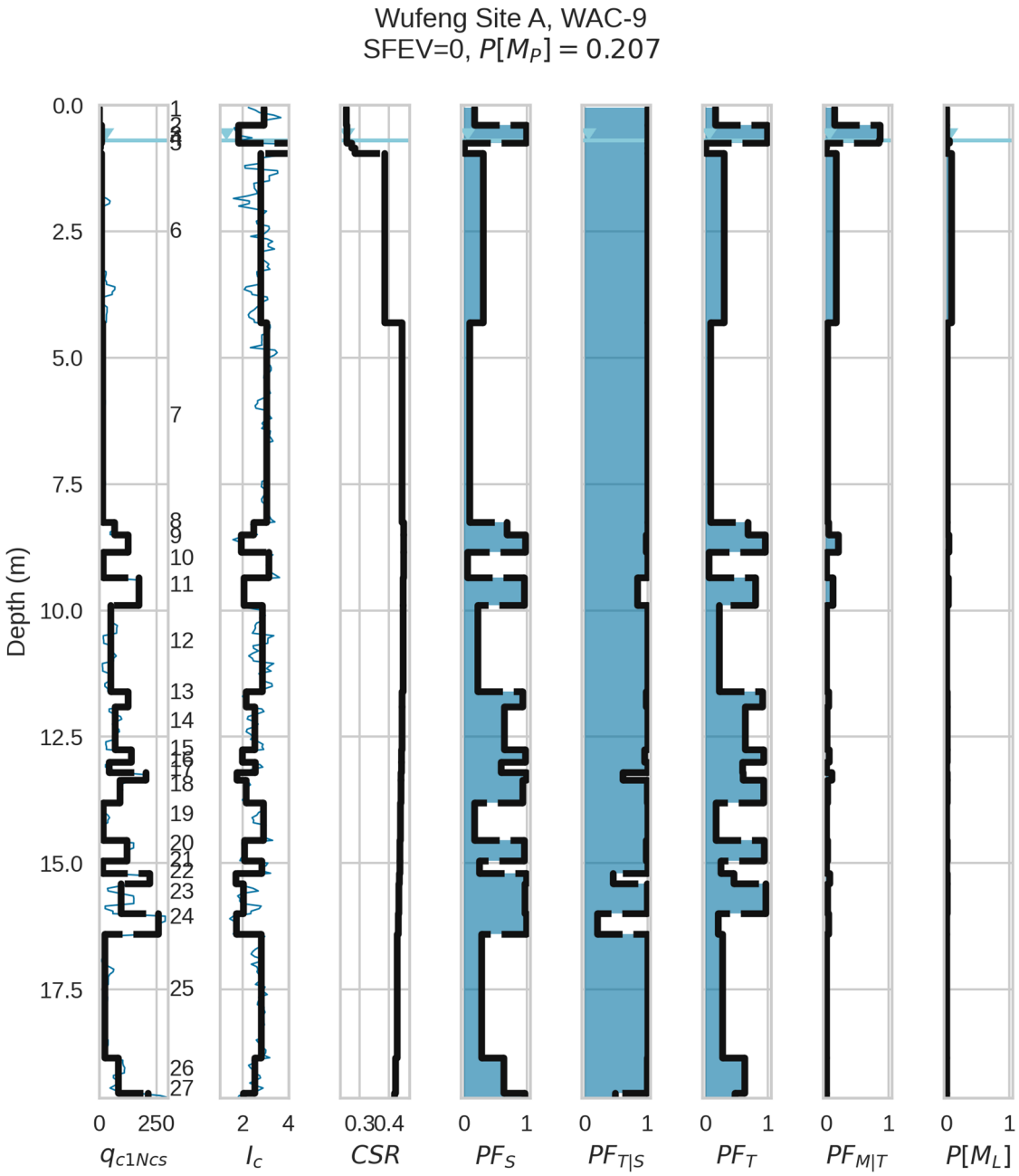

Figure B-4. **CPT "WAC-9" from Wufeng Site A with *CSR* computed using a *PGA* estimate from the 1999 Chi-Chi, Taiwan earthquake and probability factors used to compute P[M_L] for each layer. The total P[M_P] prediction is printed at the top of the figure along with the observation of manifestation (SFEV=1) or lack of manifestation (SFEV=0).**